

Development of a Planar Shipboard Skid-equipped Rotary-wing Aircraft Manoeuvring and Securing Simulation

by

Alexander R. Schock

A thesis submitted to
the Faculty of Graduate and Postdoctoral Affairs
in partial fulfilment of
the requirements for the degree of
Master of Applied Science
in
Mechanical Engineering

Ottawa-Carleton Institute for Mechanical and Aerospace Engineering
Department of Mechanical and Aerospace Engineering
Carleton University
Ottawa, Ontario, Canada
September 2020

Copyright ©
2020 – Alexander R. Schock

Abstract

The capacity of unmanned aircraft systems (UAS) to operate in environments that are hazardous to humans, their preclusion of human error during operations, and progressively-declining operating costs motivate their increasing use in maritime shipboard operations in severe weather. Their high thrust-to-weight ratio and typical stiff ‘skid-type’ landing gear constrain mechanical securing and traversing options, and present complex ship-helicopter interface behaviour which must be characterized.

A securing and traversing device concept has been developed in parallel with the development of the planar case of SRAMSS (Skid-equipped Rotary-wing Aircraft Manoeuvring and Securing Simulation). The planar case aims to verify the system formulation for the dynamic interface analysis of skid-equipped rotary-wing aircraft during shipboard operations in elevated sea and weather conditions.

SRAMSS integrates four major techniques to achieve completeness of the simulation. First, SRAMSS models the aircraft as a fully-planar mass-coupled rigid airframe and dynamic flexible finite element landing gear. Second, direct method dynamic finite element modelling is used to characterize infinitely-variable skid-type landing gear, which is adapted for use in Kane’s method, and demonstrates a powerful technique for merging rigid-body and flexible-body dynamics. Third, complex ship-aircraft contact is modelled by a Separation Axis Theorem algorithm with dynamic response capabilities, including a LuGre frictional slider model. Aerodynamic wind-induced drag, and blade element rotor disc models complete the modelling of the embarked aircraft.

Thorough verification of the planar version of SRAMSS confirms the proper implementation, and simultaneous functioning of the included models. Preliminary validation of the rotor blade element model against computational and experimental data indicates the need for refinement. Nevertheless, the planar case of SRAMSS verifies a suitable system formulation for a state-of-the-art fully-spatial dynamic interface analysis simulation for skid-equipped rotary-wing aircraft.

Dedicated to the reader,
who may find valuable insight, or simply the enjoyment of the content herein.

Acknowledgements

I would like to sincerely thank all of the people who have unconditionally supported me through to the end of this research.

First and foremost, I would like to thank my supervisor Dr. Robert G. Langlois for his invaluable guidance and the wealth of knowledge imparted to me. Rob has afforded me the freedom to progress my research in the directions I saw fit, and has equitably received and debated the ideas I have brought forward.

I would also like to thank my family, friends, and loved ones for their relentless encouragement and support, even in the most demanding of times during my research.

Further, I would like to thank my fellow researchers for their exchange of knowledge and ideas, lending their time, and sharing in the struggles of the typical graduate student.

Finally I would like to thank Carleton University's Department of Mechanical and Aerospace Engineering and the Faculty of Graduate and Postdoctoral Affairs for the opportunity to pursue graduate studies and complete this research.

Thank you.

Contents

Abstract	i
Acknowledgements	iii
Contents	iv
List of Figures	vii
List of Tables	xi
List of Symbols	xii
Acronyms	xix
1 Introduction	1
1.1 Shipboard Securing and Manoeuvring Systems	2
1.2 Shipboard Helicopter Modelling	4
1.2.1 Ship Deck Motion	4
1.2.2 Securing and Manoeuvring Models	5
1.2.3 Skid-type Landing Gear Models	7
1.2.4 Aerodynamic Ship-helicopter Interactions	8
1.2.5 Rotary-wing Aerodynamics Modelling	8
1.3 Contact Modelling	9
1.4 Friction Modelling	10
1.5 Thesis Objectives	11
1.6 Thesis Overview	13
2 System Description	15
2.1 Securing and Manoeuvring System Conceptual Design	15

2.1.1	Securing and Manoeuvring Mechanism Requirements	16
2.1.2	Skid-type Securing and Manoeuvring Concept	16
2.2	Mathematical Conventions and Methods	17
2.3	Dynamic System Definition	24
3	System Kinematics	32
3.1	Body Kinematics	33
3.2	Polygon Kinematics	42
4	System Dynamics	47
4.1	Dynamic Finite Element Model	48
4.2	Contact Dynamics Model	57
4.3	Aerodynamic Models	66
4.3.1	Aerodynamic Body Drag Forces	67
4.3.2	Aerodynamic Rotor Disc Forces	68
4.4	Other Force-generating Elements	74
4.4.1	Flexible–Rigid Body Interface Model	75
4.4.2	External Damper Model	76
4.4.3	Gravitational Model	79
4.5	Inertial Forces	79
4.6	Summary of Kinetic Quantities	80
5	System Assembly and Simulation Architecture	82
5.1	System Assembly	82
5.2	Simulation Architecture	88
5.2.1	State Propagation	89
5.2.2	Contact Event Handling	90
5.2.3	Subroutine Architecture	94
6	SRAMSS Verification and Validation	97
6.1	Generic Aircraft Description	97
6.2	Test Cases Description	102
6.3	Test Cases Verification and Validation	107
6.3.1	Case 1: Gravitational Model	107
6.3.2	Case 2: External Damper Model	108
6.3.3	Case 3: Aircraft Centre of Gravity	111

6.3.4	Case 4: Landing Gear DFE Model	113
6.3.5	Case 5: Contact Dynamics Model	119
6.3.6	Case 6: Aerodynamics Models	126
6.3.7	Case 7: Securing Concept Verification	136
6.3.8	Case 8: Comprehensive Phenomena Verification	141
6.4	General Remarks	150
7	Conclusion	153
7.1	Completed Work	153
7.2	Recommendations	155
7.3	Future Work	157
	References	158
	Appendix A SRAMSS I/O File Structure	165
A.1	Input Files	165
A.2	Output Files	171
	Appendix B Case 6 Prescribed Aerodynamics	172
B.1	Case 6.2: Rotor Thrust without Wind	172
B.2	Case 6.3: Rotor Thrust with Head-wind	173
B.3	Case 6.4: Rotor Thrust with Head-wind and Cyclic Compensation	174
	Appendix C Case 6 Experimental Blade Profiles	175
C.1	Case 6.5 S-76 Experimental Blade Profile	175
C.2	Case 6.5 S-76 SRAMSS Blade Profile	178
	Appendix D Case 8 Prescribed Parameters	180
D.1	Case 8: Prescribed Aerodynamics	180
D.2	Case 8: Prescribed Motions	181
	Appendix E Simulation Statistics	183
E.1	Case 8: 18/20/160	183

List of Figures

1.1	SH-60 Seahawk hovering over ship deck landing zone equipped with LAMPS III RAST system [1].	2
1.2	Recovery Assist, Secure and Traverse (RAST) system [1].	3
1.3	Aircraft Ship Integrated Secure and Traverse (ASIST) system [2].	3
1.4	System description of Blackwell and Feik [3].	5
1.5	Force-generating elements included in Dynaface [®] [4].	6
1.6	System description of Heliman [5].	6
1.7	Skid-type landing gear description [6].	7
2.1	Planar representation of the skid-equipped securing and manoeuvring system.	17
2.2	Planar description of SRAMSS simulation environment.	25
2.3	System frames of reference.	26
2.4	Aircraft frames of reference.	27
4.1	2D beam element degrees of freedom.	49
4.2	Arbitrarily-oriented 2D beam element frames of reference.	51
4.3	Arbitrary axis separating two polygons.	58
4.4	Separation of polygons P and Q along surface normal axis ${}^P_N\hat{\mathbf{s}}_1$	59
4.5	Separation between DFE node n_{j_c} and defined polygon P	59
4.6	Surface normal axes ${}^S_N\hat{\mathbf{s}}_m$ for the ship polygon S	60
4.7	Surface penetration penalty function diagram.	62
4.8	LuGre friction bristle model.	64
4.9	Rotor disc blade element model for generic aircraft.	69
4.10	Rotor disc BEM mesh.	70
4.11	Rotor blade element airflow and forces diagram.	71
4.12	Interface of DFE nodes to the airframe.	75

4.13	Discrete external damper mounting locations.	77
5.1	State propagation with root-finding step termination.	90
5.2	SRAMSS program architecture.	95
6.1	Generic aircraft used in verification and validation test cases.	98
6.2	Generic aircraft blade profile.	101
6.3	Case 1 Aircraft CoG y-position and y-acceleration with respect to the inertial frame.	107
6.4	Case 2 Airframe vertical response due to discrete external linear damper property variation.	109
6.5	Case 2 Landing gear vertical response due to discrete external linear damper property variation.	110
6.6	Case 2 Landing gear horizontal response due to discrete external linear damper property variation.	110
6.7	Case 3 Airframe roll-angle response to shifted CoGs.	111
6.8	Case 3 Steady-state aircraft roll versus airframe CoG x-offset.	112
6.9	Case 3 Contact node normal forces versus airframe CoG offset.	113
6.10	Case 4 DFE model mesh configurations.	115
6.11	Case 4.1 Aircraft response for fixed landing gear with DFE model mesh refinements.	116
6.12	Case 4.1 DFE model node construction.	116
6.13	Case 4.2 Aircraft response for hinged landing gear with DFE model mesh refinements.	118
6.14	Case 5.1 Steady-state simulation configurations for normal force eval- uation.	119
6.15	Case 5.2 Sliding velocity of leading (right) landing gear foot	121
6.16	Case 5.2 Trailing (n_1) and leading (n_6) landing gear feet frictional forces	122
6.17	Case 5.3 Oriented dynamic response simulation configurations.	123
6.18	Case 5.3 Position of airframe and contact nodes in the ‘RSD push’ scenario.	124
6.19	Case 5.3 Position of airframe and contact nodes in the ‘RSD drag’ scenario.	125
6.20	Case 5.3 Position of airframe and contact nodes in the ‘RSD hook’ scenario.	126

6.21	Case 6.1 Aircraft horizontal sliding velocity due to induced drag.	127
6.22	Case 6.1 Aircraft vertical acceleration due to induced drag.	128
6.23	Case 6.2 Rotor disc thrust and airframe CoG height above the RSD deck.	129
6.24	Case 6.3 Rotor disc thrust and rolling moment, and airframe CoG position relative to the RSD deck.	130
6.25	Case 6.4 Rotor disc thrust and rolling moment, and airframe CoG position relative to the RSD deck.	132
6.26	Case 6.5 Comparison of blade section thrust coefficient between SRAMSS BEM model and CFD analysis from Garcia and Barakos.	133
6.27	Case 6.5 Comparison of FoM for SRAMSS BEM and CFD model. $M_{tip} = 0.65, \theta_t = \{4^\circ, 5^\circ, 6^\circ, 7^\circ, 8^\circ, 9^\circ\}$	135
6.28	Case 6.5 Comparison of FoM for SRAMSS BEM and CFD model. $M_{tip} = 0.60, \theta_t = \{6.5^\circ, 7.5^\circ, 8.5^\circ, 9.5^\circ\}$	136
6.29	Case 7.1 Static aircraft securing simulation configurations.	137
6.30	Case 7.1 Static aircraft securing in the ‘On-centre’ scenario.	138
6.31	Case 7.1 Static aircraft securing in the ‘Off-centre’ scenario.	138
6.32	Case 7.1 Static aircraft securing in the ‘Rolled Ship’ scenario.	139
6.33	Case 7.2 Dynamic aircraft securing simulation configurations.	139
6.34	Case 7.2 Dynamic aircraft securing in the ‘Rolling Ship’ scenario.	140
6.35	Case 7.2 Dynamic aircraft securing in the ‘RSD Manoeuvre’ scenario.	140
6.36	Case 7.2 Contact force magnitudes in the ‘Rolling Ship’ scenario.	141
6.37	Case 7.2 Contact force magnitudes in the ‘RSD Manoeuvre’ scenario.	141
6.38	Case 8 Comprehensive simulation time-stamped event animations.	145
6.39	Case 8 Airframe CoG position versus time for all combinations of $n_n/N_\psi/N_e$	146
6.40	Case 8 Aircraft distances relative to RSD points.	147
6.41	Case 8 Contact force magnitudes at each contact node.	148
6.42	Case 8 Rotor disc force magnitudes.	149
B.1	Case 6.2 Prescribed aerodynamic values.	172
B.2	Case 6.3 Prescribed aerodynamic values.	173
B.3	Case 6.4 Prescribed aerodynamic values.	174
C.1	S-76 model rotor blade profile [7].	176

C.2	S-76 model rotor blade profile [8].	177
C.3	Case 6.5 SRAMSS S-76 model rotor blade profile.	178
D.1	Case 8 Prescribed aerodynamic values.	181
D.2	Case 8 Prescribed polygon motions.	182

List of Tables

1.1	Shipboard securing and manoeuvring modelling summary	12
4.1	Contact forces summary	65
4.2	Complete system forces summary	81
6.1	Generic aircraft parameters	99
6.2	DFE node functionality for generic aircraft	99
6.3	Rotor disc blade element model parameters	100
6.4	Contact dynamics parameters	100
6.5	SRAMSS verification and validation test cases	103
6.6	Case 1 Undeformed versus steady-state helicopter posture	108
6.7	Case 2 Discrete damper parameter variations	109
6.8	Modified DFE model parameters for use in Case 4	114
6.9	Case 5.1 Contact normal forces at static equilibrium	120
6.10	Modified aircraft simulation parameters for use in Sub-case 5.2	121
C.1	SRAMS S-76 model BEM parameters	179

List of Symbols

Mathematical Notations and Operators:

\mathbb{R}	Real number
\mathbb{Z}	Integer
$\vec{}$	Physical vector quantity
$\hat{}$	Unit vector quantity
$\frac{d}{dt} ()$	Time derivative of expression in parenthesis
$\dot{}$	First time derivative
$\ddot{}$	Second time derivative
$ $	Absolute value
$\ \ $	Magnitude (Euclidean norm)
\sim	Skew-symmetric matrix representation
\circ	Hadamard product (element-wise multiplication)
$'$	Adjusted value
$ _x$	Vector component along x axis of 2D frame
$ _y$	Vector component along y axis of 2D frame
$ \theta$	Vector component about z axis of 2D frame
$ _{x,3D}$	Vector component along x axis of 3D frame
$ _{y,3D}$	Vector component along y axis of 3D frame
$ _{z,3D}$	Vector component along z axis of 3D frame

Frames of Reference:

N	Inertial frame of reference (origin at mean ship speed and heading)
H	Helicopter frame of reference (origin at airframe CoG)

G	Landing gear finite element model global frame
n_j	Landing gear j th finite element node frame of reference (aligned to G-frame)
R	Rotor disc frame of reference
S	Ship deck polygon frame of reference
D	RSD deck polygon frame of reference
CL	Left wedge clamp polygon frame of reference
CR	Right wedge clamp polygon frame of reference

Indices:

d	d th external external damper
h	h th rotor blade element
i	i th generalized coordinate and generalized speed
j	j th dynamic finite element node, $\forall j \in \{1, \dots, N_n\}$
j_c	j_c th dynamic finite element node considered for contact, $j_c \subseteq j$
j_d	j_d th dynamic finite element node with attached external damper, $j_d \subseteq j$
j_u	j_u th dynamic finite element node interfacing with the airframe, $j_u \subseteq j$
k	k th body in the complete system
l	l th rotor disc sector
m	m th vertex of a polygon
r	r th generic summation element index

Variables:

A	Finite element cross-sectional area
\mathbf{A}_{eq}	Equivalent flat-plate area
$[\mathbf{A}]$	System assembly matrix
$[\mathbf{A}(t)]$	Penetration state matrix
\mathbf{B}	System assembly vector
$[\mathbf{B}(t)]$	Penetration state change matrix
CL_m	m th left wedge clamp polygon vertex
CR_m	m th right wedge clamp polygon vertex

c_h	Rotor blade element chord length
C_d	External damper linear damping coefficient
C_f	Friction micro-displacement linear damping coefficient
C_p	Penetration linear damping coefficient
$C_{L_{hl}}$	Rotor blade element lift coefficient
$C_{L_{h,\alpha=0}}$	Rotor blade element zero angle of attack lift coefficient
$\frac{dC_L}{d\alpha_{hl}}$	Lift coefficient gradient with respect to angle of attack
$C_{D_{hl}}$	Rotor blade element drag coefficient
$C_{D_{h,\alpha=0}}$	Rotor blade element zero angle of attack drag coefficient
$\frac{dC_D}{d\alpha_{hl}}$	Drag coefficient gradient with respect to angle of attack
\mathbf{C}	System assembly vector
$[\mathbf{C}]$	Dynamic finite element total structure proportional damping matrix
D_m	m th RSD deck polygon vertex
$[\mathbf{D}]$	System assembly matrix
$[\mathbf{D}(t)]$	Contact surface matrix
E	Finite element Young's modulus
F_d	Dynamic friction force
F_{dd}	d th external damper force
F_{LuGre}	LuGre model friction force
F_i	i th generalized active force
F_i^*	i th generalized inertial force
F_s	Static friction force
\mathbf{F}	System generalized active forces
\mathbf{F}^*	System generalized inertia forces
\mathbf{F}_G	Finite element external nodal forces expressed in the global element frames
\mathbf{F}_l	Finite element external nodal forces expressed in the local element frames
\mathbf{F}_{sys}	Complete system forcing vector
$g(t)$	Event root function
I_H	Airframe inertia
I	Finite element second moment of area
K_d	External damper linear stiffness coefficient
K_f	Friction micro-displacement linear stiffness coefficient
K_p	Penetration linear stiffness coefficient
$[\mathbf{K}]$	Dynamic finite element total structure stiffness matrix

$[\mathbf{K}_l]$	Element stiffness matrix expressed in local element frames
$[\mathbf{K}_G]$	Element stiffness matrix expressed in globally-aligned element frames
L	Finite element length
m_H	Airframe mass
M_{tip}	Rotor blade tip Mach number
M_{hl}	Rotor blade element Mach number
M_d	d th external damper airframe mount
$[\mathbf{M}]$	Dynamic finite element total structure consistent mass matrix
$[\mathbf{M}_l]$	Element consistent mass matrix expressed in local element frames
$[\mathbf{M}_G]$	Element consistent mass matrix expressed in globally-aligned element frames
$[\mathbf{M}_{sys}]$	Complete system mass matrix
N_b	Number of rotor blades
N_B	Number of bodies in the system
N_d	Number of external dampers
N_e	Number of rotor blade elements
N_{gc}	Number of generalized coordinates in the system
N_n	Number of dynamic finite element nodes
N_P	Number of polygons
N_u	Number of dynamic finite element interface nodes
$N_{s,P}$	Number of surfaces in polygon P
$N_{v,P}$	Number of vertices in polygon P
N_ψ	Number of rotor disc azimuth selectors
$[\mathbf{N}]$	Polynomial interpolation shape functions matrix
\vec{o}	Object contact point
P	Generic polygon P
P_m	m th generic polygon P vertex
q_i	i th generalized coordinate
\dot{q}_i	i th generalized coordinate time-derivatives
\mathbf{q}	System generalized coordinates
$\dot{\mathbf{q}}$	System generalized coordinate time-derivatives
$\dot{\mathbf{q}}_H$	Airframe generalized coordinate time-derivatives
$\dot{\mathbf{q}}_n$	Dynamic finite element node generalized coordinate time-derivatives
r	Radial position on rotor blade

dr	Rotor blade element width
R_b	Rotor blade radius
R_i	Inner effective rotor blade radius as a percentage of rotor blade radius
R_o	Outer effective rotor blade radius as a percentage of rotor blade radius
\vec{R}^k	k th body active force
\vec{R}^{*k}	k th body inertial force
S_m	m th ship deck polygon vertex
t_{curr}	Time of current state propagation
t_e	Time of detected simulation event
t_{ref}	Simulation time reference
t_{sol}	End time of last successfully propagated solution
\vec{T}^k	k th body active torque
\vec{T}^{*k}	k th body inertial torque
t/c_h	Rotor blade element thickness-to-chord ratio
u_a	Axial displacement of node a for finite element spanning from node a to node b
u_b	Axial displacement of node b for finite element spanning from node a to node b
u_i	i th generalized speed
U	Total volume strain energy
U_0	Strain energy per unit volume
\mathbf{u}	System generalized speeds
\dot{u}_i	i th generalized speed time-derivative
\mathbf{u}_n	Dynamic finite element node generalized speeds
$\dot{\mathbf{u}}$	Generalized speed time-derivatives
$\dot{\mathbf{u}}_P$	Polygon generalized speed time-derivatives
$\dot{\mathbf{u}}_H$	Airframe generalized speed time-derivatives
$\dot{\mathbf{u}}_G$	Global finite element origin generalized speed time-derivatives
$\dot{\mathbf{u}}_n$	Dynamic finite element node generalized speed time-derivatives
$v_{0_{hl}}$	Rotor blade element axial flow velocity
$v_{1_{hl}}$	Rotor blade element flow velocity
$v_{2_{hl}}$	Rotor blade element tangential flow velocity
v_a	Shear displacement of node a for finite element spanning from node a to node b

v_b	Shear displacement of node b for finite element spanning from node a to node b
v_{chl}	Rotor blade element climb velocity
v_{ihl}	Rotor blade element induced flow velocity
v_{rel}	Relative sliding velocity of contact node along contact surface
v_s	Stribeck velocity threshold
$v_{wind,x}$	Longitudinal wind velocity component
$v_{wind,y}$	Lateral wind velocity component
$v_{wind,z}$	Vertical wind velocity component
${}_k \mathbf{V}^{u_i}$	Linear partial contribution along u_i to kinematic quantity of body k , expressed in the k th frame
$[\mathbf{V}]$	Linear partial velocity matrix
$[\mathbf{V}_n]$	Array of dynamic finite element node linear and angular partial velocity matrices
$[\mathbf{V}_u]$	Array of dynamic finite element node linear and angular partial velocity matrices for interface nodes
$[\mathbf{W}]$	Angular partial velocity matrix
\mathbf{x}_{sys}	System solution
$\dot{\mathbf{x}}$	State derivative vector
$\vec{\mathbf{Y}}_k$	k th body remainder angular acceleration terms
\mathbf{Y}_n	Array of dynamic finite element node remainder angular acceleration terms
$\vec{\mathbf{Z}}_k$	k th body remainder linear acceleration terms
\mathbf{Z}_n	Array of dynamic finite element node remainder linear acceleration terms
α_{hl}	Rotor blade element angle-of-attack
α_0	Proportional damping mass constant
α_1	Proportional damping stiffness constant
β	Strain-displacement matrix
δ	Nodal displacements along degrees of freedom
$\delta_{ab,l}$	Nodal displacements expressed in local frame
$\delta_{ab,G}$	Nodal displacements expressed in globally-aligned nodal frames
δ_n	Nodal displacements expressed in globally-aligned nodal frames for all nodes
Δ_d	External damper compressed length
$\Delta_{d,0}$	External damper uncompressed length
Δ_f	Friction micro displacement

$\Delta_{f,max}$	Maximum allowable friction micro-displacement
Δ_p	Surface penetration depth
Δt	Current solution step successfully propagated time
Δt_{sol}	Default solution propagation time-step length
Δt_e	Solution propagation time-step length where event is detected
$\dot{\Delta}_d$	External damper rate of compression
$\dot{\Delta}_f$	Friction rate of micro-displacement
$\dot{\Delta}_p$	Relative surface penetration velocity
ϵ	Finite element material property matrix
γ	ratio of specific heats
μ_d	Dynamic friction coefficient
μ_s	Static friction coefficient
ω_1	Proportional damping lower bound frequency
ω_2	Proportional damping upper bound frequency
ϕ_{hl}	Flow angle relative to rotor disc plane
ψ	Rotor blade azimuth
ψ_l	l th rotor blade sector azimuth
ψ_{max}	Azimuth of maximum cyclical pitch setting
ρ	Finite element density
ρ_{air}	Density of air
θ_a	Angular displacement of node a for finite element spanning from node a to node b
θ_b	Angular displacement of node b for finite element spanning from node a to node b
θ_{coll}	Rotor blade collective pitch setting
θ_{cycl}	Rotor blade cyclical pitch setting
$\theta_{cyc,max}$	Maximum rotor blade cyclical pitch setting
θ_{hl}	Rotor blade element pitch setting
θ_{th}	Rotor blade twist angle
Θ_{ab}	Dynamic finite element orientation relative to the global finite element frame
ξ_1	Proportional damping lower bound damping ratio
ξ_2	Proportional damping upper bound damping ratio

Acronyms

ASIST	Aircraft Ship Integrated Secure and Traverse
ASV	Anti-surface vessel
ASW	Anti-submarine warfare
BDF	Back-differentiation
BEM	Blade element model
BEMT	Blade element momentum theory
BET	Blade element theory
BVH	Bounding volume hierarchy
CFD	Computational fluid dynamics
CoG	Centre of gravity
CPU	Central processing unit
CSM	Contact surface matrix
DFE	Dynamic finite element
DFMEA	Design failure mode and effect analysis
DLSODAR	Double-precision Livermore solver for ordinary differential equations with automatic solver switching and root finding
DLTV	Dead-load test vehicle
DoF	Degree-of-freedom
DRDC	Defence Research and Development Canada
OCP	Object contact point
ODE	Ordinary differential equation
PSM	Penetration state matrix
PSCM	Penetration state change matrix
RBE	Rotor blade element
SAR	Search and rescue
SAT	Separation axis theorem

SPR	Spatial partitioning representation
SRAMSS	Skid-equipped Rotary-wing Aircraft Manoeuvring and Securing Simulation
SSMASH	Spacial Securing and Manoeuvring Analysis for Shipboard Helicopters
RAO	Response amplitude operator
RAST	Recovery Assist, Secure and Traverse
RHR	Right-hand rule
RSD	Rapid securing device
TC-ASIST	Twin-claw Aircraft Ship Integrated Secure and Traverse
UAS	Unmanned aircraft system

Chapter 1

Introduction

The mobility of helicopters has been recognized and leveraged for maritime operations around the world, for the past half-century. Helicopters have seen a wide variety of roles including increasing ship line-of-sight and area-of-effect, search and rescue (SAR), maritime work-site transportation, anti-submarine warfare (ASW), and anti surface vessel (ASV) strike to name a few [1]. In mission-critical situations, ship-based helicopters are required to operate in severe weather conditions. These conditions can be hazardous to both air crew, deck crew, and the equipment itself.

Maritime shipboard operations in severe weather is an ideal example of a task considered hazardous to humans for which Unmanned Aircraft Systems (UAS) offer a widely-recognized beneficial alternative. Their capacity to operate in high-risk environments to humans, their preclusion of human error during operations, and progressively-declining operating costs are some of the motivations driving the increasing use of UASs. To this point, UAS usage has already proliferated into shipboard operations. For example: the U.S. Navy's use of the Northrop Grumman MQ-8B Fire Scout as a ship-based UAS system [9]; the Royal Canadian Navy has investigated the use of Armed Drones [10]; and QuinetiQ will be providing the Royal Canadian Navy with UAS based on the Skeldar V-200 UAS [11].

Whether a piloted helicopter or UAS, rotary-wing aircraft require assistive securing and manoeuvring devices to operate in challenging maritime conditions. For conventional maritime helicopters equipped with compliant landing gear and grippy tires, such as the SH-60 Seahawk shown in Figure 1.1, there exists assistive landing, securing, and manoeuvring devices for shipboard operations. Accordingly, simulation software specifically targeted at studying the dynamics of shipboard operations for

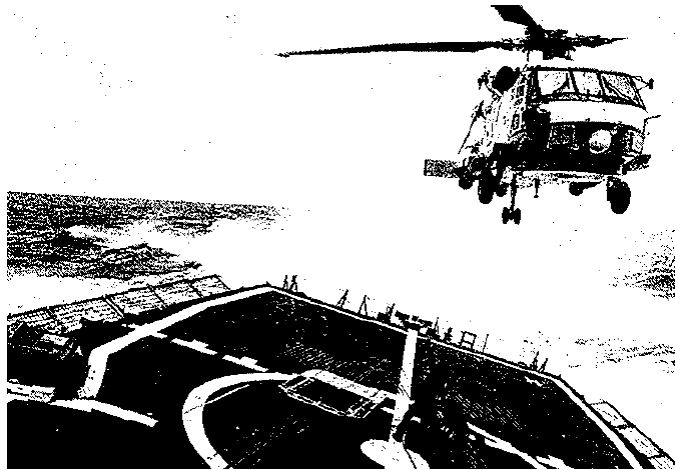


Figure 1.1: SH-60 Seahawk hovering over ship deck landing zone equipped with LAMPS III RAST system [1].

these types of helicopters is available.

The following sections present a literature review of a notable shipboard securing and manoeuvring systems and dynamic shipboard models. They will reveal the limitations in devices and associated dynamic models as they relate to UASs and other skid-equipped aircraft embarking on shipboard operations.

1.1 Shipboard Securing and Manoeuvring Systems

Transient ship motion in severe weather often exceeds the aircraft's capabilities to precisely station-keep above the ship deck while in flight, and remain stationary while on deck. In order to aid aircraft landing, securing, and on-deck manoeuvring, various assistive systems have been used to a great degree of success. Notable systems used by navies around the world include three Indal Technologies Inc. devices: Recovery Assist, Secure and Traverse (RAST), Aircraft Ship Integrated Secure and Traverse (ASIST), and the Twin-claw ASIST (TC-ASIST) [1, 2]. Although the three systems utilize a Rapid Securing Device (RSD) on rails integrated into the ship deck to secure a probe fixed to the aircraft, they vary in their modes of operation.

First, the RAST system employs a recovery assist haul-down cable under constant tension to guide the aircraft towards the ship deck and the RSD probe trap, as shown in Figures 1.1 and in the technical drawing of Figure 1.2 [1]. Second, the ASIST systems are free landing systems where the RSD tracks the motion of the aircraft

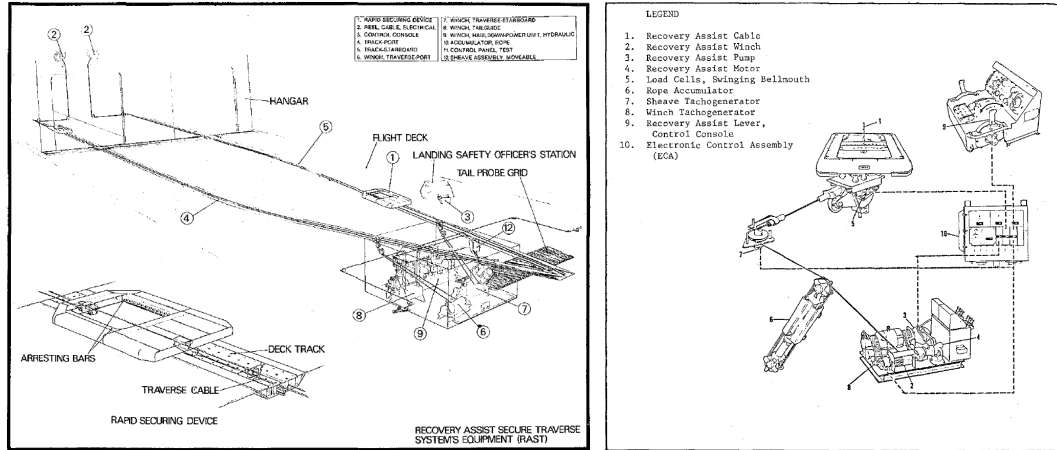


Figure 1.2: Recovery Assist, Secure and Traverse (RAST) system [1].

relative to the ship deck, and aligns to capture the securing probe upon aircraft touch-down on deck as shown in Figure 1.3 [2]. Lastly, TC-ASIST is an ASIST variant designed to work with probe-less aircraft [2]. In all cases, these devices are able to secure the aircraft to the ship. Notably, these devices are designed to work with aircraft using compliant landing gear with grippy tires, which enables the systems to both exploit available passive tire frictional forces in restraining the aircraft, and to manoeuvre the aircraft into shipborne hangars.



Figure 1.3: Aircraft Ship Integrated Secure and Traverse (ASIST) system [2].

Other ship deck securing devices exist. For example: the Cramms HLS Heligrd system uses a perforated disc fixed to the ship deck designed to receive a ‘harpoon’-style probe fixed to the aircraft which penetrates and locks to the disc [12]. This

system can accommodate various styles of landing gear; however this system is limited by its inability to manoeuvre aircraft once they are secured. This presents a problem in more severe weather where the aircraft should be sheltered from the elements by a shipborne hangar. The aircraft would necessarily have to be transferred to another system such as the SAMAHE [13] for manoeuvring, and this transfer creates a securing vulnerability. In any case, being able to model the dynamic interaction between the ship and the aircraft is an essential tool in the design and operation of these securing systems and shipboard operation-capable aircraft.

1.2 Shipboard Helicopter Modelling

The dynamic interaction between the ship and aircraft, often referred to as ‘dynamic interface analysis’, is indispensable in determining factors including design loads, operational envelopes, performance, and operating procedures. Under the scope of dynamic interface analysis, there are many aspects to consider: ship deck motion resulting from hydrodynamic interactions between the ship hull and surrounding sea, aircraft landing, securing and manoeuvring dynamics, and aerodynamic effects resulting from ship superstructure air-wake and environmental factors.

1.2.1 Ship Deck Motion

Ship deck motion dominates the dynamics of a ship-embarked aircraft. There are commercially available packages such as SHIPMo3D which use a 3D panel method to determine transient ship motion, capable of outputting linear response amplitude operator (RAO) data for use in 3rd party software [14]. Indal Technologies Inc. has developed a fully 3D, non-linear, time-domain ship motion program called SPLAShMo to generate transient ship motion to be used with their dynamic interface analysis software Dynaface[®] [15, 16]. SPLAShMo’s lack of linear simplifications makes it well suited to studying the motion of smaller naval vessels operating in higher sea states, which represent a significant subset of vessels undergoing shipboard rotary-wing aircraft operations [15].

Other ship motion software packages include strip theory-based ShipmoPC, a derivative of SHIPMO 7 developed at Defence Research and Development Canada (DRDC) [17], which can account for hydrodynamic effects of hull appendages and output RAOs. Additionally, FREDYN is a blended time-domain method package

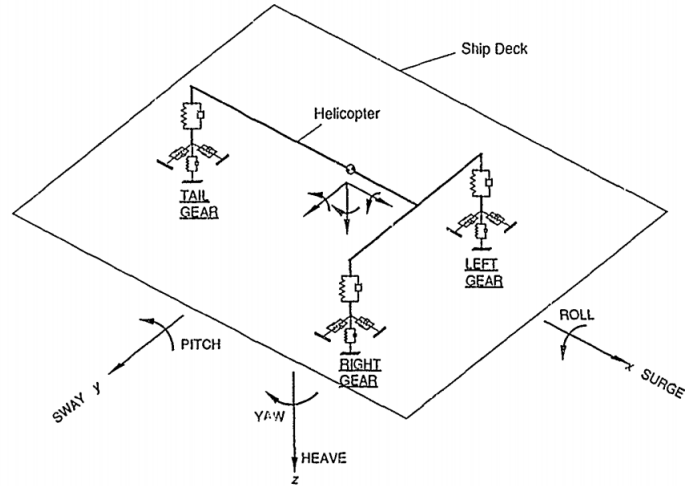


Figure 1.4: System description of Blackwell and Feik [3].

aimed at ship manoeuvring in calm waters [18].

1.2.2 Securing and Manoeuvring Models

As a culmination of many disciplines of engineering, dynamic interface analysis has been widely researched. Early research into dynamic interface modelling from Blackwell and Feik [3] characterized a single rigid body aircraft on an arbitrarily moving ship deck with two-stage non-linear damped spring oleo representation, and massless spring tire representation as shown in Figure 1.4. The work was limited to studying ship deck motion response, excluding aerodynamic, securing, and handling forces.

A refined simulation package named Dynaface[®] was developed by Langlois et al. [16] at Indal Technologies Inc. Also characterized as a single rigid body, the simulated aircraft is acted on by dynamic effects generated by ship motion, aerodynamics, landing gear suspension, tires, securing devices, and lashing cables. However, it is not capable of simulating shipboard transient manoeuvring.

Addressing embarked aircraft manoeuvring, Linn developed simulation software named *Heliman* [5] for the purpose of analyzing embarked helicopter handling and manoeuvring. Limited to the planar case without ship motion as shown in Figure 1.6, prescribed probe motion enabled the evaluation of aircraft planar translation and yaw (including castor steering) response. The lack of ship motion response analysis in *Heliman* was addressed by an experimental motion platform developed by Feldman [19],

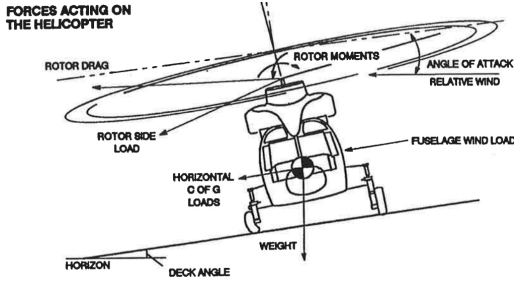


Figure 1.5: Force-generating elements included in Dynaface[®] [4].

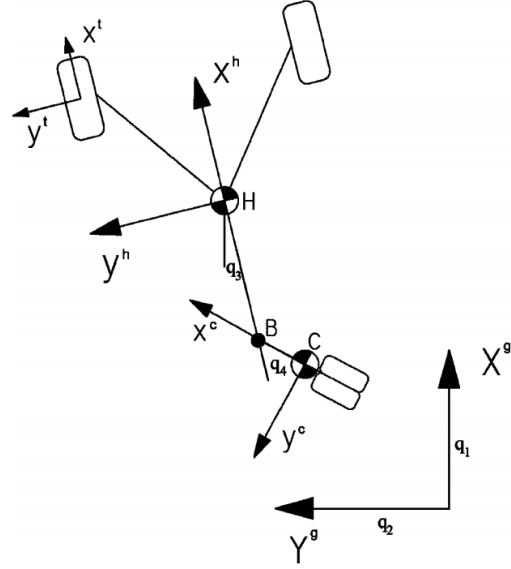


Figure 1.6: System description of Heliman [5].

capable of simulating combinations of surge, sway, heave, roll, and pitch motions. It included a 2 degree-of-freedom (DoF) scale model of Indal’s ASIST system, and a scale Dead-Load Test Vehicle (DLTV). Experimental results highlighted the additive effects of the RSD manoeuvres and ship deck motion in securing forces experienced by the DLTV. Aerodynamic effects were not considered. It also concluded that autonomous embarked aircraft manoeuvring is possible. Subsequently Feldman et al. developed and implemented an autonomous straightening and traversing procedure [20].

Building on the efforts made by Langlois et al., Linn, and Feldman, the SSMASH (Spacial Securing and Manoeuvring Analysis for Shipboard Helicopters) was developed by Léveillé [21]. It provides complete analysis capabilities for the analysis of on-deck helicopter/ship dynamic interface. A fully-spacial aircraft model with bodies representing the aircraft and its landing gear, coupled with 6-DoF ship motion, and a 5-DoF tire model allow complete simulation of securing and manoeuvring of embarked aircraft under full ship motion conditions. However, it does not include the Rotor thrust and induced rotor forces characterized by Dynaface[®] [22].

Section 1.1 has described shipboard securing and manoeuvring systems, and the modelling thereof, for rotary wing aircraft which employ compliant landing gear equipped with grippy tires. As with helicopters, managing ship deck and aircraft dynamics for UASs is critical. However, for UASs, aerodynamic forces acting on

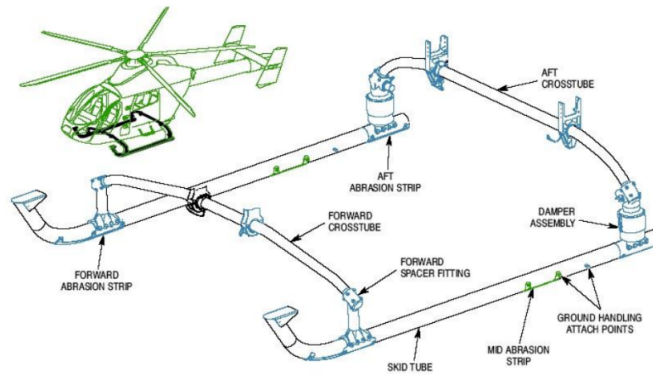


Figure 1.7: Skid-type landing gear description [6].

the UAS become even more important due to the higher thrust to weight ratio of typical UASs compared to helicopters. Furthermore, UASs often use less compliant ‘skid-type’ landing gear which constrain mechanical securing and manoeuvring options, and present more complex ship-helicopter interface behaviours which must be characterized.

1.2.3 Skid-type Landing Gear Models

Skid-type landing gear are lightweight alternatives in comparison to conventional wheeled landing gear. As shown in Figure 1.7, skid-type landing gear are composed of structural tubes assembled to form two main parallel skid-tubes for contact with the ground, which are attached to the aircraft by cross-tubes. Analyzing skid-equipped aircraft undergoing shipboard manoeuvres in hazardous weather is critical to the safety of deck crews and equipment.

With the increasing use of UASs in shipboard operations, Indal Technologies Inc. recognized both the proliferation of UAS usage in [23] and the trend of equipping UAS with skid type landing gear in [6]. As a result, an extension for Dynaface[®] was created with two skid landing gear models; one using a fast linear stiffness method, and the other using a non-linear finite element structural modelling approach [6]. The extension allowed for the dynamic interface analysis of an embarked skid-equipped aircraft acted on by aerodynamics, securing mechanisms, and ship deck motion. However, as previously stated, Dynaface[®] is unable to simulate shipboard manoeuvring.

The author is unaware of any other simulation software that specifically addresses

skid-type landing gear within the framework of dynamic interface analysis.

1.2.4 Aerodynamic Ship-helicopter Interactions

Beyond the significant effects that ship motion have on embarked helicopters, aerodynamic effects are equally important. A wide range of phenomena have been studied. Lee and Zan studied the ship's airwake effects on rotorless aircraft fuselage loads [24]. Zan conducted sub-scale experiments to determine rotor thrust in ship airwakes, and the influence of ship geometry and wind speed direction [25]. Alpman et al. combined computational fluid dynamics (CFD) and a flight dynamics simulation model to study the dynamic interface of UH-60A helicopter hovering behind an aircraft hangar and the same helicopter approaching an LHA-class ship [26]. Wall et al. used an advancing Fourier series method for correlated turbulence modelling for a point moving through space [27]. In this case, to study a point on a helicopter blade, which was part of a larger scope modelling rotor blade sailing in unsteady airwakes by Wall et al. [28]. Even in the absence of ship airwakes, Khouli et al. showed for aeroelastic models that combinations of ship roll/pitch frequencies, and rotor disc frequencies could cause rotor tip displacements outside acceptable operating ranges [29].

A comprehensive real-time simulation package named RotorLib FDM was created by RTDynamics [30]. It includes a Blade Element Theory (BET) model which captures compressibility effects, ground effects, and autorotation. Moreover, the aircraft models are highly configurable, and the full flight regime of the aircraft can be modelled, including landing and take-off from moving surfaces.

1.2.5 Rotary-wing Aerodynamics Modelling

Section 1.2.4 highlights the breadth of effects that aerodynamic phenomena induce on rotary-wing aircraft near and embarked on ships. The typically higher thrust-to-weight ratio of UASs increases the effects of these aerodynamic phenomena. Both Dynaface[®] and SSMASH make efforts to characterize aerodynamic drag forces on the aircraft fuselage based on the relative aircraft velocity with respect to the apparent wind velocity and direction. Dynaface[®] also models rotor thrust using a time-dependent profile of rotor thrust. The thrust vector is transformed to equipollent forces and moments on the aircraft. At low rotor disc RPM it models induced rotor forces on the aircraft by double interpolation of the force components against

rotor disc's angle of attack and wind direction [22]. Neither simulation package considers phenomena such as blade sailing or ship airwake in the aerodynamic effects on the aircraft. Moreover, the lookup tables used in the double interpolation for induced forces used by Dynaface[®] are typically provided and protected by the manufacturer.

Stepniewski [43] presents basic theories for approaches to modelling rotor disc thrust generation. Models derived from Blade Element Theory (BET) and Blade Element Momentum Theory (BEMT) provide adequate fidelity in rotor performance without computational costs typically associated with CFD analysis [44], or requiring manufacturer-provided experimental or computational data. These models are highly adaptable for including many aerodynamic phenomena and thereby increasing fidelity as required. Blade element models discretizes the rotor blade into rotor blade elements which are assigned individual aerodynamic parameters and properties required for the application of basic lifting theories. Since the individual elements are assigned unique properties, more complex blade profiles can be approximated without the need for computationally expensive CFD analysis.

Having reviewed a number of applicable shipboard helicopter models and aerodynamic models, there is limited consideration made for the complex transient contact states between the aircraft and ship deck. For UAS typically equipped with skid-type landing gear, the rigidity of the landing gear creates complex and evolving contact states. As a result, a more comprehensive contact model should be considered. The following sections survey contact modelling and friction modelling.

1.3 Contact Modelling

The trend of UASs being equipped with skid-type landing gear, which are less compliant than conventional landing gear, realises an important consideration in the dynamic interface modelling of these types of aircraft. The rigidity of skid-type landing gear leads to complex, intermittent contact states. This leads to the requirement for a more refined contact model for dynamic interface analysis than those included in the securing and handling models presented in Section 1.2.2.

Contact modelling can be divided into two parts. First, the detection of collisions between objects studied can be separated into 'broad-phase' and 'narrow-phase' contact determination algorithms [31]. Broad-phase is a coarse search for pairs of objects with the potential for collision whereas narrow-phase is the direct evaluation of

contact. For larger systems, collision detection algorithms typically start with broad-phase detection then pass to narrow-phase contact evaluation. Collision detection can be further classified into ‘Spatial Partitioning Representations’ (SPR) and ‘Bounding Volume Hierarchies’ (BVH) [32]. The SPR is a discrete representation the simulation environment through the use of cells where pairs of objects occupying the same cells are evaluated for contact, and is well suited to broad-phase collision detection. Bounding volume hierarchies assign a volume which bounds the object evaluated for contact. these bounding volumes can be simple shapes which greatly increases contact determination efficiency. The Separation Axis Theorem (SAT) collision detection algorithm [33], based on the BVH ‘oriented bounding box’ [34] algorithm, lends itself well to the study of dynamics since the bounding volumes can exactly take the shape of the polygons representing objects.

Second, once collision is detected, the impact must be treated. Gilardi and Sharf [35] survey different methods for contact dynamics modelling. Many models exist, including discrete, continuous, Lagrangian multiplier, Hertzian models, etc. Notably, continuous closed-form models such as the spring-dashpot, Hertz, and non-linear damping models are easily integrated with the SAT algorithm to provide appropriately-oriented dynamic response to collision. These models consider collision restitution to maintain impenetrability of the colliding bodies. Friction modelling must also be present for the handling of prolonged contact between bodies.

1.4 Friction Modelling

Friction forces are an important component in generating an appropriately-oriented dynamic response to collision. In the securing and handling models of Section 1.2.2, contact friction modelling has fallen under the scope of tire models of conventional landing gear. They rely on a frictional slider implementing a virtual spring-damper model which saturates to the Coulomb friction value. For skid-type landing gear with hard contact surfaces, the transition between sticking and slipping is rapid due to less compliant materials when compared to the soft rubber tires of wheeled landing gear. Therefore a friction model which can accurately capture more complex phenomena is required.

Lampert et al. [36], Liu et al. [37], Marques et al. [38], and Pennestrì et al. [39] generally conclude that the LuGre friction model [40], an improvement of the Dahl

model [41], captures frictional phenomena accurately. The LuGre model’s use of ‘bristles’ is analogous to the frictional-slider models of current securing and handling software packages. It is able to model static, dynamic, and viscous friction, as well as pre-sliding micro displacements through the use of a Stribeck curve [40].

Swevers et al. [42] discuss the issues present in the hysteresis curves for the LuGre model in the pre-sliding regime. They propose the Leuven model, which implements a Maxwell-slip model into a hysteretic function for the pre-sliding regime, but is otherwise identical to the LuGre model. Lampert et al. note that the Leuven model agrees best with experimental results. Despite its accuracy, the hysteretic function of the Leuven model is more computationally expensive. It requires the addition of another state variable to reset the hysteretic function if sliding motion is achieved. Furthermore, the precision required by control systems in which these models are typically used is not as significant at the scale of dynamic interface analysis.

1.5 Thesis Objectives

As reviewed above, ship-helicopter interface dynamics have been extensively studied through many avenues. It has exposed the limitations in modelling interface dynamics and securing devices for skid-equipped UASs. With the proliferation of UASs in shipboard operations, the necessity to study their interface dynamics becomes apparent.

As with helicopters, managing ship deck and aircraft dynamics for UASs is critical. However, aerodynamic forces acting on the UAS become even more important due to the UAS’s higher thrust-to-weight ratio compared to helicopters. Furthermore, UASs often use less-compliant skid-type landing gear unlike conventional maritime helicopters that most commonly use compliant suspensions and grippy tires. These typical UAS characteristics constrain mechanical securing and traversing options, and present more complex ship-helicopter interface behaviours which must be characterized. Therefore a simulation package which can accurately capture the complex interface dynamics of stiff landing gear aircraft is necessary for the investigation of securing requirements and ensuring expected performance of all components in shipboard operations. Table 1.1 presents a summary of the existing models introduced in Section 1.2.2.

Table 1.1: Shipboard securing and manoeuvring modelling summary

Model		Wheel	Skid	Securing	Manoeuv.	Ship Motion	Aero.
Blackwell-Feik	3D	✓				✓	
Heliman	2D	✓		✓	✓		
Feldman	3D	✓		✓	✓	✓	
Dynaface [®]	3D	✓		✓		✓	✓
Dynaface [®] Skid	3D		✓	✓		✓	✓
RotorLib	3D	✓	✓			✓	✓
SSMASH	3D	✓		✓	✓	✓	✓ ¹
This Work	2D ²	✓ ³	✓	✓	✓	✓	✓

¹ Only aerodynamic body drag forces.

² This work develops and verifies the planar case, with the intent of expansion into 3D

³ Not within the scope of this work, but feasible.

Table 1.1 shows significant progress has been made with respect to the dynamic interface analysis of wheeled-landing gear helicopters. The proliferation of UAS in maritime shipboard operations and lack of availability of securing systems which can manoeuvre secured skid-equipped aircraft reveal a gap in the capabilities in the current state of dynamic interface analysis. The objective of this work is to fill the gap revealed in Table 1.1 by developing the planar (2D) case of a fully-spacial simulation package specifically aimed at skid-equipped aircraft. To achieve completeness of the objective, the simulation package should:

- Identify conceptual design requirements for a shipboard securing and manoeuvring system for skid-equipped rotary-wing aircraft;
- Develop fully 2D on-and off-deck modelling of aircraft dynamics, with dynamic system derivation and methodology appropriate for expansion to 3D;
- Simulate the complete recovery flight, securing, manoeuvring, and launch phases of shipboard helicopter operations;
- Combine rigid and flexible body dynamics into a single dynamic system;
- Model infinitely-configurable skid-type and other stiff landing gear;
- Model a comprehensive set of aerodynamic phenomena present in recovery-flight, embarked, and take-off phases;

- Incorporate full-DoF ship motion, where the planar case includes heave, sway, and roll;
- Generate appropriately-oriented dynamic response at detection of contact;
- Present a suitable ship deck securing and manoeuvring system proof-of-concept.

In effect, this work represents the planar case of the combined capabilities of Dynaface[®] with the skid landing gear extension, SSMASH's fully spatial securing and manoeuvring capabilities, and includes more detailed contact mechanics and aerodynamic models. The scope of this work is to develop and verify the planar dynamic system formulation and simulation architecture for the dynamic interface analysis of skid-equipped rotary-wing aircraft such that an acceptable methodology is developed for the creation of a fully-spatial package. As it relates to the field dynamic interface analysis, this work primarily expands simulation capabilities to include the securing and manoeuvring of embarked skid-equipped aircraft. Moreover it contributes the system formulation necessary to simulate the rigid-flexible body behaviour of skid-equipped aircraft. Consequently the work also contributes a general appropriately-oriented contact dynamic algorithm as a result of characterizing the complex contact behaviour of compliant bodies which is not limited to the modelling of skid-type landing gear. An additional contribution evolves from the proposed conceptual design of a securing system which can also manoeuvre embarked skid-equipped aircraft.

Future work beyond the established scope will be performed to expand this work into a fully-spatial simulation package based on the verified methodology developed in this work.

1.6 Thesis Overview

This chapter has presented the current progression of shipboard helicopter operations, a significant cross-section of available shipboard securing and manoeuvring systems, the state-of-the-art in dynamic interface analysis software, and identified a gap in the aforementioned that this work aims to fill with respect to skid-equipped rotary-wing aircraft. Going forward, this work describes the preliminary requirements and design of the securing and manoeuvring device, mathematical definitions and methods, and dynamic system definition in Chapter 2. Following this, Chapter 3 presents the

derivations of the kinematic equations required for the dynamical system. Chapter 4 presents the derivations of forces generated by the landing gear, contact dynamics, aerodynamics, and other dynamic models. The kinematics of Chapter 3 and dynamics of Chapter 4 are assembled into a linear dynamic system in Chapter 5. Verification, and preliminary validation of the final dynamic system formulation and models implemented are discussed in Chapter 6. Conclusions of the completed work are drawn, and recommendations for future work are made in Chapter 7.

Chapter 2

System Description

This work has developed a simulation package for the dynamic interface analysis of skid-equipped rotary-wing aircraft named SRAMSS (Skid-equipped Rotary-wing Manoeuvring and Securing Simulation). This chapter presents the requirements and definitions necessary to generate the dynamic system in SRAMSS. Section 2.1 describes and defines a preliminary concept for a securing and manoeuvring device for skid-equipped aircraft as required for the SRAMSS simulation environment since embarked skid-equipped aircraft manoeuvring is a simulation requirement for SRAMSS. Section 2.2 covers mathematical notations, conventions, and the methods for dynamic equation generation and skid-type landing gear modelling. With the definitions formulated in the previous sections, Section 2.3 defines the generalized coordinates, generalized speeds, and the structure of frames of reference used for the derivation of the complete dynamic system.

2.1 Securing and Manoeuvring System Conceptual Design

SRAMSS addresses the limitations of current dynamic interface analysis software as it pertains to the simulation of embarked manoeuvring of skid-equipped aircraft. Since the author has not found the existence of any available securing and manoeuvring systems for skid-equipped aircraft, such a system must be defined to guide the development of the simulation environment in SRAMSS. The rapid securing device design contributes to the thesis objectives of system conceptual design that enables embarked securing and manoeuvring, as described in Section 1.5. The general requirements for

the securing system, and preliminary concept are described in the following sections.

2.1.1 Securing and Manoeuvring Mechanism Requirements

High-level requirements for the securing and manoeuvring concept are derived from two areas: existing securing and manoeuvring system capabilities, and UAS/skid-equipped aircraft considerations. With respect to existing systems and literature [4], requirements include:

- Passive securing: a structural member attached to the aircraft is captured to secure the aircraft to the ship deck. Loads are transferred to the ship structure;
- Controlled yaw motion of aircraft relative to the ship deck for hangar alignment;
- Controlled longitudinal motion with lateral restraining for manoeuvres across the ship deck;
- Securing aircraft against ship motion in up to sea-state 6; and
- RSD which captures the aircraft fast enough to avoid unrestrained aircraft motion.

In considering the type of aircraft used, requirements include:

- Passive securing device completely contained on the ship due to limited UAS payloads and to limit reduction in UAS range;
- Device completely contained on the ship enables a universal design philosophy which can be sized and adapted to suit the majority of skid-equipped rotary-wing aircraft;
- Manoeuvrable landing and securing platform due to immobile nature of secured skid-equipped aircraft; and
- Platform range of motion capable of correcting for expected landing dispersion.

2.1.2 Skid-type Securing and Manoeuvring Concept

Emerging from the requirements listed in Section 2.1.1, capabilities for the skid-type securing and manoeuvring device consist of:

- Device completely contained to the ship, with universal design capable of accommodating a variety of skid-equipped aircraft;
- Passive RSD capable of securing a skid-equipped aircraft in up to sea-state 6;

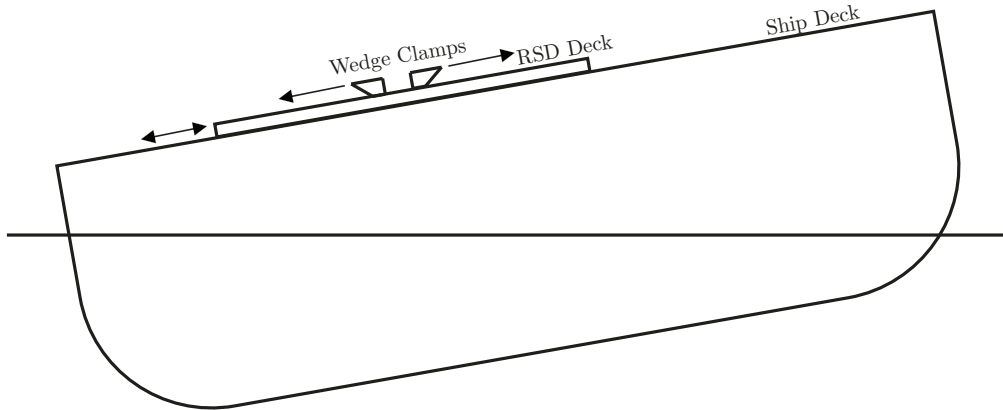


Figure 2.1: Planar representation of the skid-equipped securing and manoeuvring system.

- Landing platform with manoeuvring capabilities to move an embarked aircraft into a shipborne hangar;

To capture these capabilities, this work proposes a manoeuvrable platform with longitudinal, limited-transverse, and yaw DoFs, with wedge shaped clamps which move outwards in the transverse direction. Outward-moving clamps are expected to be less prone to causing aircraft roll-overs as the fulcrum created by a skid tube caught in the wedge is necessarily behind the aircraft's CoG under sliding motion. The platform should be able to interface with existing RAST and ASIST systems for expanded operational capabilities, though this aspect is not discussed further. For the planar case in this work, Figure 2.1 describes the proposed concept.

The planar case of the device includes only the transverse translation direction for the platform and wedge clamps. Aircraft securing with landing dispersion, transverse alignment to the hangar, and response to flight deck heave, sway, and roll are still observable in the planar case. Nevertheless, this description of the securing and manoeuvring system completes the physical description of the simulation environment for SRAMSS. Mathematical notations, methods, and system descriptions are now possible.

2.2 Mathematical Conventions and Methods

To derive the system and models present in SRAMSS, mathematical conventions, identities, and methods must be defined.

Vector Naming Conventions

A consistent vector notation is used to represent vector quantities. Boldfaced variables represent vector quantities, unless enclosed by square brackets [] which represent matrices.

Vectors with physical interpretations such as kinematic and kinetic vectors, and unit vectors are accented by a right pointing arrow ‘ \rightarrow ’ and circumflex ‘ $\hat{}$ ’ respectively. Kinematic vector quantities are used to represent displacements, velocities, and accelerations of bodies and points in space, while kinetic vectors represent forces and moments applied to bodies. Given the complexity of the developed system, a rigorous vector subscript and superscript notation is adopted from Léveillé [45] due to similar system definition and for precise vector description.

Kinematic Vectors

For the kinematic vector ${}^c_d\vec{a}^b$:

- Kinematic vector quantities are represented by lower-case bold characters.
- \mathbf{a} is the kinematic vector quantity type. In this work, \mathbf{a} takes the form of \mathbf{r} for translational displacement, \mathbf{v} for translational velocity, \mathbf{a} for translational acceleration, $\boldsymbol{\theta}$ for angular displacement, $\boldsymbol{\omega}$ for angular velocity, $\boldsymbol{\alpha}$ for angular acceleration, and \mathbf{g} for gravitational acceleration;
- b is the body for which the vector quantity is described;
- c is the body, or frame of reference relative to which the vector quantity is described;
- d is the frame of reference in which the vector quantity is expressed.
- As such, the kinematic vector quantity ${}^c_d\vec{r}^b$ is defined to be the position of body b with respect to c , expressed in frame of reference d .

Kinetic Vectors

For the kinetic vector ${}^g_h\vec{e}^f$:

- Kinetic vector quantities are represented by upper-case bold characters.
- \mathbf{e} is the kinetic vector quantity type. It takes the form of \mathbf{F} for force vectors and \mathbf{M} for moment vectors;
- f is forcing element or body;
- g is the body on which f is acting;

- h is the frame of reference in which the kinetic vector quantity is expressed.
- As such, the kinetic vector quantity ${}^c_d\vec{F}^b$ is defined to be force of b acting on c , expressed in frame of reference d .

This work presents the planar 2D case of the SRAMSS simulation environment. All translation vector quantities are in the form of 2x1 column vectors, where the first and second entries are the x and y axis vector components respectively. All angular vector quantities are in the form of 1x1 column vectors, where the entry represents the angular vector quantity about a z axis obeying the Right-Hand-Rule (RHR) for $x - y - z$ axis orthogonality, and RHR for angular quantity direction about the z axis, i.e. the z axis projects outwards from the page, and the positive angular direction is counter-clockwise.

Vector Quantity Time Derivatives

The time differentiated vector quantity is denoted

$$\frac{d}{dt}({}^c_d\vec{a}^b) = {}^c_d\dot{\vec{a}}^b \quad (2.1)$$

For this work, the differentiation is performed in the frame of reference of the differentiated vector, and is referred to as the locally evaluated time derivative. This is significant, as obtaining real accelerations for the dynamic system requires the local time differentiations be evaluated in an inertial frame of reference. Thus the relative position vector quantities, defining the position of a body through multiple frames of reference, must all be expressed with respect to the inertial frame before differentiation can take place.

Cross Product Identity

Cross products appear in many instances of kinematic and dynamic derivations, for example: in locally evaluated time derivatives, and moment evaluations due to translational forces. Per Nikravesh [46], cross product evaluation for 3x1 vectors can be expressed as the matrix multiplication:

$$\vec{a} \times \vec{b} = [\widetilde{\vec{a}}]\vec{b} = -[\widetilde{\vec{b}}]\vec{a} \quad (2.2)$$

where, for vector \vec{a} with elements a_1 , a_2 , and a_3 along the x , y , and z axes respectively, $[\widetilde{\vec{a}}]$ is the skew-symmetric matrix of \vec{a} , and takes the form:

$$[\widetilde{\vec{a}}] = \begin{bmatrix} 0 & -a_3 & a_2 \\ a_3 & 0 & -a_1 \\ -a_2 & a_1 & 0 \end{bmatrix} \quad (2.3)$$

For the planar case, evaluating cross products of kinematic vectors, Equation 2.2 reduces to:

$$\vec{\omega} \times \vec{r} = [\widetilde{\vec{\omega}}]\vec{r} = \begin{bmatrix} 0 & -\omega \\ \omega & 0 \end{bmatrix} \begin{Bmatrix} r_x \\ r_y \end{Bmatrix} = \begin{Bmatrix} v_x \\ v_y \end{Bmatrix} \quad (2.4)$$

and for evaluating cross products of kinetic vectors, Equation 2.2 reduces to:

$$\vec{r} \times \vec{F} = [\widetilde{\vec{r}}]\vec{F} = \begin{bmatrix} -r_y & r_x \end{bmatrix} \begin{Bmatrix} F_x \\ F_y \end{Bmatrix} = M_z \quad (2.5)$$

Rotational Transformation Matrix

Transformation matrices are used in the kinematic and dynamic derivations to transform the expression of a vector quantity from one frame of reference to another. In the planar case, only rotations about the z axis can occur. The transformation $[\mathbf{T}]$ from rotated frame of reference b to non-rotated frame of reference a using an Euler angle rotation matrix about the z axis is given [46]:

$$[\mathbf{T}_{a \leftarrow b}] = \begin{bmatrix} \cos(\theta) & -\sin(\theta) & 0 \\ \sin(\theta) & \cos(\theta) & 0 \\ 0 & 0 & 1 \end{bmatrix} \quad (2.6)$$

For this work, all frame of reference z axes are aligned in the same direction, and obey the RHR for axis orthogonality, therefore by inspection the transformation matrix presented in Equation 2.6 can be written

$$[\mathbf{T}_{a \leftarrow b}] = \begin{bmatrix} \cos({}_a^a\vec{\theta}^b) & -\sin({}_a^a\vec{\theta}^b) & 0 \\ \sin({}_a^a\vec{\theta}^b) & \cos({}_a^a\vec{\theta}^b) & 0 \\ 0 & 0 & 1 \end{bmatrix} = \begin{bmatrix} \cos({}_b^a\vec{\theta}^b) & -\sin({}_b^a\vec{\theta}^b) & 0 \\ \sin({}_b^a\vec{\theta}^b) & \cos({}_b^a\vec{\theta}^b) & 0 \\ 0 & 0 & 1 \end{bmatrix} \quad (2.7)$$

From this identity, the transformation matrix for 2x1 translational vectors is

$$[\mathbf{T}_{a \leftarrow b}] = \begin{bmatrix} \cos({}_b^a\vec{\theta}^b) & -\sin({}_b^a\vec{\theta}^b) \\ \sin({}_b^a\vec{\theta}^b) & \cos({}_b^a\vec{\theta}^b) \end{bmatrix} \quad (2.8)$$

and the transformation matrix for 1x1 angular vector quantities is unity. which agrees with the frame of reference interchangeability of the relative angles used in Equation 2.7 where the transformed vector is $\{x \ y \ \theta\}$.

For successive frame transformations, pre-multiplication of the consecutive transformation matrices in the chain of frames is required since consecutive frames are described with respect to the axes of the previous frame. For example, the transformation of rotated frame of reference c to non-rotated frame of reference a , passing through rotated frame of reference b is

$$[\mathbf{T}_{a \leftarrow c}] = [\mathbf{T}_{a \leftarrow b}][\mathbf{T}_{b \leftarrow c}] \quad (2.9)$$

Rotational Transformation Matrix Time Derivative Identity

Time differentiation of transformation matrices occur during the differentiation of position vectors to velocity vectors then to acceleration vectors. As a result, the time derivative of a transformation matrix is:

$$\begin{aligned} [\dot{\mathbf{T}}_{a \leftarrow b}] &= \frac{d}{dt}([\mathbf{T}_{a \leftarrow b}]) \\ &= \begin{bmatrix} -{}^a\dot{\theta}^b \sin({}^a\theta^b) & -{}^a\dot{\theta}^b \cos({}^a\theta^b) \\ {}^a\dot{\theta}^b \cos({}^a\theta^b) & -{}^a\dot{\theta}^b \sin({}^a\theta^b) \end{bmatrix} \\ &= \begin{bmatrix} \cos({}^a\theta^b) & -\sin({}^a\theta^b) \\ \sin({}^a\theta^b) & \cos({}^a\theta^b) \end{bmatrix} \begin{bmatrix} 0 & -{}^a\vec{\omega}^b \\ {}^a\vec{\omega}^b & 0 \end{bmatrix} \\ [\dot{\mathbf{T}}_{a \leftarrow b}] &= [\mathbf{T}_{a \leftarrow b}] \widetilde{[{}^a\vec{\omega}^b]} \end{aligned} \quad (2.10)$$

which agrees with the general 3-dimensional case provided by Nikravesh [46].

Kane's Method for Dynamic Equation Formulation

Generating the equations of motion and forces using the Newton-Euler method is unsuitable for this work since it is an inefficient maximal-coordinate method where every active and constraint force for every body must be considered. The Lagrangian method is not more suitable, even if it is a minimal-coordinate method, due to exhaustive partial differentiations in more complex systems such as the one present in this work. Kane's method presents an elegant alternative to these methods. It is a powerful method for generating the dynamics equations for the system through use of generalized coordinates and partial velocities, and the resulting equations of motion are easily manipulated into a first-order system which lends itself to numerical

computation and state propagation [47, 48]. System configuration definition through use of generalized coordinates distinguishes itself from typical Cartesian coordinate definition as the generalized coordinates can be selected to simplify the derivations of equations of motion and reduce the number of equations for the complete system. Kane's method states:

$$F_i + F_i^* = 0, \quad i = 1, \dots, N_{gc} \quad (2.11)$$

where Equation 2.11 is the set of N_{gc} scalar equations summing the total inertial forces F_i^* , and active forces F_i , along the i th generalized coordinate direction, with N_{gc} the number of generalized coordinates required to describe the system. For a system of N_B bodies that share the system generalized coordinates \mathbf{q} , Equation 2.11 can be vectorized and written as the system

$$0 = \mathbf{F} + \mathbf{F}^* \quad (2.12)$$

where, summed over the N_B bodies in the system, the inertial and active forces are obtained by

$$\mathbf{F} = \sum_{k=1}^{N_B} \left([{}^N \mathbf{V}^k]^T \vec{\mathbf{R}}^k + [{}^N \mathbf{W}^k]^T \vec{\mathbf{T}}^k \right) \quad (2.13)$$

$$\mathbf{F}^* = \sum_{k=1}^{N_B} \left([{}^N \mathbf{V}^k]^T \vec{\mathbf{R}}^{*k} + [{}^N \mathbf{W}^k]^T \vec{\mathbf{T}}^{*k} \right) \quad (2.14)$$

where, for the k th body, $\vec{\mathbf{R}}^k$ and $\vec{\mathbf{T}}^k$ are the resulting active force and active torque, $\vec{\mathbf{R}}^{*k}$ and $\vec{\mathbf{T}}^{*k}$ are the translational and angular inertias, and $[\mathbf{V}]$ and $[\mathbf{W}]$ are the translational and angular partial velocity matrices respectively. The partial velocity matrices are obtained from the compact expression of body velocities and accelerations in terms of the generalized velocities vector \mathbf{u} and accelerations vector $\dot{\mathbf{u}}$ where, for the k th body in the system, we have

$${}^N \vec{\mathbf{v}}^k = [{}^N \mathbf{V}^k] \mathbf{u} \quad (2.15)$$

$${}^N \vec{\boldsymbol{\omega}}^k = [{}^N \mathbf{W}^k] \mathbf{u} \quad (2.16)$$

$${}^N \vec{\mathbf{a}}^k = [{}^N \mathbf{V}^k] \dot{\mathbf{u}} + \vec{\mathbf{Z}}_k \quad (2.17)$$

$${}^N \vec{\boldsymbol{\alpha}}^k = [{}^N \mathbf{W}^k] \dot{\mathbf{u}} + \vec{\mathbf{Y}}_k \quad (2.18)$$

The partial velocity matrices represent the contribution of the system generalized speeds vector \mathbf{u} , and system generalized accelerations vector $\dot{\mathbf{u}}$ to the k th body velocity and acceleration respectively. Coined by Stoneking [49], the terms $\vec{\mathbf{Z}}_k$ and $\vec{\mathbf{Y}}_k$

are the ‘remainder translational accelerations’ and ‘remainder angular accelerations’ respectively, and include all kinematic terms which do not include the generalized accelerations.

Likewise, the transpose of the partial velocity matrices are used to project the forces acting on the N_B bodies into the permissible motions subspace defined by set of system generalized coordinates \mathbf{q} by pre-multiplication of the force vectors as shown in Equations 2.13 and 2.14 [49]. For a single body k , Equation 2.12 can be expanded

$$\begin{aligned} & \left[{}^N \mathbf{W}^k \right]^T \left(\vec{\mathbf{T}}^k - \left[{}_k \vec{\mathbf{I}}^k \right] \left(\left[{}^N \mathbf{W}^k \right] \dot{\mathbf{u}} + \vec{\mathbf{Y}}_k \right) - \left(\widetilde{\left[{}^N \vec{\boldsymbol{\omega}}^k \right]} \left[{}_k \vec{\mathbf{I}}^k \right] \left[{}^N \vec{\boldsymbol{\omega}}^k \right] \right) \right) + \\ & \left[{}^N \mathbf{V}^k \right]^T \left(\vec{\mathbf{R}}^k - m_k \left(\left[{}^N \mathbf{V}^k \right] \dot{\mathbf{u}} + \vec{\mathbf{Z}}_k \right) \right) = 0 \end{aligned} \quad (2.19)$$

The vector of unknown generalized accelerations $\dot{\mathbf{u}}$ in Equation 2.19 is common to all bodies in the system, and when Kane’s equation is summed over the N_B bodies in the system, it facilitates the manipulation of the system into the form

$$\left[\mathbf{M}_{sys} \right] \mathbf{x}_{sys} = \mathbf{F}_{sys} \quad (2.20)$$

which lends itself to numerical solvers for obtaining the solution of unknown generalized accelerations for state-propagation purposes.

Dynamic Finite Element Method

The generic aircraft in the SRAMSS simulation is modelled as a single rigid body helicopter chassis with a skid-type landing gear modelled using a dynamic finite element (DFE) approach. DFE modelling is chosen due to its readily-adaptable modelling of infinitely configurable skid-type landing gear. At a glance, a DFE model mesh physically resembles the skid landing gear which facilitates visual interpretation of the results. More importantly, skid-type landing gear comprises interconnecting, long, slender beams which are easily represented by beam elements in a DFE model.

The DFE model takes the form presented in Bathe [50]:

$$\left[\mathbf{M} \right] \ddot{\mathbf{q}} + \left[\mathbf{C} \right] \dot{\mathbf{q}} + \left[\mathbf{K} \right] \mathbf{q} = \mathbf{F}(\dot{\mathbf{q}}, \mathbf{q}) \quad (2.21)$$

where $\left[\mathbf{M} \right]$ is the consistent mass matrix, $\left[\mathbf{C} \right]$ is the proportional damping matrix, $\left[\mathbf{K} \right]$ is the stiffness matrix, $\mathbf{F}(\dot{\mathbf{q}}, \mathbf{q})$ is the vector of externally applied forces on the DFE model, and \mathbf{q} and associated time derivatives are the nodal displacements, velocities and accelerations. The mass matrix in the DFE model is constructed as a consistent

mass matrix, which captures the DFE model node’s inertial behavior in all degrees of freedom. The proportional damping matrix is obtained from the first two terms of the Caughey series expansion which satisfies modal superposition [50]:

$$[\mathbf{C}] = [\mathbf{M}] \sum_{r=0}^1 \alpha_r [[\mathbf{M}]^{-1} [\mathbf{K}]]^r \quad (2.22)$$

which yields

$$[\mathbf{C}] = \alpha_0 [\mathbf{M}] + \alpha_1 [\mathbf{K}] \quad (2.23)$$

where α_r are obtained from chosen of frequencies ω_1 , ω_2 and associated damping ratios ξ_1 and ξ_2 [51]:

$$\xi_1 = \frac{\alpha_0}{2\omega_1} + \frac{\alpha_1\omega_1}{2} \quad \xi_2 = \frac{\alpha_0}{2\omega_2} + \frac{\alpha_1\omega_2}{2} \quad (2.24)$$

The stiffness matrix is constructed using the direct stiffness method from general 2D 6-DoF beam elements to capture shearing, tension, and bending effects.

2.3 Dynamic System Definition

This work develops the planar case of SRAMSS. The system involves the modelling of a generic skid-equipped aircraft with a rigid-body airframe, flexible skid landing gear, and two external dampers joined between the skid cross-tubes and airframe winglets. Four polygons representing the ship deck, RSD deck, and two wedge clamps complete the environment evaluated for contact, and oriented dynamic response, as shown in Figure 2.2.

This represents a system with a maximum of $11 + 3N_n - r$ DoFs where there are:

- 3 DoF for ship deck motion relative to the inertial frame (heave, sway, roll)
- 1 DoF for RSD deck motion relative to the ship deck (transverse translation)
- 2 DoF of motion per wedge clamp relative to the RSD deck (transverse translation, vertical extension)
- 3 DoF for helicopter motion relative to the inertial frame (heave, sway, roll)
- 3 DoF of motion per DFE node relative to the airframe, minus r fixed-DoFs for the DFE nodes.

The degrees of freedom in the system are described through the use of $7 + N_n$ frames of references, where N_n is the number of DFE nodes and consequently the number of frames required to define the flexible landing gear. The first frame of

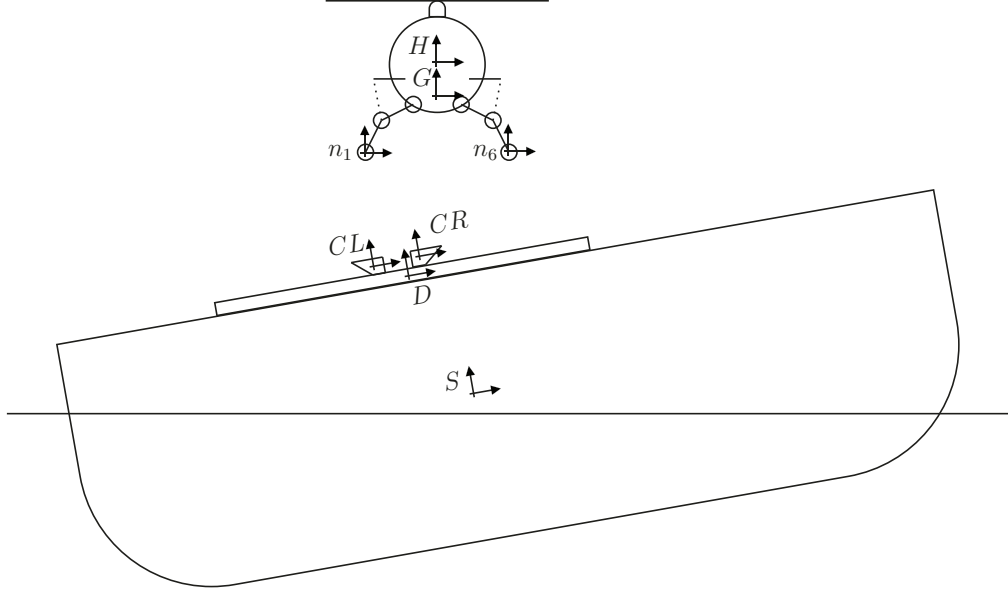


Figure 2.2: Planar description of SRAMSS simulation environment.

reference being the inertial frame N which represents the mean velocity and heading of the ship. Four frames of reference are used as origins for the polygons: S the Ship deck frame of reference, D the RSD deck frame of reference, CL the left wedge clamp frame of reference, and CR the right wedge clamp frame of reference. Three plus N_n frames are used to describe the helicopter rigid airframe and flexible elements: H the airframe's frame of reference, G the assembled DFE landing gear's global frame of reference, and n_j the j th DFE node's frame of reference. Referring to Figures 2.3 and 2.4, the frames of reference are setup in chains originating from the inertial frame – one chain describes the generic aircraft ($N - H - G - n_j$), and the other describes the included polygons ($N - S - D - CL - CR$). Figure 2.4 describes the frames used for the aircraft specifically.

For the complete system there are considerations made with respect to the ordering of the frames of references. There is a fork in the chains of frames to permit the aircraft to move independently from the motion of the ship when generating the equations of motion using Kane's method. The aircraft's frame origin is aligned with the airframe's CoG, with the z axis aligned to the airframe's roll axis, x axis aligned to helicopter's port side, and y axis aligned parallel to the rotor hub axis in the upwards direction. The global DFE frame is axis-aligned to the helicopter frame at a prescribed distance and serves as the interface between the rigid airframe and flexible landing gear. Each DFE node frame is axis-aligned to the global DFE frame, a property required for the

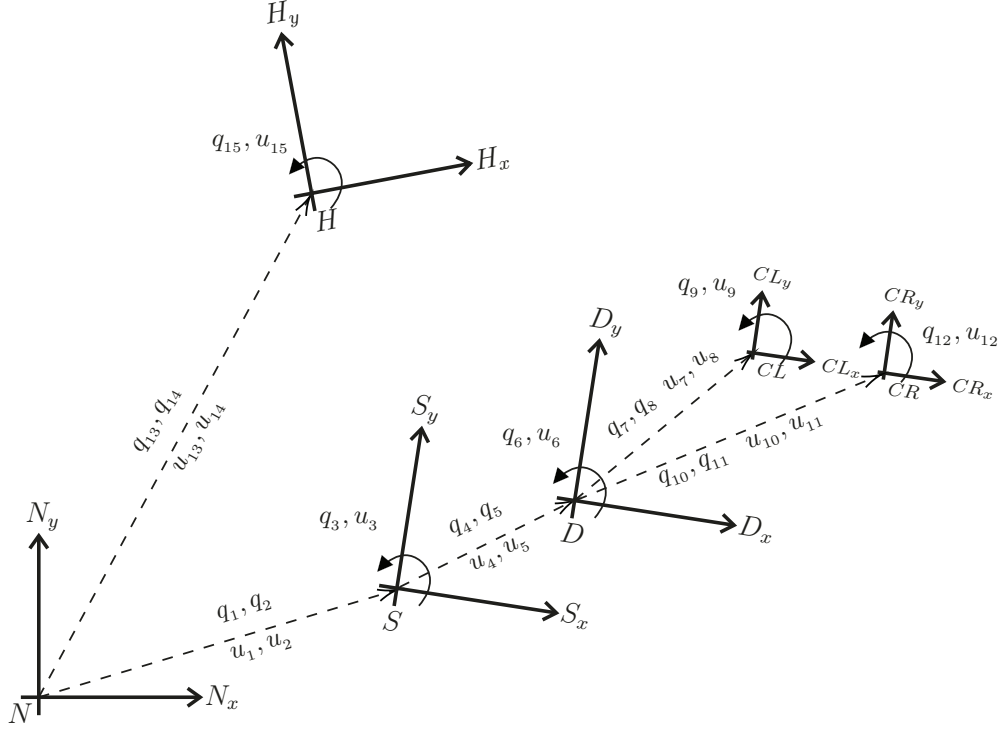


Figure 2.3: System frames of reference.

assembly of the DFE model. Consequently, the transformation matrices between the node frames and global frame are 2x2 identity matrices. The ship frame is allowed to move in all DoF relative to the inertial frame. The RSD deck frame is axis-aligned at a prescribed distance to the ship frame since its motion is relative to the ship deck. This facilitates manoeuvring prescription by limiting the transverse translation to the x direction. For similar reasons, the wedge clamp frames are axis-aligned to the RSD deck frame to limit prescribed motion to the x and y axes.

The generalized coordinates \mathbf{q} and generalized speeds \mathbf{u} for the complete system are all consistently defined to be the motion of one frame relative to the previous frame. This facilitates definition of motion and constraints between bodies. Frames which are fixed along certain DoF relative to the previous frame only require those specific generalized coordinates prescribed; and generalized velocities set to zero. Frames with prescribed motions are all defined relative to the frame from which motion would be observed, thus only those generalized coordinates and speeds need to be prescribed.

In this work, the generalized coordinates and speeds for the ship deck, RSD deck, both wedge clamps, and global DFE frame are prescribed. This renders the dynamic system over-determined as some of the generalized accelerations $\dot{\mathbf{u}}$ from Equation 2.20

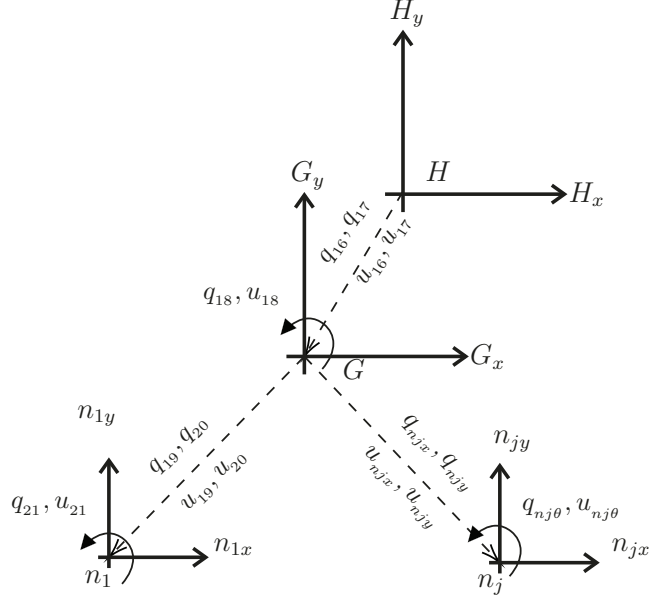


Figure 2.4: Aircraft frames of reference.

become known. Section 5 covers the manipulation of the dynamic system into an exactly-determined system, where a solution for unknown generalized accelerations can be obtained directly.

Regarding the equations of motion for the system, vector quantities must be defined. Starting along the ship's chain of frames, the position of the ship frame relative to the inertial frame, and expressed in the inertial frame, is

$${}^N \vec{r}^S = \begin{Bmatrix} q_1 \\ q_2 \end{Bmatrix} \quad (2.25)$$

with the orientation of the ship frame relative to the inertial frame, and expressed in the ship frame, being

$${}^S \vec{\theta}^S = \{q_3\} \quad (2.26)$$

The position of the RSD deck's frame relative to the ship frame, and expressed in the ship frame, is

$${}^S \vec{r}^D = \begin{Bmatrix} q_4 \\ q_5 \end{Bmatrix} \quad (2.27)$$

with the orientation of the RSD deck frame relative to the ship frame, and expressed in the RSD deck frame, being

$${}^D \vec{\theta}^D = \{q_6\} \quad (2.28)$$

The position of the left wedge frame relative to the RSD deck frame, and expressed in the RSD deck frame, is

$${}^D_D \vec{r}^{CL} = \begin{Bmatrix} q_7 \\ q_8 \end{Bmatrix} \quad (2.29)$$

with the orientation of the left wedge frame relative to the RSD deck frame, and expressed in the left wedge frame, being

$${}^D_{CL} \vec{\theta}^{CL} = \{q_9\} \quad (2.30)$$

The position of the right wedge frame relative to the RSD deck frame, and expressed in the RSD deck frame, is

$${}^D_D \vec{r}^{CR} = \begin{Bmatrix} q_{10} \\ q_{11} \end{Bmatrix} \quad (2.31)$$

with the orientation of the right wedge frame relative to the RSD deck frame, and expressed in the right wedge frame, being

$${}^D_{CR} \vec{\theta}^{CR} = \{q_{12}\} \quad (2.32)$$

Then along the aircraft chain of frames, the position of the helicopter frame relative to the inertial frame, and expressed in the inertial frame, is

$${}^N_N \vec{r}^H = \begin{Bmatrix} q_{13} \\ q_{14} \end{Bmatrix} \quad (2.33)$$

with the orientation of the helicopter frame relative to the inertial frame, and expressed in the helicopter frame, being

$${}^N_H \vec{\theta}^H = \{q_{15}\} \quad (2.34)$$

The position of the global frame relative to the helicopter frame, and expressed in the helicopter frame, is

$${}^H_H \vec{r}^G = \begin{Bmatrix} q_{16} \\ q_{17} \end{Bmatrix} \quad (2.35)$$

with the orientation of the global frame relative to the helicopter frame, and expressed in the global frame, being

$${}^H_G \vec{\theta}^G = \{q_{18}\} \quad (2.36)$$

The position of the j th DFE node frame relative to the global frame, and expressed in the global frame, is

$${}^G_G \vec{r}^{n_j} = \begin{Bmatrix} q_{17+2j} \\ q_{18+2j} \end{Bmatrix} \quad (2.37)$$

with the orientation of the j th DFE node frame relative to the global frame, and expressed in the j th DFE node frame, being

$${}^G_{n_j} \vec{\theta}^{n_j} = \{q_{19+2j}\} \quad (2.38)$$

To generate the correct partial velocity matrices, the generalized velocities are chosen to be the time derivatives of the translational generalized coordinates relative to their preceding frames of reference, and the angular generalized coordinates relative to their respective frames.

The velocity of the ship frame relative to the inertial frame, and expressed in the inertial frame, is

$${}^N \vec{v}^S = {}^N \dot{\vec{r}}^S = \begin{Bmatrix} u_1 \\ u_2 \end{Bmatrix} = \begin{Bmatrix} \dot{q}_1 \\ \dot{q}_2 \end{Bmatrix} \quad (2.39)$$

With the angular velocity of the ship frame relative to the inertial frame, and expressed in the ship frame, being

$${}^N_S \vec{\omega}^S = {}^N_S \dot{\vec{\theta}}^S = \{u_3\} = \{\dot{q}_3\} \quad (2.40)$$

The velocity of the RSD deck's frame relative to the ship frame, and expressed in the ship frame, is

$${}^S \vec{v}^D = {}^S \dot{\vec{r}}^D = \begin{Bmatrix} u_4 \\ u_5 \end{Bmatrix} = \begin{Bmatrix} \dot{q}_4 \\ \dot{q}_5 \end{Bmatrix} \quad (2.41)$$

with the angular velocity of the RSD deck frame relative to the ship frame, and expressed in the RSD deck frame, being

$${}^S_D \vec{\omega}^D = {}^S_D \dot{\vec{\theta}}^D = \{u_6\} = \{\dot{q}_6\} \quad (2.42)$$

The velocity of the left wedge frame relative to the RSD deck frame, and expressed in the RSD deck frame, is

$${}^D \vec{v}^{CL} = {}^D \dot{\vec{r}}^{CL} = \begin{Bmatrix} u_7 \\ u_8 \end{Bmatrix} = \begin{Bmatrix} \dot{q}_7 \\ \dot{q}_8 \end{Bmatrix} \quad (2.43)$$

with the angular velocity of the left wedge frame relative to the RSD deck frame, and expressed in the left wedge frame, being

$${}^D_{CL} \vec{\omega}^{CL} = {}^D_{CL} \dot{\vec{\theta}}^{CL} = \{u_9\} = \{\dot{q}_9\} \quad (2.44)$$

The velocity of the right wedge frame relative to the RSD deck frame, and expressed in the RSD deck frame, is

$${}^D_D \vec{v}^{CR} = {}^D_D \dot{\vec{r}}^{CR} = \begin{Bmatrix} u_{10} \\ u_{11} \end{Bmatrix} = \begin{Bmatrix} \dot{q}_{10} \\ \dot{q}_{11} \end{Bmatrix} \quad (2.45)$$

with the angular velocity of the right wedge frame relative to the RSD deck frame, and expressed in the right wedge frame, being

$${}^D_{CR} \vec{\omega}^{CR} = {}^D_{CR} \dot{\vec{\theta}}^{CR} = \{u_{12}\} = \{\dot{q}_{12}\} \quad (2.46)$$

Then along the aircraft chain of frames, the velocity of the helicopter frame relative to the inertial frame, and expressed in the inertial frame, is

$${}^N_N \vec{v}^H = {}^N_N \dot{\vec{r}}^H = \begin{Bmatrix} u_{13} \\ u_{14} \end{Bmatrix} = \begin{Bmatrix} \dot{q}_{13} \\ \dot{q}_{14} \end{Bmatrix} \quad (2.47)$$

with the angular velocity of the helicopter frame relative to the inertial frame, and expressed in the helicopter frame, being

$${}^N_H \vec{\omega}^H = {}^N_H \dot{\vec{\theta}}^H = \{u_{15}\} = \{\dot{q}_{15}\} \quad (2.48)$$

The velocity of the global frame relative to the helicopter frame, and expressed in the helicopter frame, is

$${}^H_H \vec{v}^G = {}^H_H \dot{\vec{r}}^G = \begin{Bmatrix} u_{16} \\ u_{17} \end{Bmatrix} = \begin{Bmatrix} \dot{q}_{16} \\ \dot{q}_{17} \end{Bmatrix} \quad (2.49)$$

with the angular velocity of the global frame relative to the helicopter frame, and expressed in the global frame, being

$${}^H_G \vec{\omega}^G = {}^H_G \dot{\vec{\theta}}^G = \{u_{18}\} = \{\dot{q}_{18}\} \quad (2.50)$$

The velocity of the j th DFE node frame relative to the global frame, and expressed in the global frame, is

$${}^G_G \vec{v}^{n_j} = {}^G_G \dot{\vec{r}}^{n_j} = \begin{Bmatrix} u_{17+2j} \\ u_{18+2j} \end{Bmatrix} = \begin{Bmatrix} \dot{q}_{17+2j} \\ \dot{q}_{18+2j} \end{Bmatrix} \quad (2.51)$$

with the angular velocity of the j th DFE node frame relative to the global frame, and expressed in the j th DFE node frame, being

$${}^G_{n_j} \vec{\omega}^{n_j} = {}^G_{n_j} \dot{\vec{\theta}}^{n_j} = \{u_{19+2j}\} = \{\dot{q}_{19+2j}\} \quad (2.52)$$

With all the vector quantities defined through use of generalized coordinates and speeds, the definition of the system is complete. The following Chapter will present the derivation of all equations of motion required both for prescribed and state-propagated bodies, including the partial translational and angular velocity matrices, and remainder accelerations required for the implementation of Kane's method.

Chapter 3

System Kinematics

To prepare for applying Kane’s method, as outlined in Section 2.2, translational and angular partial velocity matrices are required. Equations 2.15 through 2.18 show that these matrices are obtained by inspection of the kinematic equations describing a given body.

$${}^N_k \vec{v}^k = [{}^N_k \mathbf{V}^k] \mathbf{u} \quad (2.15)$$

Therefore, the kinematic equations describing the velocity and acceleration of the studied bodies must be derived.

Three important considerations must be made in the derivation of these equations. First, the complete equations of motion must be derived relative to the inertial frame to express absolute accelerations. Second, they must be expressed in the described body’s frame of reference since the equations of motion will be evaluated in their respective frames. Lastly, they must be expressed in terms of the generalized speeds and accelerations to isolate the system’s vectors of generalized speeds \mathbf{u} and accelerations $\dot{\mathbf{u}}$ for the construction of respective partial velocity matrices.

For the present work, the equations of motions require kinematic expressions for the airframe and landing gear DFE nodes. Kinematic expressions for ship deck, RSD deck, and wedge clamp polygon vertices are also obtained for contact dynamics purposes. Since the motions of the polygons representing the ship deck, RSD deck, and wedges are prescribed, the partial velocity matrices only require the inclusion of the aircraft’s airframe and DFE landing gear node generalized velocities and accelerations. Regardless, the generalized velocities and accelerations for the defined polygons are included in the partial velocity matrices to minimize re-derivations in future work where evaluating the ship’s response is required.

The kinematic development starts with the development of the equations relating to the bodies studied for dynamic response.

3.1 Body Kinematics

In this work, the bodies evaluated in Kane's method are the aircraft's airframe and DFE landing gear nodes. Working along the chain of frames of reference for the aircraft, the first body is the aircraft's airframe H . Since the H frame is centred on the airframe's CoG, the position of the airframe with respect to the inertial frame, expressed in the inertial frame, is

$${}^N\vec{r}^H \quad (3.1)$$

The airframe's velocity is obtained by differentiating Equation 3.1:

$$\begin{aligned} {}^N\vec{v}^H &= \frac{d}{dt} ({}^N\vec{r}^H) \\ &= {}^N\dot{\vec{r}}^H \end{aligned} \quad (3.2)$$

Transformed to the airframe's frame H , the airframe's translational velocity from Equation 3.2 becomes

$$\begin{aligned} {}^H\vec{v}^H &= [\mathbf{T}_{H\leftarrow N}]_N {}^N\vec{v}^H \\ &= [\mathbf{T}_{H\leftarrow N}]_N {}^N\dot{\vec{r}}^H \end{aligned} \quad (3.3)$$

The airframe's translational acceleration is obtained by differentiating Equation 3.2:

$$\begin{aligned} {}^N\vec{a}^H &= \frac{d}{dt} ({}^N\vec{v}^H) \\ &= \frac{d}{dt} ({}^N\dot{\vec{r}}^H) \\ &= {}^N\ddot{\vec{r}}^H \end{aligned} \quad (3.4)$$

Transformed to the airframe's frame H , the airframe's translational acceleration from Equation 3.4 becomes

$$\begin{aligned} {}^H\vec{a}^H &= [\mathbf{T}_{H\leftarrow N}]_N {}^N\vec{a}^H \\ &= [\mathbf{T}_{H\leftarrow N}]_N {}^N\ddot{\vec{r}}^H \end{aligned} \quad (3.5)$$

The next bodies in the aircraft's chain of frames are the DFE nodes representing the landing gear. The frame for each DFE node is located at node coordinates used in the generation of the DFE model. Since all DFE node frames share the common frame

of reference G per Figure 2.4, the general equation describing the position of the j th DFE node n_j with respect to the inertial frame, expressed in the inertial frame is

$${}^N_N\vec{r}^{n_j} = {}^N_N\vec{r}^H + {}^H_N\vec{r}^G + {}^G_N\vec{r}^{n_j} \quad (3.6)$$

Equation 3.6 can be described in terms of the generalized coordinates as

$${}^N_N\vec{r}^{n_j} = {}^N_N\vec{r}^H + [\mathbf{T}_{N\leftarrow H}]_H^H\vec{r}^G + [\mathbf{T}_{N\leftarrow H}][\mathbf{T}_{H\leftarrow G}]_G^G\vec{r}^{n_j} \quad (3.7)$$

The j th DFE node's velocity is obtained by differentiating Equation 3.7:

$$\begin{aligned} {}^N_N\vec{v}^{n_j} &= \frac{d}{dt} ({}^N_N\vec{r}^{n_j}) \\ &= \frac{d}{dt} ({}^N_N\vec{r}^H) + \frac{d}{dt} ([\mathbf{T}_{N\leftarrow H}]_H^H\vec{r}^G) + \frac{d}{dt} ([\mathbf{T}_{N\leftarrow H}][\mathbf{T}_{H\leftarrow G}]_G^G\vec{r}^{n_j}) \\ &= {}^N_N\dot{\vec{r}}^H + [\dot{\mathbf{T}}_{N\leftarrow H}]_H^H\vec{r}^G + [\mathbf{T}_{N\leftarrow H}]_H^H\dot{\vec{r}}^G + [\dot{\mathbf{T}}_{N\leftarrow H}][\mathbf{T}_{H\leftarrow G}]_G^G\vec{r}^{n_j} \\ &\quad + [\mathbf{T}_{N\leftarrow H}][\dot{\mathbf{T}}_{H\leftarrow G}]_G^G\vec{r}^{n_j} + [\mathbf{T}_{N\leftarrow H}][\mathbf{T}_{H\leftarrow G}]_G^G\dot{\vec{r}}^{n_j} \\ &= {}^N_N\dot{\vec{r}}^H + [\mathbf{T}_{N\leftarrow H}][\widetilde{{}^N_N\vec{\omega}^H}]_H^H\vec{r}^G + [\mathbf{T}_{N\leftarrow H}]_H^H\dot{\vec{r}}^G \\ &\quad + [\mathbf{T}_{N\leftarrow H}][\widetilde{{}^N_N\vec{\omega}^H}][\mathbf{T}_{H\leftarrow G}]_G^G\vec{r}^{n_j} + [\mathbf{T}_{N\leftarrow H}][\mathbf{T}_{H\leftarrow G}][\widetilde{{}^H_N\vec{\omega}^G}]_G^G\vec{r}^{n_j} \\ &\quad + [\mathbf{T}_{N\leftarrow H}][\mathbf{T}_{H\leftarrow G}]_G^G\dot{\vec{r}}^{n_j} \end{aligned} \quad (3.8)$$

By the identity presented in Equation 2.10, the time-derivative of the transformation matrices are substituted by the product of the original transformation matrix and skew angular velocity. Then Equation 3.8 transformed to the j th DFE node's frame n_j , the j th DFE node's translational velocity from Equation 3.8 becomes

$$\begin{aligned} {}^N_{n_j}\vec{v}^{n_j} &= [\mathbf{T}_{n_j\leftarrow N}]_N^N\vec{v}^{n_j} \\ &= [\mathbf{T}_{n_j\leftarrow N}] \left({}^N_N\dot{\vec{r}}^H + [\mathbf{T}_{N\leftarrow H}][\widetilde{{}^N_N\vec{\omega}^H}]_H^H\vec{r}^G + [\mathbf{T}_{N\leftarrow H}]_H^H\dot{\vec{r}}^G \right. \\ &\quad + [\mathbf{T}_{N\leftarrow H}][\widetilde{{}^N_N\vec{\omega}^H}][\mathbf{T}_{H\leftarrow G}]_G^G\vec{r}^{n_j} + [\mathbf{T}_{N\leftarrow H}][\mathbf{T}_{H\leftarrow G}][\widetilde{{}^H_N\vec{\omega}^G}]_G^G\vec{r}^{n_j} \\ &\quad \left. + [\mathbf{T}_{N\leftarrow H}][\mathbf{T}_{H\leftarrow G}]_G^G\dot{\vec{r}}^{n_j} \right) \\ &= [\mathbf{T}_{n_j\leftarrow N}]_N^N\dot{\vec{r}}^H + [\mathbf{T}_{n_j\leftarrow H}][\widetilde{{}^N_N\vec{\omega}^H}]_H^H\vec{r}^G + [\mathbf{T}_{n_j\leftarrow H}]_H^H\dot{\vec{r}}^G \\ &\quad + [\mathbf{T}_{n_j\leftarrow H}][\widetilde{{}^N_N\vec{\omega}^H}][\mathbf{T}_{H\leftarrow G}]_G^G\vec{r}^{n_j} + [\mathbf{T}_{n_j\leftarrow G}][\widetilde{{}^H_N\vec{\omega}^G}]_G^G\vec{r}^{n_j} \\ &\quad + [\mathbf{T}_{n_j\leftarrow G}]_G^G\dot{\vec{r}}^{n_j} \\ &= [\mathbf{T}_{n_j\leftarrow N}]_N^N\dot{\vec{r}}^H - [\mathbf{T}_{n_j\leftarrow H}][\widetilde{{}^H_N\vec{r}^G}]_H^N\vec{\omega}^H + [\mathbf{T}_{n_j\leftarrow H}]_H^H\dot{\vec{r}}^G \\ &\quad - [\mathbf{T}_{n_j\leftarrow H}] \left[[\mathbf{T}_{H\leftarrow G}]_G^G\vec{r}^{n_j} \right]_H^N\vec{\omega}^H - [\mathbf{T}_{n_j\leftarrow G}][\widetilde{{}^G_N\vec{r}^{n_j}}]_G^H\vec{\omega}^G \\ &\quad + [\mathbf{T}_{n_j\leftarrow G}]_G^G\dot{\vec{r}}^{n_j} \end{aligned} \quad (3.9)$$

where the angular velocities ${}^N\vec{\omega}^H$ and ${}^H\vec{\omega}^G$, composed of generalized speeds, are expressed in vector form to enable the formation of the partial velocity matrices.

The j th DFE node's translational acceleration is obtained by differentiating Equation 3.8:

$$\begin{aligned}
{}^N\vec{a}^{n_j} &= \frac{d}{dt} ({}^N\vec{v}^{n_j}) \\
&= \frac{d}{dt} ({}^N\dot{\vec{r}}^H) + \frac{d}{dt} \left([{}_{N\leftarrow H}] [\widetilde{{}^N\vec{\omega}^H}] {}_H\vec{r}^G \right) \\
&\quad + \frac{d}{dt} \left([{}_{N\leftarrow H}] {}_H\dot{\vec{r}}^G \right) + \frac{d}{dt} \left([{}_{N\leftarrow H}] [\widetilde{{}^N\vec{\omega}^H}] [{}_{H\leftarrow G}] {}_G\vec{r}^{n_j} \right) \\
&\quad + \frac{d}{dt} \left([{}_{N\leftarrow H}] [{}_{H\leftarrow G}] [\widetilde{{}^H\vec{\omega}^G}] {}_G\vec{r}^{n_j} \right) \\
&\quad + \frac{d}{dt} \left([{}_{N\leftarrow H}] [{}_{H\leftarrow G}] {}_G\dot{\vec{r}}^{n_j} \right) \\
&= {}^N\ddot{\vec{r}}^H + [\dot{{}^N\vec{\omega}^H}] [\widetilde{{}^N\vec{\omega}^H}] {}_H\vec{r}^G + [{}_{N\leftarrow H}] [\dot{\widetilde{{}^N\vec{\omega}^H}}] {}_H\vec{r}^G \\
&\quad + [{}_{N\leftarrow H}] [\dot{\widetilde{{}^N\vec{\omega}^H}}] {}_H\dot{\vec{r}}^G + [\dot{{}^N\vec{\omega}^H}] {}_H\dot{\vec{r}}^G + [{}_{N\leftarrow H}] {}_H\ddot{\vec{r}}^G \\
&\quad + [\dot{{}^N\vec{\omega}^H}] [\widetilde{{}^N\vec{\omega}^H}] [{}_{H\leftarrow G}] {}_G\vec{r}^{n_j} + [{}_{N\leftarrow H}] [\dot{\widetilde{{}^N\vec{\omega}^H}}] [{}_{H\leftarrow G}] {}_G\vec{r}^{n_j} \\
&\quad + [{}_{N\leftarrow H}] [\widetilde{{}^N\vec{\omega}^H}] [\dot{{}^N\vec{\omega}^H}] [{}_{H\leftarrow G}] {}_G\vec{r}^{n_j} + [{}_{N\leftarrow H}] [\widetilde{{}^N\vec{\omega}^H}] [{}_{H\leftarrow G}] {}_G\dot{\vec{r}}^{n_j} \\
&\quad + [\dot{{}^N\vec{\omega}^H}] [{}_{H\leftarrow G}] [\widetilde{{}^H\vec{\omega}^G}] {}_G\vec{r}^{n_j} + [{}_{N\leftarrow H}] [\dot{\widetilde{{}^N\vec{\omega}^H}}] [\widetilde{{}^H\vec{\omega}^G}] {}_G\vec{r}^{n_j} \\
&\quad + [{}_{N\leftarrow H}] [{}_{H\leftarrow G}] [\widetilde{{}^H\vec{\omega}^G}] {}_G\vec{r}^{n_j} + [{}_{N\leftarrow H}] [{}_{H\leftarrow G}] [\widetilde{{}^H\vec{\omega}^G}] {}_G\dot{\vec{r}}^{n_j} \\
&\quad + [\dot{{}^N\vec{\omega}^H}] [{}_{H\leftarrow G}] {}_G\dot{\vec{r}}^{n_j} + [{}_{N\leftarrow H}] [\dot{{}^N\vec{\omega}^H}] {}_G\dot{\vec{r}}^{n_j} \\
&\quad + [{}_{N\leftarrow H}] [{}_{H\leftarrow G}] {}_G\ddot{\vec{r}}^{n_j} \\
&= {}^N\ddot{\vec{r}}^H + [{}_{N\leftarrow H}] [\widetilde{{}^N\vec{\omega}^H}] [\widetilde{{}^N\vec{\omega}^H}] {}_H\vec{r}^G + [{}_{N\leftarrow H}] [\dot{\widetilde{{}^N\vec{\omega}^H}}] {}_H\vec{r}^G \\
&\quad + 2[{}_{N\leftarrow H}] [\dot{\widetilde{{}^N\vec{\omega}^H}}] {}_H\dot{\vec{r}}^G + [{}_{N\leftarrow H}] {}_H\ddot{\vec{r}}^G \\
&\quad + [{}_{N\leftarrow H}] [\widetilde{{}^N\vec{\omega}^H}] [\widetilde{{}^N\vec{\omega}^H}] [{}_{H\leftarrow G}] {}_G\vec{r}^{n_j} + [{}_{N\leftarrow H}] [\dot{\widetilde{{}^N\vec{\omega}^H}}] [{}_{H\leftarrow G}] {}_G\vec{r}^{n_j} \\
&\quad + 2[{}_{N\leftarrow H}] [\dot{\widetilde{{}^N\vec{\omega}^H}}] [{}_{H\leftarrow G}] [\widetilde{{}^H\vec{\omega}^G}] {}_G\vec{r}^{n_j} + 2[{}_{N\leftarrow H}] [\widetilde{{}^N\vec{\omega}^H}] [{}_{H\leftarrow G}] {}_G\dot{\vec{r}}^{n_j} \\
&\quad + [{}_{N\leftarrow H}] [{}_{H\leftarrow G}] [\widetilde{{}^H\vec{\omega}^G}] [\widetilde{{}^H\vec{\omega}^G}] {}_G\vec{r}^{n_j} + [{}_{N\leftarrow H}] [{}_{H\leftarrow G}] [\widetilde{{}^H\vec{\omega}^G}] {}_G\dot{\vec{r}}^{n_j} \\
&\quad + 2[{}_{N\leftarrow H}] [{}_{H\leftarrow G}] [\widetilde{{}^H\vec{\omega}^G}] {}_G\dot{\vec{r}}^{n_j} + [{}_{N\leftarrow H}] [{}_{H\leftarrow G}] {}_G\ddot{\vec{r}}^{n_j}
\end{aligned} \tag{3.10}$$

Transformed to the j th DFE node's frame n_j , the j th DFE node's translational

acceleration from Equation 3.10 becomes

$$\begin{aligned}
{}^N_{n_j} \vec{a}^{n_j} &= [\mathbf{T}_{n_j \leftarrow N}] ({}^N \vec{v}^{n_j}) \\
&= [\mathbf{T}_{n_j \leftarrow N}] \left({}^N \ddot{\vec{r}}^H + [\mathbf{T}_{N \leftarrow H}] [\widetilde{{}^N \vec{\omega}^H}] [\widetilde{{}^N \vec{\omega}^H}]_H^H \vec{r}^G + [\mathbf{T}_{N \leftarrow H}] [\widetilde{{}^N \dot{\vec{\omega}}^H}]_H^H \vec{r}^G \right. \\
&\quad + 2[\mathbf{T}_{N \leftarrow H}] [\widetilde{{}^N \vec{\omega}^H}]_H^H \dot{\vec{r}}^G + [\mathbf{T}_{N \leftarrow H}]_H^H \ddot{\vec{r}}^G \\
&\quad + [\mathbf{T}_{N \leftarrow H}] [\widetilde{{}^N \vec{\omega}^H}] [\widetilde{{}^N \vec{\omega}^H}] [\mathbf{T}_{H \leftarrow G}]_G^G \vec{r}^{n_j} + [\mathbf{T}_{N \leftarrow H}] [\widetilde{{}^N \dot{\vec{\omega}}^H}] [\mathbf{T}_{H \leftarrow G}]_G^G \vec{r}^{n_j} \\
&\quad + 2[\mathbf{T}_{N \leftarrow H}] [\widetilde{{}^N \vec{\omega}^H}] [\mathbf{T}_{H \leftarrow G}] [\widetilde{{}^H \vec{\omega}^G}]_G^G \vec{r}^{n_j} + 2[\mathbf{T}_{N \leftarrow H}] [\widetilde{{}^N \vec{\omega}^H}] [\mathbf{T}_{H \leftarrow G}]_G^G \dot{\vec{r}}^{n_j} \\
&\quad + [\mathbf{T}_{N \leftarrow H}] [\mathbf{T}_{H \leftarrow G}] [\widetilde{{}^H \vec{\omega}^G}] [\widetilde{{}^H \vec{\omega}^G}]_G^G \vec{r}^{n_j} + [\mathbf{T}_{N \leftarrow H}] [\mathbf{T}_{H \leftarrow G}] [\widetilde{{}^H \dot{\vec{\omega}}^G}]_G^G \vec{r}^{n_j} \\
&\quad \left. + 2[\mathbf{T}_{N \leftarrow H}] [\mathbf{T}_{H \leftarrow G}] [\widetilde{{}^H \vec{\omega}^G}]_G^G \dot{\vec{r}}^{n_j} + [\mathbf{T}_{N \leftarrow H}] [\mathbf{T}_{H \leftarrow G}]_G^G \ddot{\vec{r}}^{n_j} \right) \\
&= [\mathbf{T}_{n_j \leftarrow N}] {}^N \ddot{\vec{r}}^H + [\mathbf{T}_{n_j \leftarrow H}] [\widetilde{{}^N \vec{\omega}^H}] [\widetilde{{}^N \vec{\omega}^H}]_H^H \vec{r}^G + [\mathbf{T}_{n_j \leftarrow H}] [\widetilde{{}^N \dot{\vec{\omega}}^H}]_H^H \vec{r}^G \\
&\quad + 2[\mathbf{T}_{n_j \leftarrow H}] [\widetilde{{}^N \vec{\omega}^H}]_H^H \dot{\vec{r}}^G + [\mathbf{T}_{n_j \leftarrow H}]_H^H \ddot{\vec{r}}^G \\
&\quad + [\mathbf{T}_{n_j \leftarrow H}] [\widetilde{{}^N \vec{\omega}^H}] [\widetilde{{}^N \vec{\omega}^H}] [\mathbf{T}_{H \leftarrow G}]_G^G \vec{r}^{n_j} + [\mathbf{T}_{n_j \leftarrow H}] [\widetilde{{}^N \dot{\vec{\omega}}^H}] [\mathbf{T}_{H \leftarrow G}]_G^G \vec{r}^{n_j} \quad (3.11) \\
&\quad + 2[\mathbf{T}_{n_j \leftarrow H}] [\widetilde{{}^N \vec{\omega}^H}] [\mathbf{T}_{H \leftarrow G}] [\widetilde{{}^H \vec{\omega}^G}]_G^G \vec{r}^{n_j} + 2[\mathbf{T}_{n_j \leftarrow H}] [\widetilde{{}^N \vec{\omega}^H}] [\mathbf{T}_{H \leftarrow G}]_G^G \dot{\vec{r}}^{n_j} \\
&\quad + [\mathbf{T}_{n_j \leftarrow G}] [\widetilde{{}^H \vec{\omega}^G}] [\widetilde{{}^H \vec{\omega}^G}]_G^G \vec{r}^{n_j} + [\mathbf{T}_{n_j \leftarrow G}] [\widetilde{{}^H \dot{\vec{\omega}}^G}]_G^G \vec{r}^{n_j} \\
&\quad + 2[\mathbf{T}_{n_j \leftarrow G}] [\widetilde{{}^H \vec{\omega}^G}]_G^G \dot{\vec{r}}^{n_j} + [\mathbf{T}_{n_j \leftarrow G}]_G^G \ddot{\vec{r}}^{n_j} \\
&= [\mathbf{T}_{n_j \leftarrow N}] {}^N \ddot{\vec{r}}^H + [\mathbf{T}_{n_j \leftarrow H}] [\widetilde{{}^N \vec{\omega}^H}] [\widetilde{{}^N \vec{\omega}^H}]_H^H \vec{r}^G - [\mathbf{T}_{n_j \leftarrow H}] [\widetilde{{}^H \vec{r}^G}]_H^H \dot{\vec{\omega}}^H \\
&\quad + 2[\mathbf{T}_{n_j \leftarrow H}] [\widetilde{{}^N \vec{\omega}^H}]_H^H \dot{\vec{r}}^G + [\mathbf{T}_{n_j \leftarrow H}]_H^H \ddot{\vec{r}}^G \\
&\quad + [\mathbf{T}_{n_j \leftarrow H}] [\widetilde{{}^N \vec{\omega}^H}] [\widetilde{{}^N \vec{\omega}^H}] [\mathbf{T}_{H \leftarrow G}]_G^G \vec{r}^{n_j} - [\mathbf{T}_{n_j \leftarrow H}] \left[[\mathbf{T}_{H \leftarrow G}]_G^G \vec{r}^{n_j} \right]_H^H \dot{\vec{\omega}}^H \\
&\quad + 2[\mathbf{T}_{n_j \leftarrow H}] [\widetilde{{}^N \vec{\omega}^H}] [\mathbf{T}_{H \leftarrow G}] [\widetilde{{}^H \vec{\omega}^G}]_G^G \vec{r}^{n_j} + 2[\mathbf{T}_{n_j \leftarrow H}] [\widetilde{{}^N \vec{\omega}^H}] [\mathbf{T}_{H \leftarrow G}]_G^G \dot{\vec{r}}^{n_j} \\
&\quad + [\mathbf{T}_{n_j \leftarrow G}] [\widetilde{{}^H \vec{\omega}^G}] [\widetilde{{}^H \vec{\omega}^G}]_G^G \vec{r}^{n_j} - [\mathbf{T}_{n_j \leftarrow G}] [\widetilde{{}^G \vec{r}^{n_j}}]_G^G \dot{\vec{\omega}}^G \\
&\quad + 2[\mathbf{T}_{n_j \leftarrow G}] [\widetilde{{}^H \vec{\omega}^G}]_G^G \dot{\vec{r}}^{n_j} + [\mathbf{T}_{n_j \leftarrow G}]_G^G \ddot{\vec{r}}^{n_j}
\end{aligned}$$

where the angular accelerations ${}^N \dot{\vec{\omega}}^H$ and ${}^H \dot{\vec{\omega}}^G$, composed of generalized accelerations, are expressed in vector form to enable the formation of the partial velocity matrices.

Equations 3.1 through 3.11 represent the complete translational kinematic expressions for the bodies studied in this system. Again, working along the chain of frames of reference for the aircraft, the first body is the aircraft's airframe H . The orientation of the body with respect to the inertial frame, expressed in the inertial frame,

is

$$\begin{aligned}
{}^N\vec{\theta}^H &= [\mathbf{T}_{N\leftarrow H}]_H^N \vec{\theta}^H \\
&= [\mathbf{I}]_{1\times 1} {}^N\vec{\theta}^H \\
&= {}^N_H\vec{\theta}^H
\end{aligned} \tag{3.12}$$

Note the planar case's property where the relative angle to the previous frame is the same regardless of the frame in which it is expressed due to the transformation matrix being identity as shown in Equation 2.7. For the fully-spatial case of SRAMSS, such simplifications cannot be made.

The airframe's angular velocity is obtained by differentiating Equation 3.1:

$$\begin{aligned}
{}^N\vec{\omega}^H &= \frac{d}{dt} ({}^N\vec{\theta}^H) \\
&= \frac{d}{dt} ([\mathbf{T}_{N\leftarrow H}]_H^N \vec{\theta}^H) \\
&= [\mathbf{T}_{N\leftarrow H}]_H^N \dot{\vec{\theta}}^H \\
&= [\mathbf{T}_{N\leftarrow H}]_H^N \vec{\omega}^H \\
&= [\mathbf{I}]_{1\times 1} {}^N\vec{\omega}^H \\
&= {}^N_H\vec{\omega}^H
\end{aligned} \tag{3.13}$$

Similarly to Equation 3.12, because ${}^N\vec{\theta}^H \equiv {}^N_H\vec{\theta}^H$, Equation 3.13 finds that ${}^N\vec{\omega}^H \equiv {}^N_H\vec{\omega}^H$ for the planar case. Considering that the partial velocity matrices are expressed in the body frames, ${}^N_H\vec{\omega}^H$ is the preferred notation.

The airframe's angular acceleration is obtained by differentiating Equation 3.13:

$$\begin{aligned}
{}^N\vec{\alpha}^H &= \frac{d}{dt} ({}^N\vec{\omega}^H) \\
&= \frac{d}{dt} ([\mathbf{T}_{N\leftarrow H}]_H^N \vec{\omega}^H) \\
&= [\dot{\mathbf{T}}_{N\leftarrow H}]_H^N \vec{\omega}^H + [\mathbf{T}_{N\leftarrow H}]_H^N \dot{\vec{\omega}}^H \\
&= [\mathbf{T}_{N\leftarrow H}]_H^N \widetilde{[\vec{\omega}^H]}_H^N \vec{\omega}^H + [\mathbf{T}_{N\leftarrow H}]_H^N \dot{\vec{\omega}}^H \\
&= [\mathbf{I}]_{1\times 1} {}^N\vec{\alpha}^H \\
&= {}^N_H\vec{\alpha}^H
\end{aligned} \tag{3.14}$$

Once more, equivalence between frames of references is observed; ${}^N\vec{\alpha}^H \equiv {}^N_H\vec{\alpha}^H$ for the planar case. Considering that the partial velocity matrices are expressed in the body frames, ${}^N_H\vec{\alpha}^H$ is the preferred notation.

The next body in the aircraft's chain of frame's is the j th DFE node n_j . The general equation describing the orientation of the j th DFE node frame with respect to the inertial frame, expressed in the inertial frame is

$$\begin{aligned}
{}^N\vec{\theta}^{n_j} &= {}^N\vec{\theta}^H + {}^H\vec{\theta}^G + {}^G\vec{\theta}^{n_j} \\
&= [\mathbf{T}_{N\leftarrow H}]_H^N \vec{\theta}^H + [\mathbf{T}_{N\leftarrow H}][\mathbf{T}_{H\leftarrow G}]_G^H \vec{\theta}^G + [\mathbf{T}_{N\leftarrow H}][\mathbf{T}_{H\leftarrow G}][\mathbf{T}_{G\leftarrow n_j}]_{n_j}^G \vec{\theta}^{n_j} \\
&= [\mathbf{I}]_{1\times 1} {}^N\vec{\theta}^H + [\mathbf{I}]_{1\times 1} [\mathbf{I}]_{1\times 1} {}^H\vec{\theta}^G + [\mathbf{I}]_{1\times 1} [\mathbf{I}]_{1\times 1} [\mathbf{I}]_{1\times 1} {}^G\vec{\theta}^{n_j} \\
&= {}^N\vec{\theta}^H + {}^H\vec{\theta}^G + {}^G\vec{\theta}^{n_j}
\end{aligned} \tag{3.15}$$

The j th DFE node's angular velocity is obtained by differentiating Equation 3.15:

$$\begin{aligned}
{}^N\vec{\omega}^{n_j} &= \frac{d}{dt} \left({}^N\vec{\theta}^{n_j} \right) \\
&= \frac{d}{dt} \left([\mathbf{T}_{N\leftarrow H}]_H^N \vec{\theta}^H \right) + \frac{d}{dt} \left([\mathbf{T}_{N\leftarrow H}][\mathbf{T}_{H\leftarrow G}]_G^H \vec{\theta}^G \right) \\
&\quad + \frac{d}{dt} \left([\mathbf{T}_{N\leftarrow H}][\mathbf{T}_{H\leftarrow G}][\mathbf{T}_{G\leftarrow n_j}]_{n_j}^G \vec{\theta}^{n_j} \right) \\
&= [\mathbf{T}_{N\leftarrow H}]_H^N \dot{\vec{\theta}}^H + [\mathbf{T}_{N\leftarrow H}][\mathbf{T}_{H\leftarrow G}]_G^H \dot{\vec{\theta}}^G + [\mathbf{T}_{N\leftarrow H}][\mathbf{T}_{H\leftarrow G}][\mathbf{T}_{G\leftarrow n_j}]_{n_j}^G \dot{\vec{\theta}}^{n_j} \\
&= [\mathbf{T}_{N\leftarrow H}]_H^N \vec{\omega}^H + [\mathbf{T}_{N\leftarrow H}][\mathbf{T}_{H\leftarrow G}]_G^H \vec{\omega}^G + [\mathbf{T}_{N\leftarrow H}][\mathbf{T}_{H\leftarrow G}][\mathbf{T}_{G\leftarrow n_j}]_{n_j}^G \vec{\omega}^{n_j} \\
&= [\mathbf{I}]_{1\times 1} {}^N\vec{\omega}^H + [\mathbf{I}]_{1\times 1} {}^H\vec{\omega}^G + [\mathbf{I}]_{1\times 1} {}^G\vec{\omega}^{n_j} \\
&= {}^N\vec{\omega}^H + {}^H\vec{\omega}^G + {}^G\vec{\omega}^{n_j}
\end{aligned} \tag{3.16}$$

Given that the transformation matrices are identity, the equivalence ${}^N\vec{\omega}^{n_j} = {}^N\vec{\omega}^{n_j}$ holds. Therefore, expressing Equation 3.16 in the j th DFE node coordinate system becomes

$${}^N\vec{\omega}^{n_j} = {}^N\vec{\omega}^{n_j} = {}^N\vec{\omega}^H + {}^H\vec{\omega}^G + {}^G\vec{\omega}^{n_j} \tag{3.17}$$

The j th DFE node's angular acceleration is obtained by differentiating Equation 3.16:

$$\begin{aligned}
{}^N_N\vec{\alpha}^{n_j} &= \frac{d}{dt} ({}^N_N\vec{\omega}^{n_j}) \\
&= \frac{d}{dt} ([\mathbf{T}_{N\leftarrow H}]_H^N \vec{\omega}^H) + \frac{d}{dt} ([\mathbf{T}_{N\leftarrow H}][\mathbf{T}_{H\leftarrow G}]_G^H \vec{\omega}^G) \\
&\quad + \frac{d}{dt} ([\mathbf{T}_{N\leftarrow H}][\mathbf{T}_{H\leftarrow G}][\mathbf{T}_{G\leftarrow n_j}]_{n_j}^G \vec{\omega}^{n_j}) \\
&= [\dot{\mathbf{T}}_{N\leftarrow H}]_H^N \vec{\omega}^H + [\mathbf{T}_{N\leftarrow H}]_H^N \dot{\vec{\omega}}^H + [\dot{\mathbf{T}}_{N\leftarrow H}][\mathbf{T}_{H\leftarrow G}]_G^H \vec{\omega}^G \\
&\quad + [\mathbf{T}_{N\leftarrow H}][\dot{\mathbf{T}}_{H\leftarrow G}]_G^H \vec{\omega}^G + [\mathbf{T}_{N\leftarrow H}][\mathbf{T}_{H\leftarrow G}]_G^H \dot{\vec{\omega}}^G \\
&\quad + [\dot{\mathbf{T}}_{N\leftarrow H}][\mathbf{T}_{H\leftarrow G}][\mathbf{T}_{G\leftarrow n_j}]_{n_j}^G \vec{\omega}^{n_j} + [\mathbf{T}_{N\leftarrow H}][\dot{\mathbf{T}}_{H\leftarrow G}][\mathbf{T}_{G\leftarrow n_j}]_{n_j}^G \vec{\omega}^{n_j} \\
&\quad + [\mathbf{T}_{N\leftarrow H}][\mathbf{T}_{H\leftarrow G}][\dot{\mathbf{T}}_{G\leftarrow n_j}]_{n_j}^G \vec{\omega}^{n_j} + [\mathbf{T}_{N\leftarrow H}][\mathbf{T}_{H\leftarrow G}][\mathbf{T}_{G\leftarrow n_j}]_{n_j}^G \dot{\vec{\omega}}^{n_j} \\
&= [\mathbf{T}_{N\leftarrow H}][\widetilde{[\mathbf{T}_{H\leftarrow G}]_G^H}^N \vec{\omega}^H] + [\mathbf{T}_{N\leftarrow H}]_H^N \dot{\vec{\omega}}^H + [\mathbf{T}_{N\leftarrow H}][\widetilde{[\mathbf{T}_{H\leftarrow G}]_G^H} \vec{\omega}^G] \\
&\quad + [\mathbf{T}_{N\leftarrow H}][\mathbf{T}_{H\leftarrow G}][\widetilde{[\mathbf{T}_{G\leftarrow n_j}]_{n_j}^G}^H \vec{\omega}^G] + [\mathbf{T}_{N\leftarrow H}][\mathbf{T}_{H\leftarrow G}]_G^H \dot{\vec{\omega}}^G \\
&\quad + [\mathbf{T}_{N\leftarrow H}][\widetilde{[\mathbf{T}_{H\leftarrow G}]_G^H}^N \vec{\omega}^H][\mathbf{T}_{G\leftarrow n_j}]_{n_j}^G \vec{\omega}^{n_j} \\
&\quad + [\mathbf{T}_{N\leftarrow H}][\mathbf{T}_{H\leftarrow G}][\widetilde{[\mathbf{T}_{G\leftarrow n_j}]_{n_j}^G}^H \vec{\omega}^G][\mathbf{T}_{G\leftarrow n_j}]_{n_j}^G \vec{\omega}^{n_j} \\
&\quad + [\mathbf{T}_{N\leftarrow H}][\mathbf{T}_{H\leftarrow G}][\mathbf{T}_{G\leftarrow n_j}]_{n_j}^G \widetilde{[\vec{\omega}^{n_j}]_{n_j}^G}^G \vec{\omega}^{n_j} \\
&\quad + [\mathbf{T}_{N\leftarrow H}][\mathbf{T}_{H\leftarrow G}][\mathbf{T}_{G\leftarrow n_j}]_{n_j}^G \dot{\vec{\omega}}^{n_j} \\
&= [\mathbf{T}_{N\leftarrow H}]_H^N \dot{\vec{\omega}}^H + [\mathbf{T}_{N\leftarrow H}][\mathbf{T}_{H\leftarrow G}]_G^H \dot{\vec{\omega}}^G + [\mathbf{T}_{N\leftarrow H}][\mathbf{T}_{H\leftarrow G}][\mathbf{T}_{G\leftarrow n_j}]_{n_j}^G \dot{\vec{\omega}}^{n_j} \\
&= [\mathbf{I}]_{1 \times 1}^N \dot{\vec{\omega}}^H + [\mathbf{I}]_{1 \times 1}^H \dot{\vec{\omega}}^G + [\mathbf{I}]_{1 \times 1}^G \dot{\vec{\omega}}^{n_j} \\
&= {}^N_H \dot{\vec{\omega}}^H + {}^H_G \dot{\vec{\omega}}^G + {}^G_{n_j} \dot{\vec{\omega}}^{n_j}
\end{aligned} \tag{3.18}$$

Since the transformation matrices are identity, terms which contain transformation time-derivatives yield skew angular velocities. The cross-product $[\vec{\omega}] \vec{\omega} \equiv 0$ eliminates these terms. Similarly to Equation 3.16, the equivalence ${}^N_N\vec{\alpha}^{n_j} = {}^N_{n_j}\vec{\alpha}^{n_j}$ holds. Therefore, expressing Equation 3.18 in the j th DFE node coordinate system becomes

$${}^N_{n_j}\vec{\alpha}^{n_j} = {}^N_N\vec{\alpha}^{n_j} = {}^N_H \dot{\vec{\omega}}^H + {}^H_G \dot{\vec{\omega}}^G + {}^G_{n_j} \dot{\vec{\omega}}^{n_j} \tag{3.19}$$

At this point, The derivations of the kinematic expressions are complete for the bodies studied for dynamic response.

The equations for velocity and acceleration can be expressed in the form of Equations 2.15 through 2.18 where the kinematic equations are compactly expressed in

terms of the vector of generalized speeds \mathbf{u} . Linear velocities are compactly expressed

$$\begin{aligned} {}^N_k \vec{\mathbf{v}}^k &= [{}^N_k \mathbf{V}^k] \mathbf{u} \\ &= \begin{bmatrix} {}^k \mathbf{V}^{u_1} & \dots & {}^k \mathbf{V}^{u_{N_{gc}}} \end{bmatrix}_{2 \times N_{gc}} \begin{Bmatrix} u_1 \\ \vdots \\ u_{N_{gc}} \end{Bmatrix}_{N_{gc} \times 1} \end{aligned} \quad (3.20)$$

and angular velocities are compactly expressed

$$\begin{aligned} {}^N_k \vec{\boldsymbol{\omega}}^k &= [{}^N_k \mathbf{W}^k] \mathbf{u} \\ &= \begin{bmatrix} {}^k \mathbf{W}^{u_1} & \dots & {}^k \mathbf{W}^{u_{N_{gc}}} \end{bmatrix}_{1 \times N_{gc}} \begin{Bmatrix} u_1 \\ \vdots \\ u_{N_{gc}} \end{Bmatrix}_{N_{gc} \times 1} \end{aligned} \quad (3.21)$$

where by inspection of Equation 3.20, the linear and angular partial velocity matrices $[{}^N_k \mathbf{V}^k]$ and $[{}^N_k \mathbf{W}^k]$ are the arrays of coefficients for each of the generalized speed terms in the kinematic expressions. Each element \mathbf{V} and \mathbf{W} represent the linear and angular partial contributions along u_i to kinematic quantity of body k , expressed in the k th frame. Otherwise stated, it transforms the expression of the kinematic quantity in terms of generalized quantities to body quantities expressed in the k th body's coordinate system.

Similarly, the equations of linear and angular accelerations can be expressed in terms of the system generalized accelerations $\dot{\mathbf{u}}$ as

$$\begin{aligned} {}^N_k \vec{\mathbf{a}}^k &= [{}^N_k \mathbf{V}^k] \dot{\mathbf{u}} + \vec{\mathbf{Z}}_k \\ &= \begin{bmatrix} {}^k \mathbf{V}^{u_1} & \dots & {}^k \mathbf{V}^{u_{N_{gc}}} \end{bmatrix}_{2 \times N_{gc}} \begin{Bmatrix} \dot{u}_1 \\ \vdots \\ \dot{u}_{N_{gc}} \end{Bmatrix}_{N_{gc} \times 1} + \vec{\mathbf{Z}}_k \end{aligned} \quad (3.22)$$

and

$$\begin{aligned} {}^N_k \vec{\boldsymbol{\alpha}}^k &= [{}^N_k \mathbf{W}^k] \dot{\mathbf{u}} + \vec{\mathbf{Y}}_k \\ &= \begin{bmatrix} {}^k \mathbf{W}^{u_1} & \dots & {}^k \mathbf{W}^{u_{N_{gc}}} \end{bmatrix}_{1 \times N_{gc}} \begin{Bmatrix} \dot{u}_1 \\ \vdots \\ \dot{u}_{N_{gc}} \end{Bmatrix}_{N_{gc} \times 1} + \vec{\mathbf{Y}}_k \end{aligned} \quad (3.23)$$

In the case of acceleration expressions, the terms which do not contain generalized accelerations expressed in vector form are grouped into the remainder acceleration

terms $\vec{\mathbf{Z}}_k$ and, $\vec{\mathbf{Y}}_k$ respectively. Since $\dot{\mathbf{u}}$ is the locally evaluated derivative of \mathbf{u} , the linear and angular partial velocity matrices are identical for velocity and acceleration expressions for a given body.

As shown in Section 2.2, the partial velocity matrices are integral components of Kane's method. As such, for the aircraft's airframe, the translational partial velocity matrix ${}^N_H\mathbf{V}^H$ is obtained by inspection of Equation 3.3, and the angular partial velocity matrix ${}^N_H\mathbf{W}^H$ by inspection of Equation 3.13:

$${}^N_H\mathbf{V}^H = \begin{bmatrix} [0]_{2 \times 12} & [\mathbf{T}_{H \leftarrow N}] & [0]_{2 \times 1} & [0]_{2 \times (N_{gc} - 15)} \end{bmatrix} \quad (3.24)$$

$${}^N_H\mathbf{W}^H = \begin{bmatrix} [0]_{1 \times 12} & 0 & 0 & 1 & [0]_{1 \times (N_{gc} - 15)} \end{bmatrix} \quad (3.25)$$

For the general case of the j th DFE node, the translational partial velocity matrix ${}^N_{n_j}\mathbf{V}^{n_j}$ is obtained by inspection of Equation 3.9, and the angular partial velocity matrix ${}^N_{n_j}\mathbf{W}^{n_j}$ by inspection of Equation 3.16:

$$\begin{aligned} {}^N_{n_j}\mathbf{V}^{n_j} &= \begin{bmatrix} [0]_{2 \times 12} & [\mathbf{T}_{n_j \leftarrow N}] & -[\mathbf{T}_{n_j \leftarrow H}] \left\{ [\widetilde{{}^H_H\mathbf{r}^G}] + [\widetilde{{}^H_{H \leftarrow G}}]_G^G \widetilde{\mathbf{r}}^{n_j} \right\} \\ [\mathbf{T}_{n_j \leftarrow H}] & -[\mathbf{T}_{n_j \leftarrow G}]_G^G \widetilde{\mathbf{r}}^{n_j} & [0]_{2 \times 3(j-1)} & [\mathbf{T}_{n_j \leftarrow G}] \\ [0]_{2 \times 1} & [0]_{2 \times (i-3j-18)} \end{bmatrix} \end{aligned} \quad (3.26)$$

$$\begin{aligned} {}^N_{n_j}\mathbf{W}^{n_j} &= \begin{bmatrix} [0]_{1 \times 12} & 0 & 0 & 1 & 0 & 0 & 1 & [0]_{1 \times 3(j-1)} & 0 & 0 \\ 1 & [0]_{1 \times (N_{gc} - 18 - 3j)} \end{bmatrix} \end{aligned} \quad (3.27)$$

Recalling that there are N_{gc} generalized coordinates in the system.

The linear remainder accelerations $\vec{\mathbf{Z}}$ and angular remainder accelerations $\vec{\mathbf{Y}}$ are

$$\vec{\mathbf{Z}}_H = 0 \quad (3.28)$$

$$\begin{aligned} \vec{\mathbf{Z}}_{n_j} &= [\mathbf{T}_{n_j \leftarrow H}] [\widetilde{{}^N_H\boldsymbol{\omega}^H}] [\widetilde{{}^N_H\boldsymbol{\omega}^H}]_H^H \widetilde{\mathbf{r}}^G + 2[\mathbf{T}_{n_j \leftarrow H}] [\widetilde{{}^N_H\boldsymbol{\omega}^H}]_H^H \dot{\widetilde{\mathbf{r}}}^G \\ &\quad + [\mathbf{T}_{n_j \leftarrow H}] [\widetilde{{}^N_H\boldsymbol{\omega}^H}] [\widetilde{{}^N_H\boldsymbol{\omega}^H}] [\mathbf{T}_{H \leftarrow G}]_G^G \widetilde{\mathbf{r}}^{n_j} \\ &\quad + 2[\mathbf{T}_{n_j \leftarrow H}] [\widetilde{{}^N_H\boldsymbol{\omega}^H}] [\mathbf{T}_{H \leftarrow G}] [\widetilde{{}^H_G\boldsymbol{\omega}^G}]_G^G \widetilde{\mathbf{r}}^{n_j} \\ &\quad + 2[\mathbf{T}_{n_j \leftarrow H}] [\widetilde{{}^N_H\boldsymbol{\omega}^H}] [\mathbf{T}_{H \leftarrow G}]_G^G \dot{\widetilde{\mathbf{r}}}^{n_j} + [\mathbf{T}_{n_j \leftarrow G}] [\widetilde{{}^H_G\boldsymbol{\omega}^G}] [\widetilde{{}^H_G\boldsymbol{\omega}^G}]_G^G \widetilde{\mathbf{r}}^{n_j} \\ &\quad + 2[\mathbf{T}_{n_j \leftarrow G}] [\widetilde{{}^H_G\boldsymbol{\omega}^G}]_G^G \dot{\widetilde{\mathbf{r}}}^{n_j} \end{aligned} \quad (3.29)$$

$$\vec{\mathbf{Y}}_H = 0 \quad (3.30)$$

$$\vec{\mathbf{Y}}_{n_j} = 0 \quad (3.31)$$

Thus the complete velocities and accelerations of the studied bodies can be expressed

$${}^N_H\vec{v}^H = [{}^N_H\mathbf{V}^H] \vec{u} \quad (3.32)$$

$${}^N_H\vec{\omega}^H = [{}^N_H\mathbf{W}^H] \vec{u} \quad (3.33)$$

$${}^N_H\vec{a}^H = [{}^N_H\mathbf{V}^H] \dot{\vec{u}} + \vec{Z}_H \quad (3.34)$$

$${}^N_H\vec{\alpha}^H = [{}^N_H\mathbf{W}^H] \dot{\vec{u}} + \vec{Y}_H \quad (3.35)$$

for the airframe, and

$${}^N_{n_j}\vec{v}^{n_j} = [{}^N_{n_j}\mathbf{V}^{n_j}] \vec{u} \quad (3.36)$$

$${}^N_{n_j}\vec{\omega}^{n_j} = [{}^N_{n_j}\mathbf{W}^{n_j}] \vec{u} \quad (3.37)$$

$${}^N_{n_j}\vec{a}^{n_j} = [{}^N_{n_j}\mathbf{V}^{n_j}] \dot{\vec{u}} + \vec{Z}_{n_j} \quad (3.38)$$

$${}^N_{n_j}\vec{\alpha}^{n_j} = [{}^N_{n_j}\mathbf{W}^{n_j}] \dot{\vec{u}} + \vec{Y}_{n_j} \quad (3.39)$$

for the DFE nodes. Kinematic expressions for the studied bodies which compose the complete aircraft, have been derived. Nevertheless, the positions and velocities of the vertices defining each polygon in the simulation must be determined. This will enable proper handling of collision detection and oriented dynamic response.

3.2 Polygon Kinematics

In the SRAMSS environment, the dynamic interface formed between the aircraft and ship is governed by the interaction of the aircraft with defined polygons. In effect, this interaction is the appropriately-oriented dynamic response generated by the contact dynamics model. The dynamic interface interactions comprise aircraft response to ship motion, RSD deck manoeuvring, and RSD securing.

The polygons included in the SRAMSS environment have their vertices defined with respect to their own frame of reference. This allow the prescription of motion for the polygon while maintaining a single general equation defining each polygon vertex. For this work, only the positions and velocities of the vertices are required. Even so, the partial velocity matrices include the generalized speeds for these polygons, such that the partial velocity matrices can be determined for these polygons in the case where dynamic responses of these polygons are studied. This requires that the equations of motion be expressed relative to the inertial frame. Expression relative to this frame also facilitates calculation of relative velocities and dynamic quantities,

since the inertial frame is common to both the aircraft's and the polygon's chain of frames.

The position of the m th ship deck polygon vertex S_m with respect to the inertial frame, expressed in the inertial frame, is

$$\begin{aligned} {}^N\vec{r}^{S_m} &= {}^N\vec{r}^S + {}^S\vec{r}^{S_m} \\ &= {}^N\vec{r}^S + [\mathbf{T}_{N\leftarrow S}]_S^S \vec{r}^{S_m} \end{aligned} \quad (3.40)$$

The m th ship deck vertex velocity is obtained by differentiating Equation 3.40, resulting in

$$\begin{aligned} {}^N\vec{v}^{S_m} &= \frac{d}{dt} ({}^N\vec{r}^{S_m}) \\ &= \frac{d}{dt} ({}^N\vec{r}^S) + \frac{d}{dt} ([\mathbf{T}_{N\leftarrow S}]_S^S \vec{r}^{S_m}) \\ &= {}^N\dot{\vec{r}}^S + [\dot{\mathbf{T}}_{N\leftarrow S}]_S^S \vec{r}^{S_m} + [\mathbf{T}_{N\leftarrow S}]_S^S \dot{\vec{r}}^{S_m} \\ &= {}^N\dot{\vec{r}}^S + [\mathbf{T}_{N\leftarrow S}]_S^S [\widetilde{{}^N\vec{\omega}^S}]_S^S \vec{r}^{S_m} + [\mathbf{T}_{N\leftarrow S}]_S^S \dot{\vec{r}}^{S_m} \overset{0}{\rightarrow} \\ &= {}^N\dot{\vec{r}}^S + [\mathbf{T}_{N\leftarrow S}]_S^S [\widetilde{{}^N\vec{\omega}^S}]_S^S \vec{r}^{S_m} \end{aligned} \quad (3.41)$$

Next along the polygon chain of frames is the RSD deck. The position of the m th RSD deck polygon vertex D_m with respect to the inertial frame, expressed in the inertial frame, is

$$\begin{aligned} {}^N\vec{r}^{D_m} &= {}^N\vec{r}^S + {}^S\vec{r}^D + {}^D\vec{r}^{D_m} \\ &= {}^N\vec{r}^S + [\mathbf{T}_{N\leftarrow S}]_S^S \vec{r}^D + [\mathbf{T}_{N\leftarrow S}] [\mathbf{T}_{S\leftarrow D}]_D^D \vec{r}^{D_m} \\ &= {}^N\vec{r}^S + [\mathbf{T}_{N\leftarrow S}]_S^S \vec{r}^D + [\mathbf{T}_{N\leftarrow D}]_D^D \vec{r}^{D_m} \end{aligned} \quad (3.42)$$

The m th RSD deck vertex velocity is obtained by differentiating Equation 3.42, re-

sulting in

$$\begin{aligned}
{}^N\vec{v}^{D_m} &= \frac{d}{dt} ({}^N\vec{r}^{D_m}) \\
&= \frac{d}{dt} ({}^N\vec{r}^S) + \frac{d}{dt} ([\mathbf{T}_{N\leftarrow S}]_S^S \vec{r}^D) + \frac{d}{dt} ([\mathbf{T}_{N\leftarrow S}][\mathbf{T}_{S\leftarrow D}]_D^D \vec{r}^{D_m}) \\
&= {}^N\dot{\vec{r}}^S + [\dot{\mathbf{T}}_{N\leftarrow S}]_S^S \vec{r}^D + [\mathbf{T}_{N\leftarrow S}]_S^S \dot{\vec{r}}^D \\
&\quad + [\dot{\mathbf{T}}_{N\leftarrow S}][\mathbf{T}_{S\leftarrow D}]_D^D \vec{r}^{D_m} + [\mathbf{T}_{N\leftarrow S}][\dot{\mathbf{T}}_{S\leftarrow D}]_D^D \vec{r}^{D_m} \\
&\quad + [\mathbf{T}_{N\leftarrow S}][\mathbf{T}_{S\leftarrow D}]_D^D \dot{\vec{r}}^{D_m} \\
&= {}^N\dot{\vec{r}}^S + [\mathbf{T}_{N\leftarrow S}][\widetilde{[\mathbf{T}_{S\leftarrow D}]_S^S}^N]_S^S \vec{r}^D + [\mathbf{T}_{N\leftarrow S}]_S^S \dot{\vec{r}}^D \\
&\quad + [\mathbf{T}_{N\leftarrow S}][\widetilde{[\mathbf{T}_{S\leftarrow D}]_D^D}^N]_D^D \vec{r}^{D_m} + [\mathbf{T}_{N\leftarrow S}][\mathbf{T}_{S\leftarrow D}][\widetilde{[\mathbf{T}_{S\leftarrow D}]_D^D}^S]_D^D \vec{r}^{D_m} \\
&\quad + [\mathbf{T}_{N\leftarrow S}][\mathbf{T}_{S\leftarrow D}]_D^D \dot{\vec{r}}^{D_m} \rightarrow 0 \\
&= {}^N\dot{\vec{r}}^S + [\mathbf{T}_{N\leftarrow S}][\widetilde{[\mathbf{T}_{S\leftarrow D}]_S^S}^N]_S^S \vec{r}^D + [\mathbf{T}_{N\leftarrow S}]_S^S \dot{\vec{r}}^D \\
&\quad + [\mathbf{T}_{N\leftarrow S}][\widetilde{[\mathbf{T}_{S\leftarrow D}]_D^D}^N]_D^D \vec{r}^{D_m} + [\mathbf{T}_{N\leftarrow D}][\widetilde{[\mathbf{T}_{S\leftarrow D}]_D^D}^S]_D^D \vec{r}^{D_m}
\end{aligned} \tag{3.43}$$

Next along the polygon chain of frames are the wedge clamps. The position of the m th left and right wedge clamp polygon vertices CL_m and CR_m with respect to the inertial frame, expressed in the inertial frame, are

$$\begin{aligned}
{}^N\vec{r}^{CL_m} &= {}^N\vec{r}^S + {}^S\vec{r}^D + {}^D\vec{r}^{CL} + {}^{CL}\vec{r}^{CL_m} \\
&= {}^N\vec{r}^S + [\mathbf{T}_{N\leftarrow S}]_S^S \vec{r}^D + [\mathbf{T}_{N\leftarrow S}][\mathbf{T}_{S\leftarrow D}]_D^D \vec{r}^{CL} \\
&\quad + [\mathbf{T}_{N\leftarrow S}][\mathbf{T}_{S\leftarrow D}][\mathbf{T}_{D\leftarrow CL}]_{CL}^{CL} \vec{r}^{CL_m} \\
&= {}^N\vec{r}^S + [\mathbf{T}_{N\leftarrow S}]_S^S \vec{r}^D + [\mathbf{T}_{N\leftarrow D}]_D^D \vec{r}^{CL} + [\mathbf{T}_{N\leftarrow CL}]_{CL}^{CL} \vec{r}^{CL_m}
\end{aligned} \tag{3.44}$$

and

$$\begin{aligned}
{}^N\vec{r}^{CR_m} &= {}^N\vec{r}^S + {}^S\vec{r}^D + {}^D\vec{r}^{CR} + {}^{CR}\vec{r}^{CR_m} \\
&= {}^N\vec{r}^S + [\mathbf{T}_{N\leftarrow S}]_S^S \vec{r}^D + [\mathbf{T}_{N\leftarrow S}][\mathbf{T}_{S\leftarrow D}]_D^D \vec{r}^{CR} \\
&\quad + [\mathbf{T}_{N\leftarrow S}][\mathbf{T}_{S\leftarrow D}][\mathbf{T}_{D\leftarrow CR}]_{CR}^{CR} \vec{r}^{CR_m} \\
&= {}^N\vec{r}^S + [\mathbf{T}_{N\leftarrow S}]_S^S \vec{r}^D + [\mathbf{T}_{N\leftarrow D}]_D^D \vec{r}^{CR} + [\mathbf{T}_{N\leftarrow CR}]_{CR}^{CR} \vec{r}^{CR_m}
\end{aligned} \tag{3.45}$$

The m th left and right wedge clamp polygon vertex velocities are obtained by differ-

entiating Equations 3.44 and 3.45, resulting in

$$\begin{aligned}
{}^N\vec{v}^{CL_m} &= \frac{d}{dt} ({}^N\vec{r}^{CL_m}) \\
&= \frac{d}{dt} ({}^N\vec{r}^S) + \frac{d}{dt} ([\mathbf{T}_{N\leftarrow S}]_S^S \vec{r}^D) + \frac{d}{dt} ([\mathbf{T}_{N\leftarrow S}][\mathbf{T}_{S\leftarrow D}]_D^D \vec{r}^{CL}) \\
&\quad + \frac{d}{dt} ([\mathbf{T}_{N\leftarrow S}][\mathbf{T}_{S\leftarrow D}][\mathbf{T}_{D\leftarrow CL}]_{CL}^{CL} \vec{r}^{CL_m}) \\
&= {}^N\dot{\vec{r}}^S + [\dot{\mathbf{T}}_{N\leftarrow S}]_S^S \vec{r}^D + [\mathbf{T}_{N\leftarrow S}]_S^S \dot{\vec{r}}^D + [\dot{\mathbf{T}}_{N\leftarrow S}][\mathbf{T}_{S\leftarrow D}]_D^D \vec{r}^{CL} \\
&\quad + [\mathbf{T}_{N\leftarrow S}][\dot{\mathbf{T}}_{S\leftarrow D}]_D^D \vec{r}^{CL} + [\mathbf{T}_{N\leftarrow S}][\mathbf{T}_{S\leftarrow D}]_D^D \dot{\vec{r}}^{CL} \\
&\quad + [\dot{\mathbf{T}}_{N\leftarrow S}][\mathbf{T}_{S\leftarrow D}][\mathbf{T}_{D\leftarrow CL}]_{CL}^{CL} \vec{r}^{CL_m} + [\mathbf{T}_{N\leftarrow S}][\dot{\mathbf{T}}_{S\leftarrow D}][\mathbf{T}_{D\leftarrow CL}]_{CL}^{CL} \vec{r}^{CL_m} \\
&\quad + [\mathbf{T}_{N\leftarrow S}][\mathbf{T}_{S\leftarrow D}][\dot{\mathbf{T}}_{D\leftarrow CL}]_{CL}^{CL} \vec{r}^{CL_m} + [\mathbf{T}_{N\leftarrow S}][\mathbf{T}_{S\leftarrow D}][\mathbf{T}_{D\leftarrow CL}]_{CL}^{CL} \dot{\vec{r}}^{CL_m} \\
&= {}^N\dot{\vec{r}}^S + [\mathbf{T}_{N\leftarrow S}][\widetilde{S}^S \vec{\omega}^S]_S^S \vec{r}^D + [\mathbf{T}_{N\leftarrow S}]_S^S \dot{\vec{r}}^D \\
&\quad + [\mathbf{T}_{N\leftarrow S}][\widetilde{S}^S \vec{\omega}^S][\mathbf{T}_{S\leftarrow D}]_D^D \vec{r}^{CL} + [\mathbf{T}_{N\leftarrow S}][\mathbf{T}_{S\leftarrow D}][\widetilde{D}^D \vec{\omega}^D]_D^D \vec{r}^{CL} \\
&\quad + [\mathbf{T}_{N\leftarrow S}][\mathbf{T}_{S\leftarrow D}]_D^D \dot{\vec{r}}^{CL} + [\mathbf{T}_{N\leftarrow S}][\widetilde{S}^S \vec{\omega}^S][\mathbf{T}_{S\leftarrow D}][\mathbf{T}_{D\leftarrow CL}]_{CL}^{CL} \vec{r}^{CL_m} \\
&\quad + [\mathbf{T}_{N\leftarrow S}][\mathbf{T}_{S\leftarrow D}][\widetilde{D}^D \vec{\omega}^D][\mathbf{T}_{D\leftarrow CL}]_{CL}^{CL} \vec{r}^{CL_m} \\
&\quad + [\mathbf{T}_{N\leftarrow S}][\mathbf{T}_{S\leftarrow D}][\mathbf{T}_{D\leftarrow CL}][\widetilde{CL}^D \vec{\omega}^{CL}]_{CL}^{CL} \vec{r}^{CL_m} \\
&\quad + [\mathbf{T}_{N\leftarrow S}][\mathbf{T}_{S\leftarrow D}][\mathbf{T}_{D\leftarrow CL}]_{CL}^{CL} \dot{\vec{r}}^{CL_m} \xrightarrow{0} \\
&= {}^N\dot{\vec{r}}^S + [\mathbf{T}_{N\leftarrow S}][\widetilde{S}^S \vec{\omega}^S]_S^S \vec{r}^D + [\mathbf{T}_{N\leftarrow S}]_S^S \dot{\vec{r}}^D + [\mathbf{T}_{N\leftarrow S}][\widetilde{S}^S \vec{\omega}^S][\mathbf{T}_{S\leftarrow D}]_D^D \vec{r}^{CL} \\
&\quad + [\mathbf{T}_{N\leftarrow D}][\widetilde{D}^D \vec{\omega}^D]_D^D \vec{r}^{CL} + [\mathbf{T}_{N\leftarrow D}]_D^D \dot{\vec{r}}^{CL} + [\mathbf{T}_{N\leftarrow S}][\widetilde{S}^S \vec{\omega}^S][\mathbf{T}_{S\leftarrow CL}]_{CL}^{CL} \vec{r}^{CL_m} \\
&\quad + [\mathbf{T}_{N\leftarrow D}][\widetilde{D}^D \vec{\omega}^D][\mathbf{T}_{D\leftarrow CL}]_{CL}^{CL} \vec{r}^{CL_m} + [\mathbf{T}_{N\leftarrow CL}][\widetilde{CL}^D \vec{\omega}^{CL}]_{CL}^{CL} \vec{r}^{CL_m}
\end{aligned} \tag{3.46}$$

Similarly,

$$\begin{aligned}
{}^N_N\vec{v}^{CR_m} &= \frac{d}{dt} ({}^N_N\vec{r}^{CR_m}) \\
&= \frac{d}{dt} ({}^N_N\vec{r}^S) + \frac{d}{dt} ([\mathbf{T}_{N\leftarrow S}]_S^S \vec{r}^D) + \frac{d}{dt} ([\mathbf{T}_{N\leftarrow S}][\mathbf{T}_{S\leftarrow D}]_D^D \vec{r}^{CR}) \\
&\quad + \frac{d}{dt} ([\mathbf{T}_{N\leftarrow S}][\mathbf{T}_{S\leftarrow D}][\mathbf{T}_{D\leftarrow CR}]_{CR}^{CR} \vec{r}^{CR_m}) \\
&= {}^N_N\dot{\vec{r}}^S + [\dot{\mathbf{T}}_{N\leftarrow S}]_S^S \vec{r}^D + [\mathbf{T}_{N\leftarrow S}]_S^S \dot{\vec{r}}^D + [\dot{\mathbf{T}}_{N\leftarrow S}][\mathbf{T}_{S\leftarrow D}]_D^D \vec{r}^{CR} \\
&\quad + [\mathbf{T}_{N\leftarrow S}][\dot{\mathbf{T}}_{S\leftarrow D}]_D^D \vec{r}^{CR} + [\mathbf{T}_{N\leftarrow S}][\mathbf{T}_{S\leftarrow D}]_D^D \dot{\vec{r}}^{CR} \\
&\quad + [\dot{\mathbf{T}}_{N\leftarrow S}][\mathbf{T}_{S\leftarrow D}][\mathbf{T}_{D\leftarrow CR}]_{CR}^{CR} \vec{r}^{CR_m} + [\mathbf{T}_{N\leftarrow S}][\dot{\mathbf{T}}_{S\leftarrow D}][\mathbf{T}_{D\leftarrow CR}]_{CR}^{CR} \vec{r}^{CR_m} \\
&\quad + [\mathbf{T}_{N\leftarrow S}][\mathbf{T}_{S\leftarrow D}][\dot{\mathbf{T}}_{D\leftarrow CR}]_{CR}^{CR} \vec{r}^{CR_m} + [\mathbf{T}_{N\leftarrow S}][\mathbf{T}_{S\leftarrow D}][\mathbf{T}_{D\leftarrow CR}]_{CR}^{CR} \dot{\vec{r}}^{CR_m} \\
&= {}^N_N\dot{\vec{r}}^S + [\mathbf{T}_{N\leftarrow S}][\widetilde{[{}^N_S\vec{\omega}^S]}]_S^S \vec{r}^D + [\mathbf{T}_{N\leftarrow S}]_S^S \dot{\vec{r}}^D \\
&\quad + [\mathbf{T}_{N\leftarrow S}][\widetilde{[{}^N_S\vec{\omega}^S]}][\mathbf{T}_{S\leftarrow D}]_D^D \vec{r}^{CR} + [\mathbf{T}_{N\leftarrow S}][\mathbf{T}_{S\leftarrow D}][\widetilde{[{}^S_D\vec{\omega}^D]}]_D^D \vec{r}^{CR} \\
&\quad + [\mathbf{T}_{N\leftarrow S}][\mathbf{T}_{S\leftarrow D}]_D^D \dot{\vec{r}}^{CR} + [\mathbf{T}_{N\leftarrow S}][\widetilde{[{}^N_S\vec{\omega}^S]}][\mathbf{T}_{S\leftarrow D}][\mathbf{T}_{D\leftarrow CR}]_{CR}^{CR} \vec{r}^{CR_m} \\
&\quad + [\mathbf{T}_{N\leftarrow S}][\mathbf{T}_{S\leftarrow D}][\widetilde{[{}^S_D\vec{\omega}^D]}][\mathbf{T}_{D\leftarrow CR}]_{CR}^{CR} \vec{r}^{CR_m} \\
&\quad + [\mathbf{T}_{N\leftarrow S}][\mathbf{T}_{S\leftarrow D}][\mathbf{T}_{D\leftarrow CR}][\widetilde{[{}^D_{CR}\vec{\omega}^{CR}]}]_{CR}^{CR} \vec{r}^{CR_m} \\
&\quad + [\mathbf{T}_{N\leftarrow S}][\mathbf{T}_{S\leftarrow D}][\mathbf{T}_{D\leftarrow CR}]_{CR}^{CR} \dot{\vec{r}}^{CR_m} \rightarrow 0 \\
&= {}^N_N\dot{\vec{r}}^S + [\mathbf{T}_{N\leftarrow S}][\widetilde{[{}^N_S\vec{\omega}^S]}]_S^S \vec{r}^D + [\mathbf{T}_{N\leftarrow S}]_S^S \dot{\vec{r}}^D + [\mathbf{T}_{N\leftarrow S}][\widetilde{[{}^N_S\vec{\omega}^S]}][\mathbf{T}_{S\leftarrow D}]_D^D \vec{r}^{CR} \\
&\quad + [\mathbf{T}_{N\leftarrow D}][\widetilde{[{}^S_D\vec{\omega}^D]}]_D^D \vec{r}^{CR} + [\mathbf{T}_{N\leftarrow D}]_D^D \dot{\vec{r}}^{CR} + [\mathbf{T}_{N\leftarrow S}][\widetilde{[{}^N_S\vec{\omega}^S]}][\mathbf{T}_{S\leftarrow CR}]_{CR}^{CR} \vec{r}^{CR_m} \\
&\quad + [\mathbf{T}_{N\leftarrow D}][\widetilde{[{}^S_D\vec{\omega}^D]}][\mathbf{T}_{D\leftarrow CR}]_{CR}^{CR} \vec{r}^{CR_m} + [\mathbf{T}_{N\leftarrow CR}][\widetilde{[{}^D_{CR}\vec{\omega}^{CR}]}]_{CR}^{CR} \vec{r}^{CR_m}
\end{aligned} \tag{3.47}$$

Equations 3.40 through 3.47 complete the definition of the polygons included in the SRAMSS environment. At this point the relevant kinematic expressions and quantities have been developed such that they are available for the application of Kane's method for deriving the governing equations of motion for the system.

Chapter 4

System Dynamics

This chapter follows the development of the dynamics components required to complete the governing equations for the system using Kane's method, as outlined in Section 2.2. Ultimately, the objective of this chapter is to obtain the terms which form the active forces $\vec{\mathbf{R}}^k$ and moments $\vec{\mathbf{T}}^k$, the translational inertia forces $\vec{\mathbf{R}}^{*k}$ and angular inertia moments $\vec{\mathbf{T}}^{*k}$ for all bodies in the system.

As presented in Section 2.2, the governing equations of motion expressed in terms of N_{gc} number of generalized coordinates in Kane's method as

$$F_i + F_i^* = 0, \quad i = 1, \dots, N_{gc} \quad (2.11)$$

Vector formulation of Equation 2.11 for N_B number of bodies, yields the following expressions for the active forces and inertial forces for the k th body:

$$\mathbf{F} = \sum_{k=1}^{N_B} \left(\left[\begin{matrix} N \\ k \end{matrix} V^k \right]^T \vec{\mathbf{R}}^k + \left[\begin{matrix} N \\ k \end{matrix} W^k \right]^T \vec{\mathbf{T}}^k \right) \quad (2.13)$$

$$\mathbf{F}^* = \sum_{k=1}^{N_B} \left(\left[\begin{matrix} N \\ k \end{matrix} V^k \right]^T \vec{\mathbf{R}}^{*k} + \left[\begin{matrix} N \\ k \end{matrix} W^k \right]^T \vec{\mathbf{T}}^{*k} \right) \quad (2.14)$$

For the given system, the aircraft is modelled as a single rigid body representing the airframe, coupled to a flexible dynamic finite element model representing the skid-type landing gear. Directly applying Kane's method would treat each DFE node as an independent body with properties associated with it based on conventional finite element formulation, and with its own governing equations. This method requires the development of the externally applied active forces, but also the internal forces acting between connected DFE nodes. For dense finite element meshes, this method proves to be analytically challenging. Alternatively, as will be shown in Section 4.1, the

dynamic finite element model can be assembled separately using the ‘direct method’, then manipulated to fit the form of Equations 2.13 and 2.14 for direct integration into the governing equations.

4.1 Dynamic Finite Element Model

For reasons presented in Section 2.2, the skid-type landing gear is suited to dynamic finite element representation, and is therefore chosen as the method to model the compliant skid-type landing gear. Manipulation of the standard DFE formulation into a form usable in Kane’s presents a novel method for the mass-coupling of rigid and flexible bodies in a system.

In general, a DFE model takes the form

$$[\mathbf{M}] \ddot{\mathbf{q}}_n + [\mathbf{C}] \dot{\mathbf{q}}_n + [\mathbf{K}] \mathbf{q}_n = \mathbf{F}(\dot{\mathbf{q}}_n, \mathbf{q}_n) \quad (2.21)$$

where $[\mathbf{M}]$ is the total structure consistent mass matrix, $[\mathbf{C}]$ is the total structure proportional damping matrix, $[\mathbf{K}]$ is the total structure stiffness matrix, and $\mathbf{F}(\dot{\mathbf{q}}_n, \mathbf{q}_n)$ is the vector of externally applied nodal forces acting on the DFE model. The construction of the stiffness, mass, and damping matrices is presented below.

Stiffness Matrix

The stiffness matrix is constructed using the direct method [51]. That is, to apply known principles to individual elements then assemble them into the matrices governing the complete finite element model. Limited to simple elements, the stiffness matrix is obtained through known mechanics of materials formulas relating node displacements and node loads.

The general formula for the local element stiffness matrix $[\mathbf{K}_l]$ is derived from the expression for strain energy per unit of volume U_0 in a flexible material integrated over the total volume of the element [51]:

$$\begin{aligned} U &= \frac{1}{2} \boldsymbol{\delta}^T \int \boldsymbol{\beta}^T \boldsymbol{\epsilon} \boldsymbol{\beta} dV \boldsymbol{\delta} \\ &= \frac{1}{2} \boldsymbol{\delta}^T \mathbf{k} \boldsymbol{\delta} \end{aligned} \quad (4.1)$$

with

$$\mathbf{k} = \int \boldsymbol{\beta}^T \boldsymbol{\epsilon} \boldsymbol{\beta} dV \quad (4.2)$$

where $\boldsymbol{\delta}$ is a vector of the nodal displacements along each DoF, $\boldsymbol{\epsilon}$ the constitutive, or material property matrix, and $\boldsymbol{\beta}$ the strain-displacement matrix resulting from the partial differentiation of polynomial interpolation shape functions \mathbf{N} with respect to the nodal DoFs.

The landing gear is modelled using general 2D beam elements which resists, axial, shear, and bending loads. As shown in Figure 4.1, the general 2D beam elements have 6 DoFs. The element is composed of the superposition of a bar element which resists axial loads, and a simple 2D beam element which resists shear and bending loads.

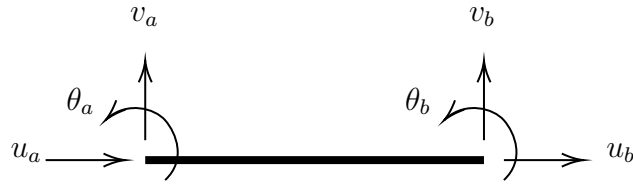


Figure 4.1: 2D beam element degrees of freedom.

For the general 2D beam element, $\boldsymbol{\delta}$ are

$$\boldsymbol{\delta} = \begin{Bmatrix} u_a \\ v_a \\ \theta_a \\ u_b \\ v_b \\ \theta_b \end{Bmatrix} \quad (4.3)$$

Due to superposition of element types, the shape functions \mathbf{N} for the general 2D beam element, which agrees with the DoFs in $\boldsymbol{\delta}$, is

$$\mathbf{N} = \begin{bmatrix} \frac{L-x}{L} & 0 & 0 & \frac{x}{L} & 0 & 0 \\ 0 & 1 - \frac{3x^2}{L^2} + \frac{2x^3}{L^3} & x - \frac{2x^2}{L} + \frac{x^3}{L^2} & 0 & \frac{3x^2}{L^2} - \frac{2x^3}{L^3} & -\frac{x^2}{L} + \frac{x^3}{L^2} \end{bmatrix} \quad (4.4)$$

where the top row is the bar-element contribution, and the bottom row is the simple 2D beam element contribution. Differentiation $\frac{d}{dx}$ yields the strain-deflection matrix $\boldsymbol{\beta}$:

$$\boldsymbol{\beta} = \frac{d}{dx} \mathbf{N} = \begin{bmatrix} \frac{-1}{L} & 0 & 0 & \frac{1}{L} & 0 & 0 \\ 0 & -\frac{6}{L^2} + \frac{12x}{L^3} & -\frac{4}{L} + \frac{6}{L^2} & 0 & \frac{6}{L^2} - \frac{12x}{L^3} & -\frac{2}{L} + \frac{6}{L^2} \end{bmatrix} \quad (4.5)$$

and, again with element superposition, the material property matrix ϵ :

$$\epsilon = \begin{bmatrix} AE & 0 \\ 0 & EI \end{bmatrix} \quad (4.6)$$

where L , A , E , and I are the element length, cross-sectional area, Young's modulus, and second moment of area respectively.

With these matrices, computing Equation 4.2 yields the general 2D beam element stiffness matrix in the local frame of reference:

$$[\mathbf{K}_l] = \int_0^L \boldsymbol{\beta}^T \boldsymbol{\epsilon} \boldsymbol{\beta} dx = \begin{bmatrix} \frac{AE}{L} & 0 & 0 & -\frac{AE}{L} & 0 & 0 \\ 0 & \frac{12EI}{L^3} & \frac{6EI}{L^2} & 0 & -\frac{12EI}{L^3} & \frac{6EI}{L^2} \\ 0 & \frac{6EI}{L^2} & \frac{4EI}{L} & 0 & -\frac{6EI}{L^2} & \frac{2EI}{L} \\ -\frac{AE}{L} & 0 & 0 & \frac{AE}{L} & 0 & 0 \\ 0 & -\frac{12EI}{L^3} & -\frac{6EI}{L^2} & 0 & \frac{12EI}{L^3} & -\frac{6EI}{L^2} \\ 0 & \frac{6EI}{L^2} & \frac{2EI}{L} & 0 & -\frac{6EI}{L^2} & \frac{4EI}{L} \end{bmatrix} \quad (4.7)$$

Equation 4.7 presents the stiffness matrix for a single general 2D beam element, yet the landing gear DFE model is composed of many elements. Since a DFE node may connect more than one element, the frames of reference of connecting beams must be consistently axis-aligned to determine the deflection at the nodes connecting multiple elements. In this work, these aligned frames of reference for each DFE node are the j th DFE node frames n_j , as presented in Section 2.3. These frames of reference are all consistently axis-aligned with the global frame G . The G frame serves as the global finite element model frame of reference, and isolates the description of the DFE model from the airframe's coordinate system H which could potentially see transient effects in future work.

Obtaining the total structure stiffness matrix $[\mathbf{K}]$ requires the assembly of all defined elements. This is achieved by transforming the arbitrarily-oriented element at angle Θ_{ab} to the global frame, spanning from node a to node b , from local frames of references n'_a and n'_b to globally aligned frames n_a and n_b as shown in Figure 4.2.

The transformation matrix describing the transformation global DoFs to local

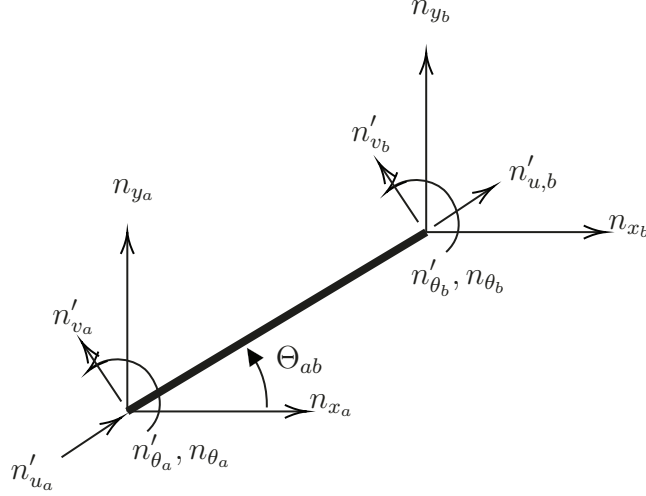


Figure 4.2: Arbitrarily-oriented 2D beam element frames of reference.

DoFs is

$$\begin{aligned}
 [\mathbf{T}_{n'_{ab} \leftarrow n_{ab}}] &= \begin{bmatrix} [\mathbf{T}_{a' \leftarrow a}] & [0] \\ [0] & [\mathbf{T}_{b' \leftarrow b}] \end{bmatrix} \\
 &= \begin{bmatrix} \cos(\Theta_{ab}) & -\sin(\Theta_{ab}) & 0 & 0 & 0 & 0 \\ \sin(\Theta_{ab}) & \cos(\Theta_{ab}) & 0 & 0 & 0 & 0 \\ 0 & 0 & 1 & 0 & 0 & 0 \\ 0 & 0 & 0 & \cos(\Theta_{ab}) & -\sin(\Theta_{ab}) & 0 \\ 0 & 0 & 0 & \sin(\Theta_{ab}) & \cos(\Theta_{ab}) & 0 \\ 0 & 0 & 0 & 0 & 0 & 1 \end{bmatrix} \quad (4.8)
 \end{aligned}$$

Therefore the relationship between globally-aligned and local DoFs is

$$\boldsymbol{\delta}_l = [\mathbf{T}_{n'_{ab} \leftarrow n_{ab}}] \boldsymbol{\delta}_G \quad (4.9)$$

$$\boldsymbol{\delta}_G = [\mathbf{T}_{n'_{ab} \leftarrow n_{ab}}]^T \boldsymbol{\delta}_l \quad (4.10)$$

The transformation matrix can be used to determine the globally aligned stiffness matrix. The transpose of the transformation matrix is used since it is a homogenous rotational transformation matrix where $[\mathbf{A}]^{-1} = [\mathbf{A}]^T$. In transforming the local forces and deflection to global quantities, we have

$$\begin{aligned}
 &[\mathbf{K}_l] \boldsymbol{\delta}_l = \mathbf{F}_l \\
 &[\mathbf{K}_l] [\mathbf{T}_{n'_{ab} \leftarrow n_{ab}}] \boldsymbol{\delta}_G = [\mathbf{T}_{n'_{ab} \leftarrow n_{ab}}] \mathbf{F}_G \\
 &[\mathbf{T}_{n'_{ab} \leftarrow n_{ab}}]^T [\mathbf{K}_l] [\mathbf{T}_{n'_{ab} \leftarrow n_{ab}}] \boldsymbol{\delta}_G = [\mathbf{T}_{n'_{ab} \leftarrow n_{ab}}]^T [\mathbf{T}_{n'_{ab} \leftarrow n_{ab}}] \mathbf{F}_G \\
 &[\mathbf{T}_{n'_{ab} \leftarrow n_{ab}}]^T [\mathbf{K}_l] [\mathbf{T}_{n'_{ab} \leftarrow n_{ab}}] \boldsymbol{\delta}_G = \mathbf{F}_G
 \end{aligned} \quad (4.11)$$

By inspection, the general 2D beam element stiffness matrix expressed in the globally-aligned frame is obtained in Equation 4.12.

$$[\mathbf{K}_{G,ab}] = [\mathbf{T}'_{n'_{ab} \leftarrow nab}]^T [\mathbf{K}_{l,ab}] [\mathbf{T}'_{n'_{ab} \leftarrow nab}] \quad (4.12)$$

Further, the element stiffness matrix spanning nodes a and b , expressed in the global frame, is partitioned to obtain sub-matrices which isolate the influence of both nodes on the displacement in each DoF.

$$\begin{aligned} [\mathbf{K}_G] \begin{Bmatrix} \delta_a \\ \delta_b \end{Bmatrix} &= \begin{Bmatrix} F_a \\ F_b \end{Bmatrix} \\ \begin{bmatrix} \mathbf{k}_{G,aa} & \mathbf{k}_{G,ab} \\ \mathbf{k}_{G,ba} & \mathbf{k}_{G,bb} \end{bmatrix} \begin{Bmatrix} \delta_a \\ \delta_b \end{Bmatrix} &= \begin{Bmatrix} F_a \\ F_b \end{Bmatrix} \end{aligned} \quad (4.13)$$

Equation 4.12 is applied to each element of the DFE model, then the stiffness matrix is partitioned as per Equation 4.13. These partitions are assembled directly to obtain the total structure stiffness matrix $[\mathbf{K}]$, which is known as the ‘direct method’.

$$[\mathbf{K}] = \begin{bmatrix} \mathbf{k}_{11} & \mathbf{k}_{1j_c} & \cdots & \mathbf{k}_{1N_n} \\ \mathbf{k}_{j_r 1} & \mathbf{k}_{j_r j_c} & & \vdots \\ \vdots & & \ddots & \vdots \\ \mathbf{k}_{N_n 1} & \cdots & \cdots & \mathbf{k}_{N_n N_n} \end{bmatrix} \quad (4.14)$$

where each element $\mathbf{k}_{j_r j_c}$, with row index r and column index c , of the total structure stiffness matrix $[\mathbf{K}]$ is the summation of all element globally-aligned stiffness matrix partitions contributing to the stiffness of the given node.

$$\mathbf{k}_{j_r j_c} = \sum_{a=j_r, b=j_c} \mathbf{k}_{G,ab}, \quad j_r, j_c = 1, \dots, N_n \quad (4.15)$$

The associated nodal displacement vector is \mathbf{q}_n from Equation 2.21). For the system at hand, it is defined as δ_n . Since the forces generated through deflection are due to nodal displacements, it suffices to define the nodal displacements to be the difference of generalized coordinates of the nodes with respect to the global frame, and the undeformed coordinates of the nodes with respect to the global frame, such that

$$\delta_n = \begin{Bmatrix} \delta_{n_1} \\ \vdots \\ \delta_{n_j} \end{Bmatrix} = \begin{Bmatrix} \mathbf{q}_{n_1} \\ \vdots \\ \mathbf{q}_{n_j} \end{Bmatrix} - \begin{Bmatrix} \mathbf{q}_{n_1,0} \\ \vdots \\ \mathbf{q}_{n_j,0} \end{Bmatrix} = \begin{Bmatrix} {}^G \vec{\mathbf{r}}^{n_1} \\ {}^G \vec{\boldsymbol{\theta}}^{n_1} \\ \vdots \\ {}^G \vec{\mathbf{r}}^{n_j} \\ {}^G \vec{\boldsymbol{\theta}}^{n_j} \end{Bmatrix} - \begin{Bmatrix} {}^G \vec{\mathbf{r}}^{n_1}_0 \\ {}^G \vec{\boldsymbol{\theta}}^{n_1}_0 \\ \vdots \\ {}^G \vec{\mathbf{r}}^{n_j}_0 \\ {}^G \vec{\boldsymbol{\theta}}^{n_j}_0 \end{Bmatrix}, \quad j = 1, \dots, N_n \quad (4.16)$$

where ${}^G\vec{\mathbf{r}}^{n_j}_0$ is the undeformed position of the j th DFE node relative to the global DFE frame G , expressed in G ; and ${}^G\vec{\boldsymbol{\theta}}^{n_j}_0$ is the undeformed orientation of the j th DFE node with respect to G , expressed in G . In the undeformed configuration, nodal angular displacements are all zero such that

$${}^G\vec{\boldsymbol{\theta}}^{n_j}_0 \equiv 0 \quad (4.17)$$

Even though the governing equations are expressed in the k th body frame, since the transformations from the node body frame n_j to global DFE frame G is identity, generalized coordinates may be used directly. For simulation purposes, it is preferable to use a separate vector for the undeformed DFE node generalized coordinates rather than the vector of initial conditions for the generalized coordinates of the DFE nodes to allow for deformed landing gear initial conditions.

Mass Matrix

The element mass matrix $[\mathbf{M}_l]$ in the local frame is derived in a similar manner to the development of the element stiffness matrix $[\mathbf{K}_l]$. Shape functions \mathbf{N} are used in both cases. For the element mass matrix, Cook [51] uses inertial forces in virtual work arguments to obtain a general formula similar to Equation 4.2.

$$\begin{aligned} \mathbf{m} &= \rho \int \mathbf{N}^T \mathbf{N} dV \\ &= \rho A \int \mathbf{N}^T \mathbf{N} dx \end{aligned} \quad (4.18)$$

where ρ and A are the element density and cross-sectional area perpendicular to the longitudinal axis respectively. Equation 4.18 generates the ‘consistent’ mass matrix as it uses the same shape functions as the element stiffness matrix. Equation 4.18 yields

$$[\mathbf{M}_l] = \frac{\rho AL}{420} \begin{bmatrix} 140 & 0 & 0 & 70 & 0 & 0 \\ 0 & 156 & 22L & 0 & 54 & -13L \\ 0 & 22L & 4L^2 & 0 & -13L & -3L^2 \\ 70 & 0 & 0 & 140 & 0 & 0 \\ 0 & 54 & 13L & 0 & 156 & -22L \\ 0 & -13L & -3L^2 & 0 & -22L & 4L^2 \end{bmatrix} \quad (4.19)$$

Using the same method as Equation 4.11 and equating $[\mathbf{M}] \ddot{\mathbf{q}} = \mathbf{F}$, the globally-aligned element mass matrix takes the form

$$[\mathbf{M}_G] = [\mathbf{T}_{n'_{ab} \leftarrow n_{ab}}]^T [\mathbf{M}_l] [\mathbf{T}_{n'_{ab} \leftarrow n_{ab}}] \quad (4.20)$$

The globally-aligned element mass matrices are assembled into the total structure consistent mass matrix $[\mathbf{M}]$ in the same way as the stiffness matrix.

The associated nodal accelerations vector is $\ddot{\mathbf{q}}_n$ per Equation 2.21. Since the governing equations for the DFE nodes are expressed in their respective body frames, but accelerations require definition with respect to the inertial frame, the associated accelerations vector is assembled from the superposition of Equation 3.11 for all DFE nodes. Then the nodal accelerations vector becomes

$$\ddot{\mathbf{q}}_n = ([\mathbf{V}_n] \dot{\mathbf{u}} + \mathbf{Z}_n) \quad (4.21)$$

where $[\mathbf{V}_n]$ is the array of all translational and angular partial velocity matrices for all nodes in the DFE model, assembled as:

$$[\mathbf{V}_n] = \begin{bmatrix} \begin{bmatrix} N \\ n_1 \end{bmatrix} \mathbf{V}^{n_1} \\ \begin{bmatrix} N \\ n_1 \end{bmatrix} \mathbf{W}^{n_1} \\ \vdots \\ \begin{bmatrix} N \\ n_j \end{bmatrix} \mathbf{V}^{n_j} \\ \begin{bmatrix} N \\ n_j \end{bmatrix} \mathbf{W}^{n_j} \end{bmatrix}, \quad j = 1, \dots, N_n \quad (4.22)$$

and \mathbf{Z}_n is the column array of all remainder acceleration terms in the governing translational and angular acceleration equations for all DFE nodes in the form

$$\mathbf{Z}_n = \left\{ \begin{array}{c} \vec{\mathbf{Z}}_{n_1} \\ \vec{\mathbf{Y}}_{n_1} \\ \vdots \\ \vec{\mathbf{Z}}_{n_j} \\ \vec{\mathbf{Y}}_{n_j} \end{array} \right\}, \quad j = 1, \dots, N_n \quad (4.23)$$

Expression of the mass matrix as a consistent mass matrix, and related nodal accelerations in the form of Equation 4.21 is advantageous for two reasons. First, the consistent mass matrix is able to capture nodal inertial phenomena in both translational and angular degrees of freedom. Second, expression of the accelerations using the partial velocity compact formulation allows direct assembly into Kane's governing equations, and subsequently the isolation of the generalized accelerations vector $\dot{\mathbf{u}}$.

Proportional Damping Matrix

Damping in structures arising from internal phenomena is difficult to mathematically characterize. However, damping forces in rigid structures often comprise less than

10% of forces in the system, and thus can be ideally modelled as viscous damping [51]. Mode superposition, assuming proportional damping, can be used to construct the total damping in a structure since element damping matrices cannot be easily formulated [50]. For this work, an explicitly-evaluated damping matrix is required to avoid recalculation of the total structure damping matrix $[\mathbf{C}]$ for each system solution evaluation.

The proportional damping matrix, as its name implies, is proportional to the mass matrix $[\mathbf{M}]$ and stiffness matrix $[\mathbf{K}]$. As presented in Equation 2.23 the total structure proportional damping matrix is

$$[\mathbf{C}] = \alpha_0 [\mathbf{M}] + \alpha_1 [\mathbf{K}] \quad (2.23)$$

where Equation 2.23, is the expansion of Equation 2.22 for the first two terms. Using the first two terms to generate proportional damping is often referred to as ‘Rayleigh damping’. The proportionality constants α are obtained by solving the simultaneous equations in Equation 2.24 for the range of frequencies of interest ω_1 to ω_2 with associated damping ratios ξ_1 and ξ_2 [51]:

$$\xi_1 = \frac{\alpha_0}{2\omega_1} + \frac{\alpha_1\omega_1}{2} \quad \xi_2 = \frac{\alpha_0}{2\omega_2} + \frac{\alpha_1\omega_2}{2} \quad (2.24)$$

The nodal velocities $\dot{\mathbf{q}}_n$ are constructed from the generalized speeds associated with the DFE nodes such that

$$\dot{\mathbf{q}}_n = [\mathbf{V}_n] \mathbf{u} \quad (4.24)$$

Complete Dynamic Finite Element Model

Assembling the finite element matrices and associated nodal vectors yields a system of the form:

$$[\mathbf{M}] ([\mathbf{V}_n] \dot{\mathbf{u}} + \mathbf{Z}_n) + [\mathbf{C}] [\mathbf{V}_n] \mathbf{u} + [\mathbf{K}] \delta_n = {}^n\mathbf{F} \quad (4.25)$$

where $\dot{\mathbf{u}}$ is the vector of generalized accelerations; the local time derivatives of the vector of generalized speeds \mathbf{u} , and ${}^n\mathbf{F}$ is the vector of externally-applied nodal forces.

For the generic skid-equipped aircraft shown in Figure 2.2, the DFE-modelled skids are attached to the rigid airframe of the aircraft. The interface forces must be considered in the formulation of Kane’s equations for both the aircraft’s airframe and the flexible DFE landing gear model. In Equation 4.25, the external nodal forces ${}^n\mathbf{F}$ can be separated into the known externally applied nodal forces ${}^n\mathbf{F}_k$, and the unknown

interface nodal forces ${}^n\mathbf{F}_u$ which act at the nodes interfacing with the aircraft's rigid body.

$$[\mathbf{M}]([\mathbf{V}_n]\dot{\mathbf{u}} + \mathbf{Z}_n) + [\mathbf{C}][\mathbf{V}_n]\mathbf{u} + [\mathbf{K}]\boldsymbol{\delta}_n = {}^n\mathbf{F}_k + {}^n\mathbf{F}_u \quad (4.26)$$

For the DFE nodes, Equation 4.26 can be manipulated into the form of Equations 2.13 and 2.14 as required for Kane's method, resulting in

$$\begin{aligned} \mathbf{F} &= [\mathbf{V}_n]^T ({}^n\mathbf{F}_k + {}^n\mathbf{F}_u - [\mathbf{C}][\mathbf{V}_n]\mathbf{u} - [\mathbf{K}]\boldsymbol{\delta}_n) \\ &= [\mathbf{V}_n]^T ({}^n\mathbf{F}_k - [\mathbf{C}][\mathbf{V}_n]\mathbf{u} - [\mathbf{K}]\boldsymbol{\delta}_n) + [\mathbf{V}_u]^T {}^n\mathbf{F}_u \end{aligned} \quad (4.27)$$

$$\mathbf{F}^* = -[\mathbf{V}_n]^T ([\mathbf{M}]([\mathbf{V}_n]\dot{\mathbf{u}} + \mathbf{Z}_n)) \quad (4.28)$$

In effect, the bracketed terms in the first line of Equation 4.27 are the active translational and angular forces $\mathbf{R}^n + \mathbf{T}^n$ acting on all DFE nodes. The bracketed terms in Equation 4.28 constitute the translational and angular inertia forces $\mathbf{R}^{*n} + \mathbf{T}^{*n}$ associated with the DFE nodes.

The known external nodal forces vector ${}^n\mathbf{F}_k$ is the sum of all known external nodal forces, expressed

$${}^n\mathbf{F}_k = \begin{Bmatrix} n_1 \vec{\mathbf{F}}_k \\ n_1 \vec{\mathbf{M}}_k \\ \vdots \\ n_j \vec{\mathbf{F}}_k \\ n_j \vec{\mathbf{M}}_k \end{Bmatrix} = \begin{Bmatrix} n_1 \vec{\mathbf{F}}_k^c + n_1 \vec{\mathbf{F}}_k^d + n_1 \vec{\mathbf{F}}_k^g \\ n_1 \vec{\mathbf{M}}_k^c + n_1 \vec{\mathbf{M}}_k^d + n_1 \vec{\mathbf{M}}_k^g \\ \vdots \\ n_j \vec{\mathbf{F}}_k^c + n_j \vec{\mathbf{F}}_k^d + n_j \vec{\mathbf{F}}_k^g \\ n_j \vec{\mathbf{M}}_k^c + n_j \vec{\mathbf{M}}_k^d + n_j \vec{\mathbf{M}}_k^g \end{Bmatrix}, \quad j = 1, \dots, N_n \quad (4.29)$$

where the known nodal external forces are denoted with superscripts c for contact forces, d for external damper forces, and g for gravitational forces. These known forces are obtained through individual models developed in the following sections of Chapter 4.

The unknown interface nodal forces vector ${}^n\mathbf{F}_u$ is expressed as a separate active forces term since it represents the unknown internal forces at the interface of the airframe and landing gear which must be solved. The set of DFE nodes with indices $j = j_u$ are nodes which interface with the airframe, such that the unknown force vector is

$${}^n\mathbf{F}_u = \begin{Bmatrix} n_1 \vec{\mathbf{F}}_u \\ n_1 \vec{\mathbf{M}}_u \\ \vdots \\ n_j \vec{\mathbf{F}}_u \\ n_j \vec{\mathbf{M}}_u \end{Bmatrix}, \quad j = 1, \dots, N_n \forall j = j_u \quad (4.30)$$

with associated nodal partial velocities array

$$[\mathbf{V}_u] = \begin{bmatrix} \begin{bmatrix} N \\ n_1 \end{bmatrix} \mathbf{V}^{n_1} \\ \begin{bmatrix} N \\ n_1 \end{bmatrix} \mathbf{W}^{n_1} \\ \vdots \\ \begin{bmatrix} N \\ n_j \end{bmatrix} \mathbf{V}^{n_j} \\ \begin{bmatrix} N \\ n_j \end{bmatrix} \mathbf{W}^{n_j} \end{bmatrix}, \quad j = 1, \dots, N_n \forall j = j_u \quad (4.31)$$

constructed in the same way as Equation 4.22. The unknown interface forces are solved along with the unknown generalized accelerations, as will be shown in Chapter 5.

In summary, manipulation of the DFE formulation into the form of Equations 4.27 and 4.28, the forcing of $[\mathbf{T}_{G \leftarrow n_j}] \equiv [I]$, and the separation of the nodal forces into ${}^n \mathbf{F}_k$, and ${}^n \mathbf{F}_u$ comprise the novel way of mass-coupling rigid and flexible bodies in Kane's method. The final consideration for integration of DFE modelling into Kane's method is presented in Section 4.4.1

4.2 Contact Dynamics Model

Transient intermittent contact states will arise due to the stiff nature of the skid-type landing gear. To accurately model this phenomena, a contact model which can characterize the complex contact states must be implemented. The contact dynamics must be able to detect colliding objects, and render an appropriately-oriented dynamic response for contact restitution. The implemented model leverages unit vectors normal and parallel to the polygon surfaces, generated for the Separation axis theorem collision detection algorithm, to apply normal and friction forces at the contact surface. The contact dynamics model implemented in SRAMSS constitutes a novel and effective application of the Separation Axis Theorem [33] beyond simple collision detection into a general contact dynamics model.

Contact Detection

As it relates to the aircraft, the DFE model nodes act as the contact points evaluated for contact response. Contact force vectors ${}^{n_j} \vec{\mathbf{F}}_k^c$ are generated for each contacting node n_{j_c} , which are then assembled into the known external nodal forces vector ${}^n \mathbf{F}_k$

in Equation 4.29. The set of DFE nodes with indices $j = j_c$ are nodes evaluated for contact response.

The objects with which the aircraft interacts, are often simple polygons with flat surfaces and well-defined geometries. As previously described in Section 2.3, the number of polygons is limited to the four polygons describing the ship deck, RSD deck, and two wedge clamps. based on the collision detection review presented in 1.3, these characteristics lend themselves to a narrow-phase, BVH contact detection algorithms [31, 32]. The limited number of polygons is small enough to skip broad-phase detection and proceed directly to evaluating all polygons for contact in the narrow-phase. Since the defined polygons are physical representations, BVH is better suited than SPR as the Bounding volumes can exactly take the form of the defined polygons. The SAT is effective in this regard, and is implemented in the SRAMSS environment.

Simply, the SAT aims to determine separation of polygons evaluated for contact along an arbitrary axis as shown in Figure 4.3; inability to find such an axis implies contact.

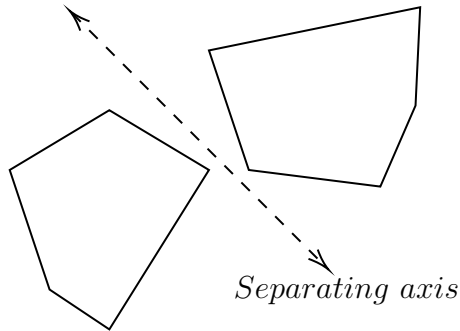


Figure 4.3: Arbitrary axis separating two polygons.

To evaluate two polygons for separation, the SAT requires outward-pointing normal axes ${}^P_N\hat{s}_m$ for each surface s_m of polygon P . As shown in Figure 4.4, separation at surface ${}^P s_1$ of polygon P is determined by projecting all vertices of evaluated polygons P and Q to surface normal ${}^P_N\hat{s}_1$. Separation occurs where there is no overlap in the projection of the vertices from both polygons. This process is repeated for each surface of polygon P . If no separation can be found along any surface normal, the two polygons are determined to be in contact.

For this work, to simplify the SAT algorithm and increase computational efficiency, the DFE nodes are treated as points, and only the DFE nodes n_j with indices j

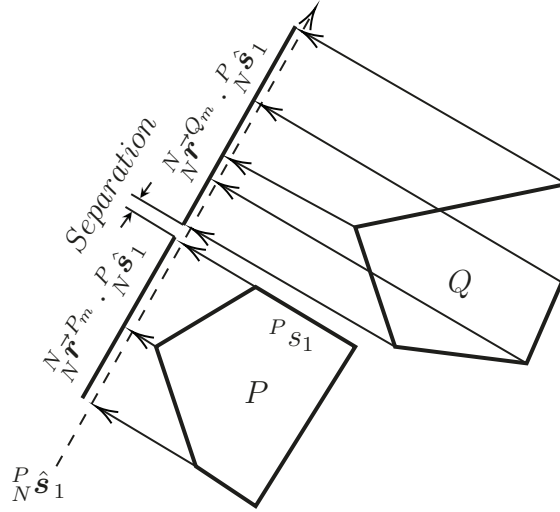


Figure 4.4: Separation of polygons P and Q along surface normal axis ${}^P_N \hat{\mathbf{s}}_1$.

belonging to the set j_c are evaluated for contact. The considerations reduce the number of pairs evaluated for contact response. Additionally, only the forces acting on contact nodes are required since the polygon motions are prescribed. It also reduces the number of point projection operations since only a single point is required to be projected to the normal axis for the DFE node evaluated for contact.

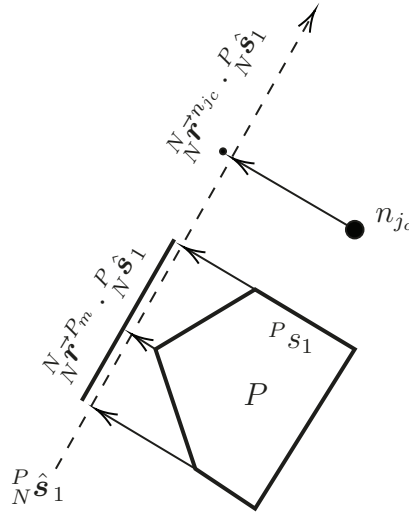


Figure 4.5: Separation between DFE node n_{j_c} and defined polygon P .

The outward-facing normal axes ${}^P_N \hat{\mathbf{s}}_m$ for the ship deck polygon S , RSD deck D , and wedge clamps CL and CD are unit vectors developed using the left-hand normal where the polygon vertices are defined in a clockwise order. The vertex positions are taken from the kinematic development captured in Equations 3.40, 3.42, 3.44,

and 3.45. The ship deck is shown as an example in Figure 4.6.

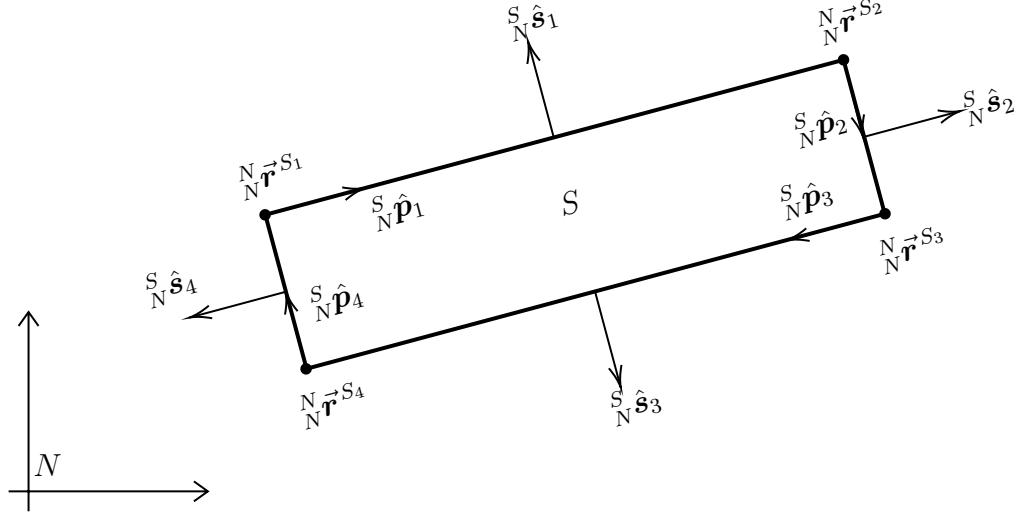


Figure 4.6: Surface normal axes ${}^S_N \hat{\mathbf{s}}_m$ for the ship polygon S .

For $N_{v,P}$ vertices in a polygon, the polygon is composed of $N_{s,P} = N_{v,P}$ surfaces. Therefore the surface unit vectors for each polygon are

$${}^S_N \hat{\mathbf{s}}_m = \begin{bmatrix} 0 & -1 \\ 1 & 0 \end{bmatrix} \left(\frac{({}^N_N \vec{\mathbf{r}}^{S_{m+1}} - {}^N_N \vec{\mathbf{r}}^{S_m})}{\|{}^N_N \vec{\mathbf{r}}^{S_{m+1}} - {}^N_N \vec{\mathbf{r}}^{S_m}\|} \right) \quad m = 1, \dots, N_{v,S} \quad (4.32)$$

$${}^D_N \hat{\mathbf{s}}_m = \begin{bmatrix} 0 & -1 \\ 1 & 0 \end{bmatrix} \left(\frac{({}^N_N \vec{\mathbf{r}}^{D_{m+1}} - {}^N_N \vec{\mathbf{r}}^{D_m})}{\|{}^N_N \vec{\mathbf{r}}^{D_{m+1}} - {}^N_N \vec{\mathbf{r}}^{D_m}\|} \right) \quad m = 1, \dots, N_{v,D} \quad (4.33)$$

$${}^{CL}_N \hat{\mathbf{s}}_m = \begin{bmatrix} 0 & -1 \\ 1 & 0 \end{bmatrix} \left(\frac{({}^N_N \vec{\mathbf{r}}^{CL_{m+1}} - {}^N_N \vec{\mathbf{r}}^{CL_m})}{\|{}^N_N \vec{\mathbf{r}}^{CL_{m+1}} - {}^N_N \vec{\mathbf{r}}^{CL_m}\|} \right) \quad m = 1, \dots, N_{v,CL} \quad (4.34)$$

$${}^{CR}_N \hat{\mathbf{s}}_m = \begin{bmatrix} 0 & -1 \\ 1 & 0 \end{bmatrix} \left(\frac{({}^N_N \vec{\mathbf{r}}^{CR_{m+1}} - {}^N_N \vec{\mathbf{r}}^{CR_m})}{\|{}^N_N \vec{\mathbf{r}}^{CR_{m+1}} - {}^N_N \vec{\mathbf{r}}^{CR_m}\|} \right) \quad m = 1, \dots, N_{v,CR} \quad (4.35)$$

For $m = N_{v,P}$, the superscript $m + 1$ equals 1. It is also important to note that the expression in parenthesis in equations 4.32 through 4.35 are the surface parallel unit vectors (or surface parallel axes) ${}^P_N \hat{\mathbf{p}}_m$.

The contact detection algorithm is developed in detail in Section 5.2.2 of Chapter 5. Nevertheless, assuming surface ${}^P S_m$ is the surface where node n_{jc} has come into contact with polygon P , the relationship in Equation 4.36 is satisfied.

$${}^N_N \vec{\mathbf{r}}^{n_{jc}} \cdot {}^P_N \hat{\mathbf{s}}_m \leq \max({}^N_N \vec{\mathbf{r}}^{P_m} \cdot {}^P_N \hat{\mathbf{s}}_m), \quad m = 1, \dots, N_{v,P} \quad (4.36)$$

or simply

$${}^N_N \vec{\mathbf{r}}^{n_{jc}} \cdot {}^P_N \hat{\mathbf{s}}_m \leq ({}^N_N \vec{\mathbf{r}}^{P_m} \cdot {}^P_N \hat{\mathbf{s}}_m) \quad (4.37)$$

since the vertex ${}^N\vec{r}^{P_m}$ is the maximum value as it defines surface ${}^P s_m$ evaluated for contact.

Equation 4.36 and 4.37 imply penetration of the contacting node n_{j_c} into surface ${}^P s_m$ since the positive direction of ${}^P\hat{\mathbf{s}}_m$ is outwards. This is the basis for contact response.

Contact Response

The normal and parrallel vectors generated in the SAT model, can be re-used to generate the oriented dynamic response due to collision. The polygon vertices and contact node points can be projected to surface normal axis ${}^P\hat{\mathbf{s}}_m$ such that a penalty function can be used to apply a contact restitution force normal to surface ${}^P s_m$. In other words, a penalty function is used to generate normal forces when in contact with surface ${}^P s_m$. The relative sliding velocity of a contact node along ${}^P s_m$ can be used to generate a sliding friction force.

Though any penalty functions can be used for collision restitution, a virtual linear spring-damper penalty function is used in the planar case of SRAMSS to apply a restitution force which is proportional to penetration depth and penetration velocity, as shown in Figure 4.7. The penalty function is expressed

$${}_{\hat{\mathbf{s}}_m}^{n_{j_c}} F^P = \begin{cases} -K_p \Delta_p - C_p \dot{\Delta}_p, & {}^N\vec{r}^{n_{j_c}} \cdot {}^P\hat{\mathbf{s}}_m \leq ({}^N\vec{r}^{P_m} \cdot {}^P\hat{\mathbf{s}}_m) \\ 0, & {}^N\vec{r}^{n_{j_c}} \cdot {}^P\hat{\mathbf{s}}_m > ({}^N\vec{r}^{P_m} \cdot {}^P\hat{\mathbf{s}}_m) \end{cases} \quad (4.38)$$

where ${}_{\hat{\mathbf{s}}_m}^{n_{j_c}} F^P$ is the restitution force applied by polygon P on node n_{j_c} along the positive direction of ${}^P\hat{\mathbf{s}}_m$, Δ_p is the surface penetration depth of n_{j_c} along ${}^P\hat{\mathbf{s}}_m$, and $\dot{\Delta}_p$ is the relative surface penetration velocity of n_{j_c} along ${}^P\hat{\mathbf{s}}_m$. The values K_p and C_p are the penetration stiffness and damping coefficients respectively. The surface penetration depth is given as the difference between vertex ${}^N\vec{r}^{P_m}$ and contact node ${}^N\vec{r}^{n_{j_c}}$ as projected to ${}^P\hat{\mathbf{s}}_m$, expressed as

$$\Delta_p = ({}^N\vec{r}^{n_{j_c}} - {}^N\vec{r}^{P_m}) \cdot {}^P\hat{\mathbf{s}}_m \quad (4.39)$$

Since the vertex ${}^N\vec{r}^{P_m}$ belongs to surface ${}^P s_m$, it serves as the surface reference point along ${}^P\hat{\mathbf{s}}_m$ to calculate penetration depth.

For the relative penetration velocity, a physical reference point on surface ${}^P s_m$ is required. This point is defined to be ${}^s_m\vec{r}^{n_{j_c}}$, the position of node n_{j_c} as projected

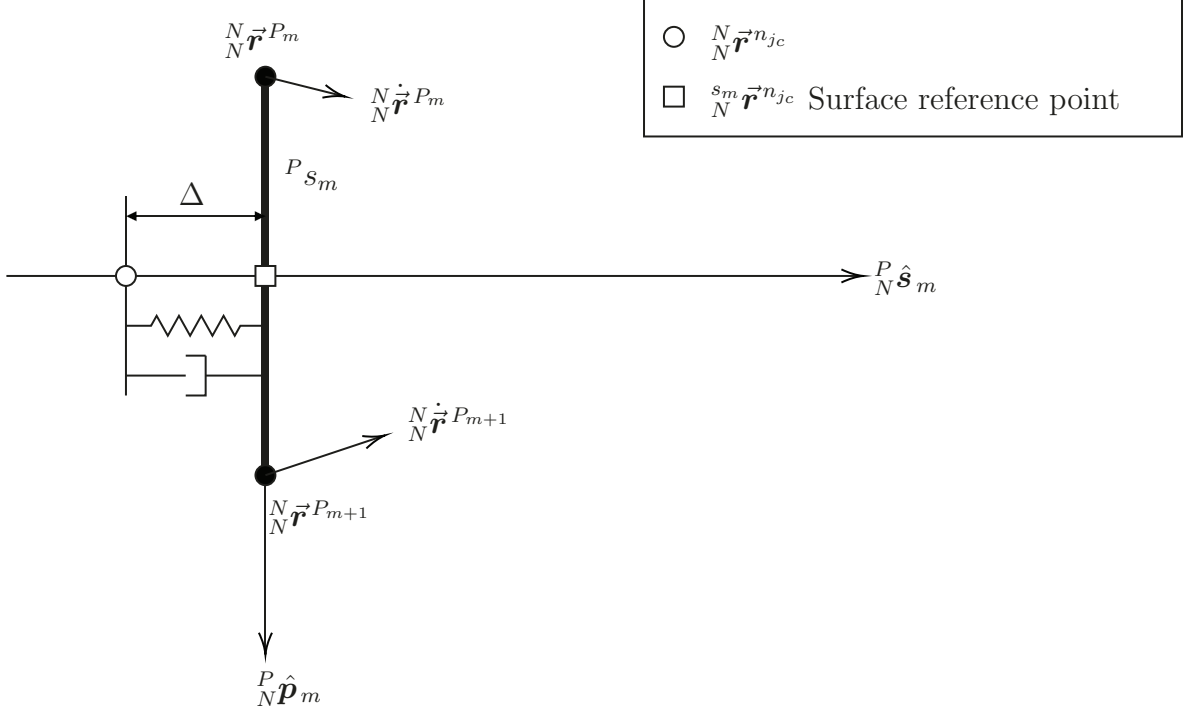


Figure 4.7: Surface penetration penalty function diagram for contact node n_{jc} in collision with surface P_{S_m}

to the surface P_{S_m} with respect to the inertial frame, and expressed in the inertial frame. In terms of the vertices of polygon P , ${}^{s_m} \vec{r}^{n_{jc}}$ is

$${}^{s_m} \vec{r}^{n_{jc}} = {}^N \vec{r}^{P_m} + \left[\left({}^N \vec{r}^{n_{jc}} - {}^N \vec{r}^{P_m} \right) \cdot {}^P \hat{\mathbf{p}}_m \right] {}^P \hat{\mathbf{p}}_m \quad (4.40)$$

Then, the velocity at the projected point ${}^{s_m} \vec{r}^{n_{jc}}$ is

$${}^{s_m} \dot{\vec{r}}^{n_{jc}} = {}^N \dot{\vec{r}}^{P_m} + \left(\frac{\| {}^{s_m} \vec{r}^{n_{jc}} - {}^N \vec{r}^{P_m} \|}{\| {}^N \vec{r}^{P_{m+1}} - {}^N \vec{r}^{P_m} \|} \right) \left({}^N \dot{\vec{r}}^{P_{m+1}} - {}^N \dot{\vec{r}}^{P_m} \right) \quad (4.41)$$

Now, the relative penetration velocity can be determined similarly to the penetration depth by calculating relative velocity between the contact node and its surface projection as

$$\dot{\Delta}_p = \left({}^N \dot{\vec{r}}^{n_{jc}} - {}^{s_m} \dot{\vec{r}}^{n_{jc}} \right) \cdot {}^P \hat{\mathbf{s}}_m \quad (4.42)$$

The equations required for the surface normal forces have been developed. Development of the equations governing contact frictional forces remain.

A frictional slider model is employed to generate friction forces along the penetrated surface P_{S_m} . Such models require a reference point, an additional state-variable, from which friction model quantities can be calculated. In this work, these

reference points are called ‘Object Contact Points’ (OCPs). The behaviour of OCPs is governed by specific rules:

- There is one OCP ${}^P_N\vec{\mathcal{O}}^{n_{jc}}$ per contact node n_{jc} per defined polygon P . This enables the generation of dynamic responses for simultaneous contact of multiple polygons.
- While not in contact with polygon P , the OCP for n_{jc} is determined by the projection of ${}^N_N\vec{\mathbf{r}}^{n_{jc}}$ onto the closest surface ${}^P s_m$.
- Once in contact with polygon P , the OCP is determined to be the initial point of contact with polygon P .
- During contact with polygon P , the OCP’s position on the surface ${}^P s_m$ is only shifted when the maximum allowable friction force is exceeded. the OCP is shifted to generate a frictional force exactly equal to the maximum allowable value, hence the frictional slider.

Outside of contact with polygon P , the OCP located as

$${}^P_N\vec{\mathcal{O}}^{n_{jc}} = {}^N_N\vec{\mathbf{r}}^{P_m} + [({}^N_N\vec{\mathbf{r}}^{n_{jc}} - {}^N_N\vec{\mathbf{r}}^{P_m}) \cdot {}^P_N\hat{\mathbf{p}}_m] {}^P_N\hat{\mathbf{p}}_m \quad (4.43)$$

It is necessary to express the position of the OCP relative to the polygon frame P . For a polygon undergoing transient motion, the OCP must follow with the polygon, yet must not shift along the surface since the maximum friction value may not have been exceeded. Thus, the OCP must follow the motion of the polygon between shifts during contact.

$${}^P_P\vec{\mathcal{O}}^{n_{jc}} = [\mathbf{T}_{N\leftarrow P}]^T ({}^P_N\vec{\mathcal{O}}^{n_{jc}} - {}^N_N\vec{\mathbf{r}}^P) \quad (4.44)$$

where $[\mathbf{T}_{N\leftarrow P}]^T$ is the inverse of the transformation from the polygon frame P through the chain of polygon frames to the inertial frame, and ${}^N_N\vec{\mathbf{r}}^P$ is the position of polygon frame P with respect to the inertial frame, and expressed in the inertial frame. For oriented dynamic response, since all other vectors are with respect to, and expressed in the inertial frame, the general expression for an OCP is

$${}^P_N\vec{\mathcal{O}}^{n_{jc}} = {}^N_N\vec{\mathbf{r}}^P + [\mathbf{T}_{N\leftarrow P}]_P^P\vec{\mathcal{O}}^{n_{jc}} \quad (4.45)$$

With the OCPs defined, the frictional-slider model can be developed. The LuGre friction model is adapted for use in SRAMSS. This model is capable of modelling static, dynamic, and viscous friction, and pre-sliding micro-displacements. For this work, viscous friction is not modelled as it is not conceptually applicable to the UAS dynamic interface problem. The remaining frictional terms are modelled by

representing surface asperities with a ‘bristle’ model as shown in Figure 4.8. The deflection Δ_f , and rate of deflection $\dot{\Delta}_f$ of the bristle are the force generating elements of the LuGre model.

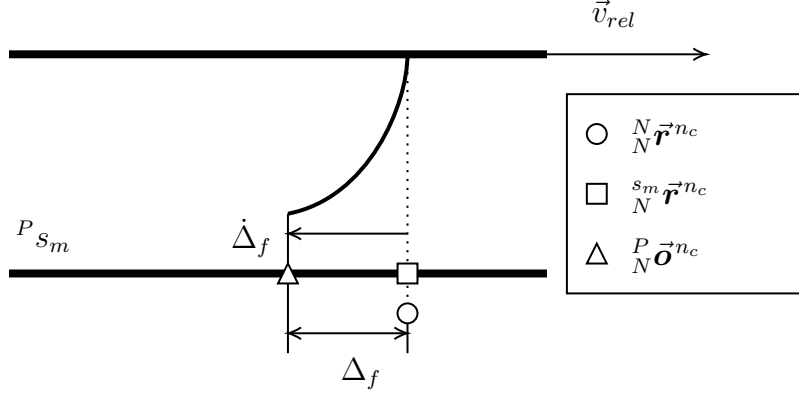


Figure 4.8: LuGre friction bristle model.

The deflection of the bristle Δ_f is determined by the distance between the OCP and the contacting node projected to surface P_{s_m} such that

$$\Delta_f = ({}^P_N \vec{o}^{n_{jc}} - {}^s_m_N \vec{r}^{n_{jc}}) \cdot {}^P_N \hat{p}_m \quad (4.46)$$

and the rate of deflection of the bristle $\dot{\Delta}_f$ is

$$\dot{\Delta}_f = -v_{rel} \left(1 - \frac{|\Delta_f|}{\Delta_{f,max}} \right) \quad (4.47)$$

where v_{rel} , is the relative velocity of n_{jc} with respect to ${}^P_N \vec{o}^{n_{jc}}$, which represents the sliding velocity along P_{s_m} . Equation 4.47 ensures that the rate of bristle deflection $\dot{\Delta}_f \equiv 0$ at maximum bristle deflection $\Delta_{f,max}$. The relative sliding velocity v_{rel} is calculated

$$\begin{aligned} v_{rel} &= \left({}^N_N \dot{\vec{r}}^{n_{jc}} - {}^P_N \dot{\vec{o}}^{n_{jc}} \right) \cdot {}^P_N \hat{p}_m \\ &= \left({}^N_N \dot{\vec{r}}^{n_{jc}} - \left[{}^N_N \dot{\vec{r}}^{P_m} + \frac{\left\| {}^P_N \dot{\vec{o}}^{n_{jc}} - {}^N_N \dot{\vec{r}}^{P_m} \right\|}{\left\| {}^N_N \dot{\vec{r}}^{P_{m+1}} - {}^N_N \dot{\vec{r}}^{P_m} \right\|} \left({}^N_N \dot{\vec{r}}^{P_{m+1}} - {}^N_N \dot{\vec{r}}^{P_m} \right) \right] \right) \cdot {}^P_N \hat{p}_m \end{aligned} \quad (4.48)$$

The maximum deformation of the bristle $\Delta_{f,max}$ is governed by a Stribeck curve which dictates the dominance of static F_s or coulomb F_d friction forces as a function of relative sliding velocity v_{rel} [40]. The Stribeck curve used for the LuGre model is

$$\Delta_{f,max} = \frac{F_d + (F_s - F_d)^{-(|v_{rel}/v_s|)^2}}{K_f} \quad (4.49)$$

with v_s the Stribeck velocity threshold under which static friction dominates, and K_f is the stiffness of the bristle[40]. For $\Delta_f \geq \Delta_{f,max}$ then $\Delta_f = \Delta_{f,max}$ in Equation 4.47.

Static and coulomb friction values are obtained from the normal force ${}^{n_{jc}}_{\hat{s}_m} F^P$ calculated in Equation 4.38, such that

$$F_s = \mu_s {}^{n_{jc}}_{\hat{s}_m} F^P \quad (4.50)$$

$$F_d = \mu_d {}^{n_{jc}}_{\hat{s}_m} F^P \quad (4.51)$$

where μ_s and μ_d are the static and dynamic coefficients of friction, respectively.

Ultimately the friction force generated on contact node n_{jc} sliding along surface ${}^P S_m$ is

$${}^{n_{jc}}_{\hat{p}_m} F^P = \begin{cases} K_f \Delta_f - C_{fric} \dot{\Delta}_f, & \Delta_f < \Delta_{f,max} \\ K_f \Delta_{f,max}, & \Delta_f \geq \Delta_{f,max} \end{cases} \quad (4.52)$$

where C_f is the bristle damping coefficient.

The complete set of forces which constitute the oriented dynamic response are presented in Table 4.1.

Table 4.1: Contact forces summary

	Direction	Quantity	Governing Formula
Normal Force	${}^P_N \hat{s}_m$	${}^{n_{jc}}_{\hat{s}_m} F^P = K_p \Delta_p - C_p \dot{\Delta}_p$	(4.38) (4.39) (4.42)
Equation Index		(4.38)	(4.39) (4.42)
Friction Force	${}^P_N \hat{p}_m$	${}^{n_{jc}}_{\hat{p}_m} F^P = K_f \Delta_f - C_f \dot{\Delta}_f$	(4.46) ¹ (4.47)
Equation Index		(4.52)	(4.46) ¹ (4.47)

¹: At maximum bristle deflection $\Delta_f = \Delta_{f,max}$, $\dot{\Delta}_f = 0$

The normal and friction forces are scalar values oriented along their respective axes. The complete oriented dynamic response on contact node n_{jc} due to contact with polygon P on surface ${}^A S_m$ is then

$${}^{n_{jc}}_N \vec{F}^P = {}^P_N \hat{s}_m {}^{n_{jc}}_{\hat{s}_m} F^P + {}^P_N \hat{p}_m {}^{n_{jc}}_{\hat{p}_m} F^P \quad (4.53)$$

The external nodal forces vector, and subsequent assembly into the governing equations of Kane's method require that the forces acting on a body be expressed in the body's frame. therefore Equation 4.53, expressed in n_{jc} 's frame, becomes:

$$\begin{aligned} {}^{n_{jc}}_{n_{jc}} \vec{F}^P &= [\mathbf{T}_{n_{jc} \leftarrow N}]_N {}^{n_{jc}}_N \vec{F}^P \\ &= [\mathbf{T}_{n_{jc} \leftarrow N}] \left({}^P_N \hat{s}_m {}^{n_{jc}}_{\hat{s}_m} F^P + {}^P_N \hat{p}_m {}^{n_{jc}}_{\hat{p}_m} F^P \right) \end{aligned} \quad (4.54)$$

In the SRAMSS environment, there are four polygons representing the ship deck S , RSD deck D , and wedge clamps CL and CR . The external nodal forces vector due to contact ${}^n\mathbf{F}_k^c$ is assembled from the contact force contributions from each polygon on all contact nodes:

$${}^n\mathbf{F}_k^c = \begin{Bmatrix} {}^{n_1}\vec{\mathbf{F}}^c \\ {}^{n_1}\vec{\mathbf{M}}^c \\ \vdots \\ {}^{n_j}\vec{\mathbf{F}}^c \\ {}^{n_j}\vec{\mathbf{M}}^c \end{Bmatrix} \quad (4.55)$$

where

$$\begin{Bmatrix} {}^{n_j}\vec{\mathbf{F}}^c \\ {}^{n_j}\vec{\mathbf{M}}^c \end{Bmatrix} = \begin{Bmatrix} {}^{n_j}\vec{\mathbf{F}}^S + {}^{n_j}\vec{\mathbf{F}}^D + {}^{n_j}\vec{\mathbf{F}}^{CL} + {}^{n_j}\vec{\mathbf{F}}^{CR} \\ 0 \end{Bmatrix} \quad (4.56)$$

$$j = 1, \dots, N_n \forall j = j_c$$

otherwise

$$\begin{Bmatrix} {}^{n_j}\vec{\mathbf{F}}^c \\ {}^{n_j}\vec{\mathbf{M}}^c \end{Bmatrix} = \begin{Bmatrix} 0 \\ 0 \end{Bmatrix}, \quad j = 1, \dots, N_n \forall j \neq j_c \quad (4.57)$$

4.3 Aerodynamic Models

Inherent to the system being simulated, aerodynamic forces acting-on, or generated by the aircraft are phenomena that must be considered. There are two major aerodynamic phenomena which are modelled in SRAMSS. The first being aerodynamic drag forces exerted on the airframe due to relative wind velocity. The second being forces and moments acting on the airframe due to the uneven thrust generated by advancing and retreating rotor blades in apparent wind. Additionally, due to the spin of the rotor blades, there are gyroscopic effects acting on the aircraft body. However, for the planar case they are not applicable.

In this work, there is no characterization of the flow field in the aircraft landing zone. This simplification eliminates the need to characterize the influence of the ship's superstructure, rotor downwash, rotor wake, and other non-uniform flow behaviours. The following sections develop the aerodynamic models present in SRAMSS.

4.3.1 Aerodynamic Body Drag Forces

Similar to DYNAFACE[®] [22] and SSMASH [21], SRAMSS models aerodynamic drag forces due to apparent wind acting at the airframe by using equivalent projected flat-plate areas \mathbf{A} which allows simplifications in the aerodynamic drag equations by treating the drag coefficient as unity [52]

$$\mathbf{A}_{eq} = \begin{Bmatrix} A_{eq,x} \\ A_{eq,y} \\ A_{eq,z} \end{Bmatrix} \quad (4.58)$$

The aerodynamic body drag forces are applied at the airframe's centre of pressure (CP). Therefore, wind velocity relative to this point is required. Orientation of the wind vector is assumed to be uniform across the ship deck. First, consider the wind velocity in the inertial frame:

$${}^N_N \vec{\mathbf{v}}^W = \begin{Bmatrix} v_{wind,x} \\ v_{wind,y} \\ v_{wind,z} \end{Bmatrix} \quad (4.59)$$

Next, the velocity of the airframe's CP with respect to the inertial frame is required. The CP is assumed to be at a fixed distance ${}^H_H \vec{\mathbf{r}}^{CP}$ from the airframe's CoG, the H -frame origin. The CP velocity is then expressed as:

$$\begin{aligned} {}^N_N \vec{\mathbf{v}}^{CP} &= \frac{d}{dt} ({}^N_N \vec{\mathbf{r}}^{CP}) \\ &= \frac{d}{dt} ({}^N_N \vec{\mathbf{r}}^H) + \frac{d}{dt} ([\mathbf{T}_{N \leftarrow H}] {}^H_H \vec{\mathbf{r}}^{CP}) \\ &= {}^N_N \dot{\vec{\mathbf{r}}}^H + [\dot{\mathbf{T}}_{N \leftarrow H}] {}^H_H \vec{\mathbf{r}}^{CP} + [\mathbf{T}_{N \leftarrow H}] {}^H_H \dot{\vec{\mathbf{r}}}^{CP} \\ &= {}^N_N \dot{\vec{\mathbf{r}}}^H + [\mathbf{T}_{N \leftarrow H}] [\widetilde{{}^N_N \vec{\boldsymbol{\omega}}^H}] {}^H_H \vec{\mathbf{r}}^{CP} + [\mathbf{T}_{N \leftarrow H}] {}^H_H \dot{\vec{\mathbf{r}}}^{CP} \rightarrow 0 \\ &= {}^N_N \dot{\vec{\mathbf{r}}}^H + [\mathbf{T}_{N \leftarrow H}] [\widetilde{{}^N_N \vec{\boldsymbol{\omega}}^H}] {}^H_H \vec{\mathbf{r}}^{CP} \end{aligned} \quad (4.60)$$

Equations 4.59 and 4.60 are both measured relative to the inertial frame, and expressed in the inertial frame. Therefore the wind velocity relative to the CP can be expressed:

$$\begin{aligned} {}^{CP}_{N} \vec{\mathbf{v}}^W &= {}^N_N \vec{\mathbf{v}}^W - {}^N_N \vec{\mathbf{v}}^{CP} \\ &= {}^N_N \vec{\mathbf{v}}^W - {}^N_N \dot{\vec{\mathbf{r}}}^H + [\mathbf{T}_{N \leftarrow H}] [\widetilde{{}^N_N \vec{\boldsymbol{\omega}}^H}] {}^H_H \vec{\mathbf{r}}^{CP} \end{aligned} \quad (4.61)$$

Body forces acting on the airframe in H require expression of Equation 4.61 in the H frame. Therefore Equation 4.61 becomes

$${}^H \vec{v}^{CP} = [{}^H \mathbf{T}_{H \leftarrow N}]_N {}^N \vec{v}^W - [{}^H \mathbf{T}_{H \leftarrow N}]_N \dot{\vec{r}}^H + [\widetilde{{}^H \boldsymbol{\omega}^H}]_H {}^H \vec{r}^{CP} \quad (4.62)$$

Then, the aerodynamic body drag forces and moments acting on the helicopter can be expressed:

$${}^H \vec{F}^W = \frac{1}{2} \rho_{air} \mathbf{A}_{eq} \circ {}^H \vec{v}^W \circ |{}^H \vec{v}^W| \quad (4.63)$$

$${}^H \vec{M}^W = [\widetilde{{}^H \vec{r}^{CP}}]_H {}^H \vec{F}^W \quad (4.64)$$

where ‘ \circ ’ is the Hadamard operator denoting element-wise multiplication, and the square of velocity is taken to be the value of velocity multiplied by its absolute value to retain vector orientation.

4.3.2 Aerodynamic Rotor Disc Forces

Where DYNAFACE[®] models rotor thrust during landing transients and induced rotor forces from free-spinning rotor blades separately [22], SRAMSS unifies these two types of forces by implementing a Blade Element Model (BEM) which can characterize the thrust forces and moments on the aircraft at any point [43]. Blade element modelling is chosen since it is versatile for representing any type of rotor blade and airfoil shape by discretization of the rotor blade, and provides accuracy to the extent desired by inclusion of different rotor blade phenomena.

Similar to the discretization of the landing gear through the DFE model, the BEM discretizes the complex rotor blade profile into N_e discrete rotor blade elements (RBEs). The h th RBE e_h is located at radial position r_h , azimuth ψ , and having width dr , as illustrated in Figure 4.9.

The local airflow over an RBE is obtained to calculate the element’s lift and moment. Then, azimuth-averaged elemental thrust and moment are calculated by discretization of the azimuth into N_ψ azimuth sectors ψ_l as shown in the BEM mesh of Figure 4.10. The averaged element values are then summed over the length of the rotor blade and multiplied by the number of rotor blades N_b to obtain the total thrust and moment generated by the rotor disc in apparent wind. The BEM in SRAMSS is an azimuth-averaged actuator disc approach which eliminates the need to propagate a state variable for the orientation of the rotor blades.

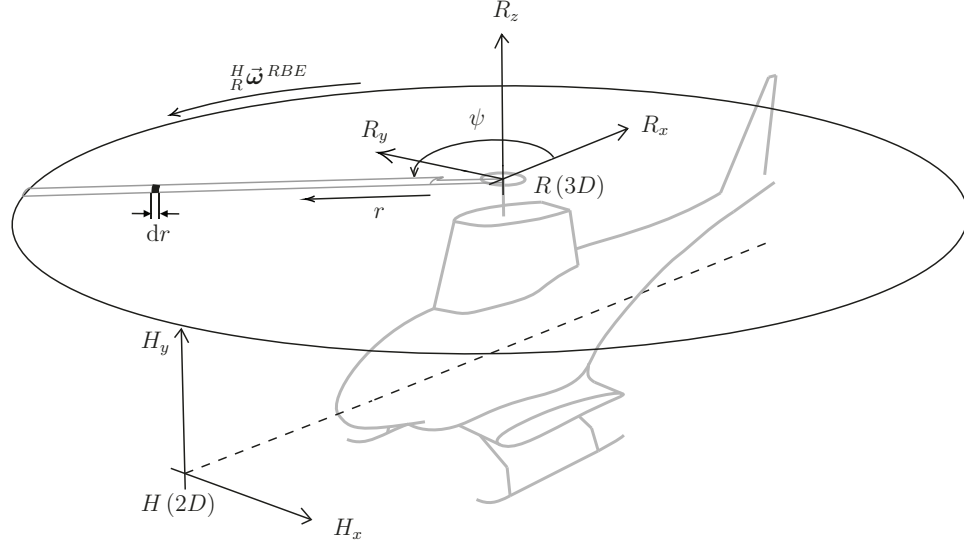


Figure 4.9: Rotor disc blade element model for generic aircraft.(H frame moved forward for clarity)

Additionally, consideration is also made for the rotor blade inner and outer effective radii R_i and R_o , outside of which the blade is considered to not be generating any significant lift. These effective radii are expressed as percentages of the physical radius of the rotor blade R_b .

The complex rotor blade profile has radially-varying parameters which affect the generation of lift. As a result, for the BEM, each RBE is prescribed specific parameter values. These radially varying parameters include:

- chord length c_h ;
- airfoil thickness to chord ratio t/c_h ;
- blade twist angle θ_{t_h} ;
- lift coefficient gradient $\frac{dC_L}{d\alpha_{hl}}$ and zero-angle of attack lift coefficient $C_{L,\alpha_{0,h}}$;
- drag coefficient gradient $\frac{dC_D}{d\alpha_{hl}}$ and zero-angle of attack lift coefficient $C_{D,\alpha_{0,h}}$.

Each RBE is also dependent on rotor disc prescribed parameters:

- collective pitch setting angle θ_{coll} ;
- maximum cyclic pitch setting angle $\theta_{cyc,max}$ at azimuth ψ_{max} .

To calculate the element thrust and moment for the h th RBE e_h at l th azimuth ψ_l , the element axial flow $v_{0_{hl}}$, tangential flow $v_{2_{hl}}$, and sectional flow $v_{1_{hl}}$ velocities illustrated in Figure 4.11 must be obtained.

To begin, the general expression of velocity of the h th RBE e_h at l th azimuth ψ_l

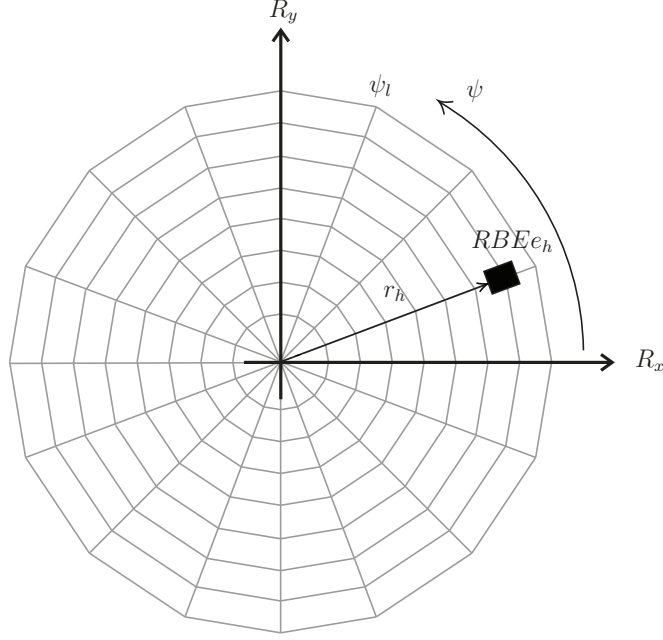


Figure 4.10: Rotor disc BEM mesh.

with respect to the inertial frame, and expressed in the inertial frame, is

$$\begin{aligned}
{}^N\vec{v}^{e_h\psi_l} &= \frac{d}{dt} ({}^N\vec{r}^{e_h\psi_l}) \\
&= \frac{d}{dt} ({}^N\vec{r}^H) + \frac{d}{dt} ([\mathbf{T}_{N\leftarrow H}]_H^H \vec{r}^R) + \frac{d}{dt} ([\mathbf{T}_{N\leftarrow H}][\mathbf{T}_{H\leftarrow R}]_R^R \vec{r}^{e_h\psi_l}) \\
&= \dot{{}^N\vec{r}}^H + [\dot{\mathbf{T}}_{N\leftarrow H}]_H^H \vec{r}^R + [\mathbf{T}_{N\leftarrow H}]_H^H \dot{\vec{r}}^R + [\dot{\mathbf{T}}_{N\leftarrow H}][\mathbf{T}_{H\leftarrow R}]_R^R \vec{r}^{e_h\psi_l} \\
&\quad + [\mathbf{T}_{N\leftarrow H}][\dot{\mathbf{T}}_{H\leftarrow R}]_R^R \vec{r}^{e_h\psi_l} + [\mathbf{T}_{N\leftarrow H}][\mathbf{T}_{H\leftarrow R}]_R^R \dot{\vec{r}}^{e_h\psi_l} \\
&= \dot{{}^N\vec{r}}^H + [\mathbf{T}_{N\leftarrow H}][\widetilde{[\mathbf{T}_{N\leftarrow H}]}_H^H \vec{r}^R + [\mathbf{T}_{N\leftarrow H}]_H^H \dot{\vec{r}}^R \overset{0}{\rightarrow} \\
&\quad + [\mathbf{T}_{N\leftarrow H}][\widetilde{[\mathbf{T}_{N\leftarrow H}]}_H^H][\mathbf{T}_{H\leftarrow R}]_R^R \vec{r}^{e_h\psi_l} \\
&\quad + [\mathbf{T}_{N\leftarrow H}][\mathbf{T}_{H\leftarrow R}][\widetilde{[\mathbf{T}_{H\leftarrow R}]}_R^R \vec{r}^{e_h\psi_l} + [\mathbf{T}_{N\leftarrow H}][\mathbf{T}_{H\leftarrow R}]_R^R \dot{\vec{r}}^{e_h\psi_l} \overset{0}{\rightarrow} \\
&= \dot{{}^N\vec{r}}^H + [\mathbf{T}_{N\leftarrow H}][\widetilde{[\mathbf{T}_{N\leftarrow H}]}_H^H \vec{r}^R + [\mathbf{T}_{N\leftarrow H}][\widetilde{[\mathbf{T}_{N\leftarrow H}]}_H^H][\mathbf{T}_{H\leftarrow R}]_R^R \vec{r}^{e_h\psi_l} \\
&\quad + [\mathbf{T}_{N\leftarrow H}][\widetilde{[\mathbf{T}_{H\leftarrow R}]}_R^R \vec{r}^{e_h\psi_l}], \quad h = 1, \dots, N_e, \quad l = 1, \dots, N_\psi
\end{aligned} \tag{4.65}$$

where ${}^H\vec{r}^R$ is the fixed position of the rotor disc frame R with respect to the airframe CoG, ${}^R\vec{r}^{e_h\psi_l}$ is the position of the h th RBE e_h on the rotor disc at azimuth ψ_l and blade radius r_h , and ${}^H\vec{\omega}^R$ is the rotor disc RPM. As with the aerodynamic body drag

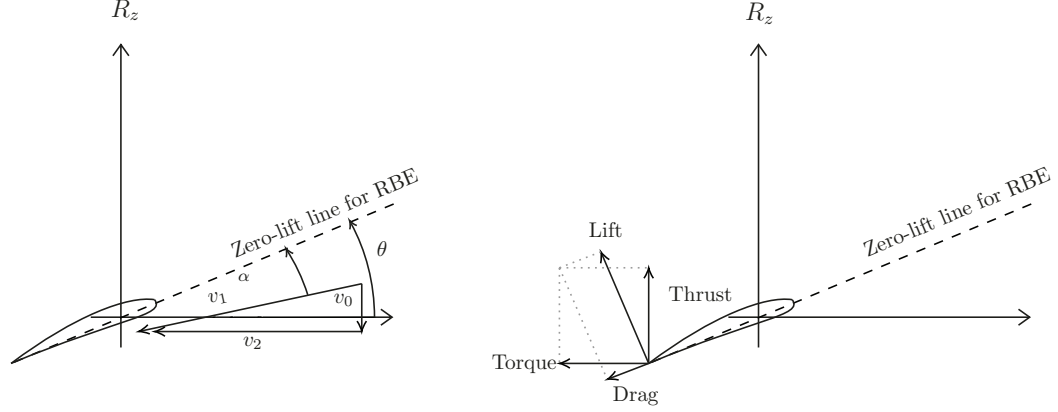


Figure 4.11: Rotor blade element airflow and forces diagram.

model, the wind velocity expressed in the inertial frame is

$${}^N_N \vec{v}^W = \begin{Bmatrix} v_{wind,x} \\ v_{wind,y} \\ v_{wind,z} \end{Bmatrix} \quad (4.59)$$

Then the general expression of velocity for the h th RBE at l th azimuth ψ_l with respect to the wind, and expressed in the inertial frame, is

$$\begin{aligned} {}^W_N \vec{v}^{e_h \psi_l} &= {}^N_N \vec{v}^{e_h \psi_l} - {}^N_N \vec{v}^W \\ &= {}^N_N \dot{\vec{r}}^H + [\mathbf{T}_{N \leftarrow H}] [{}^N_H \widetilde{\vec{\omega}}^H] {}^H_H \vec{r}^R \\ &\quad + [\mathbf{T}_{N \leftarrow H}] [{}^N_H \widetilde{\vec{\omega}}^H] [\mathbf{T}_{H \leftarrow R}] {}^R_R \vec{r}^{e_h \psi_l} \\ &\quad + [\mathbf{T}_{N \leftarrow R}] [{}^H_R \widetilde{\vec{\omega}}^R] {}^R_R \vec{r}^{e_h \psi_l} - {}^N_N \vec{v}^W, \quad h = 1, \dots, N_e, \quad l = 1, \dots, N_\psi \end{aligned} \quad (4.66)$$

Equation 4.66 expressed in the rotor disc frame R at l th azimuth ψ_l becomes

$$\begin{aligned} {}^W_R \vec{v}^{e_h \psi_l} &= [\mathbf{T}_{R \leftarrow N}] {}^W_N \vec{v}^{e_h \psi_l} \\ &= [\mathbf{T}_{R \leftarrow N}] {}^N_N \dot{\vec{r}}^H + [\mathbf{T}_{R \leftarrow H}] [{}^N_H \widetilde{\vec{\omega}}^H] {}^H_H \vec{r}^R \\ &\quad + [\mathbf{T}_{R \leftarrow H}] [{}^N_H \widetilde{\vec{\omega}}^H] [\mathbf{T}_{H \leftarrow R}] {}^R_R \vec{r}^{e_h \psi_l} \\ &\quad + [{}^H_R \widetilde{\vec{\omega}}^R] {}^R_R \vec{r}^{e_h \psi_l} - [\mathbf{T}_{R \leftarrow N}] {}^N_N \vec{v}^W, \quad h = 1, \dots, N_e, \quad l = 1, \dots, N_\psi \end{aligned} \quad (4.67)$$

Now, the element flow velocities can be developed. First, the tangential flow v_{2hl} at the h th RBE is then

$$v_{2hl} = {}^W_R \vec{v}^{e_h \psi_l} \cdot \left(\frac{\hat{R}_z \times {}^R_R \vec{r}^{e_h \psi_l}}{\| \hat{R}_z \times {}^R_R \vec{r}^{e_h \psi_l} \|} \right), \quad h = 1, \dots, N_e, \quad l = 1, \dots, N_\psi \quad (4.68)$$

The parenthetical expression in Equation 4.68 is the unit vector representing the direction of motion for the h th RBE. Next, the axial flow v_{0hl} at the h th RBE is

$$v_{0hl} = v_{ihl} + v_{chl}, \quad h = 1, \dots, N_e, \quad l = 1, \dots, N_\psi \quad (4.69)$$

where the climbing velocity v_{chl} at the RBE is

$$v_{chl} = \frac{W}{R} \vec{\theta}^{e_h \psi_l} \cdot \hat{R}_z, \quad h = 1, \dots, N_e, \quad l = 1, \dots, N_\psi \quad (4.70)$$

and where the induced velocity v_{ihl} at the RBE is

$$v_{ihl} = v_{2hl} \left[- (A) + \sqrt{(A)^2 + B - C} \right] \quad h = 1, \dots, N_e, \quad l = 1, \dots, N_\psi$$

$$A = \frac{\frac{dC_L}{d\alpha_{hl}} c_h}{16\pi R_b} + \frac{v_{chl}}{2v_{2hl}}$$

$$B = \frac{\frac{dC_L}{d\alpha_{hl}} c_h \theta_h r}{8\pi R_b^2}$$

$$C = \frac{\frac{dC_L}{d\alpha_{hl}} c_h v_{chl}}{8\pi R_b v_{2hl}}$$
(4.71)

The induced velocity is obtained from the solution of the quadratic formulation of equating element lift from basic lifting and momentum theories [43]. The element lift coefficient gradient $\frac{dC_L}{d\alpha_{hl}}$ is corrected for Mach Number M_{hl} in the $0 \leq M \leq 0.84$ region. The closed form correction is taken from Smith [53] as

$$\frac{dC_L}{d\alpha_{hl}} = \frac{dC_L}{d\alpha_{hl}} (M = 0, Re = 10^6) \left\{ \mu_{hl} + \frac{t/c_h}{1 + t/c_h} \left[\mu_{hl}(\mu_{hl} - 1) + \frac{1}{4}(\gamma + 1) (\mu_{hl}^2 - 1)^2 \right] \right\} \quad (4.72)$$

$$\mu_{hl} = \left(\sqrt{1 - M_{hl}^2} \right)^{-1} \quad (4.73)$$

$$\gamma = 1.4 \quad (4.74)$$

Lastly, knowing the element axial and tangential flow velocities, the element flow velocity v_{1hl} is obtained by

$$v_{1hl} = \sqrt{v_{0hl}^2 + v_{2hl}^2} \quad (4.75)$$

In addition, the element angle of attack α_{hl} can be obtained from these velocities and the total blade pitch setting:

$$\alpha_{hl} = \theta_{hl} - \phi_{hl} \quad (4.76)$$

where

$$\phi_{hl} = \tan^{-1} \left(\frac{v_{0hl}}{v_{2hl}} \right) \quad (4.77)$$

$$\theta_{hl} = \theta_{t_h} + \theta_{coll} + \theta_{cyc_l} \quad (4.78)$$

$$\theta_{cyc_l} = \theta_{cyc,max} \cos(\psi_l - \psi_{max}) \quad (4.79)$$

and where θ_{hl} is the element total blade pitch setting, ϕ_{hl} is the element flow angle relative to the rotor disc plane at RBE e_h , and $\theta_{cyc,max}$ is the maximum second harmonic cyclic pitch setting contribution at azimuth ψ_{max} .

The development of Equations 4.65 through 4.79 lead to the elementary lift of an RBE acting at the rotor disc. The element force is transformed to an equipollent force and moment acting on the airframe in H as

$${}^R_R \vec{F}^{e_h \psi_l} = \left\{ \begin{array}{c} 0 \\ 0 \\ \frac{1}{2} \rho_{air} v_{1hl}^2 c_h dr [C_{Lhl} \cos(\phi) - C_{Dhl} \sin(\phi)] \end{array} \right\} \quad (4.80)$$

$${}^H_H \vec{F}^{e_h \psi_l} = [{}^H_{H \leftarrow R}] {}^R_R \vec{F}^{e_h \psi_l} \quad (4.81)$$

$${}^H_H \vec{M}^{e_h \psi_l} = \widetilde{[{}^H_H \vec{r}^{e_h \psi_l}]} [{}^H_{H \leftarrow R}] {}^R_R \vec{F}^{e_h \psi_l} \quad (4.82)$$

$$(4.83)$$

where

$$C_{Lhl} = \frac{dC_L}{d\alpha_{hl}} \alpha_{hl} + C_{L,\alpha_0,h} \quad (4.84)$$

$$C_{Dhl} = \frac{dC_D}{d\alpha_{hl}} \alpha_{hl} + C_{D,\alpha_0,h} \quad (4.85)$$

where the lift coefficient C_{L_h} and drag coefficient C_{D_h} are expressed as linear functions proportional to the angle of attack, where $\frac{dC_L}{d\alpha_{hl}}$ and $\frac{dC_D}{d\alpha_{hl}}$ are the coefficient gradients corrected for Mach number, and $C_{D,\alpha_0,h}$ and $C_{L,\alpha_0,h}$ being the coefficient values at $\alpha_h = 0$.

To remove the dependency on a propagated state-variable in calculating rotor disc thrust and moment, an azimuth-averaged approach is taken. The average force and moment generated by an RBE is taken through one full revolution around the rotor disc then summed over the length of the rotor blade because analytical formulation and integration of Equations 4.81 and 4.82 through one revolution is impractical. Hence the BEM mesh described in Figure 4.11.

The average thrust of an RBE e_h at radius r_h over one full rotor disc revolution $\psi = [0, 2\pi]$ is

$${}^H\vec{\mathbf{F}}^{e_h}_{avg} = \frac{1}{N_\psi} \sum_{l=1}^{N_\psi} {}^H\vec{\mathbf{F}}^{e_h\psi_l} \quad h = 1, \dots, N_e \quad (4.86)$$

$${}^H\vec{\mathbf{M}}^{e_h}_{avg} = \frac{1}{N_\psi} \sum_{l=1}^{N_\psi} {}^H\vec{\mathbf{M}}^{e_h\psi_l} \quad h = 1, \dots, N_e \quad (4.87)$$

The average thrust and pitching moment is then summed over the effective length of the rotor blade, from the effective inner radius $r_1 = R_i R_b$ to the effective outer radius $r_{N_e} = R_o R_b$, to determine the total thrust and pitching moment generated on the airframe by the complete BEM model:

$${}^H\vec{\mathbf{F}}^{BEM} = N_b \sum_{h=1}^{N_e} {}^H\vec{\mathbf{F}}^{e_h}_{avg} \quad (4.88)$$

$${}^H\vec{\mathbf{M}}^{BEM} = N_b \sum_{h=1}^{N_e} {}^H\vec{\mathbf{M}}^{e_h}_{avg} \quad (4.89)$$

where N_b is the number of rotor blades.

The aerodynamic models included in Section 4.3 have been developed in three dimensions. For the planar case of SRAMSS, the kinetic quantities expressed in Equations 4.63, 4.64, 4.88, and 4.89 are projected onto the two-dimensional plane of the simulation environment.

4.4 Other Force-generating Elements

Sections 4.1, 4.2, and 4.3 develop the kinetic quantities that act on either the rigid-body airframe, or the flexible-body skid landing gear. The dynamic finite element landing gear model, in conjunction with the contact dynamics model generate the primary forces acting on the landing gear. Whereas the aerodynamic drag and BEM models generate the primary forces acting on the aircraft's airframe.

Yet, there are forces which act on both sets of bodies. In Section 4.4.1 the expressions for the unknown forces at the interface between the rigid and flexible bodies will be developed. The known external damper forces acting between the rigid airframe and flexible landing gear are developed in Section 4.4.2. The gravitational forces are developed in Section 4.4.3. Finally the remaining inertial force terms are developed in Section 4.5.

4.4.1 Flexible–Rigid Body Interface Model

Since the DFE landing gear model is developed separately from the rest of the aircraft, upon assembly into the final dynamic system, the internal loads at the DFE nodes interfacing to the rigid airframe must be considered as illustrated in Figure 4.12. More specifically, the forces acting on both must be equipollent since the landing gear and airframe are ultimately considered part of the same aircraft body. This represents the final consideration which must be made to combine rigid and flexible body dynamics in Kane’s method

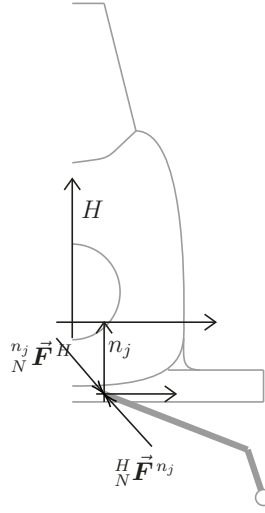


Figure 4.12: Interface of DFE nodes to the airframe.

Hence, the unknown nodal forces vector ${}^n \mathbf{F}_u$ acting on the DFE nodes must also be considered to be acting on the airframe in H . Since the interface nodes are attached to the airframe, applying Newton’s third law for interface DFE node indices j_u , must yield equal in magnitude but opposing interface forces. The forces and moments For rigid DFE node interfaces are

$${}^H \vec{\mathbf{F}}_u = - \sum_{j=j_u} [{}^T_{H \leftarrow n_j}]_{n_j}^{n_j} \vec{\mathbf{F}}_u \quad (4.90)$$

$$\begin{aligned} {}^H \vec{\mathbf{M}}_u &= - \sum_{j=j_u} \left([{}^H \widetilde{\mathbf{r}}^{n_j}] [{}^T_{H \leftarrow n_j}]_{n_j}^{n_j} \vec{\mathbf{F}}_u - [{}^T_{H \leftarrow n_j}]_{n_j}^{n_j} \vec{\mathbf{M}}_u \right) \\ &= - \sum_{j=j_u} \left([{}^H \vec{\mathbf{r}}^G + [{}^T_{H \leftarrow G}]_G^G \widetilde{\mathbf{r}}^{n_j}] [{}^T_{H \leftarrow n_j}]_{n_j}^{n_j} \vec{\mathbf{F}}_u - [{}^T_{H \leftarrow n_j}]_{n_j}^{n_j} \vec{\mathbf{M}}_u \right) \end{aligned} \quad (4.91)$$

The unknown nodal forces are expressed in the nodal frames, therefore to agree with Newton’s third law, the unknown forces acting on the airframe must be negative to

satisfy $\sum \vec{\mathbf{F}} = {}^H_n \vec{\mathbf{F}}_u + {}^{n_j}_{n_j} \vec{\mathbf{F}}_u = 0$.

For hinged DFE node interfaces, where the interface node is free to rotate about the z axis, the forces and moments are

$${}^H \vec{\mathbf{F}}_u = - \sum_{j=j_u} [{}^H_{H \leftarrow n_j}]_{n_j} \vec{\mathbf{F}}_u \quad (4.90)$$

$$\begin{aligned} {}^H \vec{\mathbf{M}}_u &= - \sum_{j=j_u} \left(\widetilde{[{}^H_{H \leftarrow n_j}]_{n_j}} [{}^H_{H \leftarrow n_j}]_{n_j} \vec{\mathbf{F}}_u \right) \\ &= - \sum_{j=j_u} \left([{}^H_{H \leftarrow G}]_{G} \widetilde{[{}^G_{G \leftarrow n_j}]_{n_j}} [{}^H_{H \leftarrow n_j}]_{n_j} \vec{\mathbf{F}}_u \right) \end{aligned} \quad (4.91)$$

For the fixed degrees of freedom in each interface node, their generalized coordinates and speeds relative to the G frame are prescribed.

4.4.2 External Damper Model

The structure of skid landing gear typically does not provide adequate damping for energy dissipation during contact. Often in helicopter design, this is addressed by the addition of discrete external dampers and hinged members in the skid structure configuration. Using the compression axis vector between the two mounting points of the damper, a damper force can be calculated as a directed force element then applied at both damper mount points.

For the generic aircraft used in the planar case of SRAMSS as shown in Figure 4.13, the external damper is mounted to the rigid airframe on one side, and at a DFE node on the other.

The directed force element in SRAMSS, used to model external dampers, is a simple spring-damper system for verification purposes. However, any suitable model can be used.

Given N_d number of external dampers integrated into the aircraft, the relative position and speed along the d th damper's compression axis must be determined. The position of the d th airframe mount M_d relative to the airframe's frame H , expressed in the H frame, is ${}^H_H \vec{\mathbf{r}}^{M_d}$. The n_{j_d} th DFE node mount is

$${}^H_H \vec{\mathbf{r}}^{n_{j_d}} = {}^H_H \vec{\mathbf{r}}^G + [{}^H_{H \leftarrow G}]_{G} \vec{\mathbf{r}}^{n_{j_d}} \quad (4.92)$$

The position of the DFE node mount n_{j_d} relative to the airframe mount M_d becomes

$${}^{M_d}_H \vec{\mathbf{r}}^{n_{j_d}} = {}^H_H \vec{\mathbf{r}}^{n_{j_d}} - {}^H_H \vec{\mathbf{r}}^{M_d} \quad (4.93)$$

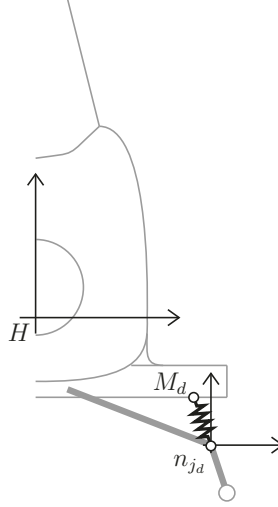


Figure 4.13: Discrete external damper mounting locations.

Differentiating Equation 4.93 yields the velocity of n_{jd} relative to the airframe mount M_d :

$$\begin{aligned}
\frac{M_d}{H} \vec{v}^{n_{jd}} &= \frac{d}{dt} \frac{M_d}{H} \vec{r}^{n_{jd}} \\
&= \frac{d}{dt} \left(\frac{H}{H} \vec{r}^{n_{jd}} \right) - \frac{d}{dt} \left(\frac{H}{H} \vec{r}^{M_d} \right) \\
&= \frac{d}{dt} \left(\frac{H}{H} \vec{r}^G + [\mathbf{T}_{H \leftarrow G}]_G^H \vec{r}^{n_{jd}} \right) - \frac{d}{dt} \left(\frac{H}{H} \vec{r}^{M_d} \right) \\
&= \frac{H}{H} \dot{\vec{r}}^G + [\dot{\mathbf{T}}_{H \leftarrow G}]_G^H \vec{r}^{n_{jd}} + [\mathbf{T}_{H \leftarrow G}]_G^H \dot{\vec{r}}^{n_{jd}} - \frac{H}{H} \dot{\vec{r}}^{M_d} \\
&= \frac{H}{H} \dot{\vec{r}}^G + [\mathbf{T}_{H \leftarrow G}]_G^H [\widetilde{H} \vec{\omega}^H]_G^H \vec{r}^{n_{jd}} + [\mathbf{T}_{H \leftarrow G}]_G^H \dot{\vec{r}}^{n_{jd}} - \frac{H}{H} \dot{\vec{r}}^{M_d} \\
&= [\mathbf{T}_{H \leftarrow G}]_G^H \dot{\vec{r}}^{n_{jd}}
\end{aligned} \tag{4.94}$$

The unit vector expressing the orientation of the compression axis is required to obtain the relative position and velocity for the spring-damper model. The unit vector describing the orientation of n_{jd} with respect to M_d is

$$\frac{M_d}{H} \hat{r}^{n_{jd}} = \frac{\frac{M_d}{H} \vec{r}^{n_{jd}}}{\left\| \frac{M_d}{H} \vec{r}^{n_{jd}} \right\|} \tag{4.95}$$

With Equation 4.95, the compressed damper length Δ_d and velocity $\dot{\Delta}_d$ along the d th damper compression axis is

$$\Delta_d = \frac{M_d}{H} \vec{r}^{n_{jd}} \cdot \frac{M_d}{H} \hat{r}^{n_{jd}} \tag{4.96}$$

$$\dot{\Delta}_d = \frac{M_d}{H} \vec{v}^{n_{jd}} \cdot \frac{M_d}{H} \hat{r}^{n_{jd}} \tag{4.97}$$

Then the damper force generated in the positive direction along the compression axis unit vector is

$$F_{d_d} = -K_d (\Delta_d - \Delta_{d,0}) - C_d \dot{\Delta}_d \quad (4.98)$$

where F_{d_d} is the force generated by the d th external damper expressed along the compression axis ${}^M_d \hat{\mathbf{r}}^{n_{j_d}}$, K_d and C_d are the stiffness and damping coefficients for the external damper spring-damper model, and $\Delta_{d,0}$ is the uncompressed damper length.

Multiplied by the compression axis unit vector, the external damper forces acting on the airframe mount M_d and on the DFE node n_{j_d} , expressed in the H frame are

$${}^M_d \vec{\mathbf{F}}^{d_d} = -F_{d_d} {}^M_d \hat{\mathbf{r}}^{n_{j_d}} \quad (4.99)$$

$${}^{n_{j_d}} \vec{\mathbf{F}}^{d_d} = F_{d_d} {}^M_d \hat{\mathbf{r}}^{n_{j_d}} \quad (4.100)$$

Transforming Equations 4.100 to the nodal frame, assuming the force is acting directly at the node, yields:

$${}^{n_{j_d}} \vec{\mathbf{F}}^{d_d} = [\mathbf{T}_{n_{j_d} \leftarrow H}] {}^M_d \vec{\mathbf{F}}^{d_d} \quad (4.101)$$

$${}^{n_{j_d}} \vec{\mathbf{M}}^{d_d} = 0 \quad (4.102)$$

Assembly into the vector of known external nodal forces due to external dampers ${}^n \mathbf{F}_k^d$ takes the form:

$${}^n \mathbf{F}_k^d = \begin{Bmatrix} {}^{n_1} \vec{\mathbf{F}}^d \\ {}^{n_1} \vec{\mathbf{M}}^d \\ \vdots \\ {}^{n_j} \vec{\mathbf{F}}^d \\ {}^{n_j} \vec{\mathbf{M}}^d \end{Bmatrix} \quad (4.103)$$

where

$$\begin{Bmatrix} {}^{n_j} \vec{\mathbf{F}}^d \\ {}^{n_j} \vec{\mathbf{M}}^d \end{Bmatrix} = \begin{Bmatrix} \sum_{n_j}^d {}^{n_j} \vec{\mathbf{F}}^{d_d} \\ 0 \end{Bmatrix}, \quad j = 1, \dots, N_n \forall j = j_d \quad (4.104)$$

otherwise

$$\begin{Bmatrix} {}^{n_j} \vec{\mathbf{F}}^d \\ {}^{n_j} \vec{\mathbf{M}}^d \end{Bmatrix} = \begin{Bmatrix} 0 \\ 0 \end{Bmatrix}, \quad j = 1, \dots, N_n \forall j \neq j_d \quad (4.105)$$

The external damper forces acting at the airframe mounts M_d are transformed to

equipollent forces and moments acting on the airframe

$${}^H_H \vec{\mathbf{F}}^d = \sum_{d=1}^{N_d} M_d {}^H_H \vec{\mathbf{F}}^{d_d} \quad (4.106)$$

$${}^H_H \vec{\mathbf{M}}^d = \sum_{d=1}^{N_d} \widetilde{[{}^H_H \vec{\mathbf{r}}^{M_d}]} M_d {}^H_H \vec{\mathbf{F}}^{d_d} \quad (4.107)$$

4.4.3 Gravitational Model

The final active force required for the system is the gravitational force acting on the airframe and all DFE nodes. The gravitational forces on each body are

$${}^H_H \vec{\mathbf{F}}^g = m_H [{}^H_H \mathbf{T}_{H \leftarrow N}] \begin{Bmatrix} 0 \\ g \end{Bmatrix} \quad (4.108)$$

$${}^n_n \mathbf{F}_k^g = [\mathbf{M}]_{3N_n \times 3N_n} \begin{bmatrix} [{}^H_H \mathbf{T}_{n_1 \leftarrow N}]_{2 \times 2} & [0]_{2 \times 1} \\ [0]_{1 \times 2} & 1 \\ \vdots & \vdots \\ [{}^H_H \mathbf{T}_{n_j \leftarrow N}]_{2 \times 2} & [0]_{2 \times 1} \\ [0]_{1 \times 2} & 1 \end{bmatrix}_{3N_n \times 3} \begin{Bmatrix} 0 \\ g \\ 0 \end{Bmatrix} \quad \text{for } j = 1, \dots, N_n \quad (4.109)$$

where m_H is the mass of the airframe, $[\mathbf{M}]$ is the total structure mass matrix of the DFE model, and $g = -9.81$ m/s is the gravitational acceleration constant. Since the gravitational acceleration vector acts in the inertial frame N , it must be transformed to the body frames before multiplication with the body masses.

4.5 Inertial Forces

At this point, Chapter 4 has developed the dynamic models required to generate the terms comprising the active forces $\vec{\mathbf{R}}^k$ and moments $\vec{\mathbf{T}}^k$, as well as inertial forces \mathbf{R}^{*n} and moments \mathbf{T}^{*n} acting at the DFE nodes. These are ready for introduction into Kane's equation. Only the inertial forces on the airframe remain to be developed.

The translational and angular inertias of the airframe are

$$\begin{aligned}\vec{\mathbf{R}}^{*H} &= -m_H {}^N \vec{\mathbf{a}}^H \\ &= -m_H \left([{}^N \mathbf{V}^H] \dot{\mathbf{u}} + \vec{\mathbf{Z}}_H \right)\end{aligned}\quad (4.110)$$

$$\begin{aligned}\vec{\mathbf{T}}^{*H} &= -I_H {}^N \vec{\boldsymbol{\alpha}}^H - \widetilde{[{}^N \vec{\boldsymbol{\omega}}^H]} I_H {}^N \vec{\boldsymbol{\omega}}^H \\ &= -I_H \left([{}^N \mathbf{W}^H] \dot{\mathbf{u}} + \vec{\mathbf{Y}}_H \right)\end{aligned}\quad (4.111)$$

To re-iterate, the translational and angular inertias for all nodes, extracted from Equation 4.28, are

$$\mathbf{R}^{*n} + \mathbf{T}^{*n} = -[\mathbf{M}] ([\mathbf{V}_n] \dot{\mathbf{u}} + \mathbf{Z}_n) \quad (4.112)$$

This completes the kinetic development of the planar case of SRAMSS. The following section summarizes the active and inertial kinetic quantities.

4.6 Summary of Kinetic Quantities

The SRAMSS simulation environment comprises many dynamic models which act on various parts of the aircraft. Table 4.2 lists all inertial and active force terms acting on the airframe and DFE nodes. Each term or vector includes the associated equation number assigned during the developments in Chapter 4.

The structure of dynamic model interactions can be summarized as follows. First, the entire aircraft response is modelled by a mass-coupled rigid airframe and flexible dynamic finite element skid landing gear representation through a novel integration of DFE modelling in Kane's method. The two categories of bodies are mass coupled by the interface force model which is represented by an internal force compiled to the active force and moment term acting on the aircraft, and to the nodal forces vector acting at the DFE nodes. Second, rotor disc thrust, body drag forces, gravitational forces, and external damper forces are compiled into the active force and torque vectors acting on the rigid airframe. Third, The contact dynamics model which includes linear penalty normal forces and LuGre friction forces due to polygon contact, the DFE model gravitational forces, and external damper forces are compiled into the known external forces acting at the DFE nodes. The summation of the known external force and unknown interface forces constitute the total active forces and torques acting on the DFE node bodies.

Table 4.2: Complete system forces summary

Forces	Airframe				DFE nodes	
	$\vec{\mathbf{R}}^{*H}$	$\vec{\mathbf{T}}^{*H}$	$\vec{\mathbf{R}}^H$	$\vec{\mathbf{T}}^H$	$\mathbf{R}^{*n} + \mathbf{T}^{*n}$	$\mathbf{R}^n + \mathbf{T}^n$
Inertial						
Inertia	$\vec{\mathbf{R}}^{*H}$ (4.110)	$\vec{\mathbf{T}}^{*H}$ (4.111)	-	-	$\mathbf{R}^{*n} + \mathbf{T}^{*n}$ (4.112)	-
Active						
Damping	-	-	-	-	-	$-\mathbf{[C]} [\mathbf{V}_n] \mathbf{u}$ (4.27)
Stiffness	-	-	-	-	-	$-\mathbf{[K]} \delta_n$ (4.27)
Contact	-	-	-	-	-	${}^n \mathbf{F}_k^c$ (4.55)
Aero. drag	-	-	${}^H \vec{\mathbf{F}}^W$ (4.63)	${}^H \vec{\mathbf{M}}^W$ (4.64)	-	-
Rotor Disc	-	-	${}^H \vec{\mathbf{F}}^{BEM}$ (4.88)	${}^H \vec{\mathbf{M}}^{BEM}$ (4.89)	-	-
Damper	-	-	${}^H \vec{\mathbf{F}}^d$ (4.106)	${}^H \vec{\mathbf{M}}^d$ (4.107)	-	${}^n \mathbf{F}_k^d$ (4.103)
Gravity	-	-	${}^H \vec{\mathbf{F}}^g$ (4.108)	-	-	${}^n \mathbf{F}_k^g$ (4.109)
Interface	-	-	${}^H \vec{\mathbf{F}}_u$ (4.90)	${}^H \vec{\mathbf{M}}_u$ (4.91)	-	${}^n \mathbf{F}_u$ (4.30)

Chapter 5

System Assembly and Simulation Architecture

Chapters 3 and 4 presented the development of the kinematic and kinetic terms required to develop the dynamical system according to Kane's method. This chapter will present the assembly of the developed terms into a single dynamical system, and manipulation of the system into a form suitable for numerical solutions and state propagation.

Section 5.1 develops the assembly of the system and its manipulation into a suitable form. Then, Section 5.2 covers the simulation architecture used in SRAMSS, with an emphasis on how the states are propagated, how contact events are handled, and the general file structure of SRAMSS.

5.1 System Assembly

As presented in Section 2.2, Kane's method for the formulation of the governing dynamical equations is stated

$$\mathbf{F} + \mathbf{F}^* = 0 \quad (2.12)$$

with

$$\mathbf{F} = \sum_{k=1}^{N_B} \left(\left[\begin{matrix} N \\ k \end{matrix} V^k \right]^T \vec{\mathbf{R}}^k + \left[\begin{matrix} N \\ k \end{matrix} W^k \right]^T \vec{\mathbf{T}}^k \right) \quad (2.13)$$

$$\mathbf{F}^* = \sum_{k=1}^{N_B} \left(\left[\begin{matrix} N \\ k \end{matrix} V^k \right]^T \vec{\mathbf{R}}^{*k} + \left[\begin{matrix} N \\ k \end{matrix} W^k \right]^T \vec{\mathbf{T}}^{*k} \right) \quad (2.14)$$

where N_B is the number of bodies in the system. While the aircraft and its landing gear are considered a single physical body, the developments in Chapters 3 and 4 consider them to be individual flexible and rigid bodies. Equations 4.30 and 4.90 serve to unify the separate bodies into a single body with rigid and flexible characteristics. Separation into these smaller ‘sub-bodies’ allows the landing gear DFE model to be developed separately, and eases the integration of infinitely configurable landing gear into the governing equations.

The generic aircraft simulated in SRAMSS comprises one rigid body centred at the H frame representing the airframe, and N_n number of equivalent nodal bodies from the DFE model centred respectively at the n_j frames representing the skid landing gear.

For the airframe body in H , and with the forces summary in Table 4.2 in Section 4.6, Equations 2.13 and 2.14 become

$$\begin{aligned}
\mathbf{F}^H &= [{}^N_H\mathbf{V}^H]^T \vec{\mathbf{R}}^H + [{}^N_H\mathbf{W}^H]^T \vec{\mathbf{T}}^H \\
&= [{}^N_H\mathbf{V}^H]^T \left({}^H_H\vec{\mathbf{F}}^W + {}^H_H\vec{\mathbf{F}}^{RBE} + {}^H_H\vec{\mathbf{F}}^d + {}^H_H\vec{\mathbf{F}}^g + {}^H_H\vec{\mathbf{F}}^u \right) \\
&\quad + [{}^N_H\mathbf{W}^H]^T \left({}^H_H\vec{\mathbf{M}}^W + {}^H_H\vec{\mathbf{M}}^{RBE} + {}^H_H\vec{\mathbf{M}}^d + {}^H_H\vec{\mathbf{M}}^u \right) \\
&= [{}^N_H\mathbf{V}^H]^T \left({}^H_H\vec{\mathbf{F}}^W + {}^H_H\vec{\mathbf{F}}^{RBE} + {}^H_H\vec{\mathbf{F}}^d + {}^H_H\vec{\mathbf{F}}^g \right) \\
&\quad + [{}^N_H\mathbf{W}^H]^T \left({}^H_H\vec{\mathbf{M}}^W + {}^H_H\vec{\mathbf{M}}^{RBE} + {}^H_H\vec{\mathbf{M}}^d \right) \\
&\quad - \left[[{}^N_H\mathbf{V}^H]^T [{}^N_H\mathbf{W}^H]^T \right] \left([\boldsymbol{\tau}_{H \leftarrow n_u}]^n \mathbf{F}^u \right)
\end{aligned} \tag{5.1}$$

and

$$\begin{aligned}
\mathbf{F}^{*H} &= [{}^N_H\mathbf{V}^H]^T \vec{\mathbf{R}}^{*H} + [{}^N_H\mathbf{W}^H]^T \vec{\mathbf{T}}^{*H} \\
&= - [{}^N_H\mathbf{V}^H]^T \left(m_H {}^N_H\vec{\mathbf{a}}^H \right) - [{}^N_H\mathbf{W}^H]^T \left(I_H {}^N_H\vec{\boldsymbol{\alpha}}^H \right) \\
&= - [{}^N_H\mathbf{V}^H]^T \left(m_H \left([{}^N_H\mathbf{V}^H] \dot{\mathbf{u}} + \vec{\mathbf{Z}}_H \right) \right) \\
&\quad - [{}^N_H\mathbf{W}^H]^T \left(I_H \left([{}^N_H\mathbf{W}^H] \dot{\mathbf{u}} + \vec{\mathbf{Y}}_H \right) \right) \\
&= - [{}^N_H\mathbf{V}^H]^T m_H [{}^N_H\mathbf{V}^H] \dot{\mathbf{u}} - [{}^N_H\mathbf{V}^H]^T m_H \vec{\mathbf{Z}}_H \\
&\quad - [{}^N_H\mathbf{W}^H]^T I_H [{}^N_H\mathbf{W}^H] \dot{\mathbf{u}} - [{}^N_H\mathbf{W}^H]^T I_H \vec{\mathbf{Y}}_H
\end{aligned} \tag{5.2}$$

where $[\boldsymbol{\tau}_{H \leftarrow n_u}]$ is the matrix representation of all coefficients to each ${}^{n_j}_H\vec{\mathbf{F}}^u$ in Equations 4.90 and 4.91, expressed

$$\begin{aligned}
[\boldsymbol{\tau}_{H \leftarrow n_u}] &= \begin{bmatrix} [{}^N_H\mathbf{T}_{H \leftarrow n_1}] & [0]_{2 \times 1} & \dots & [{}^N_H\mathbf{T}_{H \leftarrow n_j}] & [0]_{2 \times 1} \\ [\widehat{{}^H_H\vec{\mathbf{r}}^{n_1}}] & 1 & \dots & [\widehat{{}^H_H\vec{\mathbf{r}}^{n_j}}] & 1 \end{bmatrix}, \\
j &= 1, \dots, N_n \forall j = j_u
\end{aligned} \tag{5.3}$$

for rigidly fixed nodes, or

$$[\boldsymbol{\tau}_{H \leftarrow n_u}] = \begin{bmatrix} [\mathbf{T}_{H \leftarrow n_1}] & \cdots & [\mathbf{T}_{H \leftarrow n_j}] \\ [0]_{2 \times 1} & \cdots & [0]_{2 \times 1} \end{bmatrix}, \quad (5.3)$$

$$j = 1, \dots, N_n \forall j = j_u$$

for hinged interface nodes. The matrix $[\boldsymbol{\tau}_{H \leftarrow n_u}]$ transforms the unknown nodal forces acting on the interface DFE nodes into equivalent but opposed forces ${}^H_H \vec{\mathbf{F}}_u$ and moments ${}^H_H \vec{\mathbf{M}}_u$ acting on the airframe as shown in the development of Equation 5.1.

In Equation 5.1, the unknown interface forces acting on the helicopter are expressed in terms of the unknown external nodal forces ${}^n_n \mathbf{F}_u$ such that it can be isolated in the manipulation of the final dynamical system.

For the DFE node bodies in frames n_j , since the terms in Table 4.2 are vectors of nodal forces acting on all nodes, in all degrees of freedom, Equations 2.13 and 2.14 are written compactly as

$$\begin{aligned} \mathbf{F}^n &= [\mathbf{V}_n]^T (\mathbf{R}^n + \mathbf{T}^n) \\ &= [\mathbf{V}_n]^T ({}^n_n \mathbf{F}_k + {}^n_n \mathbf{F}_u - [\mathbf{C}] [\mathbf{V}_n] \mathbf{u} - [\mathbf{K}] \boldsymbol{\delta}_n) \\ &= [\mathbf{V}_n]^T ({}^n_n \mathbf{F}_k - [\mathbf{C}] [\mathbf{V}_n] \mathbf{u} - [\mathbf{K}] \boldsymbol{\delta}_n) + [\mathbf{V}_u]^T {}^n_n \mathbf{F}_u \end{aligned} \quad (5.4)$$

and

$$\begin{aligned} \mathbf{F}^{*n} &= [\mathbf{V}_n]^T (\mathbf{R}^{*n} + \mathbf{T}^{*n}) \\ &= -[\mathbf{V}_n]^T ([\mathbf{M}] ([\mathbf{V}_n] \dot{\mathbf{u}} + \mathbf{Z}_n)) \\ &= -[\mathbf{V}_n]^T [\mathbf{M}] [\mathbf{V}_n] \dot{\mathbf{u}} - [\mathbf{V}_n]^T [\mathbf{M}] \mathbf{Z}_n \end{aligned} \quad (5.5)$$

For the system at hand, by Equation 2.13, the total active forces are the summation of Equations 5.1 and 5.4, such that it incorporates the airframe body and DFE node

bodies as

$$\begin{aligned}
\mathbf{F} &= \mathbf{F}^H + \mathbf{F}^n \\
&= [{}^N\mathbf{V}^H]^T \left({}^H\vec{\mathbf{F}}^W + {}^H\vec{\mathbf{F}}^{RBE} + {}^H\vec{\mathbf{F}}^d + {}^H\vec{\mathbf{F}}^g \right) \\
&\quad + [{}^N\mathbf{W}^H]^T \left({}^H\vec{\mathbf{M}}^W + {}^H\vec{\mathbf{M}}^{RBE} + {}^H\vec{\mathbf{M}}^d \right) \\
&\quad - \left[[{}^N\mathbf{V}^H]^T \quad [{}^N\mathbf{W}^H]^T \right] \left([{}^n\boldsymbol{\tau}_{H \leftarrow n_u}]^n \mathbf{F}_u \right) \\
&\quad + [\mathbf{V}_n]^T \left({}^n\mathbf{F}_k - [\mathbf{C}] [\mathbf{V}_n] \mathbf{u} - [\mathbf{K}] \boldsymbol{\delta}_n \right) + [\mathbf{V}_u]^T {}^n\mathbf{F}_u \\
&= [{}^N\mathbf{V}^H]^T \left({}^H\vec{\mathbf{F}}^W + {}^H\vec{\mathbf{F}}^{RBE} + {}^H\vec{\mathbf{F}}^d + {}^H\vec{\mathbf{F}}^g \right) \\
&\quad + [{}^N\mathbf{W}^H]^T \left({}^H\vec{\mathbf{M}}^W + {}^H\vec{\mathbf{M}}^{RBE} + {}^H\vec{\mathbf{M}}^d \right) \\
&\quad + [\mathbf{V}_n]^T \left({}^n\mathbf{F}_k - [\mathbf{C}] [\mathbf{V}_n] \mathbf{u} - [\mathbf{K}] \boldsymbol{\delta}_n \right) \\
&\quad + \left([\mathbf{V}_u]^T - \left[[{}^N\mathbf{V}^H]^T \quad [{}^N\mathbf{W}^H]^T \right] [{}^n\boldsymbol{\tau}_{H \leftarrow n_u}] \right) {}^n\mathbf{F}_u \\
\mathbf{F} &= \mathbf{F}_k + [\mathbf{D}] \mathbf{F}_u
\end{aligned} \tag{5.6}$$

and the total inertial forces as the summation of Equations 5.2 and 5.5:

$$\begin{aligned}
\mathbf{F}^* &= \mathbf{F}^{*H} + \mathbf{F}^{*n} \\
&= - [{}^N\mathbf{V}^H]^T m_H [{}^N\mathbf{V}^H] \dot{\mathbf{u}} - [{}^N\mathbf{V}^H]^T m_H \vec{\mathbf{Z}}_H \\
&\quad - [{}^N\mathbf{W}^H]^T I_H [{}^N\mathbf{W}^H] \dot{\mathbf{u}} - [{}^N\mathbf{W}^H]^T I_H \vec{\mathbf{Y}}_H \\
&\quad - [\mathbf{V}_n]^T [\mathbf{M}] [\mathbf{V}_n] \dot{\mathbf{u}} - [\mathbf{V}_n]^T [\mathbf{M}] \mathbf{Z}_n
\end{aligned} \tag{5.7}$$

Equation 5.7 can be rearranged to isolate the generalized accelerations vector $\dot{\mathbf{u}}$,

$$\mathbf{F}^* = [\mathbf{A}] \dot{\mathbf{u}} + \mathbf{B} \tag{5.8}$$

such that

$$\begin{aligned}
\mathbf{F}^* &= - \left(m_H [{}^N\mathbf{V}^H]^T [{}^N\mathbf{V}^H] + [{}^N\mathbf{W}^H]^T I_H [{}^N\mathbf{W}^H] + [\mathbf{V}_n]^T [\mathbf{M}] [\mathbf{V}_n] \right) \dot{\mathbf{u}} \\
&\quad - m_H [{}^N\mathbf{V}^H]^T \vec{\mathbf{Z}}_H - I_H [{}^N\mathbf{W}^H]^T \vec{\mathbf{Y}}_H - [\mathbf{V}_n]^T [\mathbf{M}] \mathbf{Z}_n
\end{aligned} \tag{5.9}$$

Now, Equations 5.9 and 5.7 can be assembled as Equation 2.11, then solved for $\dot{\mathbf{u}}$.

$$\begin{aligned}
\mathbf{F} + \mathbf{F}^* &= 0 \\
\mathbf{F} + [\mathbf{A}]\dot{\mathbf{u}} + \mathbf{B} &= 0 \\
[\mathbf{A}]\dot{\mathbf{u}} &= -\mathbf{B} - \mathbf{F} \\
[\mathbf{A}]\dot{\mathbf{u}} &= -\mathbf{B} - \mathbf{F}_k - [\mathbf{D}]\mathbf{F}_u \\
[\mathbf{A}]\dot{\mathbf{u}} &= -\mathbf{C} - [\mathbf{D}]\mathbf{F}_u \\
[\mathbf{A}] \begin{Bmatrix} \dot{\mathbf{u}}_P \\ \dot{\mathbf{u}}_H \\ \dot{\mathbf{u}}_G \\ \dot{\mathbf{u}}_n \end{Bmatrix} &= -\mathbf{C} - [\mathbf{D}]\mathbf{F}_u
\end{aligned} \tag{5.10}$$

with the respective partitions

$$[\mathbf{A}] = \begin{bmatrix} [\mathbf{A}_{11}]_{12 \times 12} & [\mathbf{A}_{12}]_{12 \times 3} & [\mathbf{A}_{13}]_{12 \times 3} & [\mathbf{A}_{14}]_{12 \times 3N_n} \\ [\mathbf{A}_{21}]_{3 \times 12} & [\mathbf{A}_{22}]_{3 \times 3} & [\mathbf{A}_{23}]_{3 \times 3} & [\mathbf{A}_{24}]_{3 \times 3N_n} \\ [\mathbf{A}_{31}]_{3 \times 12} & [\mathbf{A}_{32}]_{3 \times 3} & [\mathbf{A}_{33}]_{3 \times 3} & [\mathbf{A}_{34}]_{3 \times 3N_n} \\ [\mathbf{A}_{41}]_{3N_n \times 12} & [\mathbf{A}_{42}]_{3N_n \times 3} & [\mathbf{A}_{43}]_{3N_n \times 3} & [\mathbf{A}_{44}]_{3N_n \times 3N_n} \end{bmatrix} \tag{5.11}$$

$$\dot{\mathbf{u}} = \begin{Bmatrix} \{\dot{\mathbf{u}}_P\}_{12 \times 1} \\ \{\dot{\mathbf{u}}_H\}_{3 \times 1} \\ \{\dot{\mathbf{u}}_G\}_{3 \times 1} \\ \{\dot{\mathbf{u}}_n\}_{3N_n \times 1} \end{Bmatrix} \tag{5.12}$$

$$\mathbf{C} = \begin{Bmatrix} \{\mathbf{C}_1\}_{12 \times 1} \\ \{\mathbf{C}_2\}_{3 \times 1} \\ \{\mathbf{C}_3\}_{3 \times 1} \\ \{\mathbf{C}_4\}_{3n_n \times 1} \end{Bmatrix} \tag{5.13}$$

$$[\mathbf{D}] = \begin{bmatrix} [\mathbf{D}_1]_{12 \times 3N_u} \\ [\mathbf{D}_2]_{3 \times 3N_u} \\ [\mathbf{D}_3]_{3 \times 3N_u} \\ [\mathbf{D}_4]_{3 \times 3N_u} \end{bmatrix} \tag{5.14}$$

$$\mathbf{F}_u = \{\mathbf{F}_u\}_{3N_u \times 1} \tag{5.15}$$

where N_u is the number of DFE nodes interfacing with the airframe. Since $\dot{\mathbf{u}}_P$ is

prescribed, and $\dot{\mathbf{u}}_G = 0$, the system presented in Equation 5.10 reduces to

$$\begin{aligned} \begin{bmatrix} [\mathbf{A}_{22}] & [\mathbf{A}_{24}] \\ [\mathbf{A}_{42}] & [\mathbf{A}_{44}] \end{bmatrix} \begin{Bmatrix} \dot{\mathbf{u}}_H \\ \dot{\mathbf{u}}_n \end{Bmatrix} &= - \begin{Bmatrix} \mathbf{C}_2 \\ \mathbf{C}_4 \end{Bmatrix} - \begin{bmatrix} [\mathbf{D}_2] \\ [\mathbf{D}_4] \end{bmatrix} \mathbf{F}_u - \begin{bmatrix} [\mathbf{A}_{21}] \\ [\mathbf{A}_{41}] \end{bmatrix} \dot{\mathbf{u}}_{Poly} \\ [\mathbf{A}'] \begin{Bmatrix} \dot{\mathbf{u}}_H \\ \dot{\mathbf{u}}_n \end{Bmatrix} &= -\mathbf{C}' - [\mathbf{D}'] \mathbf{F}_u \end{aligned} \quad (5.16)$$

For this work, the last term of Equation 5.16 can be eliminated since the contributions of the ship, RSD deck, and wedge clamp motions are accounted for through the contact forces since the polygons are not part of the aircraft's chain of frames.

The system in Equation 5.16 includes $\dot{\mathbf{u}}$ which contains known interface node accelerations $\dot{\mathbf{u}}_{n_j} = 0, \forall j = j_u$. The vector of known nodal accelerations is equivalent in size to \mathbf{F}_u , therefore Equation 5.16 can be manipulated to express the solution vector containing the unknown generalized accelerations and unknown interface forces such that

$$\begin{aligned} \begin{bmatrix} [\mathbf{A}'_H] & [\mathbf{A}'_1] & \dots & [\mathbf{A}'_j] \end{bmatrix} \begin{Bmatrix} \dot{\mathbf{u}}_H \\ \dot{\mathbf{u}}_n \end{Bmatrix} &= -\mathbf{C}' - [\mathbf{D}'] \mathbf{F}_u, \quad j = 1, \dots, N_n \\ \begin{bmatrix} [\mathbf{A}''] & [\mathbf{D}'] \end{bmatrix} \begin{Bmatrix} \dot{\mathbf{u}}_H \\ \dot{\mathbf{u}}'_n \\ \mathbf{F}_u \end{Bmatrix} &= -\mathbf{C}' - [\mathbf{A}''] \dot{\mathbf{u}}'_n \\ \begin{bmatrix} [\mathbf{A}'''] \end{bmatrix} \begin{Bmatrix} \dot{\mathbf{u}}_H \\ \dot{\mathbf{u}}'_n \\ \mathbf{F}_u \end{Bmatrix} &= -\mathbf{C}' \end{aligned} \quad (5.17)$$

where: $[\mathbf{A}''] = [\mathbf{A}'_a] \forall a \neq j_u$

$\dot{\mathbf{u}}'_n = \dot{\mathbf{u}}_{n_j} \forall j \neq j_u$

Equation 5.17 is the final linear system of equations in the form $[\mathbf{M}_{sys}] \mathbf{x}_{sys} = \mathbf{F}_{sys}$, and can be solved using numerical linear equation solvers. The size of the system to be solved is dependent on the number of unknown generalized accelerations and the size of the unknown interface forces vector. Once the solution \mathbf{x}_{sys} is obtained, the interface force elements are removed from the system solution vector. The non-prescribed generalized coordinate time-derivatives are included for state-propagation

purposes, such that the state derivative vector $\dot{\mathbf{x}}$ becomes

$$\dot{\mathbf{x}} = \begin{Bmatrix} \dot{\mathbf{u}}_H \\ \dot{\mathbf{u}}'_n \\ \dot{\mathbf{q}}_H \\ \dot{\mathbf{q}}'_n \end{Bmatrix} = \begin{Bmatrix} \begin{matrix} \dot{\mathbf{v}}^H \\ \dot{\boldsymbol{\omega}}^H \\ \dot{\mathbf{v}}^{n_1} \\ \dot{\boldsymbol{\omega}}^{n_1} \\ \vdots \\ \dot{\mathbf{v}}^{n_j} \\ \dot{\boldsymbol{\omega}}^{n_j} \\ \dot{\mathbf{r}}^H \\ \dot{\boldsymbol{\theta}}^H \\ \dot{\mathbf{r}}^{n_1} \\ \dot{\boldsymbol{\theta}}^{n_1} \\ \vdots \\ \dot{\mathbf{r}}^{n_j} \\ \dot{\boldsymbol{\theta}}^{n_j} \end{matrix} \end{Bmatrix} = \begin{Bmatrix} \dot{\mathbf{u}}_H \\ \dot{\mathbf{u}}'_n \\ \begin{matrix} \dot{\mathbf{v}}^H \\ \dot{\boldsymbol{\omega}}^H \\ \dot{\mathbf{v}}^{n_1} \\ \dot{\boldsymbol{\omega}}^{n_1} \\ \vdots \\ \dot{\mathbf{v}}^{n_j} \\ \dot{\boldsymbol{\omega}}^{n_j} \end{matrix} \end{Bmatrix}, \quad \forall j = 1, \dots, N_n, j \neq j_u \quad (5.18)$$

The solution vector in Equation 5.18 is propagated forward in time using numerical integration methods described in Section 5.2.1.

5.2 Simulation Architecture

SRAMSS was initially written in the interpreted programming language MATLAB[®] for its extensive mathematical libraries, plotting capabilities, and ease of code modification and verification. Once the architecture of SRAMSS was established and verified, the code was ported to the Intel[®] Fortran compiled language. Fortran is well suited to the large number of array and vector manipulations required by the SRAMSS code. The compiled Fortran code provides computational speeds orders of magnitude faster than MATLAB[®]. Depending on the simulation scenario, these speed increases reduced simulation run-time to near-real-time values. In non-stiff state-propagation regimes, SRAMSS well exceeded the real-time threshold. Such performance was achieved on an Intel[®] i5-6600k CPU clocked at 4.10 Ghz. Extensive optimizations could potentially have SRAMSS cross the real-time threshold in all cases; a desirable characteristic for integration into real-time interactive simulation environments.

While the dynamical system in SRAMSS can be reduced to a system of linear equations as presented in Section 5.1, the dynamics involved are highly non-linear. Intermittent contact requires the reformulation of the linear system at each internal time-step. In effect, SRAMSS is a ‘switched’ hybrid system that switches between in-contact, and no-contact dynamic system formulations [54]. While both regimes are linear and continuous, the switch between regimes is not. Further, in the case of the DFE model, they are also numerically stiff. Specific techniques are used to optimize performance and increase fidelity in modelling the included dynamic phenomena.

5.2.1 State Propagation

For state-propagation in SRAMSS, multiple considerations are made in the selection of the numerical integrator.

The first thing to be considered is the numerical-stiffness of the system developed in SRAMSS. The inclusion of a DFE model into the system causes numerical stiffness; the DFE model eigenvalues are significantly different in order of magnitude compared to those of the overall system. Large nodal forces and small nodal displacements would require extremely small time-steps for generic solvers. Secondary contributions to system stiffness arise from the unilateral contact forces applied to the rigid skid-landing gear which significantly change the system dynamics on contact. Third, the system is relatively non-stiff when out of contact with the environment. However, the selection of a stiff solver to address the stiffness considerations is inefficient in the ‘no-contact’ regime.

Based on these considerations, the ‘DLSODAR.for’ ordinary differential equation (ODE) solver was chosen for the Fortran version of SRAMSS [55, 56]. DLSODAR is a solver which automatically switches between a non-stiff explicit ‘Adams’ method and a stiff implicit BDF method, using an algorithm developed by Petzhold [57]. This addresses the third consideration by choosing the appropriate solver based on the current apparent stiffness of the system. In both cases, the implemented solvers are linear-multistep methods which increase efficiency by usage of previous state information. The BDF solver is particularly suited to the stiff contact regimes where the DFE model is undergoing transient deformation.

Additionally, DLSODAR provides ‘root-finding’ capabilities from Hiebert and Shampine [58], which are leveraged to address the second consideration. In the transitions between no-contact and in-contact states for the contacting nodes, the dynamics

of the system explicitly change due to unilateral contact. Zero contact forces are generated in the ‘no-contact’ regime ${}^n\mathbf{F}_k^c = 0$, whereas the in-contact regime generates a non-zero contact force ${}^n\mathbf{F}_k^c \neq 0$. The root function provided to DLSODAR by SRAMSS models the contact states of the contact nodes n_{j_c} . The contact states are formulated such that a root is found at contact or release there from. This root function allows the termination of the current solution time-step Δt_{sol} at the time of contact event (or release) t_e as shown in Figure 5.1. This termination, resulting in shorter solution time-step Δt_e , separates the stiff in-contact regime from the non-stiff no-contact regimes. DLSODAR is then able to switch between solvers which results in improved simulation performance around these transitions since increasingly small solver internal time-steps are avoided around these discontinuities.

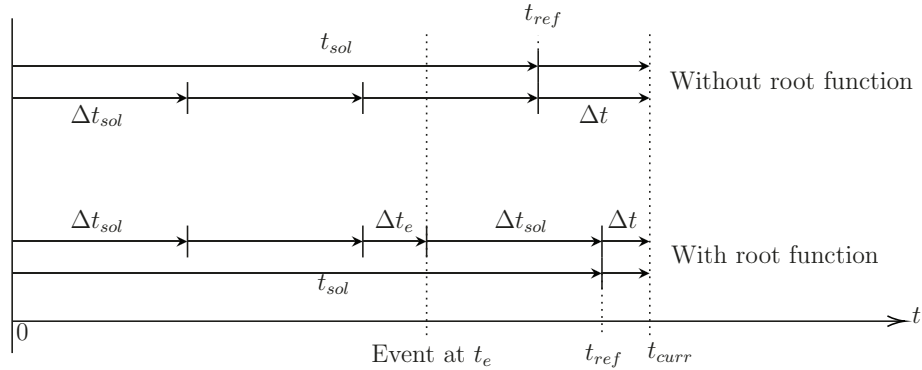


Figure 5.1: State propagation with root-finding step termination.

The root function algorithm employed in SRAMSS for contact event handling is developed in the following section.

5.2.2 Contact Event Handling

The instance where contact or release from contact occurs is called an ‘event’. Time-step termination at these events makes SRAMSS’ implementation of the DLSODAR solver partially event-driven. Detection of these events is handled by the contact detection algorithm implemented in SRAMSS. The algorithm is integrated into the SAT contact dynamics model to provide appropriate surface determination for dynamic response, and contact event detection. In each case, a scalar value is calculated. The index m of polygon contact surface ${}^P S_m$ is determined to apply contact forces in the correct direction. A scalar-valued root function ${}^P g^{n_{j_c}}(t)$, representing the contact-pair of node n_{j_c} and polygon P , crosses zero at a contact event to enable solution

time-step termination at Δt_e .

Appropriate Surface Detection

In Section 4.2 of Chapter 4, it was assumed that surface ${}^P s_m$ was in contact with node n_{jc} . The objective of the contact detection algorithm is to determine the value of index m corresponding to the contact surface ${}^P s_m$ of polygon P . The SAT algorithm inherently provides a straight-forward method for detecting surface collision by use of the surface normal axes.

Contact detection using the SAT first requires a binary penetration state matrix (PSM) $[{}^P \mathbf{A}^{n_{jc}}(t)]$ which indicates penetration (no axis of separation) of contact node n_{jc} along surface ${}^P s_m$ of polygon P at time t such that

$$[{}^P \mathbf{A}^{n_{jc}}(t)] = \begin{bmatrix} \mathbf{A}_{s_1} \\ \vdots \\ \mathbf{A}_{s_m} \end{bmatrix} = \begin{cases} \mathbf{A}_{s_m} = 0, & \frac{N}{N} \vec{\mathbf{r}}^{n_{jc}} \cdot \frac{P}{N} \hat{\mathbf{s}}_m > \left(\frac{N}{N} \vec{\mathbf{r}}^{P_m} \cdot \frac{P}{N} \hat{\mathbf{s}}_m \right) \\ \mathbf{A}_{s_m} = 1, & \frac{N}{N} \vec{\mathbf{r}}^{n_{jc}} \cdot \frac{P}{N} \hat{\mathbf{s}}_m \leq \left(\frac{N}{N} \vec{\mathbf{r}}^{A_m} \cdot \frac{P}{N} \hat{\mathbf{s}}_m \right) \end{cases} \quad (5.19)$$

$$m = 1, \dots, N_{s,P}$$

By Equation 4.37, penetration can be obtained by the projection of the contact node n_{jc} to the separation axis of surface ${}^P s_m$. Since the surface normals $\frac{P}{N} \hat{\mathbf{s}}_m$ point outwards, there is no penetration along ${}^P s_m$ ($\mathbf{A}_{s_m} = 0$) when the projected node exceeds the projected polygon vertex, and penetration otherwise ($\mathbf{A}_{s_m} = 1$).

Next, by the existence of an arbitrary axis separating two objects as shown in Figure 4.3, contact only occurs when such an axis cannot be found. During contact, all surfaces are penetrated, $[{}^P \mathbf{A}^{n_{jc}}(t)] = 1$. For the application of an appropriately-oriented dynamic response, the surface involved in collision must be determined. The desired surface can be determined through monitoring of the transient penetration state changes in $[{}^P \mathbf{A}^{n_{jc}}(t)]$. Let the binary penetration state change matrix (PSCM) $[{}^P \mathbf{B}^{n_{jc}}(t)]$ indicate the change in penetration with surface ${}^P s_m$ between reference time t_{ref} and desired time t , such that

$$\begin{aligned} [{}^P \mathbf{B}^{n_{jc}}(t)] &= [{}^P \mathbf{A}^{n_{jc}}(t)] - [{}^P \mathbf{A}^{n_{jc}}(t_{ref})] \\ [{}^P \mathbf{B}^{n_{jc}}(t_{curr})] &= [{}^P \mathbf{A}^{n_{jc}}(t_{curr})] - [{}^P \mathbf{A}^{n_{jc}}(t_{sol})] \end{aligned} \quad (5.20)$$

where

$$[{}^P \mathbf{B}^{n_{jc}}(t)] = \begin{bmatrix} \mathbf{B}_{s_1} \\ \vdots \\ \mathbf{B}_{s_m} \end{bmatrix}, \quad \mathbf{B}_{s_m} = \begin{cases} 1, & \text{into penetration} \\ 0, & \text{no change} \\ -1, & \text{out of penetration} \end{cases} \quad m = 1, \dots, N_{s,P} \quad (5.21)$$

In the case of the linear multistep solver DLSODAR which aims to propagate the solution by a time-step increment of Δt_{sol} , t_{ref} is chosen as the start time of the solver time-step t_{sol} . This reference time coincides with a solution propagated fully through Δt_{sol} where the contact state has not changed, or the early termination at Δt_e , the time where an event was detected and the PSM takes on a new penetration state configuration.

The desired time is taken as t_{curr} the time currently being evaluated by the solver. Usage of these definitions of times for the PSCM eliminates errors arising from failed internal time-steps, and aligns with the objective of using the root-finding function to start new solution time-steps at changes in collision states.

Along with the PSM and PSCM, a contact surface matrix (CSM) $[{}^P \mathbf{D}^{n_{jc}}(t)]$ is required. The CSM indicates which surface ${}^P s_m$ is in contact at time t . The CSM determines if a change in penetration state indicated by the PSCM constitutes contact, or release from contact, with a polygon surface. The CSM at time t is constructed

$$[{}^P \mathbf{D}^{n_{jc}}(t)] = \begin{bmatrix} \mathbf{D}_{s_1} \\ \vdots \\ \mathbf{D}_{s_m} \end{bmatrix}, \quad \mathbf{D}_{s_m} = \begin{cases} 0, & \text{not contact surface} \\ 1, & \text{contact surface} \end{cases} \quad m = 1, \dots, N_{s,P} \quad (5.22)$$

For a given solver step Δt_{sol} , $[{}^P \mathbf{D}^{n_{jc}}(t_{sol})]$ is required to indicate the contact state at the beginning of the current solution time-step, and to determine if $[{}^P \mathbf{B}^{n_{jc}}(t_{curr})]$ indicates a change with respect to the contact surface during the current solver step Δt_{sol} . The CSM at time t_{curr} is then determined by the following algorithm:

$$\mathbf{D}_{s_m}(t_{curr}) = \begin{cases} 1, & \sum [{}^P \mathbf{A}^{n_{jc}}(t_{curr})] = N_{s,P} \wedge \mathbf{B}_{s_m}(t_{curr}) = 1 \\ \mathbf{D}_{s_m}(t_{sol}), & \sum [{}^P \mathbf{A}^{n_{jc}}(t_{curr})] = N_{s,P} \wedge \mathbf{B}_{s_m}(t_{curr}) = 0 \\ 0, & \text{otherwise} \end{cases} \quad (5.23)$$

$$m = 1, \dots, N_{s,P}$$

where at the current time t_{curr} if the summation of all elements of $[{}^P\mathbf{A}^{n_{jc}}(t_{curr})] \neq N_{s,P}$, then a separation axis exists since not all surfaces are penetrated, and the node is not in contact with any surface. As a result the CSM takes on the value $[{}^A\mathbf{D}^{n_{jc}}(t_{curr})] = 0$; no surface is in contact. If $\sum [{}^P\mathbf{A}^{n_{jc}}(t_{curr})] = N_{s,P}$, then the PSCM element where $\mathbf{B}_{s_m}(t_{curr}) = 1$ indicates a node coming into contact with surface ${}^P s_m$ since the last penetration state \mathbf{A}_{s_m} to change into penetration ($\mathbf{B}_{s_m}(t_{curr}) = 1$) is the contact surface. Otherwise the CSM maintains its Δt_{sol} value since the PSM has not changed, i.e. the contact node remains in its current penetration state of ${}^P s_m$. For $B_m(t_{curr}) = -1$, $\sum [{}^P\mathbf{A}^{n_{jc}}(t_{curr})] = N_{s,P}$ cannot be satisfied since -1 indicates coming out of penetration of surface ${}^P s_m$ and the existence of a separation axis as before.

Then, for a CSM with r elements, the index m of the contact surface ${}^P s_m$ of polygon P is determined

$$[{}^P\mathbf{D}^{n_{jc}}(t_{curr})] = \begin{bmatrix} \mathbf{D}_{s_1} \\ \vdots \\ \mathbf{D}_{s_r} \end{bmatrix}, \text{ where } \mathbf{D}_{s_r}(t_{curr}) = 1 : m = r \quad (5.24)$$

If $[{}^P\mathbf{D}^{n_{jc}}(t_{curr})] = 0$ then m cannot be found. Therefore node n_{jc} is not in contact with polygon P and ${}^{n_{jc}}\vec{\mathbf{F}}^P = 0$. Otherwise, where index m of the contacted surface is found, application of the contact dynamics model along the appropriate surface for dynamic response is then possible.

This, the first objective of the contact detection algorithm provides the index m of the contact surface ${}^P s_m$ when in contact, which can then be fed to the contact dynamics model presented in Section 4.2 to apply the appropriately-oriented dynamic response. The precise time t_e at which the contact state changes, and thusly the application of the contact forces, remains to be determined.

Event root function

As previously stated, the dynamics in SRAMSS change drastically when a change in contact state for node n_{jc} occurs. Providing a set of root functions ${}^P g^{n_{jc}}(t)$ for all contact-pairs to the DLSODAR solver allows for early termination of the solution time-step at Δt_e . The solution is propagated to $t_e = t_{sol} + \Delta t_e$, where t_e is the contact event time where one of the provided root functions crosses zero.

Each root function in the set provided to DLSODAR crosses zero at the event-time where a contact-pair changes contact state. Definition of the root functions in

this manner splits the unilateral dynamics into two separate and smooth regimes. On one side, in the ‘no-contact’ regime, the contact forces for the j_c th contact node ${}^{n_{j_c}}\vec{\mathbf{F}}_k^c = 0$. On the other, in the ‘in-contact’ regime, ${}^{n_{j_c}}\vec{\mathbf{F}}_k^c$ is given by Equation 4.55. At initial contact of surface ${}^A S_m$, Δ_p from Equation 4.39 equals zero. Therefore the root function can be defined using distances to the contact surface ${}^P S_m$.

For the in-contact regime, the indice m is known, thus the root function can be expressed using the penetration depth ${}^{s_m}\Delta_p$ along surface normal ${}^P_N \hat{\mathbf{s}}_m$. For the no-contact regime, the distance must be assumed. Initial contact is assumed to occur at the closest surface to node n_{j_c} . The closest surface is determined by the minimum positive value of ${}^{s_m}\Delta_p$ for all surfaces $m = 1, \dots, N_{s,P}$ belonging to polygon P , given by Equation 4.39. The root function for a contact pair is then expressed as

$${}^P g^{n_{j_c}}(t_{curr}) = \begin{cases} {}^{s_m}\Delta_p, & \mathbf{D}_{S_m}(t_{curr}) = 1 \\ \min({}^{s_m}\Delta_p > 0), & [{}^P \mathbf{D}^{n_{j_c}}(t_{curr})] = 0 \end{cases} \quad (5.25)$$

This Section completes the definitions of the contact dynamics, and numerical integration method used in SRAMSS. The next section presents an overview of the SRAMSS architecture as a whole.

5.2.3 Subroutine Architecture

SRAMSS can be described as a variable-output-time-step simulation which propagates the solution vector forwards in time by use of an event-driven linear multistep ODE solver. Figure 5.2 shows a high-level representation of the SRAMSS software architecture.

Per note 1 in Figure 5.2, SRAMSS requires the following input files, the contents of which are described in Appendix A.1:

- *Simulation.inp*: Simulation parameters;
- *Output_options.inp*: flag file for output files desired;
- *ICs.inp*: generalized coordinate and speed initial conditions;
- *Properties_helo.inp*: Helicopter properties;
- *Properties_contact_mech.inp*: contact mechanics properties;
- *Properties_FE_map.inp*: DFE node-element mapping, and elemental properties;
- *Properties_FE_IC.inp*: Undeformed DFE node mesh ${}^G \vec{\mathbf{r}}^{n_{j_0}}$ and ${}^G \vec{\boldsymbol{\theta}}^{n_{j_0}}$;
- *Properties_FE_Mmat.inp*: externally-generated DFE mass matrix (optional);

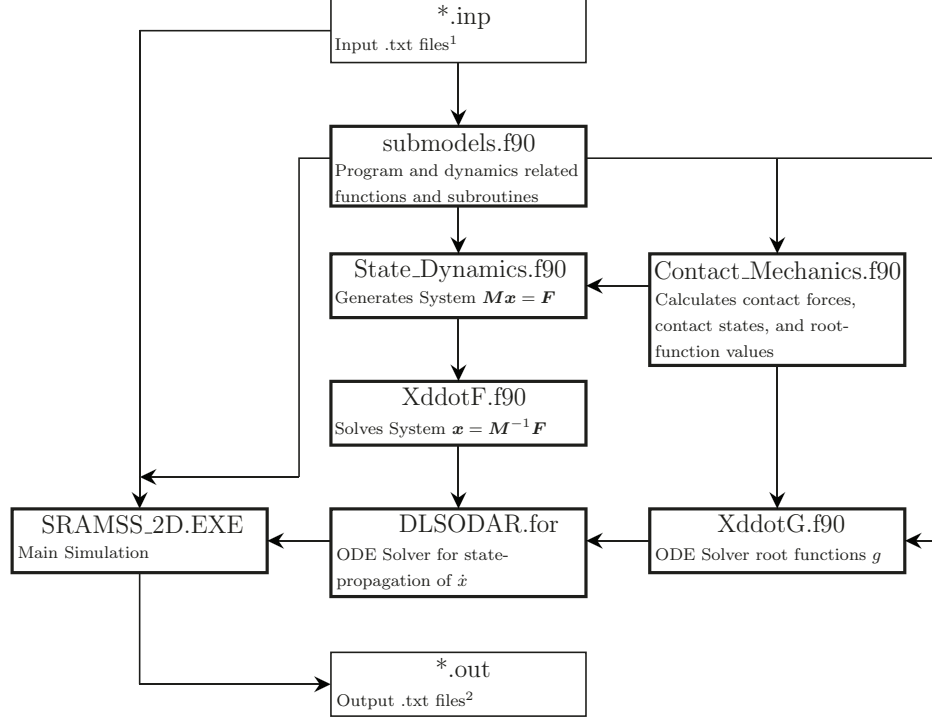


Figure 5.2: SRAMSS program architecture.

- *Properties_FE_Kmat.inp*: externally-generated total structure stiffness matrix (optional);
- *Properties_FE_Cmat.inp*: externally-generated total structure proportional damping matrix (optional);
- *Polygon_ship.inp*: Ship polygon vertex positions $^S_S \vec{\mathbf{r}}^{S_m}$;
- *Polygon_rsd.inp*: RSD deck polygon vertex positions $^D_D \vec{\mathbf{r}}^{D_m}$;
- *Polygon_clamplleft.inp*: Left wedge clamp polygon vertex positions $^{CL}_{CL} \vec{\mathbf{r}}^{CL_m}$;
- *Polygon_clampright.inp*: Right wedge clamp polygon vertex positions $^{CR}_{CR} \vec{\mathbf{r}}^{CR_m}$;
- *Prescribed_ship.inp*: prescribed motion for S -frame;
- *Prescribed_rsd.inp*: prescribed motion for D -frame;
- *Prescribed_clamplleft.inp*: prescribed motion for CL -frame;
- *Prescribed_clampright.inp*: prescribed motion for CR -frame; and
- *Prescribed_aero.inp*: prescribed aerodynamics including wind velocity $^N_N \vec{\mathbf{v}}^W$, rotor RPM $^H_R \vec{\omega}^R$, collective pitch setting θ_{coll} , and cyclic pitch settings $\theta_{cyc,max}$ and ψ_{max} .

Per note 2 in Figure 5.2, SRAMSS can currently generate the following output files where appropriately flagged in *Output_options.inp*, the contents of which are described

in Appendix A.2:

- *GEN_SOLUTION.out*: output time-stamped solution vectors of generalized speeds and coordinates;
- *POLY_SHIP.out*: output time-stamped ship polygon vertices ${}^N_N \vec{\mathbf{r}}^{S_m}$;
- *POLY_RSD.out*: output time-stamped RSD deck polygon vertices ${}^N_N \vec{\mathbf{r}}^{D_m}$;
- *POLY_L_CLAMP.out*: output time-stamped left wedge clamp polygon vertices ${}^N_N \vec{\mathbf{r}}^{CL_m}$;
- *POLY_R_CLAMP.out*: output time-stamped right wedge clamp polygon vertices ${}^N_N \vec{\mathbf{r}}^{CR_m}$;
- *OCP_SHIP.out*: output time-stamped ship polygon OCP for all contact nodes ${}^S_N \vec{\mathbf{o}}^{n_{jc}}$;
- *OCP_RSD.out*: output time-stamped RSD deck OCP for all contact nodes ${}^D_N \vec{\mathbf{o}}^{n_{jc}}$;
- *OCP_L_CLAMP.out*: output time-stamped left wedge clamp OCP for all contact nodes ${}^{CL}_N \vec{\mathbf{o}}^{n_{jc}}$;
- *OCP_R_CLAMP.out*: output time-stamped right wedge clamp OCP for all contact nodes ${}^{CR}_N \vec{\mathbf{o}}^{n_{jc}}$;
- *FORCE_CONTACT.out*: output time-stamped contact forces for all contact nodes ${}^{n_{jc}}_N \mathbf{F}_k^c$;
- *FORCE_INDUCED.out*: output time-stamped rotor disc induced forces ${}^H_H \vec{\mathbf{F}}^{BEM}$ and ${}^H_H \vec{\mathbf{M}}^{BEM}$; and
- *SIM_STATS.out*: output time-stamped simulation and ‘DLSODAR.for’ statistics.

Chapter 6

SRAMSS Verification and Validation

Dynamic simulation packages such as Dynaface[®], SSMASH, and SRAMSS, serve a unique purpose in cost-effectively performing faithful dynamic interface analyses without the need for full-scale experiments. Yet the accuracy of these packages is bounded by the fidelity of implemented virtual models. Accuracy must then be measured. For SRAMSS, this involves the verification of proper implementation of model formulas and algorithms, and the validation of simulation results against experimental data and known physical theories and laws. For the planar case of SRAMSS developed in this work, validation is made mostly by comparison with theories and laws since the planar simulation environment cannot capture the out-of-plane effect present in fully-spatial commercially available dynamic interface packages.

This chapter discusses the verification and validation of SRAMSS. The generic aircraft used for simulation test cases, and the description of these test cases follow in Sections 6.1 and 6.2 respectively. Results from the test cases are discussed in Section 6.3. Finally, Section 6.4 provides other general remarks and observations made for SRAMSS.

6.1 Generic Aircraft Description

To ensure consistency between the test cases presented in the following section, a single generic aircraft is defined. The generic aircraft definition and parameters remain constant for all test cases, unless a given test case is specifically evaluating the effect

of a parameter variation. For example, the DFE model mesh may vary for a test case to observe convergence as the DFE model mesh is refined.

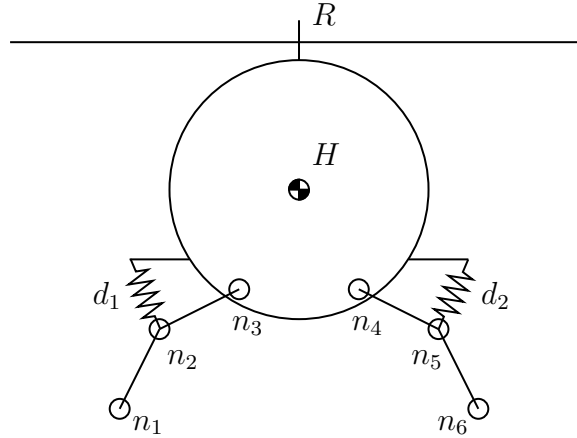


Figure 6.1: Generic aircraft used in verification and validation test cases.

The generic aircraft used for verification purposes is as shown in Figure 6.1. The aircraft body is composed of a single rigid-body H representing the airframe, and a 6-node DFE model representing the left and right legs of a skid-type landing gear. In addition, the generic aircraft has two discrete external dampers attached between the middle nodes of the DFE landing gear legs and the airframe's winglets. There is also a rotor disc R with rectangular blades located on the top-side of the airframe.

For the complete description of the aircraft,

- Table 6.1 presents the physical parameters of the aircraft;
- Table 6.2 describes the functionality of each DFE node by node index j ;
- Table 6.3 and Figure 6.2 present the rotor disc BEM model parameters; and
- Table 6.4 presents the contact dynamics properties.

From Figure 6.2, the Mach number effects from Equation 4.72 are ignored by setting the thickness ratio to zero. Since the drag coefficient is set to zero, rotor blade drag is also effectively not considered.

Table 6.1: Generic aircraft parameters

Parameter	Variable	Value
Airframe Parameters		
Airframe mass	m_H	50 kg
Airframe mass moment of inertia	I_H	6.25 kg·m ²
Discrete damper spring coefficient	K_d	2.5X10 ⁴ N/m
Discrete damper damping coefficient	C_d	500 Ns/m
Equivalent flat plate area	\mathbf{A}_{eq}	{2 2 2} ^T m ²
Centre of pressure	${}^H_H \vec{r}^{CP}$	{0 -0.5 0} ^T m
DFE Model Landing Gear Parameters		
Number of nodes	N_n	6
Number of elements		4
Element Young's modulus	E	6.9X10 ¹⁰ Pa
Element second moment of area	I	5.00X10 ⁻⁷ m ⁴
Element density	ρ	2710 kg/m ³
Element cross-section	A	1.2X10 ⁻⁴ m ²
Rayleigh damping lower frequency	ω_1	0 rad/s
Rayleigh damping lower damping ratio	ξ_1	0.15
Rayleigh damping upper frequency	ω_2	6.5X10 ⁵ rad/s
Rayleigh damping upper damping ratio	ξ_2	0.15
Skid-tube cross-section radius		0.01 m

Table 6.2: DFE node functionality for generic aircraft

Node Type	Node Variable	Set of Indices
All	n_j	$j = \{1, 2, 3, 4, 5, 6\}$
Contact	n_{j_c}	$j_c = \{1, 6\}$
Interface	n_{j_u}	$j_u = \{3, 4\}$
Damper	n_{j_d}	$j_d = \{2, 5\}$

Table 6.3: Rotor disc blade element model parameters

Parameter	Variable	Value
Number of rotor blades	N_b	4
Number of blade elements	N_e	80
Number of rotor disc sectors	N_ψ	20
Rotor blade radius	R_b	3 m
Inner effective rotor disc radius	R_i	0.2
Outer effective rotor disc radius	R_o	0.9
Blade chord length	c	Fig.6.2
Blade thickness ratio	t/c	↓
Blade twist	θ_t	
Uncorrected lift coefficient gradient	$\frac{dC_L}{d\alpha}$	
Uncorrected lift coefficient at $\alpha = 0$	$C_{L,0}$	
Uncorrected drag coefficient gradient	$\frac{dC_D}{d\alpha}$	
Uncorrected drag coefficient $\alpha = 0$	$C_{D,0}$	

Table 6.4: Contact dynamics parameters

Parameter	Variable	Value
Penetration stiffness	K_p	1X10 ⁶ N/m
Penetration damping	C_p	3130 Ns/m
Friction micro-displacement stiffness	K_f	3X10 ³ N/m
Friction micro-displacement damping	C_f	600 Ns/m
Stribeck velocity threshold	v_s	0.001m/s
Dynamic friction coefficient	μ_d	0.4
Static friction coefficient	μ_s	0.9

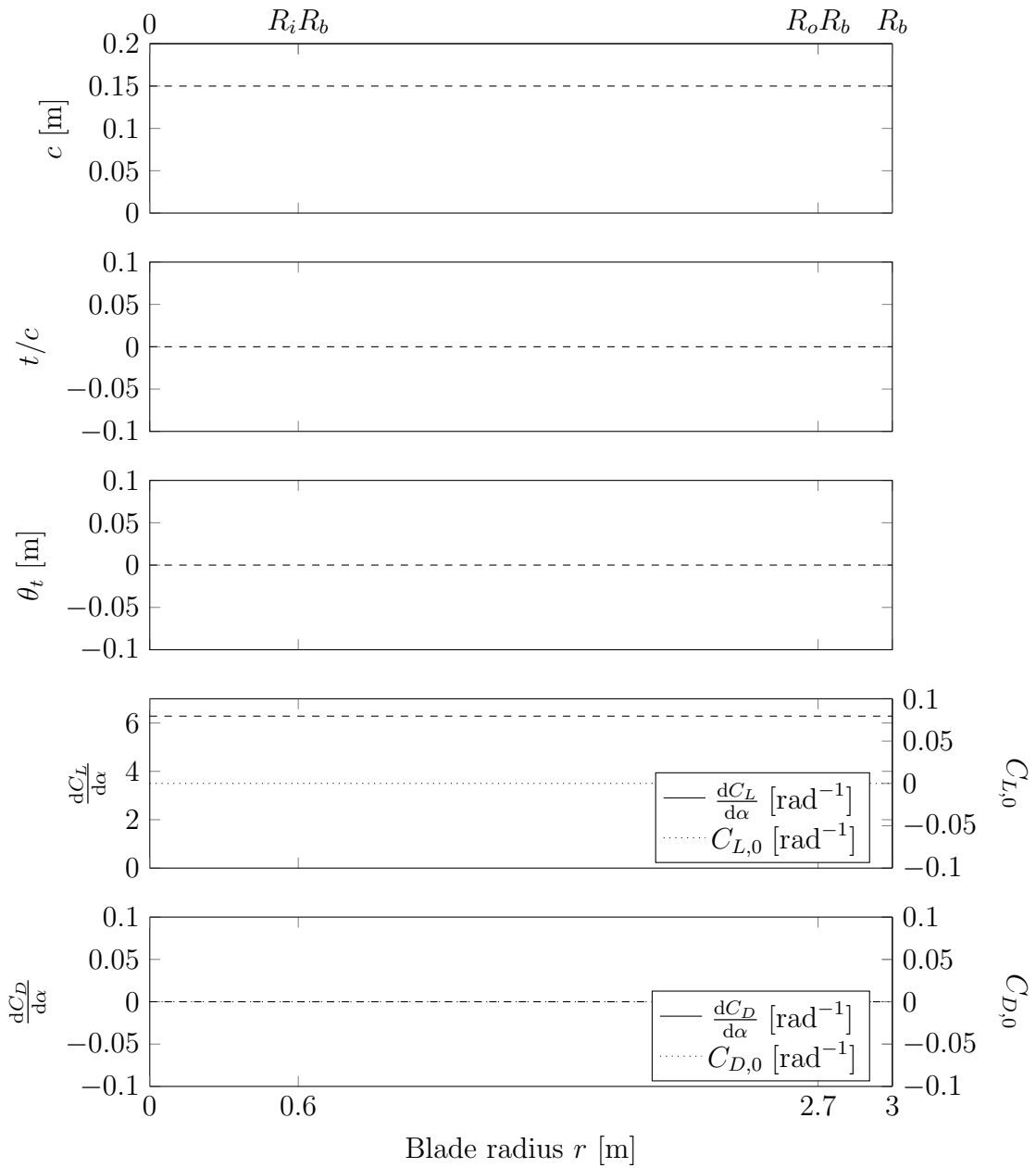


Figure 6.2: Generic aircraft blade profile.

6.2 Test Cases Description

While the 2D version of SRAMSS discussed in this work cannot capture the out-of-plane effects present in a complete 3D simulation, it can be used to verify planar test cases to verify the equations of motion and models included in SRAMSS.

SRAMSS is composed of many complex models which generate a wide variety of dynamic phenomena. The test cases are designed to isolate and address implemented models individually such that the implementation of each model can be independently verified. Additionally, the isolation of the models allows validation against known theories and experimental data.

For this work, there are many models which must be verified:

- the correct implementation of gravity in the gravitational model;
- the forces generated in the external damper model;
- interfacing the rigid airframe to the flexible landing gear, and the dynamic response of the DFE model;
- the appropriately-oriented dynamic response of the contact dynamics model;
- the response of the aircraft in cross-winds and the induced thrust of the rotor disc in the aerodynamic models; and
- and the preliminary design of the skid securing system.

Beyond verification, some of these models can also be validated against known physical theories and experimental data. Static equilibrium can be validated when the aircraft comes to rest, gravitational acceleration can be validated in free fall, and the Rotor BEM can be validated against experimental data where blade geometry is provided since the model exists in 3D.

The test cases developed to evaluate the planar case of SRAMSS are presented in Table 6.5.

Table 6.5: SRAMSS verification and validation test cases

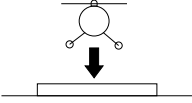
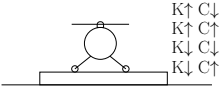
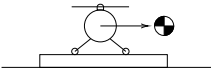
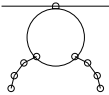
Test Case	Configuration	Objectives	Results
1. Gravitational model		<ul style="list-style-type: none"> • Verify gravitational acceleration and numerical integration implemented correctly. • Verify on-deck deformed steady-state posture. 	<ul style="list-style-type: none"> • Refer to Figure 6.3 in Section 6.3.1 for acceleration plot. • Refer to Table 6.6 in Section 6.3.1 for deformed aircraft values.
2. External damper model		<ul style="list-style-type: none"> • Verify behaviour of aircraft landing with varied damper stiffness and damping parameters. 	<ul style="list-style-type: none"> • Refer to Figures 6.4 through 6.6 in Section 6.3.2 for transient aircraft behaviour.
3. Aircraft CoG		<ul style="list-style-type: none"> • Verify aircraft posture as CoG is shifted horizontally. • Validate load distribution on landing gear and vertical static equilibrium. 	<ul style="list-style-type: none"> • Refer to Figures 6.7 and 6.8 in Section 6.3.3 for airframe roll angles. • Refer to Figure 6.9 in Section 6.3.3 for landing gear load distribution and static equilibrium validation.
4.1 Fixed DFE landing gear		<ul style="list-style-type: none"> • Verify fixed interface node behavior. • Verify implementation of DFE model and damping matrix. • Verify convergence of DFE model with fixed skid landing gear. 	<ul style="list-style-type: none"> • Refer to Figure 6.11 in Section 6.3.4 for aircraft transient behaviour.

Table 6.5: (continued)

Test Case	Configuration	Objectives	Results
4.2 Hinged DFE landing gear		<ul style="list-style-type: none"> • Verify hinged interface node behavior. • Verify convergence of DFE model with hinged, externally-dampened landing gear. • Compare dominance of external damping of hinged landing gear against fixed landing gear. 	<ul style="list-style-type: none"> • Refer to Figure 6.13 in Section 6.3.4 for aircraft transient behaviour.
5.1 Contact normal forces		<ul style="list-style-type: none"> • Verify normal force generation while at rest on polygons. • Validate normal force generation in static conditions. 	<ul style="list-style-type: none"> • Refer to Table 6.9 in Section 6.3.5 for equilibrium force analysis.
5.2 Contact friction forces		<ul style="list-style-type: none"> • Verify the behaviour of LuGre model. • Compare LuGre friction model to simple Coulomb model for progressively-increasing ship roll angle. 	<ul style="list-style-type: none"> • Refer to Figure 6.15 in Section 6.3.5 for sliding velocity plot. • Refer to Figure 6.16 in Section 6.3.5 for transient friction forces plot.
5.3 Oriented dynamic response		<ul style="list-style-type: none"> • Verify appropriately oriented dynamic response of the contact dynamics model. • Verify aircraft–polygon interaction behaves as predicted. 	<ul style="list-style-type: none"> • Refer to Figure 6.18 through 6.20 in Section 6.3.5 for aircraft behaviour plot in different simulation scenarios.

Table 6.5: (continued)

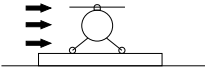
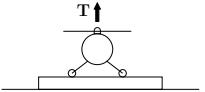
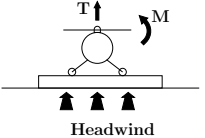
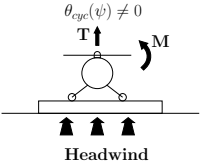
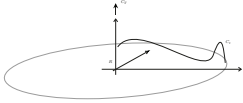
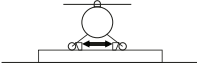
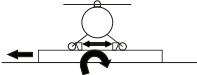
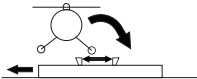
Test Case	Configuration	Objectives	Results
6.1 Aerodynamic body drag forces		<ul style="list-style-type: none"> • Verify aerodynamic drag forces in horizontal direction due to relative wind. • Verify aerodynamic drag forces in vertical direction due to air resistance. 	<ul style="list-style-type: none"> • Refer to Figure 6.21 in Section 6.3.6 for translational velocities plot. • Refer to Figure 6.22 in Section 6.3.6 for vertical acceleration plot.
6.2 Rotor thrust without wind		<ul style="list-style-type: none"> • Verify that the BEM is implemented correctly. • Verify aircraft will generate uniform thrust in zero wind conditions. 	<ul style="list-style-type: none"> • Refer to Figure 6.23 in Section 6.3.6 for thrust and vertical displacement plots. • Refer to Figure B.1 in Section B.1 for the time-varying BEM parameters.
6.3 Rotor thrust with head-wind		<ul style="list-style-type: none"> • Continuation of BEM verification. • Verify non-uniform thrust and moment generation in headwinds. 	<ul style="list-style-type: none"> • Refer to Figure 6.24 in Section 6.3.6 for thrust, rolling moment, and airframe displacement plots. • Refer to Figure B.2 in Section B.2 for the time-varying BEM parameters.
6.4 Rotor thrust with head-wind and cyclic compensation		<ul style="list-style-type: none"> • Continuation of BEM verification. • Verify cyclic pitch setting compensation on retreating blades side generates enough thrust to counter rolling moment on aircraft in the same test environment as Sub-case 6.3. • Refer to Figure B.3 in Section B.3 for the time-varying BEM parameters. 	<ul style="list-style-type: none"> • Refer to Figure 6.25 in Section 6.3.6 for thrust, rolling moment, and airframe displacement plots.

Table 6.5: (continued)

Test Case	Configuration	Objectives	Results
6.5 BEM validation		<ul style="list-style-type: none"> • Validate BEM model against CFD simulations and experimentally obtained data • Refer to Figure C.3 and Table C.1 in Section C.2 for the BEM parameters. 	<ul style="list-style-type: none"> • Refer to Figure 6.26 in Section 6.3.6 for blade sectional thrust coefficients comparison. • Refer to Figures 6.28 6.27 and in Section 6.3.6 aircraft figure of merit comparison.
7.1 Static aircraft securing		<ul style="list-style-type: none"> • Verify implementation of RSD deck securing device. • Verify aircraft's response to securing mechanism under static conditions. 	<ul style="list-style-type: none"> • Refer to Figures 6.30 through 6.32 in Section 6.3.7 for securing performance in static scenarios.
7.2 Dynamic aircraft securing		<ul style="list-style-type: none"> • Verify aircraft's response to securing mechanism under dynamic conditions. 	<ul style="list-style-type: none"> • Refer to Figures 6.34 and 6.35 in Section 6.3.7 for securing performance in dynamic scenarios. • Refer to Figures 6.36 and 6.37 in Section 6.3.7 for securing device contact node loads.
8. Comprehensive Dynamic Phenomena		<ul style="list-style-type: none"> • Verify aircraft behavior under fully-dynamic conditions. • Verify collision behavior with multiple objects (RSD and ship deck). • Compare impact of DFE and BEM mesh refinements. • RSD deck and aircraft have non-zero initial velocity conditions. • Refer to Figure D.1 and D.2 in Section D for the time-varying BEM parameters, and polygon prescribed motion. 	<ul style="list-style-type: none"> • Refer to Figure 6.38 in Section 6.3.8 for significant simulation event animations. • Refer to Figure 6.39 in Section 6.3.8 for airframe response. • Refer to Figures 6.40 through 6.41 in Section 6.3.8 for securing performance and contact node loads in dynamic scenarios. • Refer to Figure 6.39 in Section 6.3.8 for rotor disc forces.

6.3 Test Cases Verification and Validation

The following sections present the observations and results for each set of test cases, and discuss their relevance to verification and validation of the planar case of SRAMSS.

6.3.1 Case 1: Gravitational Model

The first test case is a level drop from 0.8 m of the generic aircraft towards the RSD deck with zero-velocity initial conditions. Aerodynamic models and contact friction models are turned off for this test case. Figure 6.3 shows the airframe's CoG position as the solid line, acceleration as the dot-dashed line, and gravitational acceleration as the dotted line. While in the air, the aircraft maintains a downwards acceleration of 9.81 m/s^2 . When the aircraft's CoG falls below 0.5500 metres (in contact with RSD deck) the acceleration value deviates from 9.81 m/s^2 . At steady-state, the acceleration settles to 0 m/s^2 . This test verifies the correct implementation of gravity.

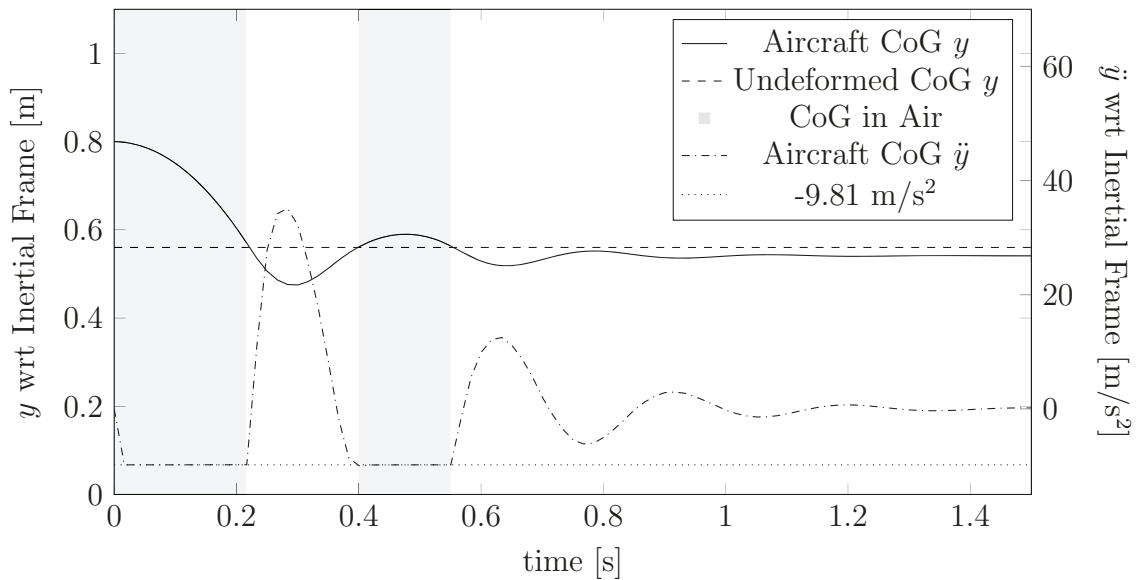


Figure 6.3: Aircraft CoG y -position and y -acceleration with respect to the inertial frame. The dashed line is the height of the aircraft body CoG resting on a level 0.1 metres thick RSD deck with respect to the inertial frame, with an undeformed landing-gear.

The root-finding function implemented into the ODE solver is also verified to be implemented correctly as the deviations in acceleration occur exactly at times where contact and release from contact occur in the raw generalized solution data.

Once steady state is achieved as the aircraft rests on the RSD deck, as shown in Table 6.6, the increase in distances of the landing gear feet (in the x direction) from undeformed to steady-state confirms an outward-splayed stance of the landing gear. The resting height of the CoG at steady-state also decreased which is expected from a splayed landing gear deforming under the weight of the aircraft.

Table 6.6: Case 1 Undeformed versus steady-state helicopter posture

DoF	Underformed [m]	Steady-state [m]
aircraft CoG x	0.0000	8.08E-7
aircraft CoG y	0.5500	0.5411
Left Foot x	-0.3500	-0.3687
Left Foot y	0.1100	0.1098
Right Foot x	0.3500	0.3687
Right Foot y	0.1100	0.1098

Case 1 verifies that the gravitational model from Equations 4.108 and 4.109 is implemented correctly such that a free-falling aircraft with no air-resistance falls downwards (with respect to the inertial frame) with an acceleration equal to the gravitational acceleration constant g . The test case also indicates proper detection of node contact with the RSD deck polygon, and appropriately-oriented upwards normal forces to maintain impenetrability of the polygon.

6.3.2 Case 2: External Damper Model

With Case 1 having verified contact response with the RSD deck, more complex test cases can be performed. The discrete external dampers play an important role during the aircraft's touch-down phase. It is expected that variation in damper constants K_d and C_d will generate different transient responses during touchdown. For Case 2, the aerodynamic models and contact friction model remain turned off to isolate the aircraft collision response from the external dampers. Figures 6.4 through 6.6 show the transient response of the airframe and contact nodes as the stiffness and damping parameters of the external dampers are varied. The parameters used for Case 2 are presented in Table 6.7.

As expected, in Figure 6.4 the higher stiffness coefficient $K_d \uparrow$ generates a contact response with larger magnitudes in the oscillations during contact for all bodies and

Table 6.7: Case 2 Discrete damper parameter variations

Parameter	Value
$K_d \uparrow$	40 000 N/m
$K_d \downarrow$	25 000 N/m
$C_d \uparrow$	500 Ns/m
$C_d \downarrow$	200 Ns/m

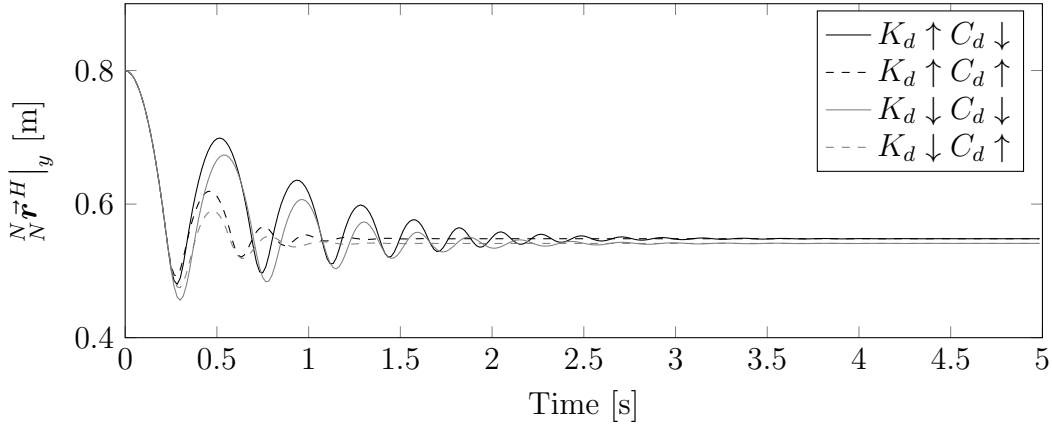


Figure 6.4: Case 2 Airframe vertical response due to discrete external linear damper property variation.

for higher damping coefficient $C_d \uparrow$ steady-state was achieved faster due to greater damping response to collision. Further, the steady-state height of the airframe CoG in Figure 6.4 is lower for $K_d \downarrow$ which agrees with the notion that with a lower stiffness coefficient, the external damper, and therefore the landing gear, must deflect more to generate an equal amount of force.

Overall, the variation in stiffness and damping parameters show the expected responses. As observed in Figure 6.4, the variation in the damping coefficient affects the damping ratio from apparent log decrements, and the variation of the stiffness coefficient affects the frequency of the oscillations.

The touch-down responses presented in Case 2 verify that the linear external dampers behave as expected when their stiffness and damping parameters are modified, and the symmetrical response at the contact nodes in Figure 6.6 indicates that the general formulas for the external damper forces (Equations 4.106 and 4.103) are implemented correctly for arbitrary external damper configuration.

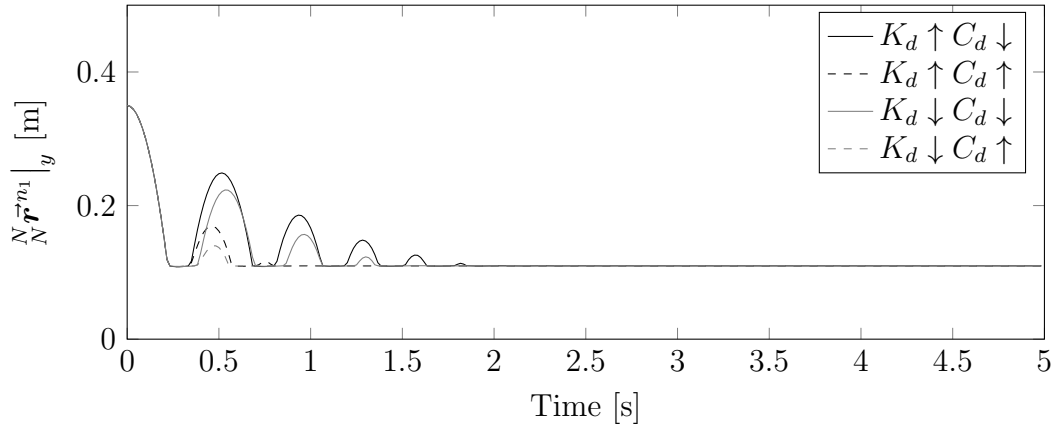


Figure 6.5: Case 2 Landing gear vertical response due to discrete external linear damper property variation.

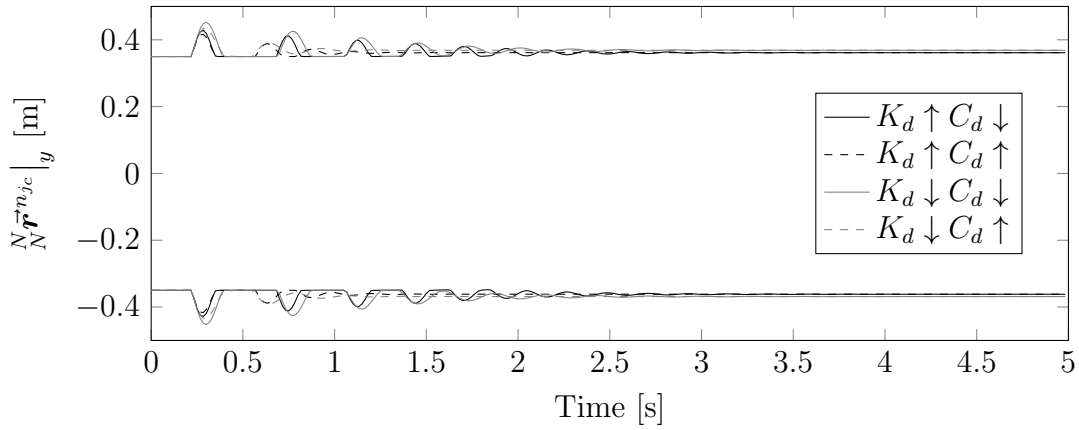


Figure 6.6: Landing gear horizontal response due to discrete external linear damper property variation. Upper data set corresponds to the right landing gear foot n_1 , while the lower data set corresponds to the left landing gear foot n_6 .

6.3.3 Case 3: Aircraft Centre of Gravity

The previous test cases verified level aircraft response for an airframe with a CoG centered between the two landing gear legs. For Case 3, the airframe CoG is horizontally shifted to verify steady-state roll posture, and static equilibrium for asymmetrical loading at the landing gear feet. The aerodynamic models and contact friction model remain turned off for Case 3.

Figure 6.7 shows the transient roll angle response of the airframe for each CoG position as the aircraft settles on the RSD. Figure 6.8 presents the steady-state roll posture of the airframe as a function of the horizontal shift in position of the airframe CoG.

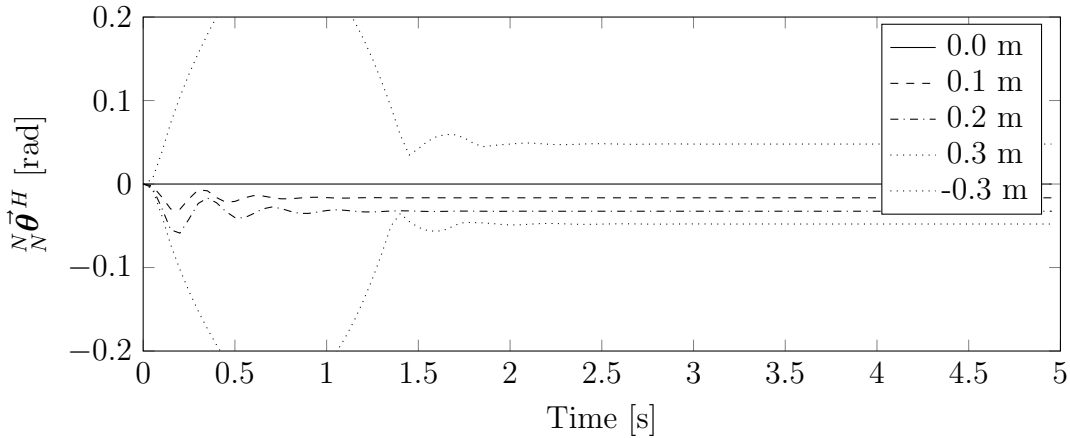
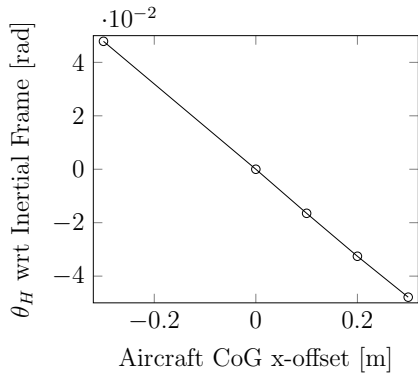


Figure 6.7: Airframe roll-angle response to shifted CoGs. Significant initial roll angles in the ± 0.3 m offsets result from the aircraft rolling onto a single landing gear foot upon initial contact with the ground.

The results from Figures 6.7 and 6.8 show that the airframe roll angle at steady-state increases as the airframe CoG is shifted. This verifies the expected behavior for the generic aircraft. As the CoG is shifted further over one side of the hinged landing gear, that landing gear leg assumes more of the load which increases damper compression and lowers that side of the aircraft, resulting in airframe roll. Notably in Figure 6.8, the roll angles at ± 0.3 m are identical, further verifying the implementation of the damper model and hinged airframe interface.

Preliminary validation of the normal forces against basic statics theory is also feasible. Data presented in Figure 6.9 shows that static equilibrium in the vertical direction in inertial frame is satisfied. Airframe and landing gear weights are calculated



(a) Plotted Data

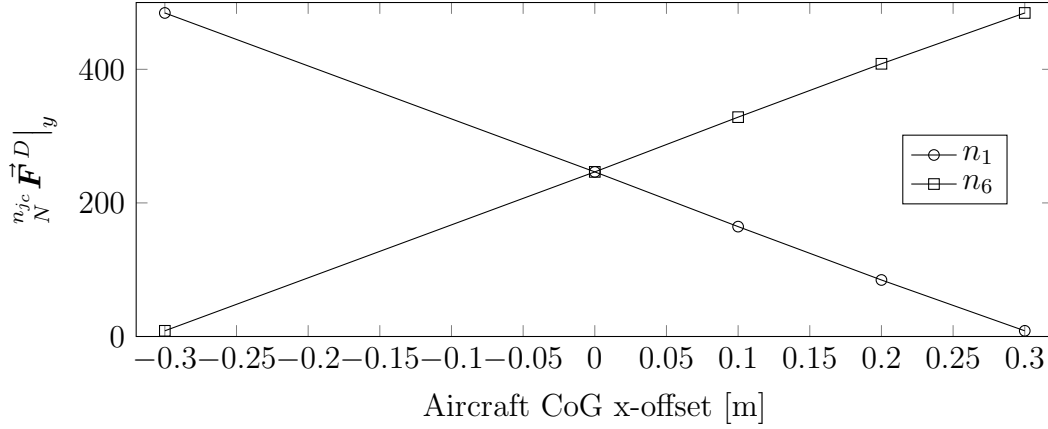
x-offset [m]	θ_H Roll [rad]
-0.3000	0.0479
0.0000	5.74E-10
0.1000	-0.0165
0.2000	-0.0326
0.3000	-0.0479

(b) Tabulated Data

Figure 6.8: Case 3 Steady-state aircraft roll versus airframe CoG x-offset.

from Equations 4.108 and 4.109 transformed to the inertial frame.

In summary, Case 3 verifies the effects of airframe CoG offset on the posture of the aircraft. The airframe rolls in the expected direction as the CoG is shifted. Case 3 also validates the gravitational model and the contact normal forces model under static equilibrium conditions.



(a) Plotted data

CoG Offset [m]		-0.3	0.0	0.1	0.2	0.3
$\frac{n_1}{N} \vec{F}^D _y$ [N]	+	485.71	246.42	164.05	83.71	7.13
$\frac{n_6}{N} \vec{F}^D _y$ [N]	+	7.13	246.42	328.79	409.13	485.71
Airframe [N]	-	490.50	490.50	490.50	490.50	490.50
L.G. [N]	-	2.34	2.34	2.34	2.34	2.34
$\sum F_y$ [N]	=	0.00	0.00	0.00	0.00	0.00

(b) Tabulated Data

Figure 6.9: Case 3 Contact node normal forces versus airframe CoG offset.

6.3.4 Case 4: Landing Gear DFE Model

This test case verifies the implementation of the DFE model for fixed and hinged landing gear. The sub-cases for each interface configuration are composed of four level-drop simulations from 0.8 m, where contact friction, and aerodynamic models are turned off. For these sub-cases, the DFE model parameters are modified to exaggerate the behavior of the landing gear during contact. Modified parameters are presented in Table 6.8.

Between each drop test the DFE mesh is also progressively refined. The generic aircraft's landing gear DFE mesh has 6-node, 10-node, 14-node, and 18-node configurations as shown in Figure 6.10. For the hinged configurations, the external dampers are attached to the middle node on each side.

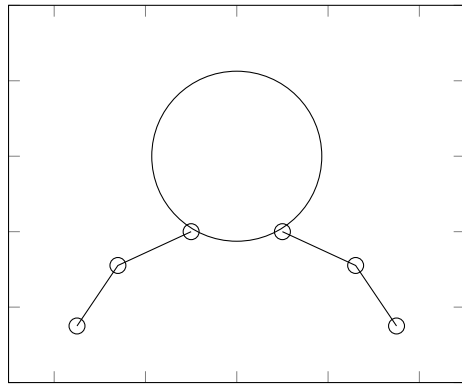
Table 6.8: Modified DFE model parameters for use in Case 4

Parameter	Variable	Value
Element young's modulus	E	6.9×10^{10} Pa
Element second moment of area	I	5.44×10^{-9} m ⁴
Element density	ρ	2710 kg/m ³
Element cross section	A	3.02×10^{-4} m ²
Rayleigh damping lower frequency	ω_1	0 rad/s
Rayleigh damping lower damping Ratio	ξ_1	0.05
Rayleigh damping upper Frequency	ω_2	mesh dependent
Rayleigh damping upper damping ratio	ξ_2	0.10
Skid-tube cross-section radius		0.01 m

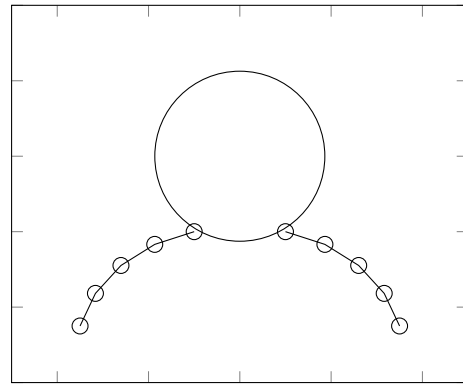
Case 4.1 Fixed interface

Figure 6.11 plots the transient vertical behavior of the airframe and left contact node during the drop tests for the fixed landing gear. The right foot contact node has the same magnitude of values as the left foot. The plots show that there is energy dissipation in the system between each impact with the RSD deck. This verifies that the proportional damping matrix $[\mathbf{C}]$ is working as intended.

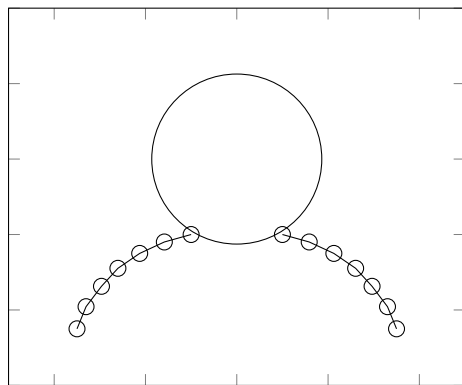
Between all DFE meshes, it is difficult to determine if the results converge as is expected for h-method (mesh density) refinement. Yet, if only the 6-, 10-, and 18-node meshes are considered, Figure 6.11 indicates the beginning of convergence in results as the mesh density increases. This is most probably due to the alignment of the common nodes between these DFE meshes as shown in Figure 6.12. The mode shapes of coarser meshes can be expressed as the linear combination of the mode shapes of finer meshes. Moreover, the total structure proportional damping matrix is derived from the superposition of mode damping. Hence, the observed converging behavior as the DFE model is refined from 6, 10, to 18 nodes. The 14-node model has a different set of eigenvalues due to mesh construction, therefore different mode shapes, and more importantly, slightly different values for ω_1 and ω_2 as a result.



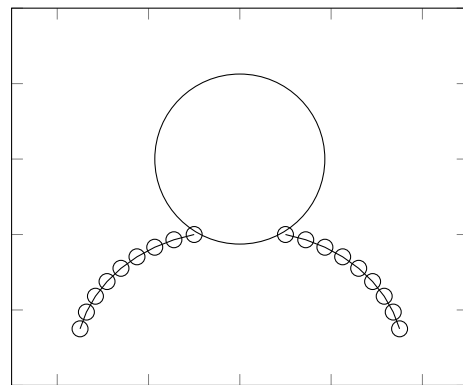
6 nodes, $N_n = 6$



10 nodes, $N_n = 10$



14 nodes, $N_n = 14$



18 nodes, $N_n = 18$

Figure 6.10: Case 4 DFE model mesh configurations.

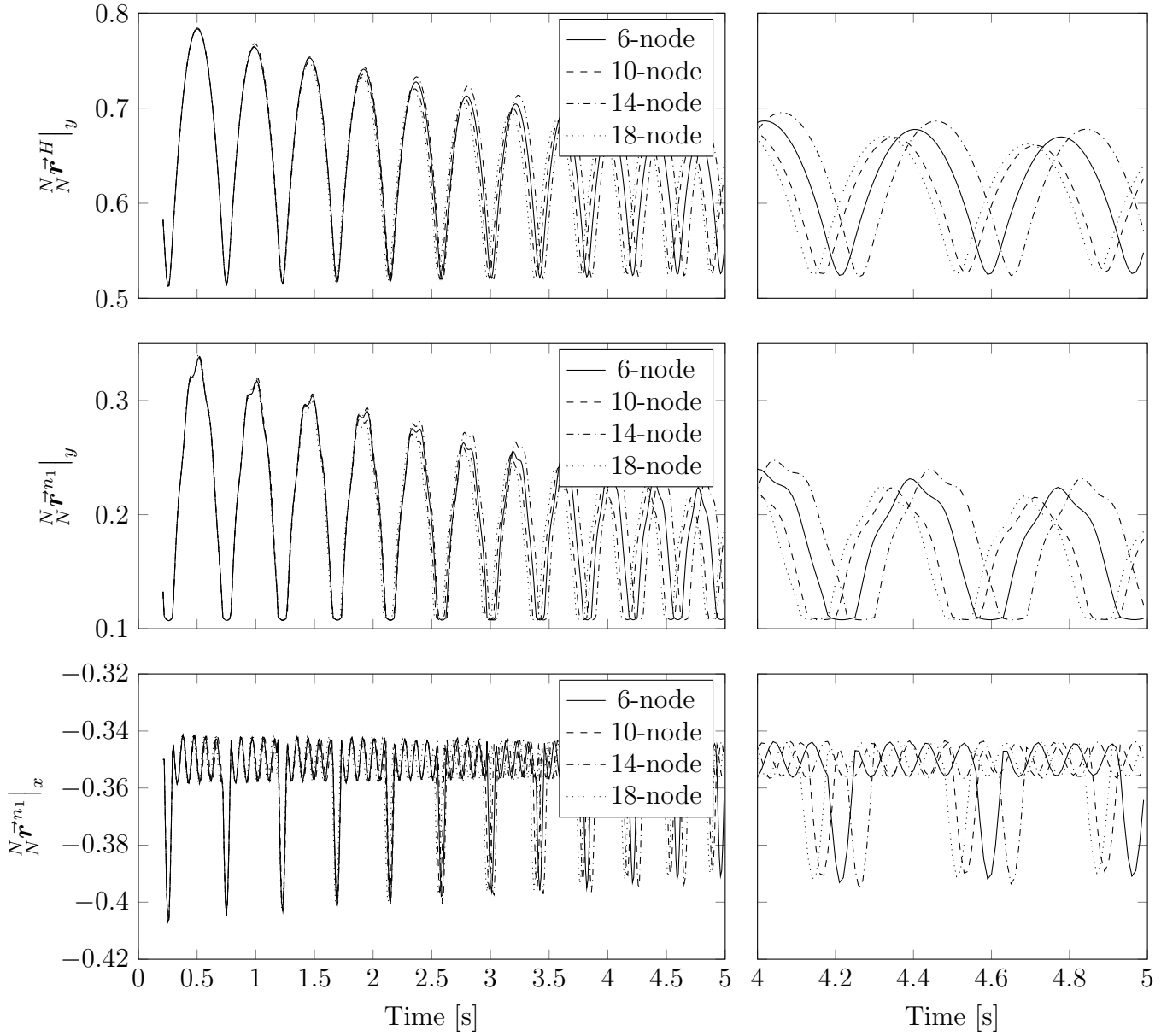


Figure 6.11: Case 4.1 Aircraft response for fixed landing gear with DFE model mesh refinements.

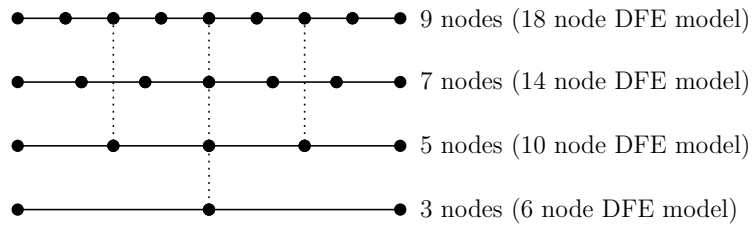


Figure 6.12: Case 4.1 DFE model node construction.

Case 4.2 Hinged interface

Figure 6.13 plots the transient vertical behavior of the airframe and left contact node during the drop tests for the hinged landing gear. As the left column of plots show, the energy is dissipated faster through the compression of the external dampers compared to fixed interface landing gear. Due to the hinged interface, the pivoting of the landing gear about this point dominates the deflection in the DFE model. As such, it is not as sensitive to the definition of the DFE mesh as the fixed interface in Sub-case 4.1. Figure 6.13 shows that the results have effectively converged for the 10-, 14-, and 18-node meshes. Therefore, with external dampers, coarser meshes can be used to increase simulation performance.

Sub-cases 4.1 and 4.2 verify the implementation of the DFE model for the skid-type landing gear. First, the aircraft response has verified the correct implementation of Equations 4.90 and 4.91 for fixed and hinged interfaces, and the complete assembly and manipulation of rigid and flexible body dynamics of Section 5.1. Second, the sub-cases have shown that energy is dissipated with each successive impact, which has verified the implementation of a dynamic finite element model which includes damping component. Lastly, the sub-cases have verified the expected convergence through h-method refinement. Though, as Figure 6.11 has shown, fixed-interface landing gear are sensitive to their DFE mesh definitions.

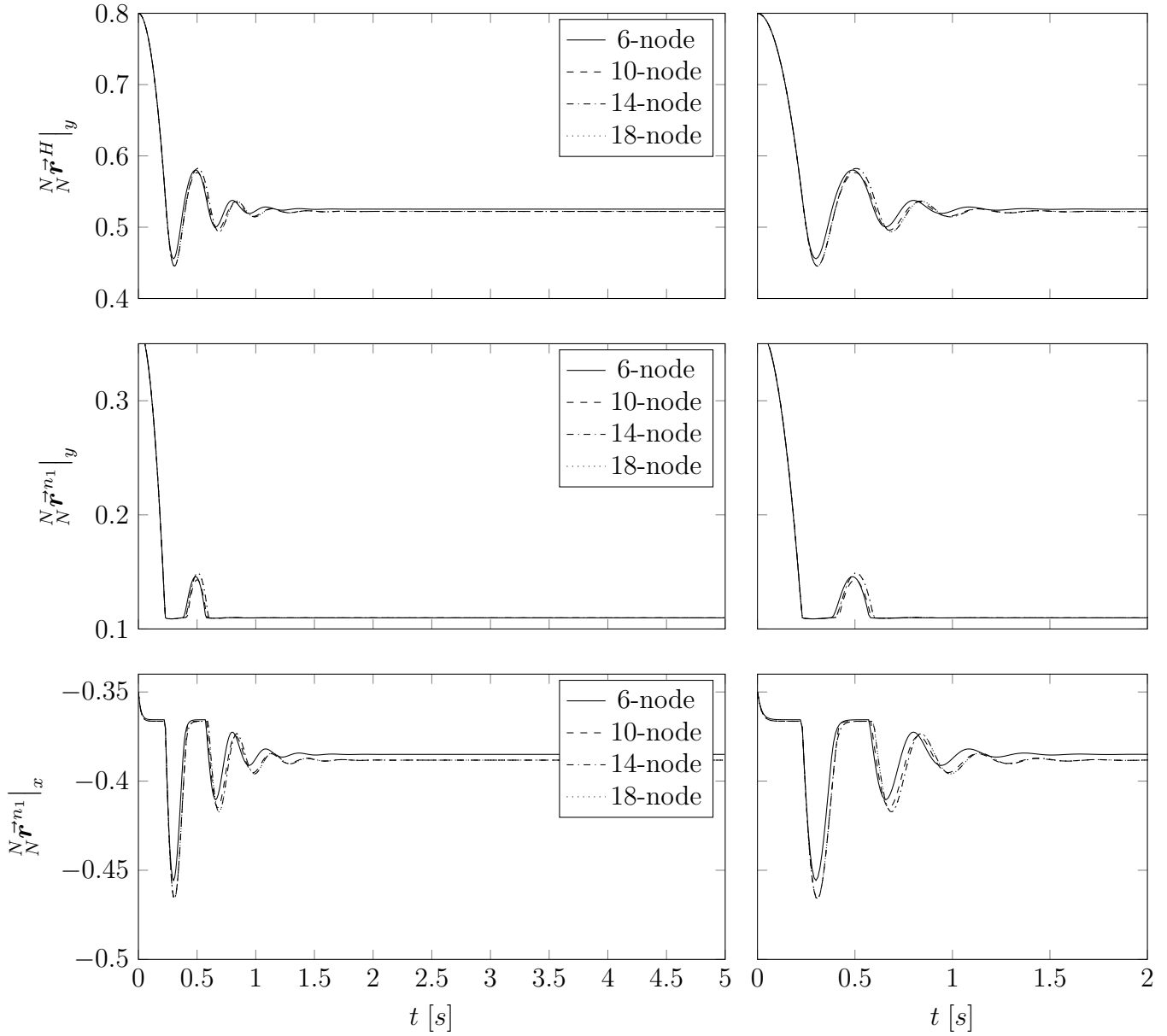


Figure 6.13: Case 4.2 Aircraft response for hinged landing gear with DFE model mesh refinements.

6.3.5 Case 5: Contact Dynamics Model

The contact dynamics model is the core model in SRAMSS. It forms the basis for aircraft-ship interactions and thereby enabling dynamic interface analysis. Case 5 is divided into three sub-cases which independently evaluate normal forces, friction forces, and finally the complete oriented dynamic response.

Case 5.1 Contact Normal Forces

Similarly to Case 3, Sub-case 5.1 verifies and validates the generation of normal forces under static conditions. Four simulations are performed with configurations as shown in Figure 6.14. For each simulation, the aircraft is dropped onto the ship, and sufficient time is allowed to achieve steady-state rest on deck. Once more, the friction and aerodynamic models are turned off for these simulations.

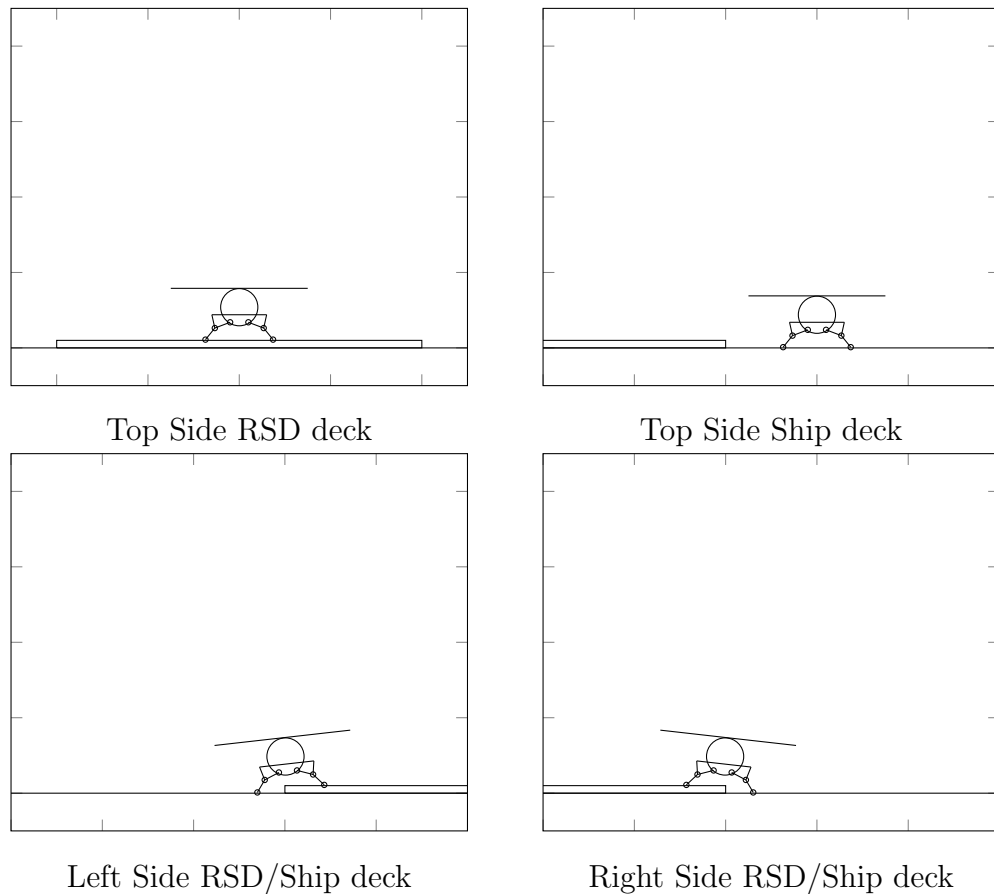


Figure 6.14: Case 5.1 Steady-state simulation configurations for normal force evaluation.

After 5 seconds of elapsed simulated time, the aircraft is considered to be at rest on deck. At this time, the contact normal forces are evaluated. For each simulation, the contact normal forces are listed in Table 6.9. Once more, static equilibrium is validated.

Table 6.9: Case 5.1 Contact normal forces at static equilibrium

Test		RSD deck	Ship deck	L RSD/ship	R RSD/Ship
$\frac{n_1}{N} \vec{F}^c _y$ [N]	+	246.42	246.42	280.01	212.82
$\frac{n_6}{N} \vec{F}^c _y$ [N]	+	246.42	246.42	212.82	280.01
Airframe [N]	–	490.50	490.50	490.50	490.50
L.G. [N]	–	2.34	2.34	2.34	2.34
$\sum F_y$ [N]	=	0.00	0.00	0.00	0.00

Case 5.2 Contact Friction Forces

As part of the oriented dynamic response to contact, a friction force is applied to the landing gear nodes parallel to the contact surface. The flexibility of the contact mechanics algorithm in SRAMSS allows many friction models to be used. Currently, the LuGre model has been implemented. The LuGre model can also be reduced to a simple Coulomb frictional slider model by equating $\mu_s = \mu_d$.

In the Sub-case 5.2 simulations, for a generic aircraft at rest on deck, the ship’s roll angle is increased through the point where the aircraft begins to slide across the ship deck. This case verifies that the generic aircraft begins to slide at a ship roll angle $\frac{N}{N} \vec{\theta}^S = \tan^{-1} \mu$.

For Sub-case 5.2, friction parameters have been modified to capture the desired phenomena before the aircraft’s roll-over point is reached. The modified parameters of Table 6.1 are found in Table 6.10.

Given the parameters from Table 6.10, the aircraft is predicted to roll at $\frac{N}{N} \vec{\theta}^S = -0.3806$ radians using the LuGre model, and $\frac{N}{N} \vec{\theta}^S = -0.1974$ radians using the Coulomb model.

Figure 6.15 shows the relative sliding velocity of the leading landing gear foot, DFE node n_6 . As expected, the aircraft begins sliding at a larger ship roll angle for the LuGre model since it is able to model static friction. Figure 6.15 also confirms the

Table 6.10: Modified aircraft simulation parameters for use in Sub-case 5.2

Parameter	Variable	Value
Friction micro-displacement stiffness	K_f	1×10^6 N/m
Friction micro-displacement damping	C_f	1×10^4 Ns/m
Stribeck velocity threshold	v_s	0.01m/s
Dynamic friction coefficient (LuGre)	μ_d	0.2
Static friction coefficient (LuGre)	μ_s	0.4
Dynamic friction coefficient (Coulomb)	μ_d	0.2
Static friction coefficient (Coulomb)	μ_s	0.2

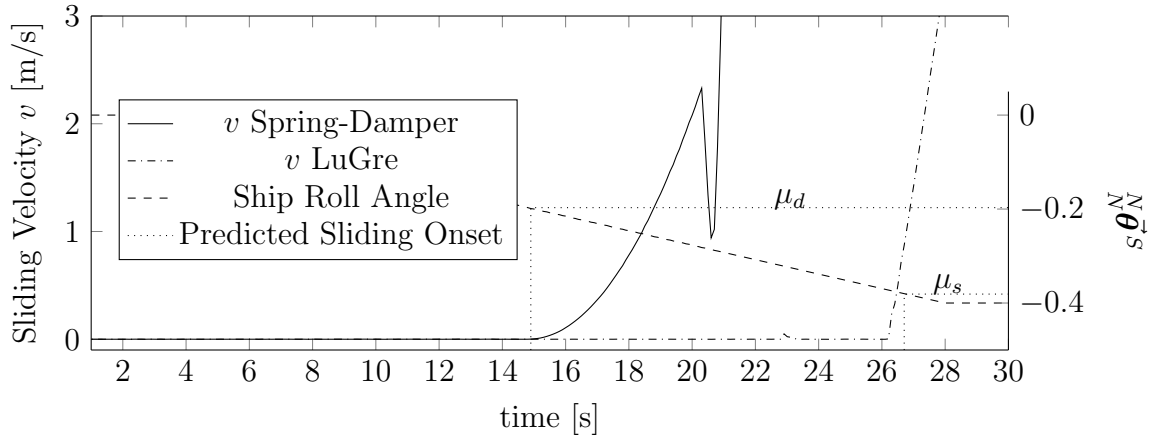


Figure 6.15: Case 5.2 Sliding velocity of leading (right) landing gear foot along the RSD deck as the roll angle of the ship increases.

predicted roll angle -0.1974 radians for the Coulomb model. The drop in Coulomb sliding velocity after 20 seconds is an artifact of the aircraft falling off the ship deck.

However, the LuGre model lets the aircraft slip at -0.3724 radians, earlier than predicted. The trailing foot (n_1) exhibits stick-slip behavior as indicated by the oscillating friction value in Figure 6.16. These oscillations are the result of weight transfer from the trailing to leading foot (n_6) due to a reduction in normal force at the trailing foot. This is apparent from the decreasing values of F_d and F_s for n_1 , and increase for n_6 . The drop in friction force on n_1 shifts the aircraft, which increases the friction force generated by the frictional slider of n_6 . Immediately before slipping around 26 seconds, the third weight transfer to n_6 saturates F_{LuGre} to F_s . The maximum frictional slider distance (bristle deflection) $\Delta_{f,max}$ allowed by Stribeck equation (Eq. 4.49) is achieved. No greater frictional force can be generated to maintain the

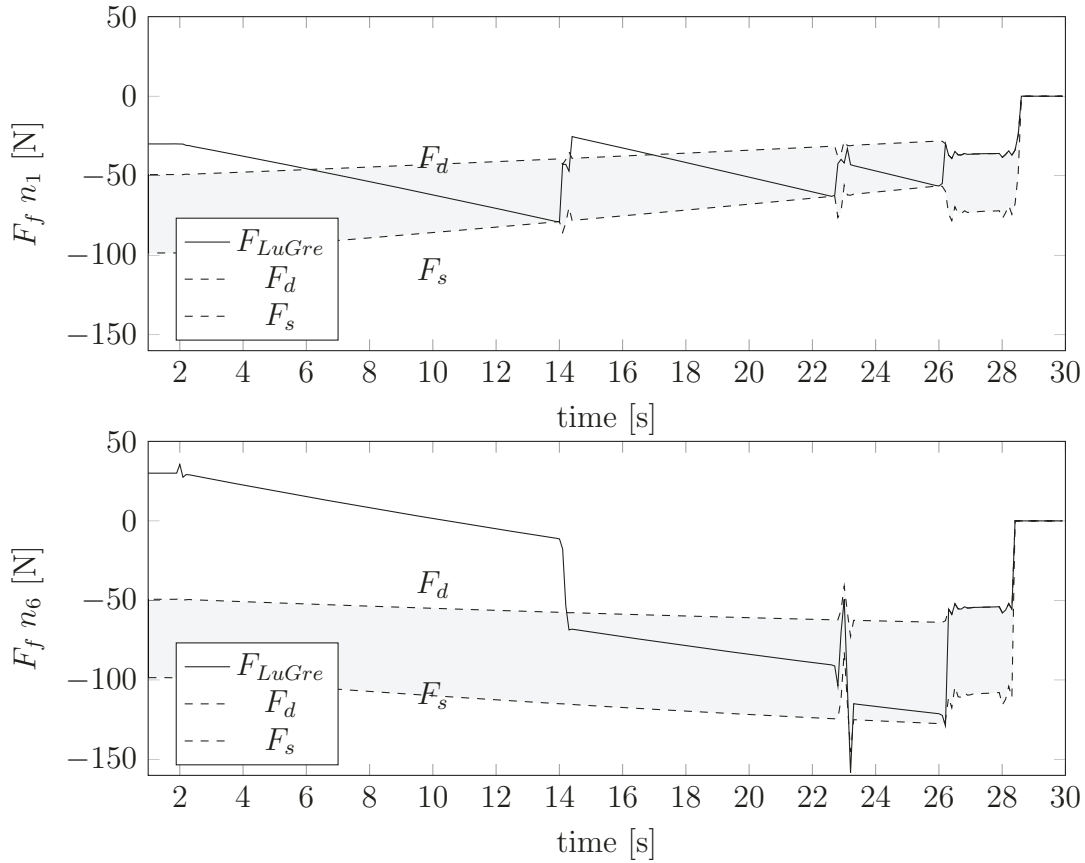


Figure 6.16: Case 5.2 Trailing (n_1) and leading (n_6) landing gear foot frictional forces

aircraft's position on deck, thus it begins to slide pre-maturely.

While the LuGre model does not exactly verify the prediction, the predicted value does not consider transient phenomena which dynamically varies the upper limit of static friction. In any case, the implementation of the LuGre model can still be verified. Through the Stribeck equation, the maximum friction force is dynamically tuned to exhibit static and dynamic friction phenomena. In Figure 6.16, F_{LuGre} is allowed to grow as required to maintain the aircraft's position. Once F_{LuGre} saturates to the maximum allowable static friction F_s , sliding occurs. At the onset of sliding, F_{LuGre} immediately drops to the dynamic friction value F_d . This verifies that both static and dynamic friction phenomena of the LuGre model are implemented correctly.

The parameters used for this sub-case are arbitrary, and tuned to visually show the desired phenomena. True parameters can only be determined through extensive experimental testing. Nevertheless, the LuGre model is verified to capture the friction phenomena predicted.

Case 5.3 Oriented dynamic response

For Case 5, the generation for normal and friction forces has been verified. Response to contact on surfaces other than the top sides of polygons, and when polygons are prescribed non-zero motion remain to be verified.

Oriented dynamic response is verified through three simulations. Each simulation is configured to involve different interactions with a moving RSD deck. A visual description of the simulations is presented in Figure 6.17.

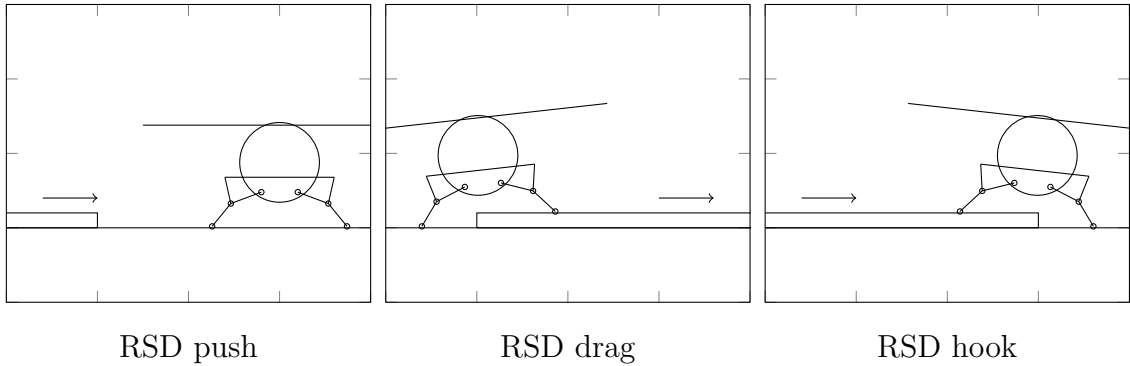


Figure 6.17: Case 5.3 Oriented dynamic response simulation configurations.

For the first simulation, the aircraft starts at rest on the ship deck. The RSD deck is prescribed translational velocity of 0.3 m/s starting at 2 seconds. For this simulation, the aircraft's response is predicted to be pushed along the ship deck through appropriately-oriented normal forces from the side of the RSD deck acting at n_1 .

As shown in Figure 6.18, the aircraft is dropped onto the deck where it comes to rest. At 2 seconds, the RSD deck begins translation. Shortly thereafter, the RSD deck comes into contact with the left foot (n_1). The normal forces generated by the side of the RSD deck overcome the friction forces of the ship deck acting at the contact nodes which allows the RSD deck to push the aircraft along. The 'push' is evidenced by the overlapping 'RSD Right Surface' and $\frac{N}{N} \vec{r}^{n_1} \Big|_x$ plot lines. At 9.4 seconds, the aircraft begins to fall off the ship deck, indicated by the large drop in y -position in Figure 6.18. This simulation verifies the physically-expected response of the aircraft.

The second simulation has the aircraft at rest with the left foot (n_1) on the ship deck and right foot (n_6) on the RSD deck. Again, the RSD deck is prescribed translational velocity of 0.3 m/s starting at 2 seconds. Here, it is expected that the aircraft's response is to be dragged along by friction forces until the aircraft has slipped off the

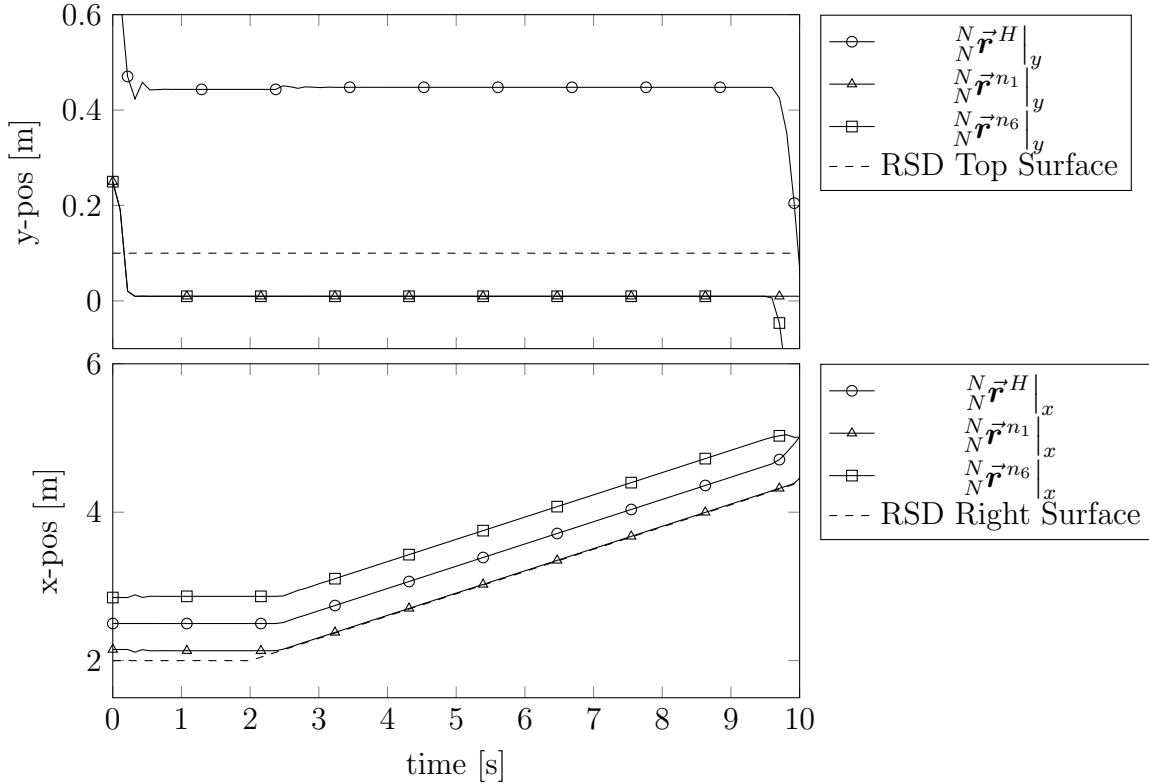


Figure 6.18: Case 5.3 Position of airframe and contact nodes in the ‘RSD push’ scenario.

RSD deck. The slipping is predicted by the weight shift over the left foot, the nodal forces in Table 6.9 support this prediction.

The aircraft response prediction is verified in Figure 6.19. As the RSD deck starts moving, the posture of the landing gear is expanded by friction forces until equilibrium is reached through the external dampers. The drop in y -position for the airframe and n_6 just before 4 seconds indicates that the aircraft has slipped off the RSD deck onto the ship deck. From 2 seconds until the drop off the RSD deck, the translational motion of the RSD deck drags the aircraft along. Due to the higher normal forces on n_1 , and the relative sliding velocity between n_6 and the RSD deck, the friction forces on n_1 are greater. The larger friction force at n_1 allows the aircraft to slide along the ship deck, but not at the same velocity as the translation of the RSD deck. This difference in translational velocities causes n_6 to eventually fall off the RSD deck as previously stated.

For the third simulation of Sub-case 5.3, the aircraft is at rest with the left foot (n_6) on the ship deck and right foot (n_1) on the RSD deck. Again, the RSD deck

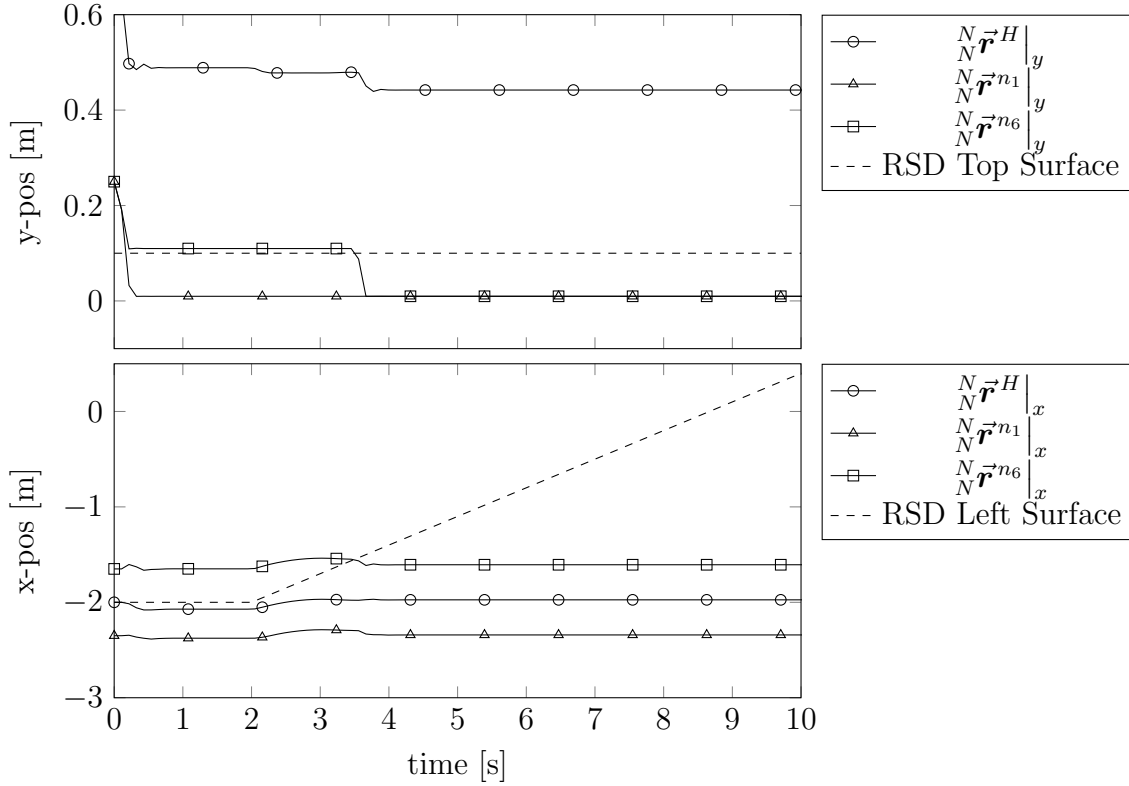


Figure 6.19: Case 5.3 Position of airframe and contact nodes in the ‘RSD drag’ scenario.

is prescribed translational velocity of 0.3 m/s starting at 2 seconds. Opposite to the second case, the predicted response is such that n_1 slides atop the RSD deck until the side of the RSD deck comes into contact with n_6 . At this point, n_6 is hooked into the corner formed by the ship deck and side of the RSD deck. This ‘hook’ will drag the aircraft along at the same rate as the prescribed translational motion of the RSD deck.

Figure 6.20 shows the aircraft coming to rest with the left foot (n_6) on the ship deck and right foot (n_1) on the RSD deck. At the onset of RSD deck translation, the aircraft exhibits a slight translational motion due to the difference in frictional forces. Around 3 seconds, the right side of the RSD deck comes into contact with n_6 resting on the ship deck, the ‘hook’, and begins to drag the aircraft along. The ‘hook’ is evidenced by the overlapping ‘RSD Right Surface’ and $\frac{N}{N} \vec{r}^{n_6} \Big|_x$ plot lines. The aircraft response expressed in this simulation verifies the predictions made.

Through the simulations performed in Sub-cases 5.1, 5.2, and 5.3, the contact dynamics model is verified to be implemented correctly. Regardless of the contact

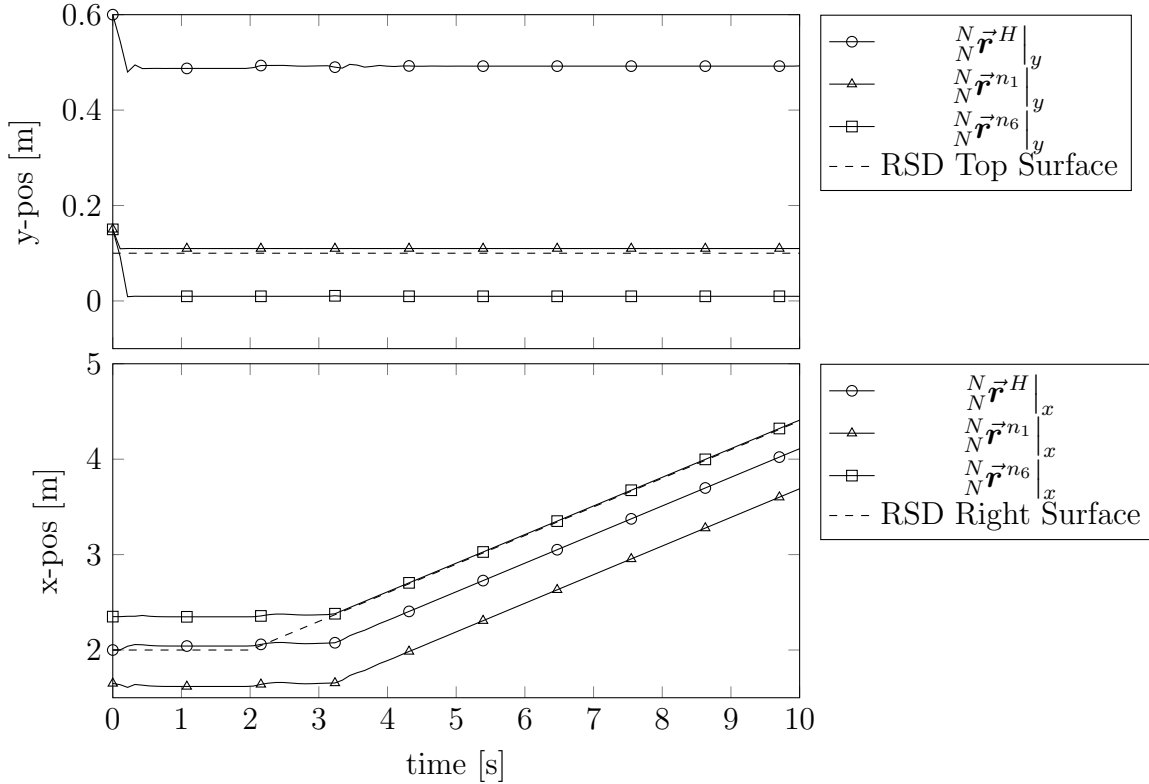


Figure 6.20: Case 5.3 Position of airframe and contact nodes in the ‘RSD hook’ scenario.

surface, the normal and friction forces are appropriately-oriented such that predictable aircraft response is observed in the simulations.

6.3.6 Case 6: Aerodynamics Models

Case 6 focuses on the verification of the aerodynamic body drag models, and BEM model for rotor thrust. This case is divided into four sub-cases verifying the aerodynamic drag model; rotor thrust without wind; rotor thrust with cross-wind; and rotor thrust with cross-wind and cyclic setting compensation. Additionally, there is preliminary validation of the BEM model against published CFD data.

Case 6.1 Aerodynamic Body Drag Model

In this sub-case, implementation of the aerodynamic model is verified. The aerodynamic body drag model, presented in Equations 4.58 through 4.64, is developed in three dimensions. For the planar verification of the model, drag forces induced by

relative wind velocity in the N frame x and y directions are evaluated.

For the x -direction, cross-winds are applied to the aircraft at rest on the RSD deck. For this test, the friction model is turned off to isolate the effects of aerodynamic drag. Between 1.0 and 1.5 seconds in simulation time, the cross-wind velocity is linearly increased from 0 m/s to the prescribed value.

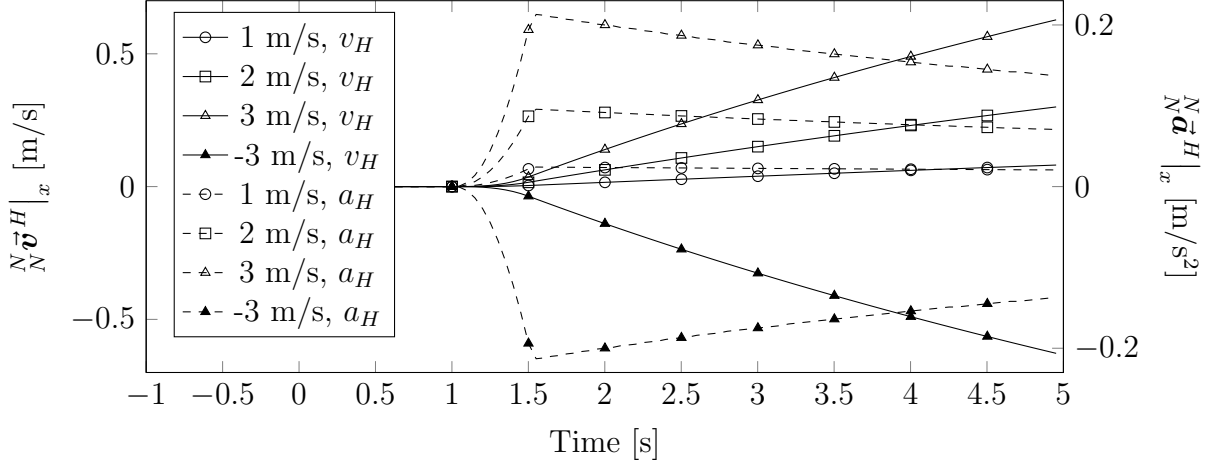


Figure 6.21: Case 6.1 Aircraft horizontal sliding velocity due to induced drag.

The sliding velocity and acceleration of the aircraft under different cross-wind velocity conditions is presented in Figure 6.21. As expected, an increase in the wind velocity increases the rate of sliding velocity of the aircraft. The aircraft exhibits large initial accelerations at the onset of sliding. As the aircraft's sliding velocity increases, its acceleration decreases since the relative wind speed with respect to the CP is decreasing.

A simple force balance verifies that the aerodynamic drag formula in Equation 4.63 is implemented correctly. For a cross-wind speed of 3 m/s at simulated time of 3 seconds and total aircraft mass of 50.2383 kg, the aircraft's sliding velocity is 0.3262 m/s with an acceleration of 0.1745 m/s².

$$\sum F_x = ma_x$$

where

$$\begin{aligned} ma_x &= (m_H + [M]_x) a_x = (50.2383 \text{ kg})(0.1745 \text{ m/s}^2) = 8.7666 \text{ N} \\ \sum F_x &= \frac{1}{2} \rho \mathbf{A}_x (C_H^{CP} \vec{v}^W|_x)^2 \\ &= (0.5)(1.225 \text{ kg/m}^3)(2 \text{ m}^2) (3 \text{ m/s} - 0.3262 \text{ m/s})^2 = 8.7578 \text{ N} \end{aligned}$$

Interpolation within raw simulation data to obtain sliding acceleration, and slight aircraft roll due to the $\frac{H}{H}\vec{r}^{CP}$ should account for the error in the calculations above.

In the y direction test, the aircraft is dropped towards the RSD deck from a height of 0.8 metres. Cross-winds are set to 0 m/s and the friction model is turned off.

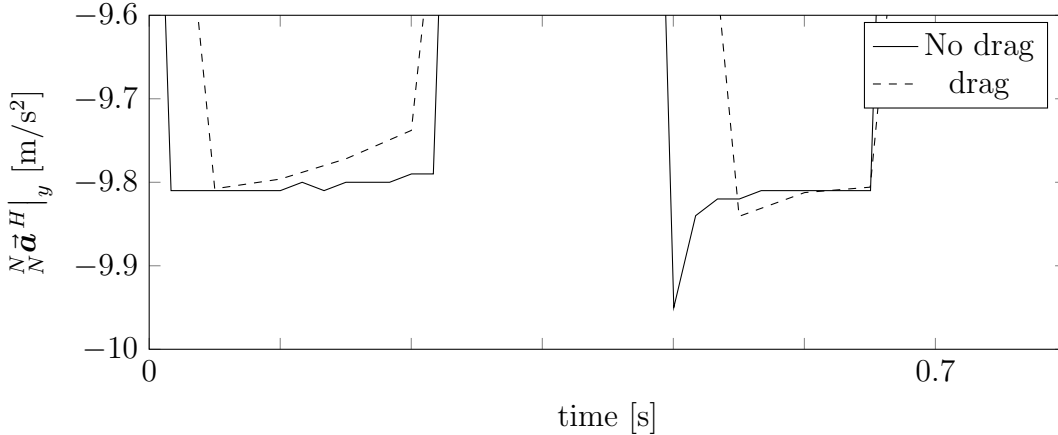


Figure 6.22: Case 6.1 Aircraft vertical acceleration due to induced drag.

Figure 6.22 shows the vertical accelerations of the airframe during drop tests with and without aerodynamic body drag. The drop without drag maintains an acceleration equal to gravitational acceleration, whereas the induced drag reduces the vertical acceleration of the aircraft in the other case.

The magnitude and orientation of drag forces in the simulations of Sub-case 6.1 verify that Equation 4.63 is implemented correctly in SRAMSS.

Case 6.2 Rotor Thrust Without Wind

Sub-cases 6.2 through 6.4 evaluate the implementation of the BEM model for rotor disc thrust and roll moment generation. In Sub-case 6.2, the rotor thrust is evaluated for an aircraft beginning at rest on the RSD deck without relative wind across the deck. The number of BEM sectors N_ψ and rotor blade elements N_e is varied between each simulation in Sub-case 6.2. The time-varied parameters for the BEM model are found in Figure B.1 in Appendix B.1. Further, the aerodynamic body drag model is turned off for this test to isolate thrust force and rolling moment acting on the aircraft.

Figure 6.23 shows that rotor disc RPM increase from 0 rad/s to 135 rad/s from 2 to 6 seconds increases rotor disc thrust from 0 N to nearly 600 N. Since there is no relative

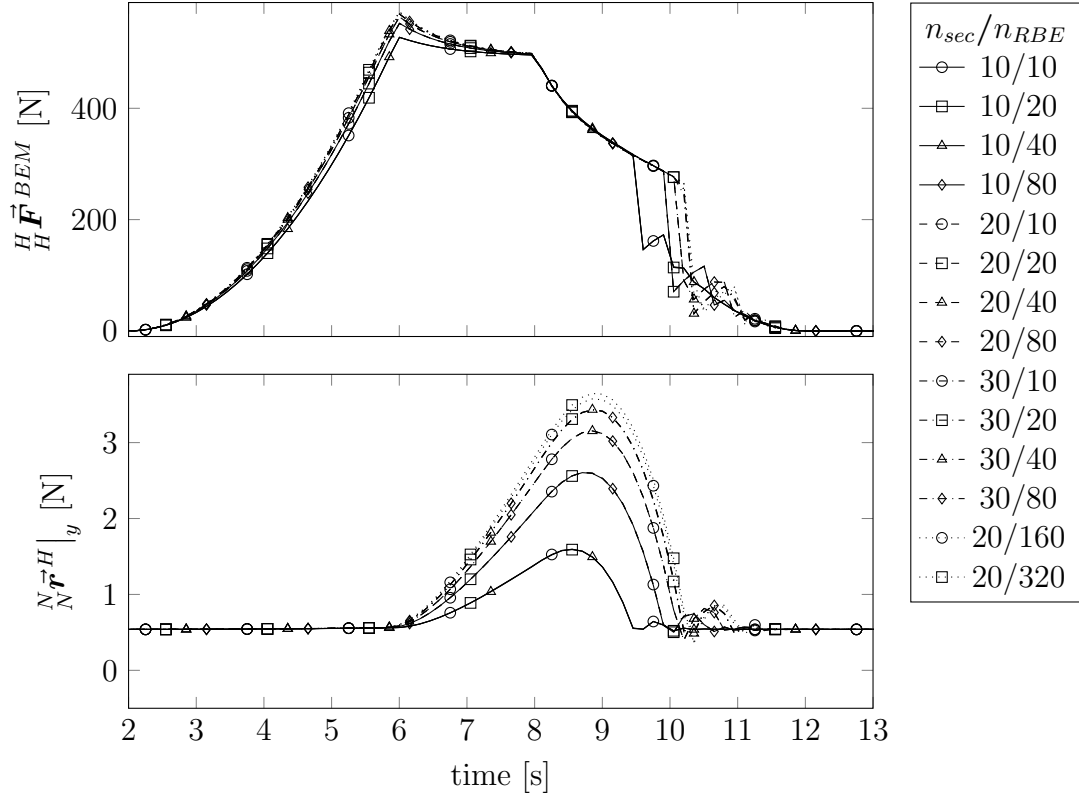


Figure 6.23: Case 6.2 Rotor disc thrust and airframe CoG height above the RSD deck.

wind, the advancing and retreating sides of the rotor disc generate equal amounts of thrust, which results in a vertical ascent by the aircraft beginning at 6 seconds. The magnitude of thrust drops as the aircraft lifts off due to an increasing axial flow through the rotor disc. The RPM is decreased to 0 rad/s from 8 to 12 seconds which allows the aircraft to touch down on the RSD desk around the 10-second mark. Strictly vertical aircraft motion, and zero rotor disc moment generation verifies uniformity in thrust generated in no relative wind conditions.

Another aspect to verify the correct implementation of the BEM model is the convergence of thrust and displacement values as the BEM mesh is refined. Interestingly, N_ψ/N_e combinations 20/80 and 30/80 have comparable values to 20/160 and 20/320, which could indicate an optimal parameter configuration for simulation performance with acceptable results.

Case 6.3 Rotor Thrust With Cross-wind

This Sub-case builds on Sub-case 6.2 with the addition of a relative headwind increasing to 0.5 m/s from 0 to 2 seconds. All other time-varying parameters are presented in Figure B.2 in Appendix B.2. A more refined set of N_ψ/N_e combinations is tested. Due to the headwind, it is expected that the advancing rotor blades see an increase in thrust generation while the retreating blades see a loss in thrust generation which should cause a rolling moment on the airframe. As a result the aircraft will exhibit some translational motion relative to the ship deck.

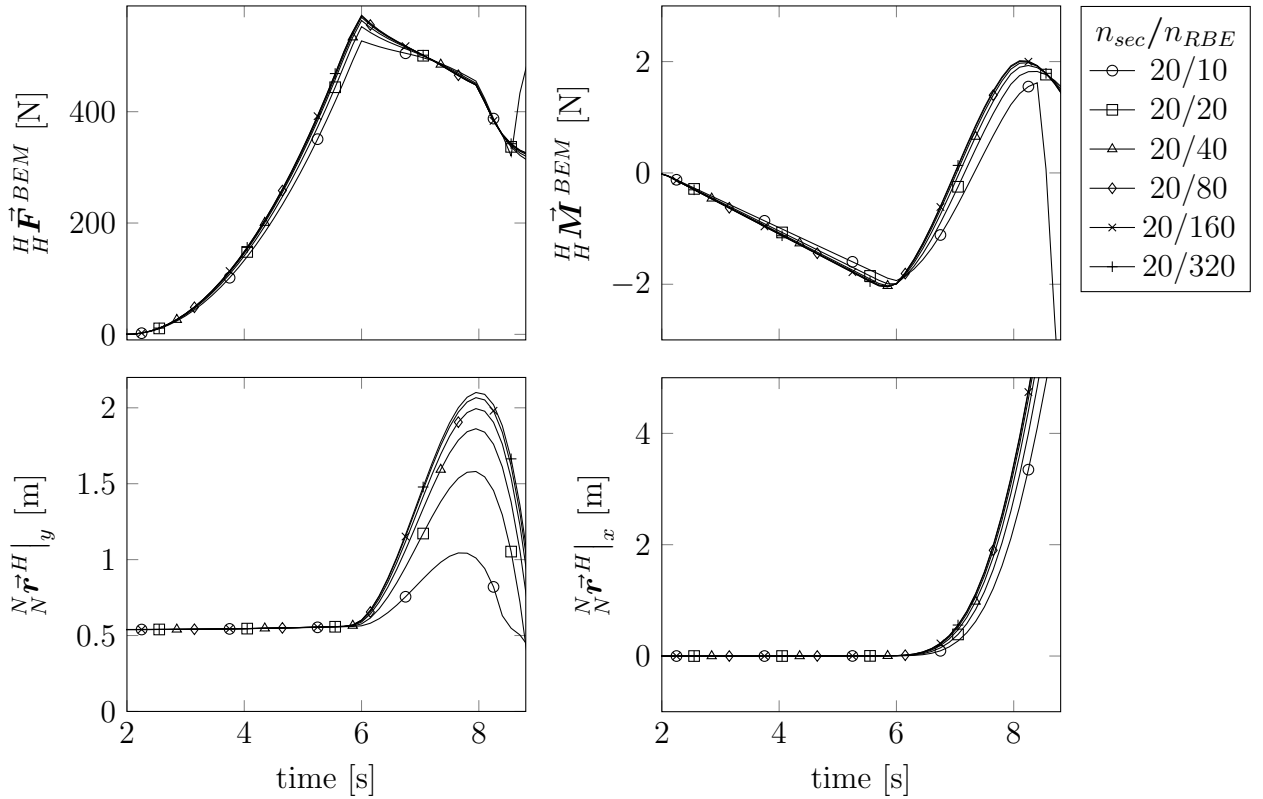


Figure 6.24: Case 6.3 Rotor disc thrust and rolling moment, and airframe CoG position relative to the RSD deck.

The uneven forces on the advancing and retreating blades are inferred from the non-zero rolling moment of the rotor disc acting on the airframe $\frac{H}{H}\vec{M}^R$. Even so, the rotor disc generates enough thrust for the aircraft to take-off. Immediately after take-off, the rolling moment causes the aircraft to roll in the clockwise direction. This roll causes the thrust vector to develop a horizontal component relative to the inertial frame which results in the sway of the aircraft. At 8.8 seconds, the aircraft exceeds

5 metres of horizontal displacement ($\left. \frac{N}{N} \vec{r}^H \right|_x$), which is beyond the edge of the defined ship polygon. This accounts for the large drop in vertical displacement and thrust and moment spikes as the aircraft has fallen off the ship.

Nevertheless, in the planar case, the advancing blades are on the left side of the aircraft, coming out of plane. The higher forces on the advancing side cause negative moment as predicted while on deck from 0 to 6 seconds. Once in the air, the negative rolling moment causes the aircraft to invert to the point where a positive rolling-moment is generated.

The non-zero rolling moment due to uneven rotor disc forces verifies the interaction of the rotor disc with apparent winds, and generates the expected aircraft response to the rotor disc loading. The kinematic development of the BEM model (Eqs. 4.65-4.67) is then implemented correctly.

Case 6.4 Rotor Thrust With Cross-wind and Cyclic Compensation

Sub-case 6.4 is identical to Sub-case 6.3 with the exception of the cyclic pitch setting function. This Sub-case aims to verify the correct implementation of the cyclical pitch setting for the rotor blades. The cyclical pitch setting causes second harmonic variation of the total blade pitch about one revolution of the rotor disc. The cyclical settings can be used to counteract uneven rotor disc loading. The time varying parameters for this Sub-case are found in Figure B.3 in Appendix B.3.

At 7 seconds, when the rotor has reached peak RPM, there is an increase in collective setting to 0.145 radians, and a cyclic setting of 0.005 radians at maximum azimuth $\pi/2$. Effectively, this sets the advancing blade minimum pitch to 0.14 radians, and the retreating blade maximum pitch to 0.15 radians. This counteracts the negative roll of the aircraft by generating a large positive rolling moment as shown in Figure 6.25. This causes the aircraft to level out and limit horizontal translation as indicated in the bottom right of Figure 6.25. The aircraft is able to touch back down onto the RSD deck, similarly to Sub-case 6.2. However, since the rotor blades are still spinning and the cyclical setting compensation has subsided, the aircraft begins to exhibit a response similar to Sub-case 6.3 to the point where the aircraft translates until it falls off the ship around 11 seconds.

The response exhibited in this Sub-case verifies the proper implementation of the cyclical pitch function. Prescribing maximum cyclic pitch at the retreating blades allowed for compensation of uneven rotor disc forces due to apparent wind, and

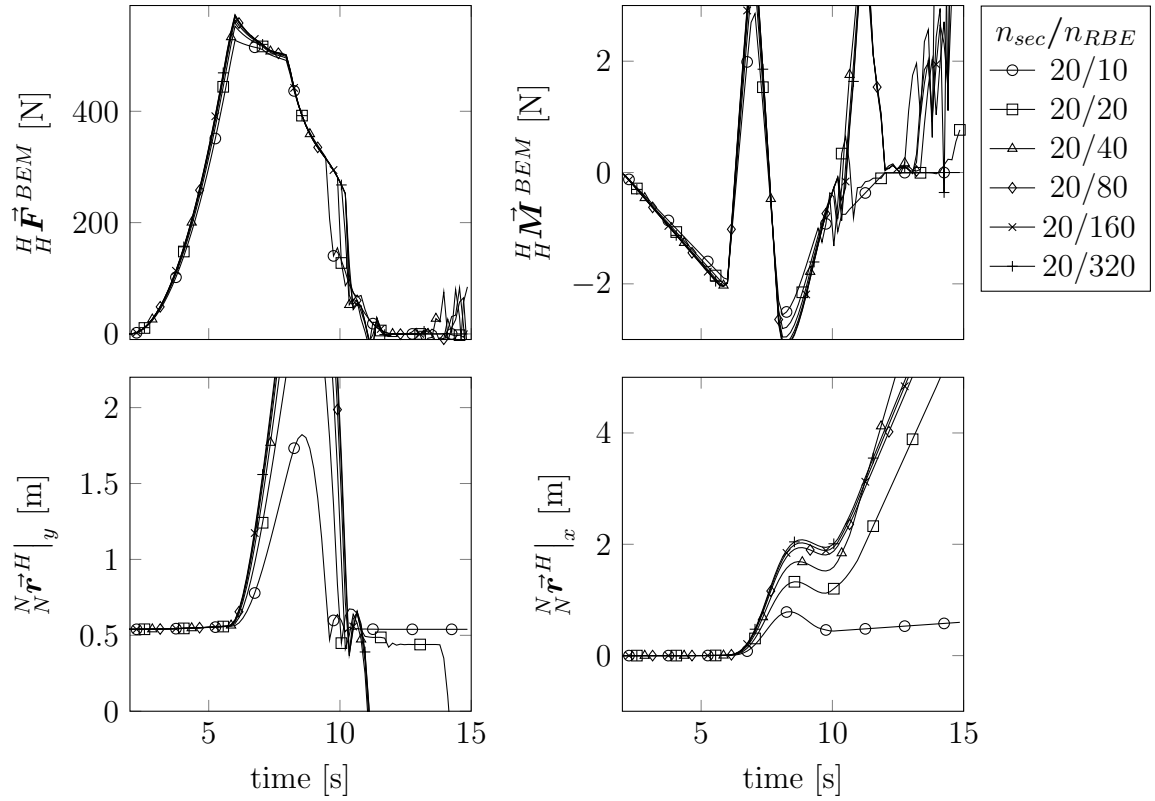


Figure 6.25: Case 6.4 Rotor disc thrust and rolling moment, and airframe CoG position relative to the RSD deck.

ultimately to corrects the roll of the aircraft for the time period where it is active.

Case 6.5 Blade Element Model Validation

The BEM model implemented in SRAMSS was developed in three dimensions. While the scope of this work is mostly limited to verification of the planar version of SRAMSS, the BEM model is independently validated against published experimental data.

During the eighties, comprehensive experimental testing of the UH-60A helicopter rotor blades had been undertaken. Enough published data exists to create a blade model for SRAMSS. The BEM model implemented in SRAMSS is evaluated against CFD model data presented in Garcia and Barakos [7], and the experimental data to which it is evaluated from Balch et al [8]. The blade profile used in these experiments is presented in Figures C.1 and C.2, and the equivalent rotor blade profile used in SRAMSS is presented in Figure C.3 with additional parameters presented in Table C.1. These figures and tables are found in Appendix C. The SRAMSS blade profile was modelled from the profile presented in Garcia and Barkados since it is more detailed. $\frac{dC_L}{d\alpha}(M = 0, Re = 10^6)$ and $\frac{dC_D}{d\alpha}(M = 0, Re = 10^6)$ are obtained from Xfoil-generated data published at *Airfoiltool.com* [59] and corroborated by Totah [60].

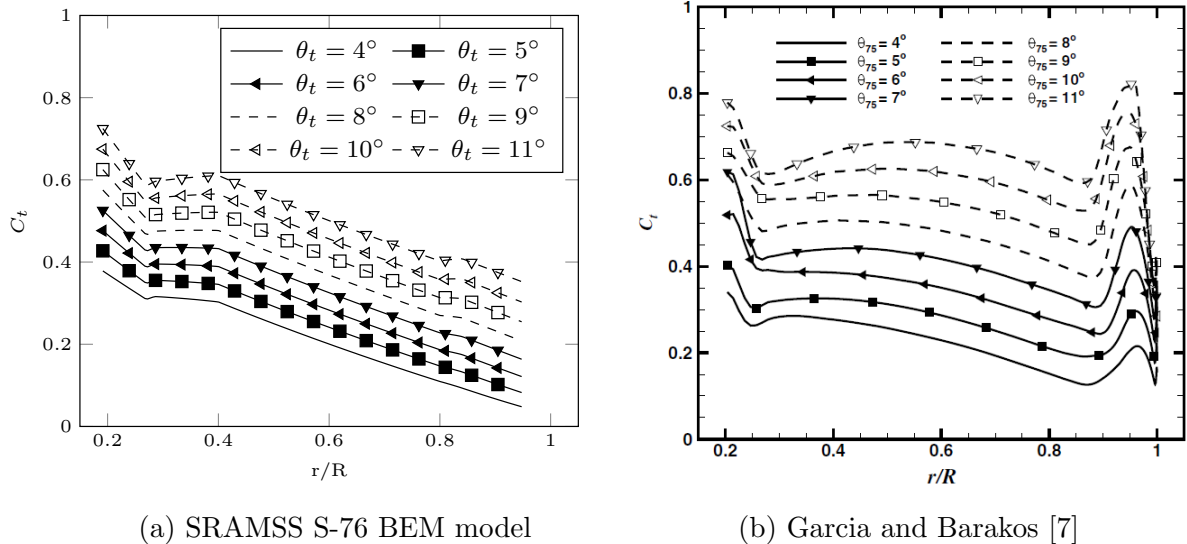


Figure 6.26: Case 6.5 Comparison of blade section thrust coefficient between SRAMSS BEM model and CFD analysis from Garcia and Barakos.

Given that the blade is divided into elements for the BEM model, the sectional thrust coefficient C_t , a non-dimensional measure of the generated thrust, is calculated

as $C_t = dT/(\rho_{air}(\Omega r)^2 cdr)$. As shown in Figure 6.26, the BEM model exhibits similar blade section thrust coefficient variation to the results from Garcia and Barakos for a 1/4.71-scale S-76 rotor in hover, with blade-tip Mach number $M_{tip} = 0.65$. However, the SRAMSS BEM model overestimates C_t near the root of the blade, and underestimates C_t closer to the blade tip, where complex blade-tip geometries are present.

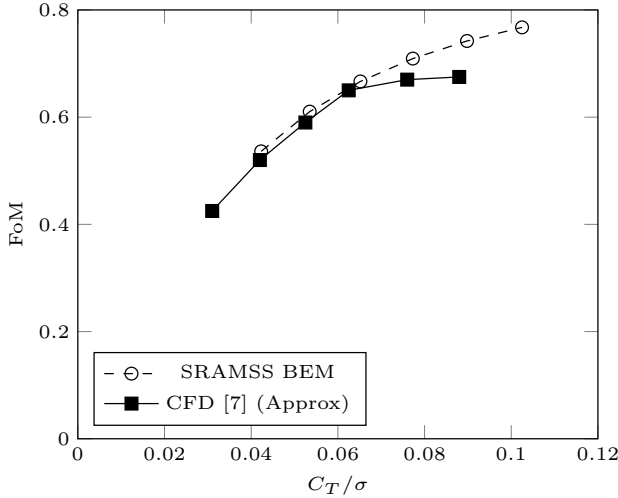
Discrepancies between the two models arise from their core differences. The SRAMSS BEM model, still in its developmental phase, is a basic lift and momentum-based elemental approach which has minimal corrections for aerodynamic phenomena. Whereas the work done by Garcia and Barakos is based in high-fidelity computational fluid dynamics (CFD). The discrepancies in the estimation of C_t are most likely due to the simplistic calculation of the coefficient of drag for the BEM model. The linear drag coefficient model does not capture the parabolic nature of drag under different flight speeds where either parasitic drag or lift-induced drag dominate. Additionally, no effort is made to consider the drag-divergence Mach number where there is a rapid increase in drag coefficient, such as Figure 2.4 of Keys [61]. The limited consideration of drag overestimates the value of thrust in calculation per Equation 4.88, which affects C_t accordingly.

With respect to the CFD analysis, blade wake, wing tip vortices, and wing tip shape are considerations not modelled by the SRAMSS BEM model. These ultimately affect the sectional thrust coefficient. Specifically, the wing tip modelling, and wing tip vortices are reasoned to influence the C_t values at the wing tips according to Garcia and Barakos.

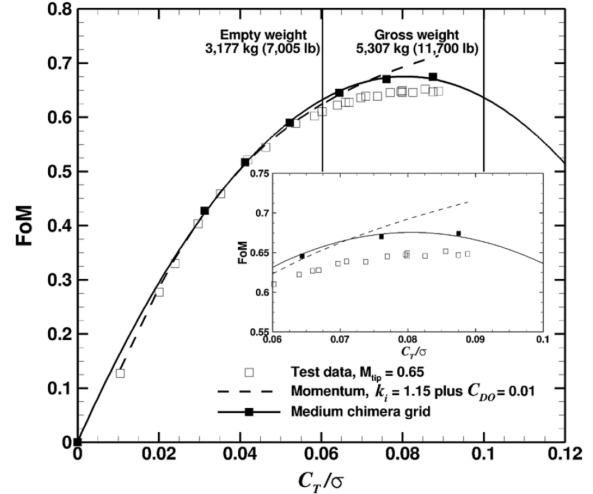
Another estimation of performance for the aircraft in hover, is the figure of merit (FoM). The BEM model is matched closest to the rectangular, flat-cap tip blade model from Garcia and Barakos. For tip Mach-numbers of $M_{tip} = 0.65$ and $M_{tip} = 0.60$, the FoM versus blade loading coefficient C_T/σ for the BEM model and CFD analyses are given in Figures 6.27 and 6.28. The rotor thrust coefficient is $C_T = T/(\rho_{air}(\Omega R)^2 \pi R^2)$, where σ is the rotor solidity ratio. For the BEM model, the momentum-based estimation of the FoM is

$$\text{FoM} = \frac{C_T^{3/2}}{\sqrt{2} \left(\sigma(C_{D0}/8) + k_i \left(C_T^{3/2}/\sqrt{2} \right) \right)}$$

where $k_i = 1.1$ is the induced power factor, and $C_{D0} = 0.01$ is the overall profile drag coefficient [7].



(a) SRAMSS S-76 BEM model



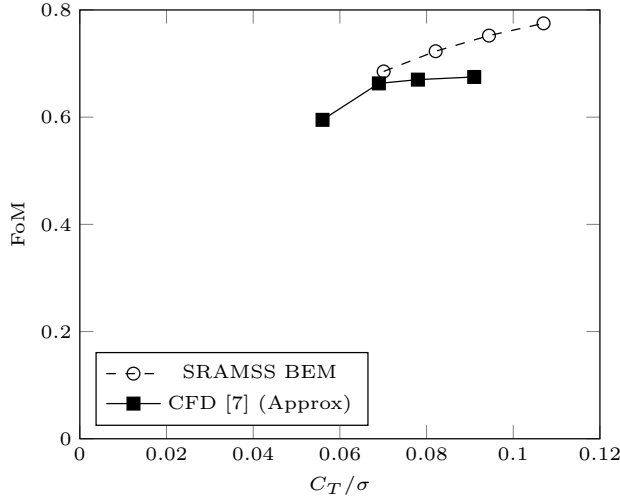
(b) Garcia and Barakos [7]

Figure 6.27: Case 6.5 Comparison of FoM for SRAMSS BEM and CFD model. $M_{tip} = 0.65$, $\theta_t = \{4^\circ, 5^\circ, 6^\circ, 7^\circ, 8^\circ, 9^\circ\}$.

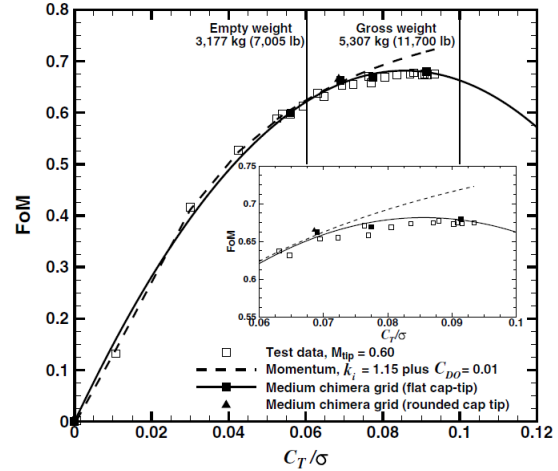
Similar to the sectional thrust coefficients, the rotor thrust coefficient is also overestimated, which leads to an overestimation in the momentum-based FoM number. This overestimation causes a shift in the FoM values predicted by the BEM model. While there is some variation with respect to the values obtained through CFD analysis, The BEM model values align with the momentum trends from Figures 6.27b and 6.28b which supports the proper implementation of the BEM model in SRAMSS.

The simulations performed for Sub-cases 6.2 through 6.4 verify that the BEM model for rotor disc forces has been implemented correctly. The rotor generates appropriately-oriented thrust vectors and roll moments to the airframe in various wind conditions.

Initial validation of the BEM model in Sub-case 6.5 reveals that the trends in performance measures are similar to CFD and experimental values, yet highlights the need for more accurate modelling of aerodynamic phenomena at the rotor disc. The accuracy required of the BEM model for dynamic interface analysis, can only be determined by the comparison of full three-dimensional simulations against experimental data.



(a) SRAMSS S-76 BEM model



(b) Garcia and Barakos [7]

Figure 6.28: Case 6.5 Comparison of FoM for SRAMSS BEM and CFD model. $M_{tip} = 0.60$, $\theta_t = \{6.5^\circ, 7.5^\circ, 8.5^\circ, 9.5^\circ\}$.

6.3.7 Case 7: Securing Concept Verification

Having shown that the contact dynamics model generates an appropriately-oriented dynamic response to collision through the simulations performed in Case 5 in Section 6.3.5, the wedge clamps as a skid-equipped aircraft securing device can be qualified.

Case 7 is split into static and dynamic Sub-cases. First, the static Sub-case 7.1 verifies that the aircraft reacts appropriately to the securing device on a stationary ship. Second, the dynamic Sub-case 7.2 verifies the securing device's ability to secure and manoeuvre the aircraft under various prescribed ship and RSD deck motions.

Case 7.1 Static Aircraft Securing

For Sub-case 7.1 the generic aircraft is secured to the RSD deck under three different initial conditions. In the first simulations, the aircraft undergoes a level drop towards the RSD deck, while being on-centre with respect to the RSD, where it is then secured by the device. Next, the aircraft is similarly dropped, but off-centre from the RSD. Lastly, the aircraft is dropped onto a ship with a fixed roll angle. In all simulations, the securing device is 'activated' at 1 second of simulation time, and requires 0.5 seconds to spread the wedge clamps. These configurations are illustrated in Figure 6.29.

It is convenient to quantify the device's ability to secure the aircraft by evaluating

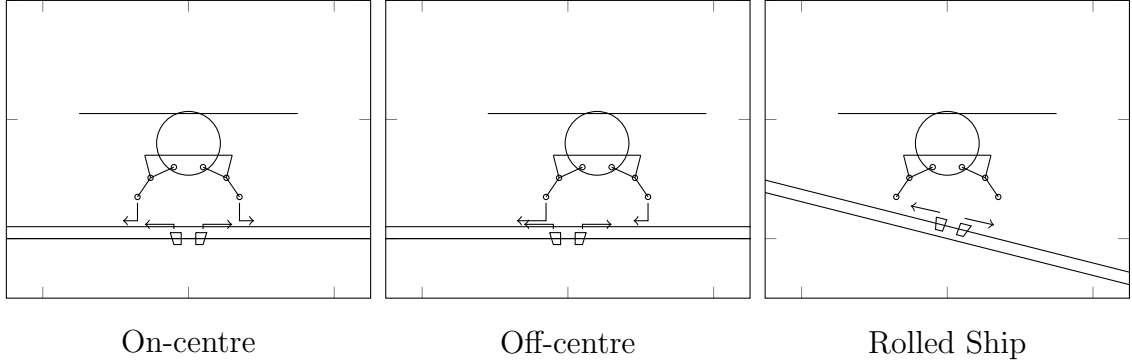


Figure 6.29: Case 7.1 Static aircraft securing simulation configurations.

the magnitude of distances of specific parts of the aircraft with respect to parts of the securing device. Three distances are used to evaluate the performance of the securing device. First, the position of the airframe relative to the RSD frame $\|{}^D_N\vec{r}^H\|$ shows the ability of the RSD deck to manoeuvre a secured aircraft. Second, the distances between the contact nodes and their respective clamping wedges $\|{}^{CL}_N\vec{r}^{n_1}\|$ and $\|{}^{CR}_N\vec{r}^{n_6}\|$ show the wedge clamp's ability to retain the skid-tubes. These distances quantify the aircraft's position relative to the securing device, and as such, indicates the ability of the device to retain the aircraft independent of any prescribed ship or RSD deck motion.

These distances are obtained from the kinematic developments of Chapter 3 as follows:

$$\begin{aligned}\|{}^D_N\vec{r}^H\| &= \|{}^N_N\vec{r}^H - {}^N_N\vec{r}^D\| \\ \|{}^{CL}_N\vec{r}^{n_1}\| &= \|{}^N_N\vec{r}^{n_1} - {}^N_N\vec{r}^{CL}\| \\ \|{}^{CR}_N\vec{r}^{n_6}\| &= \|{}^N_N\vec{r}^{n_6} - {}^N_N\vec{r}^{CR}\|\end{aligned}$$

The results of the three simulations are presented in Figures 6.30 through 6.32.

In the first two simulations, the three distances settle to the same values of $\|{}^D_N\vec{r}^H\| = 0.4247$ metres, $\|{}^{CL}_N\vec{r}^{n_1}\| = \|{}^{CR}_N\vec{r}^{n_6}\| = 0.0757$ metres. For the last case, the values settle to $\|{}^D_N\vec{r}^H\| = 0.4247$ metres, $\|{}^{CL}_N\vec{r}^{n_1}\| = 0.0756$ metres, and $\|{}^{CR}_N\vec{r}^{n_6}\| = 0.0757$ metres respectively. The difference in the last simulation is attributed to the weight of the aircraft being held at the interface of n_1 and the left wedge clamp, whereas there is only friction keeping n_6 from sliding down the inclined RSD deck.

Nevertheless, there is one significant commonality between each simulation. Be-

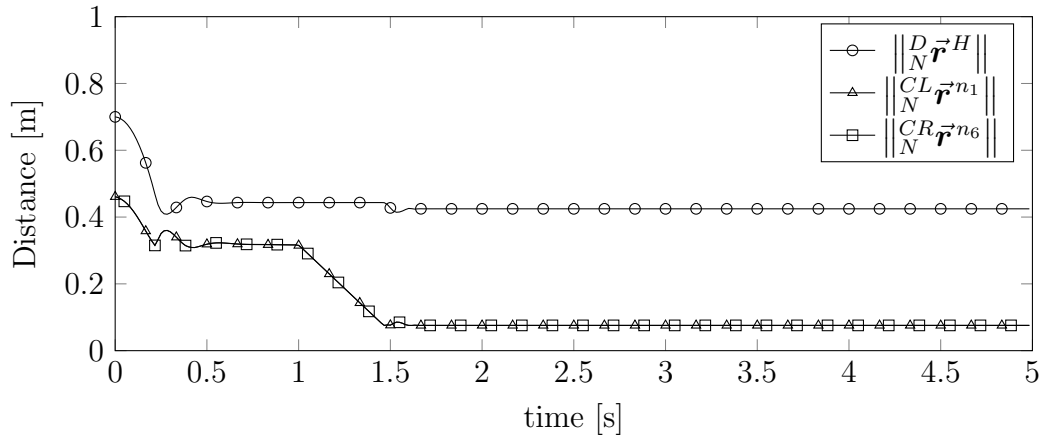


Figure 6.30: Case 7.1 Static aircraft securing in the ‘On-centre’ scenario.

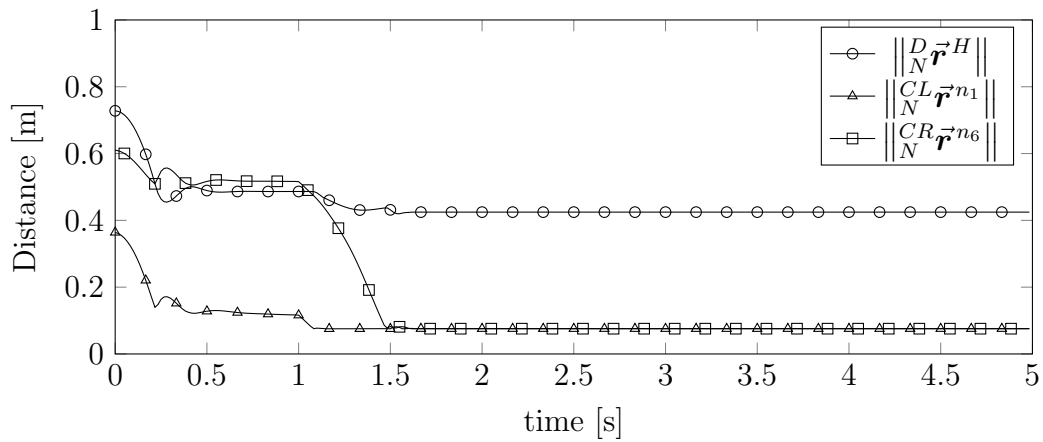


Figure 6.31: Case 7.1 Static aircraft securing in the ‘Off-centre’ scenario.

tween 1.0 and 1.5 seconds the three distances settle to their final values. This verifies that the aircraft is secured for the static scenarios. By extension, the securing device concept is initially verified.

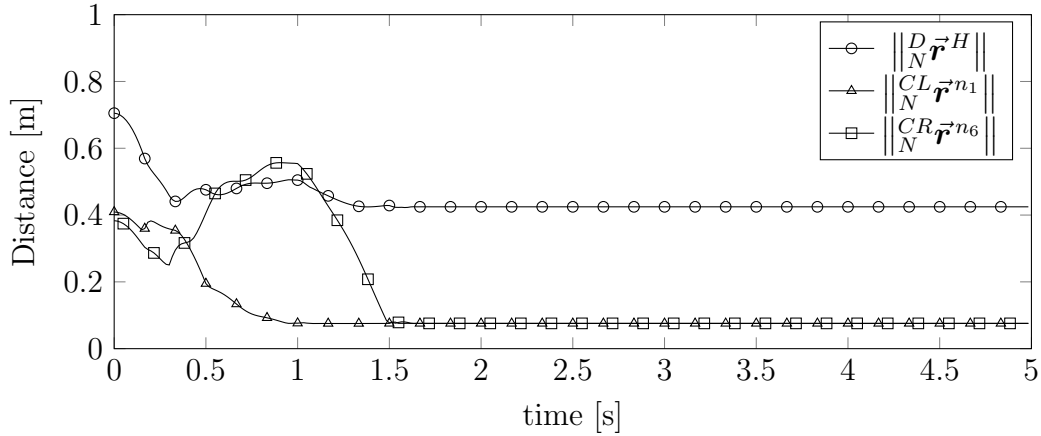


Figure 6.32: Case 7.1 Static aircraft securing in the ‘Rolled Ship’ scenario.

Case 7.2 Dynamic Aircraft securing

Under normal operations, the RSD is used to secure an aircraft to a moving ship in extremely dynamic conditions. A similar analysis to that of Sub-case 7.1 is performed for dynamic ship and RSD deck conditions using the same metrics to evaluate aircraft securing. For Sub-case 7.2 there are two simulations. In the first simulation, the aircraft is dropped onto a rolling ship, then is secured at 3 seconds. In the second simulation, the aircraft is secured at 1 second, then manoeuvred across the ship deck by means of the RSD deck. A more complex dynamic securing scenario is simulated for comprehensive testing in Case 8. The two simulation configurations are shown in Figure 6.33.

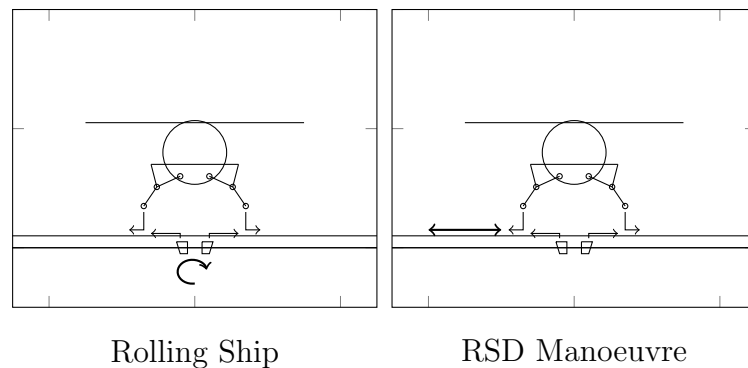


Figure 6.33: Case 7.2 Dynamic aircraft securing simulation configurations.

The results of the two dynamic simulations are presented in Figures 6.34 through 6.37. As with the static tests, once the aircraft is secured, the distances are maintained at

the expected values which verifies that the securing device is able to initially secure and keep secured the aircraft under dynamic conditions.

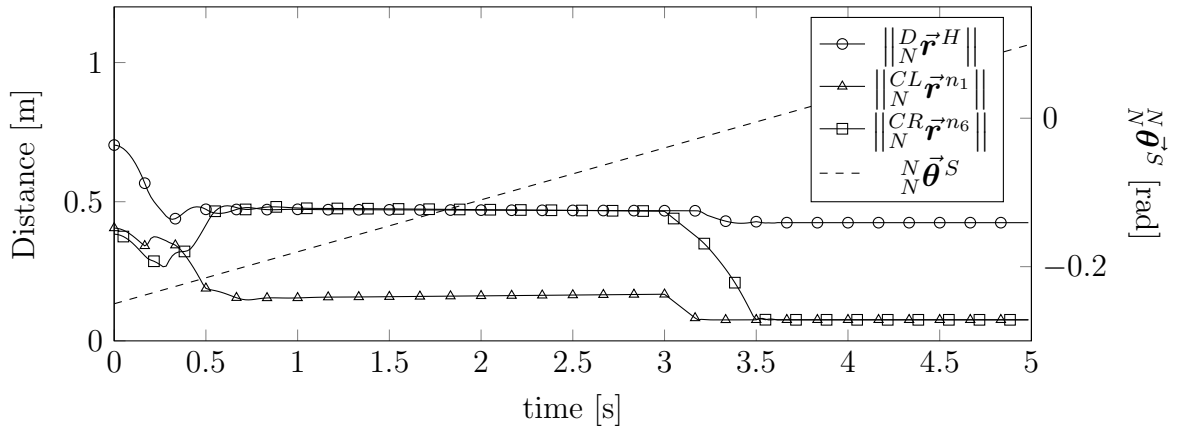


Figure 6.34: Case 7.2 Dynamic aircraft securing in the ‘Rolling Ship’ scenario.

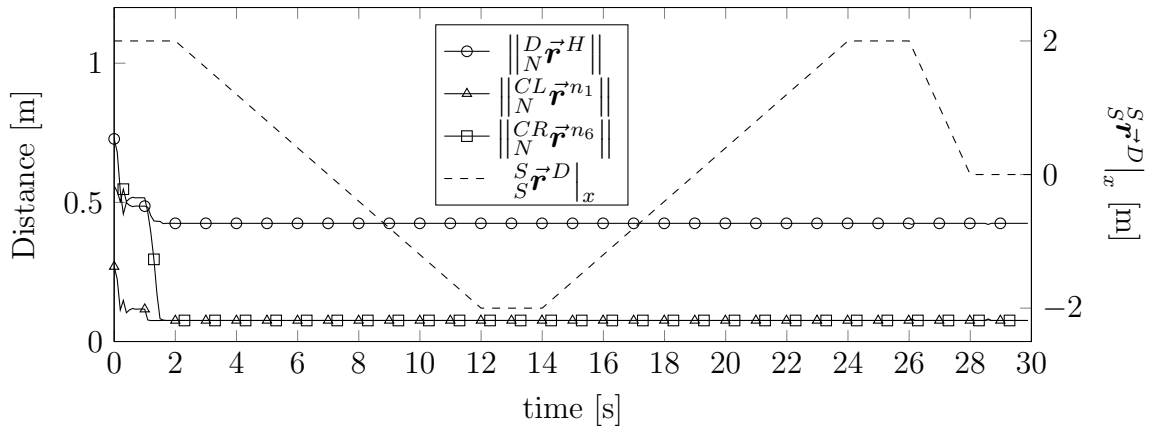


Figure 6.35: Case 7.2 Dynamic aircraft securing in the ‘RSD Manoeuvre’ scenario.

Figures 6.36 and 6.37 show the magnitude of the contact forces acting at the contact nodes in both tests. The data indicates that the trailing wedge clamp on deceleration of the RSD deck, and the leading wedge clamp on acceleration generate larger contact forces.

In any case, under static and dynamic conditions, Sub-cases 7.1 and 7.2 verify the implementation of the securing device conceptual design presented in this work. It further verifies the contact dynamics model, as the RSD deck, and wedge clamps are polygons defined in the SRAMSS environment. Moreover, it suggests that the concept is effective and warrants further investigation and design refinement.

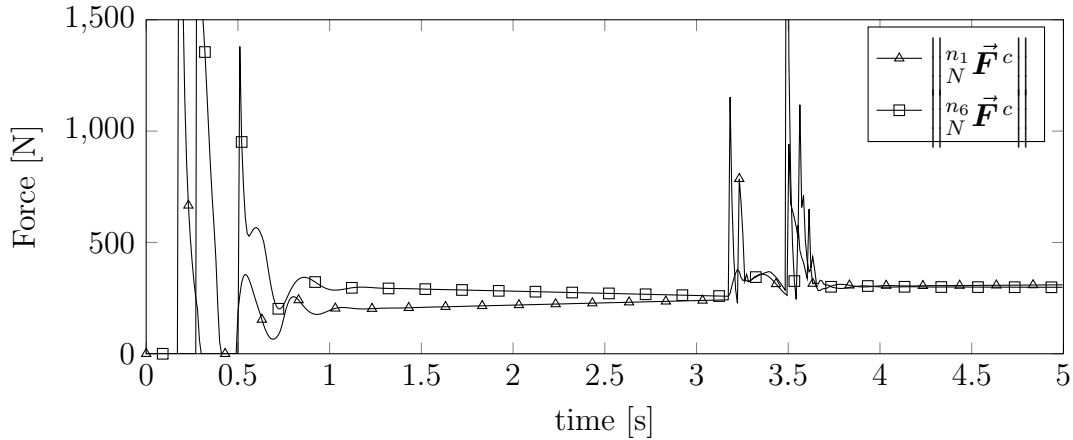


Figure 6.36: Case 7.2 Contact force magnitudes in the ‘Rolling Ship’ scenario.

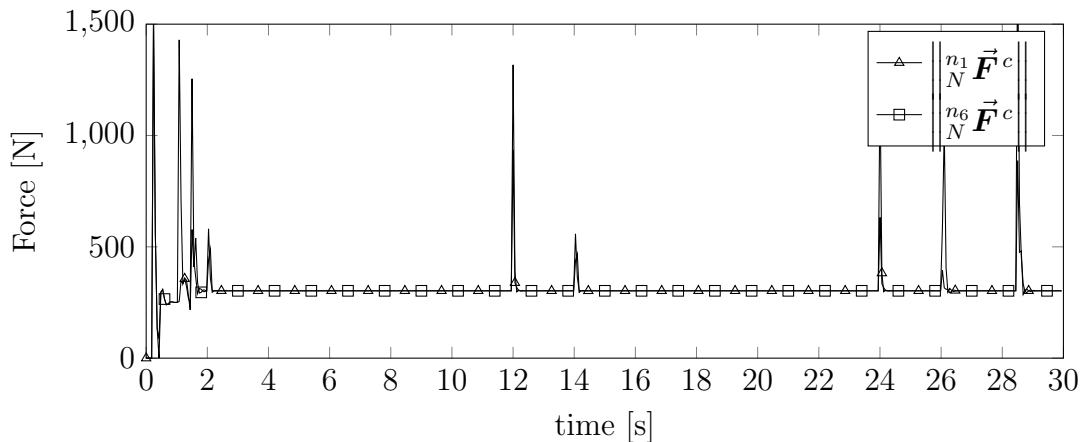


Figure 6.37: Case 7.2 Contact force magnitudes in the ‘RSD Manoeuvre’ scenario.

6.3.8 Case 8: Comprehensive Phenomena Verification

At this point, all models implemented in SRAMSS have been isolated to the extent possible for independent evaluation. All models have been verified to be properly implemented in the planar version of SRAMSS. Yet in comprehensive simulation conditions, simultaneous functioning of all models is required.

Case 8 incorporates the complete recovery flight, securing, manoeuvring, and launch phases of shipboard helicopter operations. Aircraft flight and securing system control is outside of this work, therefore prescribed aerodynamic parameters and polygon motions were iterated to obtain the desired visual behaviour. First, the aircraft enters recovery flight where it station-keeps over a ship deck moving all three degrees of freedom, while correcting its flight attitude against head and cross-winds.

When ship-motion velocity slows, the aircraft lands on the ship where it is then secured to the RSD deck via the wedge clamp securing device. Once secured, the aircraft is powered-down. Then, the RSD performs a translational manoeuvre of the embarked aircraft to simulate secured aircraft manoeuvring under large ship motions. Near the end of the manoeuvre, large cross-winds act on the aircraft. Finally, the aircraft begins pre-flight power-up, and is eventually released from the securing device to take-off in headwinds.

Simulation-time-varying parameters are presented in Figures D.1 and D.2 in Appendix D. The scenario is run for all combinations of $N_n = \{6, 10, 14, 18\}$ by $N_\psi = \{20\}$ by $N_e = \{40, 80, 160\}$ over a 47-second simulated time period.

Figure 6.38 showcases eventful timestamps in the Case 8 simulation. At 0 seconds, headwinds cause the aircraft to roll and sway to the right. The roll is overcompensated by cyclical pitch settings at 1 second which causes rolling in the opposite direction. Sway in the opposing direction is prevented by correction to the cyclical pitch settings and large cross-winds. Around 6 seconds, the aircraft lands on the now-level ship deck. The securing device and RSD deck capture the landed aircraft at 7 seconds. Between then and 10 seconds, the aircraft powers down. The RSD performs translational manoeuvres of the embarked aircraft until 33 seconds while the ship heaves, sways, and rolls. Near the end of the manoeuvres, a large gust of wind crosses the ship. Power-up of the aircraft begins at 39 seconds. Around 42 seconds, the aircraft reaches full power, with collective pitch set to its maximum value, then is immediately released. Beyond 43 seconds, the aircraft performs manoeuvres to exit the immediate area of the ship.

The transient position of the aircraft’s airframe is shown in Figure 6.39. There are two major observations which can be made. First, the refinement of the BEM mesh has greater influence on aircraft response than DFE mesh refinement since the plot lines appear to be superimposed for N_e . This is expected as external-damper-equipped DFE models showed little difference in response for the 10-, 14-, and 18-node meshes as illustrated in Case 4.2’s Figure 6.13, and convergence of results for different BEM meshes is slower as Case 6.4’s Figure 6.25 shows. Second, the discrepancy in response for combinations where $N_e = 40$ causes the aircraft to miss the securing device (for equal prescribed motions and time-varying parameters). Interestingly, when the securing device activates, the left contact node is wedged against the right wedge clamp. Then, when the collective setting is increased to 0.14 radians after

40 seconds, enough lift is generated to take off. However, since the left node is wedged, the generated thrust causes the aircraft to pivot about the right wedge clamps and roll over into the RSD deck as shown by the drop in y -position and spike in x -position around the 42-second mark in Figure 6.39.

Referencing to the ‘complex dynamic securing scenario’ mentioned in Section 6.3.7, the same analysis can be done to verify the RSD’s performance for Case 8’s fully-dynamic scenario. Figure 6.40 shows the measured distances, while Figure 6.41 shows the magnitude of the corresponding contact forces. Figure 6.40 corroborates the observation that the $N_e = 40$ combinations fail to secure to the RSD. For the combinations where $N_e \neq 40$, Figure 6.40 settles to values similar to those in Figures 6.29 through 6.35 of Case 7 under secured conditions.

With respect to the contact forces, Figure 6.41 follows the trend that the results are nearly identical for combinations where $N_e \neq 40$. For the tests where the aircraft has been secured to the ship between 7 and 42 seconds, there are fluctuations in the contact forces due to the shift in aircraft weight as the ship moves. For the unsecured aircraft, the fluctuations are more apparent since friction is the dominating force keeping the aircraft on deck. Correspondingly, in Figure 6.40, $\|{}^C_N \vec{r}^{n_1}\|$ and $\|{}^C_N \vec{r}^{n_6}\|$ are near-constant for the secured condition, while $\|{}^C_N \vec{r}^{n_1}\|$ and $\|{}^C_N \vec{r}^{n_6}\|$ show slight deviations for the unsecured condition. This suggests that the aircraft is beginning to slide in the unsecured condition.

The thrust and rolling moment generated by the rotor disc are the major forces governing the response of the aircraft while not secured. Figure 6.42 shows their magnitudes for the duration of the simulations.

The roll corrections made by the aircraft in the recovery flight phase correspond to the reversals in the values for $\frac{H}{H} \vec{M}^{BEM}|_{y,2D}$. Between 31 and 33 seconds a large gust of wind crosses the ship. While the rotor blades are not spinning, the apparent wind across the rotor disc does generate some value for thrust and rolling-moments which affect the aircraft. In Figure 6.42, when the aircraft is released from the RSD at 42 seconds, there is a drop in thrust from roughly 500 N to 200 N. For the unsecured aircraft, the thrust drops down to 200 N as it rolls over, then jumps to 500 N once inverted.

Case 8 comprehensively tests all models implemented in SRAMSS concurrently. The results presented for Case 8 match those of independently evaluated models in preceding cases, which verifies that the models are able to function properly in fully-

dynamic environments. Moreover, Case 8 has verified that the contact dynamics model functions properly for multiple polygons in the same simulation, and for contact states where the contact node is in contact with more than one polygon at a time.

At this point, all models contained in the Planar version of SRAMSS are verified. Consequently, it lays the architectural foundation and system formulation for a future fully-spatial version of SRAMSS.

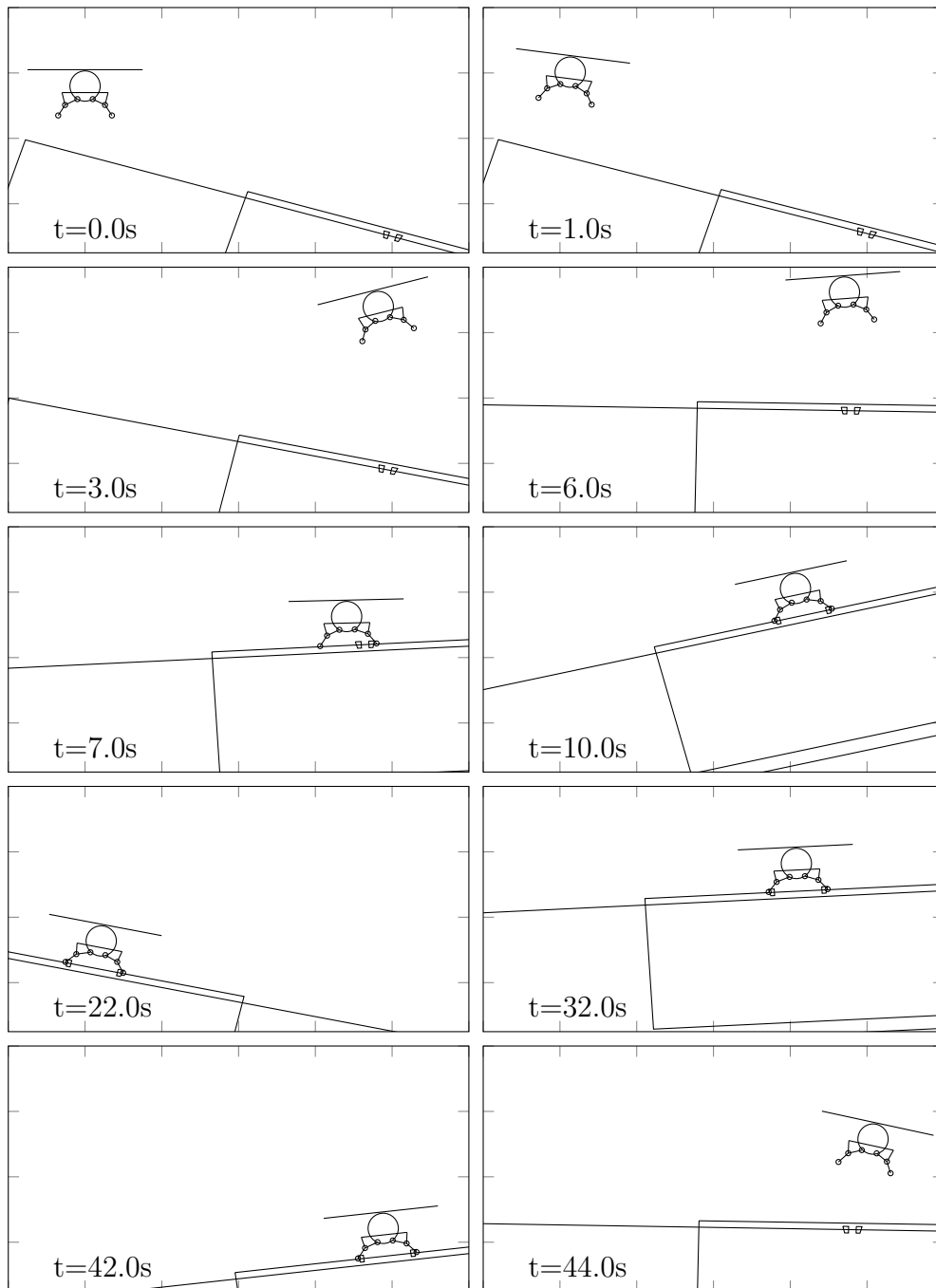


Figure 6.38: Case 8 Comprehensive simulation time-stamped event animations.

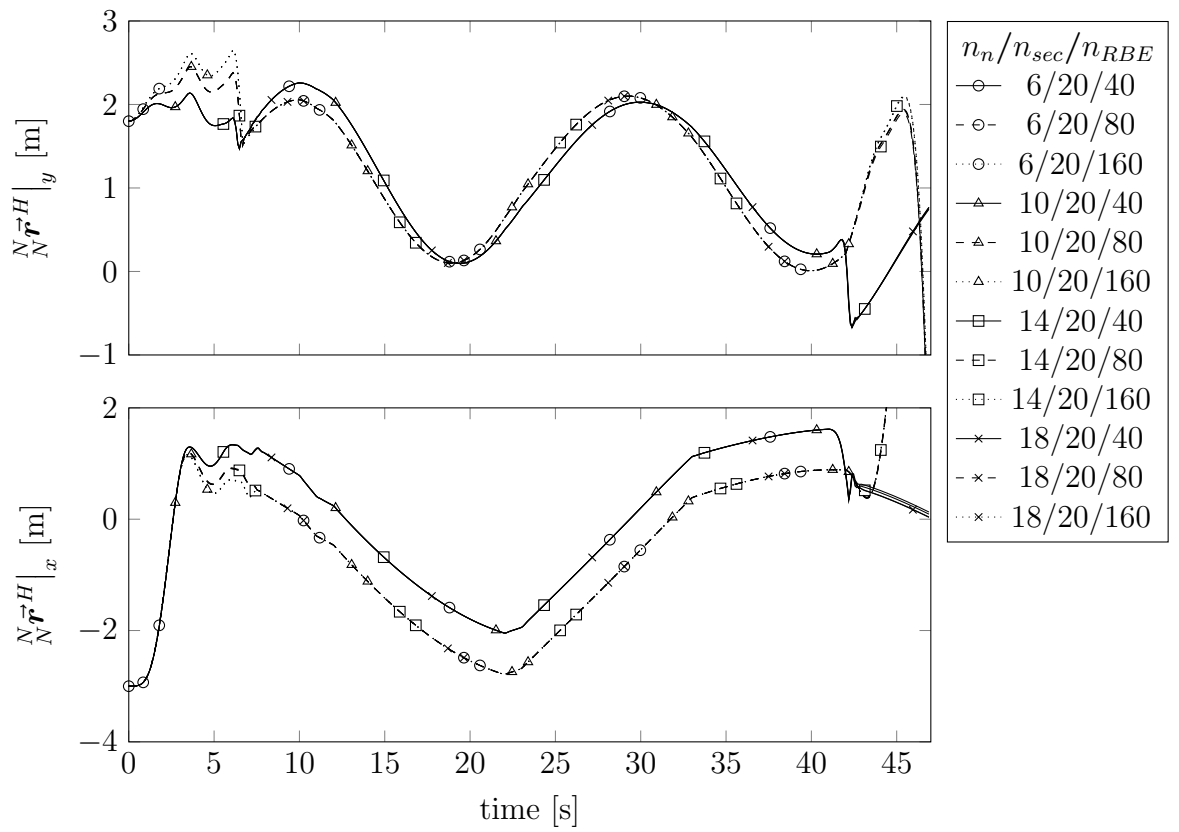


Figure 6.39: Case 8 Airframe CoG position versus time for all combinations of $n_n/N_\psi/N_e$.

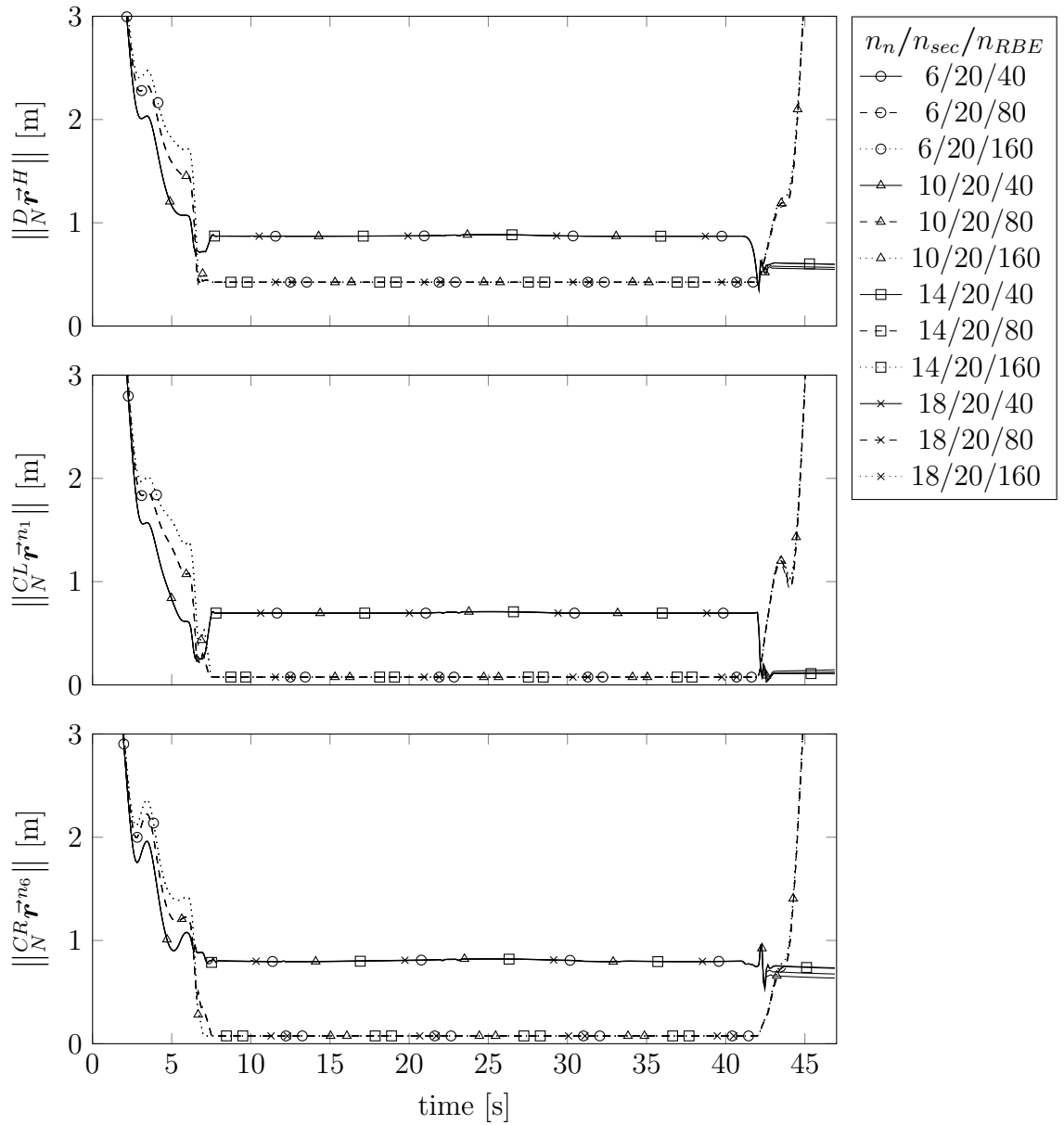


Figure 6.40: Case 8 Aircraft distances relative to RSD points.

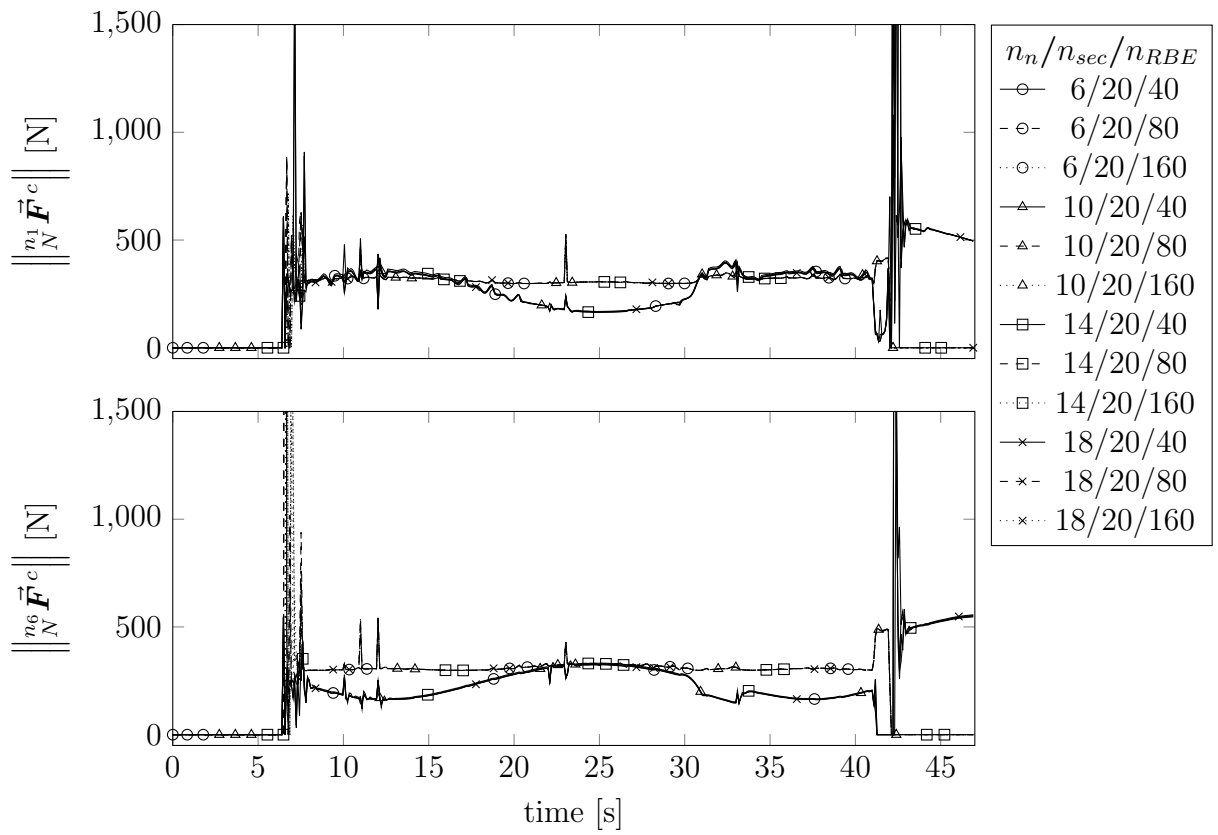


Figure 6.41: Case 8 Contact force magnitudes at each contact node.

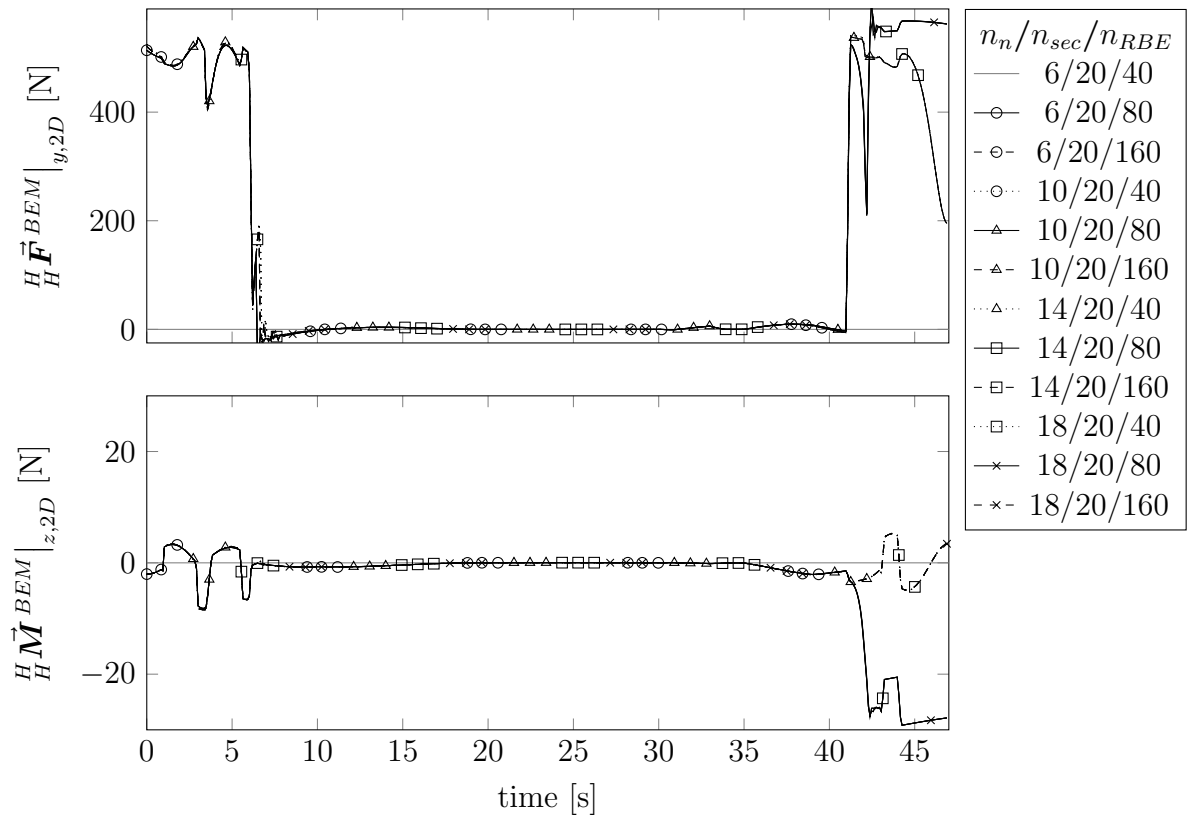


Figure 6.42: Case 8 Rotor disc force magnitudes.

6.4 General Remarks

Test Cases 1 through 8 extensively analyse the models derived in Chapter 4 for proper integration into SRAMSS. Even so, there are key aspects which have not been explicitly tested in any test case, yet their proper functioning is required nonetheless.

The development of the equations of motion in Chapter 3 through to system assembly in Chapter 5, follows a particular variation of Kane’s method for generating the equations of motion. Typically, an active force vector is assembled directly for each body in the system. In the case of the DFE model in SRAMSS, this would require that an active force vector be developed for each DFE node with consideration for the internal forces generated by other DFE nodes attached to it. However, the development presented in this work independently generates, then assembles the DFE model into the general system. This leaves the active force vector acting at each node to the assembly of externally-applied forces. In a system where a large body has flexible and rigid elements such as SRAMSS, an independently-generated DFE model allows direct use of any method for DFE model generation since only the $[M]$, $[C]$, and $[K]$ matrices need to be supplied for the system. Moreover, it enables infinitely-configurable and substitutable DFE models. Though, independent DFE matrix generation requires a way to interface the DFE model to the rigid components of the body. Section 4.4.1 and Section 5.1 present the methodology used to integrate the DFE model into the complete system. No test case in this chapter explicitly tests this interface model. An example which verifies this method and highlights the proper integration of the DFE model is the RSD manoeuvring simulation of Subcase 7.2. Even while the RSD is in motion, all distance magnitudes remain constant in Figure 6.35 when secured. This indicates that the rigid airframe and comparatively-flexible DFE-modelled landing gear are moving as a single body. In all other cases, the airframe and DFE responses suggest that the DFE model remains attached to the airframe in the expected way.

Specifically for the DFE model, a full-DoF 2D beam element is used. It can be argued that a simple beam element is sufficient since the axial compression of the element is negligible compared to the deflections in shear and bending. As it relates to simulation performance, time-complexity is exponential with respect to the size of the system, therefore reducing the number of DoFs would increase simulation performance. For analysis capabilities, retaining the axial DoFs would allow direct evaluation of buckling loads during simulations. This could be beneficial to the pre-

liminary design of skid-landing gear, which often use long slender beams, suited to maritime shipboard operations.

At the observable level, the contact dynamics model has been verified to generate appropriately-oriented dynamic responses in every test case. It is required to work properly as all cases depend on ship-aircraft interaction to varying degrees. The most significant being Case 8 where all four defined polygons are in motion and the aircraft interacts with multiple polygons simultaneously. At a more fundamental level, the underlying contact detection algorithm presented in Section 5.2.2 is required to work correctly. In all test cases, surface contact was correctly detected which allowed for appropriate orientation of the dynamic response.

Furthermore, the contact dynamics formulas and algorithms used to express the response of a given surface on a contact node were developed with respect to a non-specific generalized surface defined by two vertices in the two-dimensional Cartesian plane. The general case allows for infinitely configurable convex polygons to be defined for the system. This capability was exploited to represent major simulation elements as physical bodies. The ship deck, RSD deck, and wedge clamps were all successfully modelled using defined polygons. Additionally, the defined polygons could be considered for solution in the equations of motion, provided kinematic development to the appropriate frame of reference and force vectors are compiled. Such considerations could allow the simulation of ship response due to aircraft interaction, or even the RSD deck response in ‘power-failure’ or ‘damaged’ simulation scenarios.

Concerning the BEM model, Sub-case 6.5 indicates that the BEM model requires refinement to generate more accurate thrust profiles. Even so, the question of required BEM model fidelity remains: what accuracy is required to generate accurate aircraft response. In the case of SRAMSS, the BEM model is used to model a single rotor disc force and moment vector acting on the airframe. When the three-dimensional case of SRAMSS is implemented, the minimum accuracy required for the BEM model would only require that the simulated aircraft response matches experimental data. Such a model might not need to make considerations for more complex rotor disc phenomena such as downwash, blade wake, and vortex generation.

With respect to simulation performance, an ODE solver with root-finding capabilities is the required minimum as the contact detection algorithm leverages root functions. The choice of the DLSODAR solver also has the benefit of automatic selection of integration method based on system numerical stiffness. Simulation phases

where the aircraft was in flight benefited from the non-stiff method as computational time fell well below the real-time threshold. While in contact, the stiff method allowed for state propagation in reasonable time.

For the most complex verification test case, Case 8 “18/20/160”, Appendix E.1 lists the ratio of propagated simulation time to CPU computation time for the 6 to 10 seconds simulated time range. The range corresponds to the landing and aircraft securing phase. Values greater than 1 indicate faster than real-time solution propagations. Where the ratio is equal to ‘inf’, the CPU computation time was exceedingly small such that the Intel[®] Fortran’s intrinsic ‘CPU_TIME()’ function considered t and $t + \Delta t_{sol}$ to be the same time. Drops in the ratio mostly occur where there is a non-smooth transition in any of the prescribed time-varying values or contact states. A smoothing function to remedy the transition points in prescribed values could yield significant simulation performance improvements.

Chapter 7

Conclusion

As it pertains to the gap in dynamic interface analysis capabilities identified in Table 1.1, this work, the planar case of SRAMSS has demonstrated the ability to address the limitations presented by the current state-of-the-art. The kinematic and kinetic developments presented in Chapters 3 and 4 render a system formulation which, through extensive verification and validation of SRAMSS in Chapter 6, has shown extensive capabilities with respect to the simulation of securing and manoeuvring of skid-equipped rotary wing aircraft undergoing shipboard operations. The combination of rigid and flexible dynamics, oriented contact dynamics, and three-dimensional aerodynamics allows SRAMSS to include a wide range of phenomena and generate a detailed aircraft response for all phases of shipboard operations.

7.1 Completed Work

Resulting from achieving the objectives framed in Section 1.5, the following conclusions regarding the planar case of SRAMSS are drawn:

- Through the identification of major requirements for the shipboard securing and manoeuvring of skid-equipped rotary wing aircraft, a ‘wedge clamp’ mobile securing platform was conceptualized. Evaluation of SRAMSS has shown this design to be an effective securing and manoeuvring device even under large ship movement, all while being a passive member completely contained on the ship.
- A versatile contact dynamics model coupled with prescribed ship motion and aerodynamic aircraft control has enabled the complete simulation of recovery flight, securing, manoeuvring, and launch phases of shipboard helicopter oper-

ations. The contact dynamics model is a novel application of the Separation Axis Theorem for collision detection. the SAT has been leveraged to both detect collision and generate an appropriately-oriented dynamic response. The contact dynamics model was verified to provide appropriately-oriented dynamic responses under the complex contact conditions present for stiff skid-type landing gear. Furthermore, the model was sufficiently generalized that it can incorporate any shaped convex polygons, which could be leveraged to model current and future securing and manoeuvring systems.

- The novel variant on Kane’s method presented in this work has allowed the DFE model to be generated independently into the equations of motion from the rest of the system. Provided the correct DFE element mapping and element properties, the method enables the capability to model a wide range of skid and other rigid landing gear configurations. Not only this, the formulations and developed in this work to merge rigid and flexible body dynamics in Kane’s method have applications beyond the scope of this work. It has shown the methodical integration of rigid and flexible components for a given body. This capability permits granularity in the selection of rigid and flexible elements when developing any complex dynamical system.
- The aerodynamic models developed in this work form a comprehensive foundation for capturing the aerodynamic phenomena present in shipboard operations. The aerodynamic body drag force model addressed the forces induced by the apparent wind over the ship deck, while the rotor disc BEMT model captured controlled rotor disc thrust and induced forces in apparent wind. The two aerodynamic models integrated into SRAMSS were verified to work correctly. Yet the BEM requires further development to provide more accurate results. Nevertheless, the BEM limits the dependency on manufacturer-provided and protected look-up tables, and is not limited by the range of data provided in these tables.
- The planar case of SRAMSS captures a wide variety of phenomena present in shipboard operations. The verification of the models implemented to capture these phenomena indicates that the simulation architecture and system formulation used for the planar case should form an appropriate base for the fully-spatial version of SRAMSS. The equations presented are sufficiently general that the development of the additional DoFs in the augmentation to three dimensions

requires minimal re-derivation of equations. In certain areas, formula derivations become simpler as the kinematic-dynamic context of skew matrices is not needed. In other areas, additional formulae would be required for the new DoFs, such as the torsional stiffness in the DFE elements. High-level recommendations for the augmentation to three dimensions are presented in Section 7.2.

- The simulation package has been successfully written in the Intel[®] Fortran language. Step-wise simulation run-time has indicated the potential for simulations which run faster than real-time—a desirable trait for simulations. As such, SRAMSS could form the dynamical response component of real-time simulations for training pilots and deck crews.

7.2 Recommendations

The SRAMSS simulation package has the potential to provide a comprehensive simulation environment for skid-equipped rotary-wing aircraft undergoing shipboard manoeuvres. These capabilities are ultimately necessary in the study of shipboard UAS operations due to their emerging role in maritime shipboard environments. While this work develops and discusses the 2D verification of SRAMSS, the governing equations and algorithms contained within the SRAMSS simulation package are written to be easily extended to a three-dimensional simulation environment. Recommendations for the development of the three-dimensional version of SRAMSS follow below.

- The architecture of SRAMSS, including but not limited to the generation of the equations of motion, DFE model and system assembly, choice of ODE solver, collision detection, and contact dynamics algorithms should be re-used for the fully-spatial SRAMSS simulation package as this work has been verified to function correctly in comprehensive simulation test cases.
- Due to the high manoeuvrability of UAS, Euler parameters should be used to describe orientation and transformation matrix construction, rather than the currently-implemented Euler angles, to avoid potential singularities in the transformation matrices.
- Analogous to the left-normal unit vectors describing a surface in two dimensions, polygon surface normal unit vectors can be defined by the normal vector describing the surface plane in three dimensions. Similar to the use of the surface origin vertex as the maximum of projected vertices along a surface normal

in 2D, the first vertex in a set of vertices defining a surface can be used in 3D.

- The DFE model elements should be upgraded to 12-DoF general beam elements to capture behaviour in all degrees of freedom.
- The aerodynamics models used in the planar case have already been developed in three dimensions, and thus can be directly re-used in the full version of SRAMSS.
- Simulation statistics show a degradation in performance around simulation times where time-varying prescribed inputs undergo instantaneous change. A smoothing function to pre-process these regions could increase simulation performance.
- The inclusion of the third dimension approximately doubles the number of generalized coordinates and velocities. The increase in size of the system to be solved will considerably affect simulation performance. Investigation of code optimizations and executable parallelization will be necessary to exceed or simply retain performance at a level similar to the planar version of SRAMSS, excluding the consideration of faster computers.
- SRAMSS and SSMASH follow similar developments of the equations of motion by using Kane's method. SRAMSS's more sophisticated contact dynamics model and comprehensive aerodynamics model could form the basis for a universal dynamic interface analysis package. Integration of the wheeled-landing gear developments in SSMASH would allow the package to comprehensively evaluate aircraft regardless of landing gear type. It also presents the possibility of modelling hybrid wheeled-rigid landing gear.
- As it stands, the response of the aircraft to ship motion is of bigger concern than the opposite in regards to dynamic interface analysis. The partial velocity matrices could be reduced in size to eliminate the columns associated with prescribed ship deck, RSD deck, and wedge clamp motions. As a result, simulation performance would increase through a reduction of array size, and subsequent array manipulation time in 'XddotF.f90'.
- Nevertheless, for other applications, the ship and RSD deck response might be significant. Since the defined polygons form part of the partial velocity matrices and the polygon velocities have been developed, minimal additional derivations are required for inclusion of their response in simulations. Design failure mode and effect analysis (DFMEA) and extreme edge-case simulations would benefit

from ship and RSD response inclusion.

7.3 Future Work

The planar case of SRAMSS is an intermediate step in the development of the fully-spatial version of SRAMSS. This work has demonstrated that the system formulation works as intended. Accordingly, work will be undertaken to expand the system formulation into the third dimension. There, the fully-spatial version of SRAMSS will be validated against experimental dynamic interface data collected in aerodynamic test facilities such as Carleton University's state-of-the-art WInDLab wind tunnel equipped with a 6-DoF motion platform.

References

- [1] F. Cracknell, “LAMPS III Recovery Assist, Securing and Traversing (RAST) System,” DAF Indal Ltd., Mississauga, ON, Canada, SAE Technical Paper Series 811080, 1981.
- [2] (2015) Naval Handling Systems. Curtiss-Wright Indal. [Online]. Available: https://s2.q4cdn.com/767595508/files/doc_downloads/indal/modeling/INDAL-Brochure.pdf [Accessed: 2020-06-28]
- [3] J. Blackwell and R. A. Feik, “A Mathematical Model of the On-deck Helicopter/ship Dynamic Interface,” Aeronautical Research Laboratory, Melbourne, Australia, Tech. Rep. ARL-AERO-TM-405, 1989.
- [4] A. R. Tadros and R. G. Langlois, “Securing and Handling Helicopters on Board Ships, Essential Factors for Meeting Safety and Operational Requirements,” Indal Technologies Inc., Mississauga, ON, Canada, Tech. Rep. [Online]. Available: <https://www.cw-ems.com/indal/products/helicopter-securing-and-traversing/default.aspx>
- [5] D. R. Linn and R. G. Langlois, “Development and Experimental Validation of a Shipboard Helicopter On-Deck Maneuvering Simulation,” *Journal of Aircraft*, vol. 43, no. 4, pp. 895–906, 2006.
- [6] D. R. Langlois, D. Z. H. Zhu, and M. LaRosa, “Modelling and Simulation of Skid-equipped Shipboard Rotorcraft,” Curtiss-Wright - INDAL Technologies, Mississauga, ON, Canada, Tech. Rep., 2015. [Online]. Available: <https://www.cw-ems.com/indal/products/helicopter-securing-and-traversing/default.aspx>

- [7] A. J. Garcia and G. Barakos, “Accurate Predictions of Rotor Hover Performance at Low and High Disc Loadings,” *Journal of Aircraft*, vol. 55, no. 1, pp. 89–110, January 2018.
- [8] D. T. Balch, A. Saccullo, and T. W. Sheehy, “Experimental study of Main Rotor Tip Geometry and Tail rotor Interactions in Hover - Volume I,” Ames Research Center, Moffett Field, CA, Tech. Rep. NASA CR-166485, June 1983.
- [9] R. Ernst and B. Ferrier, “Fire Scout Launch and Recovery Considerations in Unexpected Ship Roll Motion Conditions,” *Naval Engineers Journal*, vol. 129, no. 4, pp. 87–98(12), December 2017.
- [10] C. N. Manley, “Armed Drones for the Royal Canadian Navys,” Canadian Forces College, Toronto, ON, Canada, Tech. Rep., 2017. [Online]. Available: <https://www.cfc.forces.gc.ca/259/290/405/305/manley.pdf>
- [11] H. Kumar and T. Hussein. (2019) QinetiQ to Supply Unmanned Aircraft Systems to Canadian Armed Forces. [Online]. Available: <https://www.naval-technology.com/news/canadian-navy-drones-qinetiq/> [Accessed: 2020-06-27]
- [12] Heligrid Helicopter Landing System. Cramm HLS. [Online]. Available: <https://pdf.nauticexpo.com/pdf/cramm-yachting-systems-bv/heligrid/22833-41191.html> [Accessed: 2020-06-28]
- [13] (2016) Helicopter and UAV Flight Deck Securing and Handling Devices. Naval Group. [Online]. Available: <https://www.naval-group.com/wp-content/uploads/2017/01/helicopter-and-uav-flight-deck-securing-and-handling-devices.pdf> [Accessed: 2020-06-28]
- [14] R. T. Schmitke and B. W. Whitten, “SHIPMO - A FORTRAN Program to Predict Ship Motions in Waves (1981),” 1981, DREA Technical Memorandum 81/C.
- [15] G. L. Loeff and F. van Walree, “ITI Developed New Time Domain Ship Motion Program for High Sea State Conditions (SPLASHMo),” February 2006, naval Forces.
- [16] R. G. Langlois, M. LaRosa, and D. A. R. Tadros, “Development, Validation, and Application of the Dynaface[®] Helicopter/Ship Dynamic Interface Simulation Software Package,” vol. 35, San Diego, CA, 2003, edited by V. W. Ingalls.

- [17] (2016) Seakeeping Prediction Software. BMT. [Online]. Available: https://www.bmt.org/media/3646/shipmopc_seakeeping_prediction.pdf [Accessed: 2020-08-31]
- [18] G. L. Loeff and F. van Walree, “Validation of Maneuvering Prediction Capabilities of FREDYN, FREDYN version 9.6,” MARIN, Tech. Rep. No. 08883-45-CPM, February 2006.
- [19] A. R. Feldman and R. G. Langlois, “Development of an Experimental Aircraft/ship Dynamic Interface Analysis Motion Facility,” in *In Proc. 7th Canadian Marine Hydromechanics and Structures Conference*, Halifax, NS, Canada, September 2005.
- [20] —, “Autonomous Straightening and Traversing of Shipboard Helicopters,” *Journal of Field Robotics*, vol. 23, no. 2, pp. 123–139, February 2006.
- [21] M. J. Léveillé and R. G. Langlois, “Spacial Modelling and Simulation of On-deck Helicopter Securing and Manoeuvring,” in *Proceedings of the 70th Annual Forum of the American Helicopter Society*, Montreal, QC, Canada, May 2014, pp. 740–749.
- [22] D. R. G. Langlois and D. A. R. Tadros, “User’s Manual for the Aircraft/Ship Dynamic Interface Simulation Dynaface[®] Release 5.0.” Indal Technologies Inc, Mississauga, ON, Canada, Tech. Rep. ITI Report No. 99/419, January 1998.
- [23] S. R. Borneman, J. McCallum, and M. LaRosa, “Extending UAV Operating Envelopes,” Curtiss-Wright - INDAL Technologies, Mississauga, ON, Canada, Tech. Rep., 2015. [Online]. Available: <https://www.cw-ems.com/indal/products/helicopter-securing-and-traversing/default.aspx>
- [24] R. G. Lee and S. J. Zan, “Unsteady Aerodynamic Loads On a Helicopter Fuselage In a Ship Air Wake,” Montreal, QC, Canada, May 2002.
- [25] S. J. Zan, “Experimental Determination of Rotor Thrust in a Ship Airwake,” *Journal of the American Helicopter Society*, vol. 47, no. 2, pp. 100–118, April 2002.
- [26] E. Alpman, L. N. Long, D. O. Bridges, and J. F. Horn, “Fully-coupled Simulations of the Rotorcraft/ship Dynamic Interface,” American Helicopter Society 63rd Annual Forum, Virginia Beach, VA, U.S.A., May 2007.

- [27] A. S. Wall, S. J. Zan, R. G. Langlois, and F. F. Afagh, “Correlated Turbulence Modelling: An Advancing Fourier Series Method,” *Journal of Wind Engineering and Industrial Aerodynamics*, vol. 123, no. Part A, pp. 155–162, December 2013.
- [28] A. S. Wall, R. G. Langlois, F. F. Afagh, and S. J. Zan, “Modelling Helicopter Blade Sailing: Contributions From Ship Motion and Unsteady Airwake to Blade Dynamic Response,” Toronto, Canada, April 2007.
- [29] F. Khouli, A. S. Wall, F. F. Afagh, and R. G. Langlois, “Influence of Ship Motion On the Aeroelastic Response of a Froude-scaled Maritime Rotor System,” vol. 54, January 2007, pp. 170–181.
- [30] *RotorLib FDM for C++*, RTDynamics, Rosenheim, Germany. [Online]. Available: http://www.rtdynamics.com/products-services/simulation-and-training/rotorlib-fdm-for-c/?doing_wp_cron=1593700957.7624619007110595703125
- [31] S. Kockara, T. Halic, K. Iqbal, C. Bayrak, and R. Rowe, “Collision detection: A survey,” in *2007 IEEE International Conference on Systems, Man and Cybernetics*, 2007, pp. 4046–4051.
- [32] M. Figueiredo, L. Marcelino, and T. Fernando, “A Survey on Collision Detection Techniques for Virtual Environments,” 2002.
- [33] C. Liang and X. Liu, “The Research of Collision Detection Algorithm Based on Separating axis Theorem,” *International Journal of Science*, vol. 2, no. 10, pp. 110–114, 2015.
- [34] S. Gottschalk, “Separating Axis Theorem,” Department of Computer Science, UNC Chapel Hill, Tech. Rep. TR96-024, 1996.
- [35] G. Gilardi and I. Sharf, “Literature Survey of Contact Dynamics Modelling,” *Mechanism and Machine Theory*, vol. 37, no. 10, pp. 1213 – 1239, 2002.
- [36] V. Lampaert, J. Swevers, and F. Al-Bender, “Experimental Comparison of Different Friction Models for Accurate Low-velocity Tracking,” 2002.
- [37] Y. Liu, J. Li, Z. Zhang, X. Hu, and W. Zhang, “Experimental Comparison of Five Friction Models on the Same Test-bed of the Micro Stick-slip Motion System,” *Mechanical Sciences*, vol. 6, pp. 15–28, March 2015.

- [38] F. Marques, P. Flores, J. C. P. Claro, and H. M. Lankarani, “A Survey and Comparison of Several Friction Force Models for Dynamic Analysis of Multi-body Mechanical Systems,” *Nonlinear Dynamics*, vol. 86, no. 3, pp. 1407–1443, November 2016.
- [39] E. Pennestrì, V. Rossi, P. Salvini, and P. P. Valentini, “Review and Comparison of Dry Friction Force Models,” *Nonlinear Dynamics*, vol. 83, no. 4, pp. 1785–1801, March 2016.
- [40] C. C. de Wit, H. Olsson, K. J. Astrom, and P. Lishinsky, “A New Model for Control of Systems with Friction,” *IEEE Transactions On Automatic Controls*, vol. 40, no. 3, pp. 418–425, March 1995.
- [41] P. R. Dahl, “A Solid Friction Model,” The Aerospace Corporation, El Segundo, CA, Tech. Rep. SAMSO-TR-77-131, 1968.
- [42] J. Swevers, F. Al-Bender, C. G. Ganseman, and T. Prajogo, “An Integrated Friction Model Structure with Improved Pre-sliding Behavior for Accurate Friction Compensation,” *IEEE Transactions On Automatic Control*, vol. 45, no. 4, pp. 675–686, 2000.
- [43] W. Z. Stepniewski, “Basic Theories of Rotor Aerodynamics (With Applications to Helicopters),” Boeing Vertol Company, Philadelphia, PA, Tech. Rep. N79-22039, January 1979.
- [44] D. V. Leza, “Development of A Blade Element Method for CFD Simulations of Helicopters Using the Actuator Disc Approach,” Master’s thesis, Delft University of Technology, Delft, 2018.
- [45] M. J. Léveillé, “Development of a Spacial Dynamic Handling and Securing Model for Shipboard Helicopters,” Master’s thesis, Carleton University, Ottawa, ON, Canada, 2013.
- [46] P. E. Nikravesh, *Computer-Aided Analysis of Mechanical Systems*. Englewood Cliffs, NJ: Prentice Hall, 1988.
- [47] T. R. Kane, P. W. Likins, , and D. A. Levinson, *Spacecraft Dynamics*. New York: McGraw-Hill, 1983.

- [48] A. Purushotham and J. Anjeneyulu, “Kane’s Method for Robotic Arm Dynamics: a Novel Approach,” *IOSR Journal of Mechanical and Civil Engineering (IOSR-JMCE)*, vol. 6, no. 4, pp. 7–13, May-June 2013.
- [49] E. Stoneking, “Implementation of Kane’s Method for a Spacecraft Composed of Multiple Rigid Bodies,” August 2013.
- [50] K.-J. Bathe, *Finite Element Procedures*. New Jersey: Prentice Hall, 1996, p. 768.
- [51] R. D. Cook, *Finite Element Modelling for Stress Analysis*. Canada: Wiley, 1995, pp. 230–232.
- [52] B. W. McCormick, *Aerodynamics, Aeronautics, and Flight Mechanics*. Wiley, August 1979, p. 196.
- [53] R. L. Smith, “Closed-form Equations for the Lift, Drag, and Pitching-Moment Coefficients of Airfoil Sections in Subsonic Flow,” Ames Research Center, Moffett Field, CA, Tech. Rep. NASA-TM-78492, August 1978.
- [54] B. Stellato, S. Ober-Blöbaum, and P. Goulart, 2017.
- [55] A. C. Hindmarsh, *ODEPACK.f*, Center for Applied Scientific Computing, L-561, Livermore, CA, February 2008, (DLSO-DAR Subroutine, 12 November 2003 Version). [Online]. Available: https://people.sc.fsu.edu/~jburkardt/f77_src/odepack/odepack.html
- [56] —, “A Systematized Collection of ODE Solvers,” *IMACS Transactions on Scientific Computation*, vol. 1, pp. 55–64, 1983, r. S. Stepleman et al. edits.
- [57] L. R. Petzold, “Automatic Selection of Methods for Solving Stiff and Nonstiff Systems of Ordinary Differential Equations,” *SIAM Journal on Scientific and Statistical Computing*, vol. 4, no. 1, pp. 136–148, 1983.
- [58] K. L. Hiebert and L. F. Shampine, “Implicitly Defined Output Points for Solutions of ODEs,” Sandia Labs, Albuquerque, NM, Tech. Rep. SAND-80-0180, February 1980.
- [59] (2020) Airfoil Tools. [Online]. Available: <http://airfoiltools.com/index> [Accessed: 2020-08-04]

- [60] J. J. Totah, "A Critical Assesment of UH-60 Main Rotor Blade Airfoil Data," Ames Research Center, Moffett Field, CA, Tech. Rep. NASA-TM-103985.
- [61] C. N. Keys, "Performance Prediction of Helicopters," Boeing Vertol Company, Philadelphia, PA, Tech. Rep. NASA-CR-3083, January 1979.

Appendix A

SRAMSS I/O File Structure

This appendix outlines the structure of the input and output files for SRAMSS. The input files include the complete description of Initial conditions, aircraft parameters, prescribed motions, and simulation parameters required. The output Files contain the time-stamped raw data calculated by SRAMSS.

A.1 Input Files

Simulation.inp

- Line 1:** t_{start} t_{end} simulation time start and end [s]
- Line 2:** Δt_{sol} integrator default solution time-step [s]
- Line 3:** t_{mult} Multiplier for number of solution vectors stored before print to file ($t_{end} - t_{start}$)/ $\Delta t_{sol} t_{mult}$
- Line 4:** N_P Number of polygons in simulation environment
- Line 5:** \mathbb{Z} DFE [\mathbf{M}] assembly method [0=SRAMSS automatic generation, 1=Read-in]
- Line 6:** \mathbb{Z} DFE [\mathbf{C}] assembly method [0=SRAMSS automatic generation, 1=Read-in]
- Line 7:** \mathbb{Z} DFE [\mathbf{K}] assembly method [0=SRAMSS automatic generation, 1=Read-in]
- Line 8:** \mathbb{Z} DLSODAR: ITOL error control option.
- Line 9:** \mathbb{R} DLSODAR: RTOL relative error tolerance
- Line 10:** \mathbb{R} DLSODAR: ATOL absolute error tolerance

- Line 11:** \mathbb{Z} DLSODAR: ITASK integration task type
- Line 12:** \mathbb{Z} DLSODAR: ISTATE ==1 for initialization
- Line 13:** \mathbb{Z} DLSODAR: JT Jacobian type flag
- Line 14:** \mathbb{Z} DLSODAR: IOPT optional inputs flag, if any of RWORK or IWORK are set to 0.d0 or 0, DLSODAR will use default value
- Line 15:** \mathbb{R} DLSODAR: RWORK(5) if IOPT==1, H0 step size attempted on first step
- Line 16:** \mathbb{R} DLSODAR: RWORK(6) if IOPT==1, HMAX the max absolute step size allowed
- Line 17:** \mathbb{R} DLSODAR: RWORK(7) if IOPT==1, HMIN the min absolute step size allowed
- Line 18:** \mathbb{Z} DLSODAR: IWORK(5) if IOPT==1, Flag to generate extra printing at method switches. [IXPR=0 extra printing, IXPR=1print data on each switch]
- Line 19:** \mathbb{Z} DLSODAR: IWORK(6) if IOPT==1, Max number of internal solver steps
- Line 20:** \mathbb{Z} DLSODAR: IWORK(7) if IOPT==1, Maximum number of messages printed per problem.
- Line 21:** \mathbb{Z} DLSODAR: IWORK(8) if IOPT==1, The maximum order to be allowed for the nonstiff (Adams) method. default value is 12, [≤ 12].
- Line 22:** \mathbb{Z} DLSODAR: IWORK(9) if IOPT==1, The maximum order to be allowed for the stiff (BDF) method. The default value is 5, [≤ 5].
- Line 23:** \mathbb{Z} Print Δt_{sol} Solver stats [0=no stats, 1=time propagation stats, 2=full solution stats]

Output_options.inp

- Line 1:** \mathbb{Z} Generalized states solution output file [1=yes, 0=no]
- Line 2:** \mathbb{Z} Simulation stats
- Line 3:** \mathbb{Z} Ship polygon output file
- Line 4:** \mathbb{Z} RSD polygon output file

- Line 5:** \mathbb{Z} Left RSD clamp output file
- Line 6:** \mathbb{Z} Right RSD clamp output file
- Line 7:** \mathbb{Z} Ship OCP solution output file
- Line 8:** \mathbb{Z} RSD OCP solution output file
- Line 9:** \mathbb{Z} Left RSD clamp OCP output file
- Line 10:** \mathbb{Z} right RSD clamp OCP output file
- Line 11:** \mathbb{Z} Contact forces vector on n_{jc} in N output file
- Line 12:** \mathbb{Z} Induced thrust vector on H in H output file

ICs.inp

- Line i:** \mathbf{u}_i \mathbb{Z} Initial condition of generalized speed u_i [m/s], and generalized speed type $u_{i,type}$ [0=free, 1=contact, 2=fixed, 3=prescribed]. repeated line through all u
- Line i:** \mathbf{q}_i \mathbb{Z} Initial condition of generalized coordinate q_i [m], and generalized coordinate type $q_{i,type}$ [0=free, 1=contact, 2=fixed, 3=prescribed]. repeated line through all q

Properties_helo.inp

- Line 1:** m_H Airframe mass [kg]
- Line 2:** I_H Airframe moment of Inertia [kg m²]
- Line 3:** N_d Number of external dampers
- Line 4:** $\left. \frac{H}{H} \vec{\mathbf{r}}^{M_1} \right|_x, \dots, \left. \frac{H}{H} \vec{\mathbf{r}}^{M_{N_d}} \right|_x$ Winglet external shock mount x-position [m]
- Line 5:** $\left. \frac{H}{H} \vec{\mathbf{r}}^{M_1} \right|_y, \dots, \left. \frac{H}{H} \vec{\mathbf{r}}^{M_{N_d}} \right|_y$ Winglet external shock mount y-position [m]
- Line 6:** $\left. \frac{H}{H} \vec{\mathbf{v}}^{M_1} \right|_x, \dots, \left. \frac{H}{H} \vec{\mathbf{v}}^{M_{N_d}} \right|_x$ Winglet external shock mount x-velocity [m/s]
- Line 7:** $\left. \frac{H}{H} \vec{\mathbf{v}}^{M_1} \right|_y, \dots, \left. \frac{H}{H} \vec{\mathbf{v}}^{M_{N_d}} \right|_y$ Winglet external shock mount y-velocity [m/s]
- Line 8:** n_{j_1}, \dots, n_{j_d} DFE node mount number
- Line 9:** $\Delta_{d_1,0}, \dots, \Delta_{d_n,0}$ Underformed discrete damper lengths [m]

- Line 10:** K_d Spring constant for linear discrete damper [N/m]
- Line 11:** C_d Damping constant for linear discrete damper [Nm/s]
- Line 12:** $\frac{H}{H}\vec{r}^{CP}$ Airframe Centre of pressure [m]
- Line 13:** $A_{eq,x}$ Airframe equivalent flat plate area [m²]
- Line 14:** $\frac{H}{H}\vec{r}^R$ Rotor disc center [m]
- Line 15:** N_b Number of rotor blades
- Line 16:** R_b Radius of rotor blade [m]
- Line 17:** R_i Inner effective blade radius as percentage of R_b [%]
- Line 18:** R_o Outer effective blade radius as percentage of R_b [%]
- Line 19:** N_e Number of blade elements
- Line 20:** N_ψ Number of rotor disc sectors
- Line 21:** \mathbb{Z} Number of data points for rotor blade profile (r)
- Line 22:** r Blade data point radii [$r = 0$ to $r = R$] limits of blade radius must be outside bounds set by $R_i R_b$ to $R_o R_b$ [m]
- Line 23:** $c(r)$ Blade chord length for each blade data point radii [m]
- Line 24:** $\theta_t(r)$ Blade twist angle @radius [rad]
- Line 25:** $t/c(r)$ Blade thickness ratio [%]
- Line 26:** $\frac{dC_L}{d\alpha}(r)$ Linear slope C_L vs α [rad⁻¹]
- Line 27:** $C_{L,0}(r)$ zero angle of attack C_L
- Line 28:** $\frac{dC_D}{d\alpha}(r)$ Linear slope C_D vs α [rad⁻¹]
- Line 29:** $C_{D,0}(r)$ zero angle of attack C_D

Properties_contact_mech.inp

- Line 1:** K_p Penetration stiffness [N/m]
Line 2: C_p Penetration damping [Nm/s]
Line 3: K_f Friction stiffness coefficient [N/m]
Line 4: C_f Friction damping coefficient [Nm/s]
Line 5: μ_d Dynamic friction coefficient
Line 6: μ_s Static Friction coefficient
Line 7: v_s Stribeck velocity threshold [m/s]

Properties_FE_map.inp

- Line i:** $e_r, n_a, n_b, E_r, I_r, A_r, R$ r th DFE element properties: element no., node a, node b, E [Pa], I [m⁴], xA [m²], density [kg m⁻³]. line repeated for all elements in DFE model.

Properties_FE_IC.inp

- Line i:** \mathbf{q}_i \mathbb{Z} Undeformed DFE generalized coordinate \mathbf{q}_i [m], and generalized coordinate type $\mathbf{q}_{i,type}$ =[0=free, 1=contact, 2=fixed, 3=prescribed]. repeated line through to \mathbf{q}_{18+3N_n}

Properties_FE_*mat.inp

- Line i:** [$*_i$] Row i of optional read-in DFE matrix. [$*=M$ Properties_FE_Mmat.inp, $*=C$ Properties_FE_Cmat.inp, $*=K$ Properties_FE_Kmat.inp]. Repeated for all rows of DFE matrix

Polygon_*.inp

- Line 1:** $*\vec{r}^{*1}|_x, \dots, *\vec{r}^{*m}|_x$ * polygon vertices x-positions [m], polygon designation [$*=S$ Prescribed_ship.inp, $*=D$ Prescribed_rsd.inp $*=CL$ Prescribed_clamplleft.inp, $*=CR$ Prescribed_clampright.inp]

Line 2: ${}^*_{*}\vec{r}^{*1}|_y, \dots, {}^*_{*}\vec{r}^{*m}|_y$ * polygon vertices y-positions [m], polygon designation [*=S ship deck, *=D RSD deck, *=CL left wedge clamp, *=CR right wedge clamp]

Prescribed_*.inp

Line t: ${}^*_{*-1}\vec{r}^{*}$ At time t [s], prescribed position of frame with respect to preceding frame in chain of frames [m]. ${}^N_N\vec{r}^S, {}^S_S\vec{r}^D, {}^D_D\vec{r}^{CL}, {}^D_D\vec{r}^{CR}$ in separate *Prescribed_*.inp* files.

Prescribed_aero.inp

Line t: $t, {}^N_N\vec{v}^W, {}^R_R\vec{\omega}^{RBE}, \theta_{coll}, \theta_{cyc,max}, \psi_{max}$ At time t [s], wind velocity [m/s], rotor rpm [rad/s], collective pitch setting [rad], cyclical pitch setting [rad], maximum cyclic pitch azimuth [rad].

A.2 Output Files

GEN_SOLUTION.out

Line t : $t, \mathbf{u}, \mathbf{q}$ Time-stamped vector of generalized speeds and positions.

POLY_*.out

Line t : $t, \frac{N}{N}\vec{\mathbf{r}}^{*1}|_x, \frac{N}{N}\vec{\mathbf{r}}^{*1}|_y, \dots, \frac{N}{N}\vec{\mathbf{r}}^{*m}|_x, \frac{N}{N}\vec{\mathbf{r}}^{*m}|_y$ Time-stamped polygon vertices relative to the inertial frame [m], polygon designation [*=S POLY_SHIP.out, *=D POLY_RSD.out, *=CL POLY_L_CLAMP.out, *=CR POLY_R_CLAMP.out]

OCP_*.out

Line t : $t, \frac{*}{N}\vec{\mathbf{o}}^{n_{j1}}|_x, \frac{*}{N}\vec{\mathbf{o}}^{n_{j1}}|_y, \dots, \frac{*}{N}\vec{\mathbf{o}}^{n_{jc}}|_x, \frac{*}{N}\vec{\mathbf{o}}^{n_{jc}}|_y$ Time-stamped polygon OCPs relative to the inertial frame[m], polygon designation [*=S OCP_SHIP.out, *=D OCP_RSD.out, *=CL OCP_L_CLAMP.out, *=CR OCP_R_CLAMP.out]

FORCE_CONTACT.out

Line t : $t, \frac{n_{j1}}{N}\vec{\mathbf{F}}^c_k, \dots, \frac{n_{jc}}{N}\vec{\mathbf{F}}^c_k$ Time-stamped total contact forces on all contact nodes, expressed in the inertial frame [N, N, Nm]

FORCE_INDUCED.out

Line t : $t, \frac{H}{H}\vec{\mathbf{F}}^{BEM}, \frac{H}{H}\vec{\mathbf{M}}^{BEM}$ Time-stamped rotor disc thrust and rolling-moments [N, N, Nm]

SIM_STATS.out

Line t : $t, \mathbb{Z}, \mathbb{Z}, \mathbb{Z}, \mathbb{Z}, \mathbb{Z}, \mathbb{Z}, \mathbb{R}, \mathbb{R}, \mathbb{Z}$ Time-stamped simulation and *DLSODAR*.for statistics and simulation summary. time [s], XddotF.f90 evaluations/ Δt_{sol} , XddotF.f90 evaluations/ t , XddotG.f90 evaluations/ Δt_{sol} , XddotG.f90 evaluations/ t , DLSODAR internal steps/ Δt_{sol} , DLSODAR internal steps/ t , $t_{CPU}/\Delta t_{sol}$ [sCPU], t_{CPU}/t [sCPU], $\#\Delta t_{sol}$

Appendix B

Case 6 Prescribed Aerodynamics

B.1 Case 6.2: Rotor Thrust without Wind

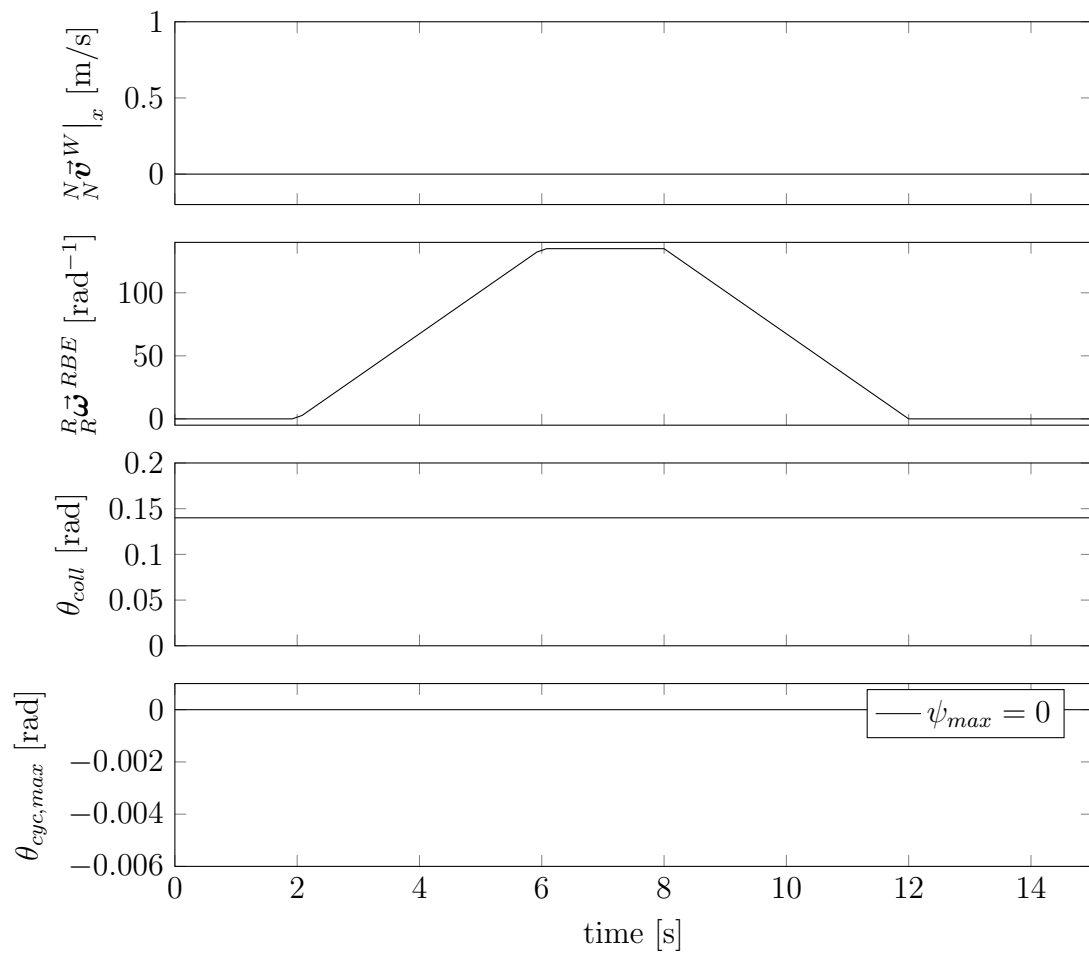


Figure B.1: Case 6.2 Prescribed aerodynamic values.

B.2 Case 6.3: Rotor Thrust with Head-wind

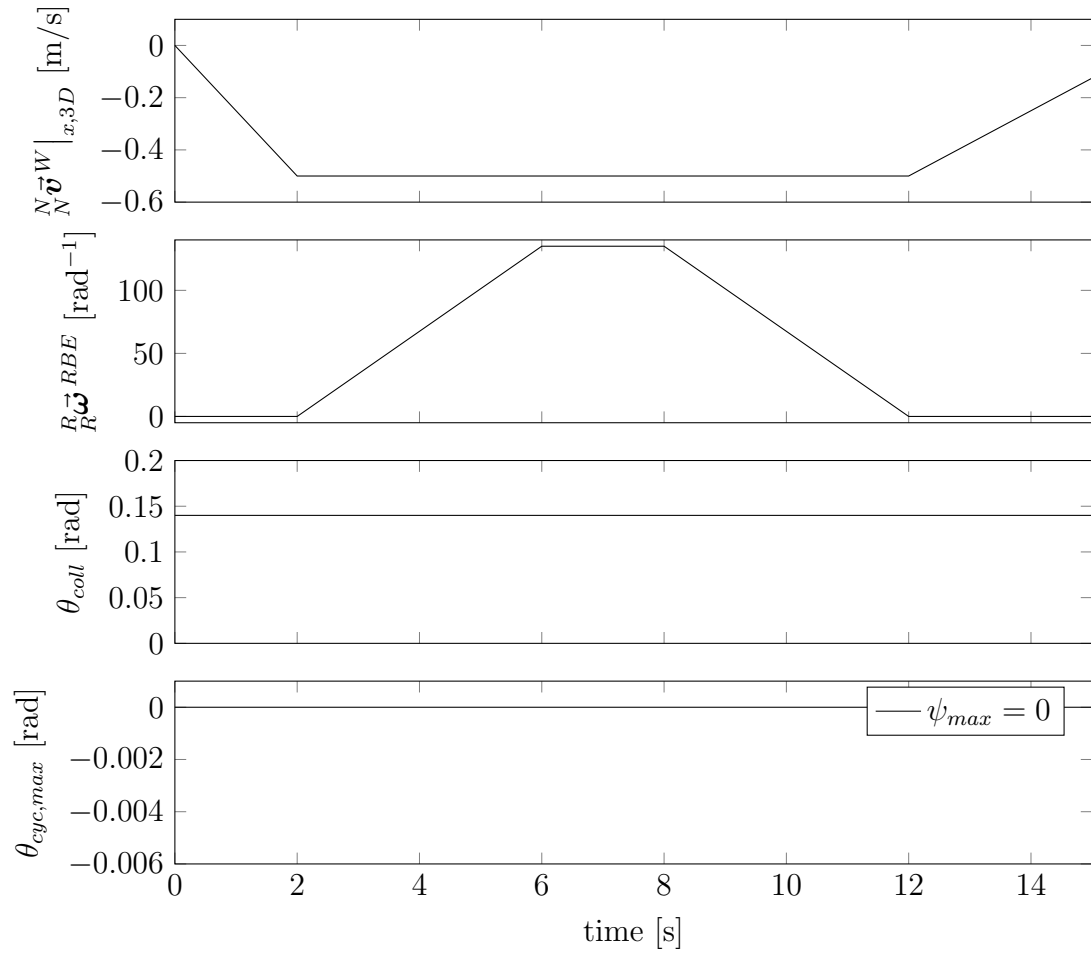


Figure B.2: Case 6.3 Prescribed aerodynamic values.

B.3 Case 6.4: Rotor Thrust with Head-wind and Cyclic Compensation

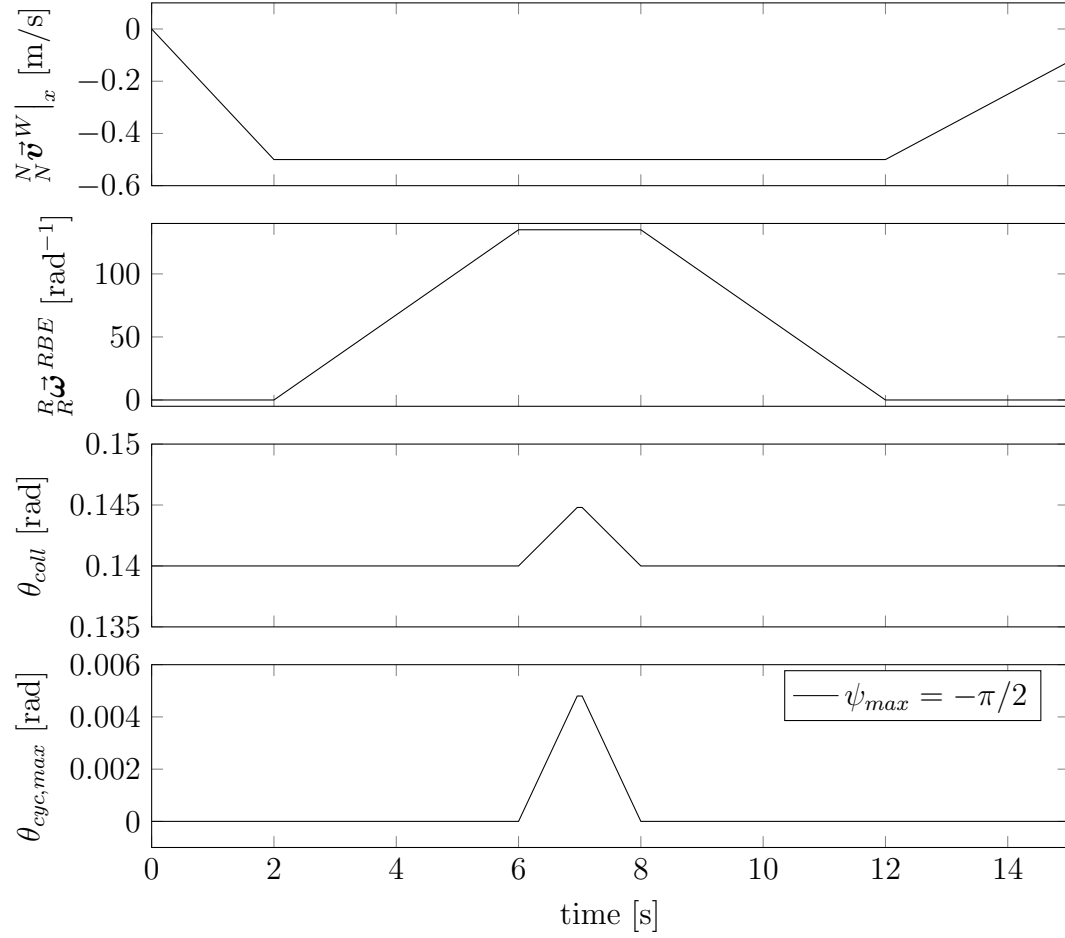


Figure B.3: Case 6.4 Prescribed aerodynamic values.

Appendix C

Case 6 Experimental Blade Profiles

C.1 Case 6.5 S-76 Experimental Blade Profile

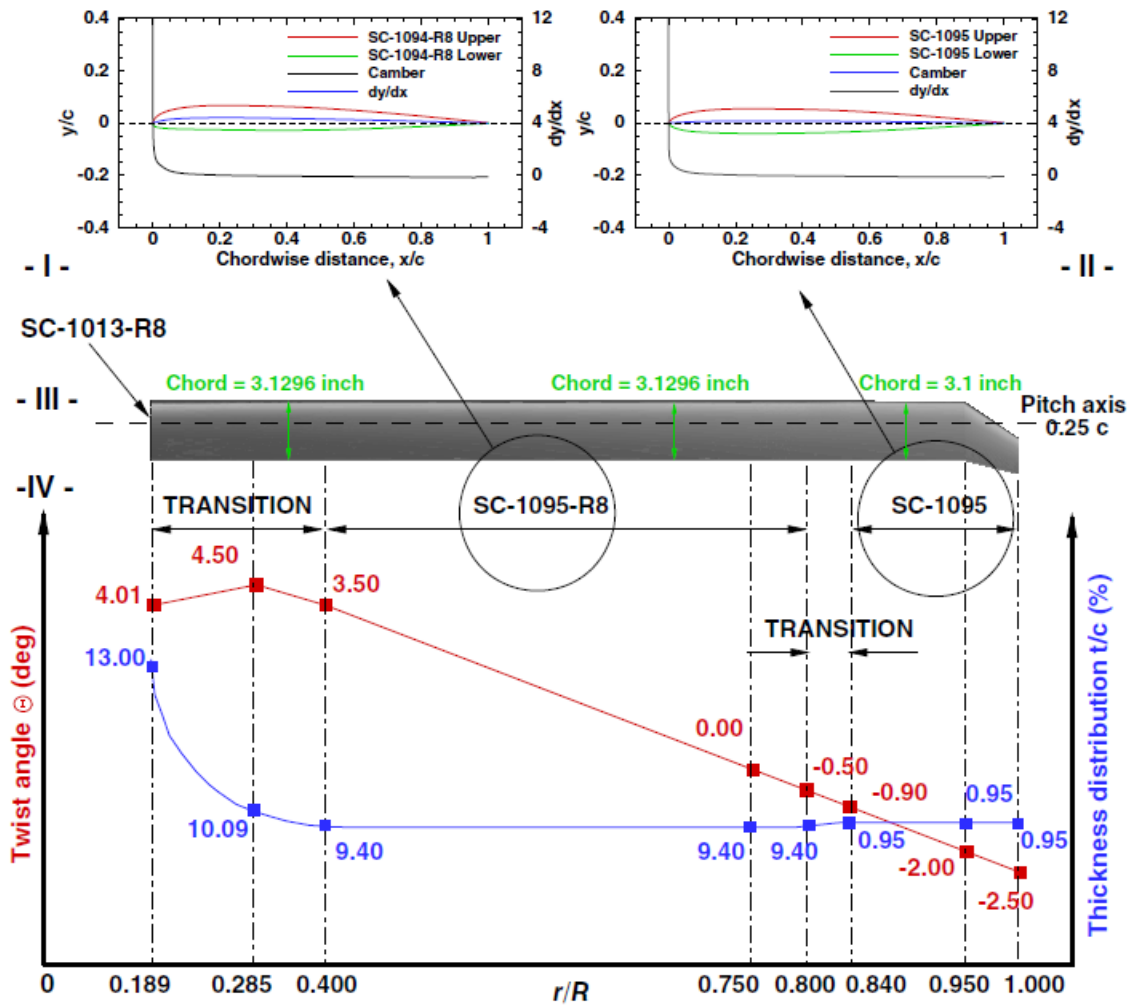


Figure C.1: S-76 model rotor blade profile [7].

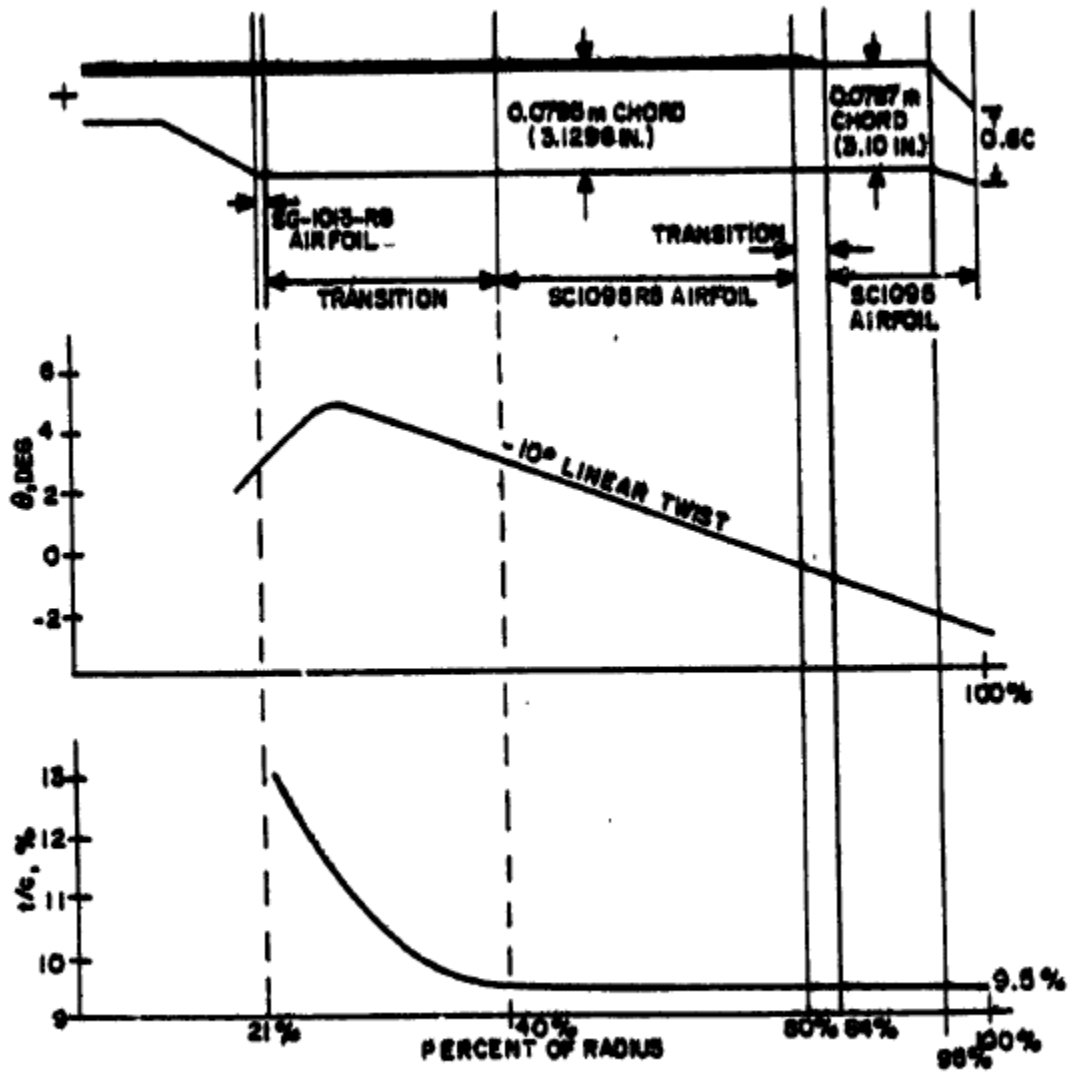


Figure C.2: S-76 model rotor blade profile [8].

C.2 Case 6.5 S-76 SRAMSS Blade Profile

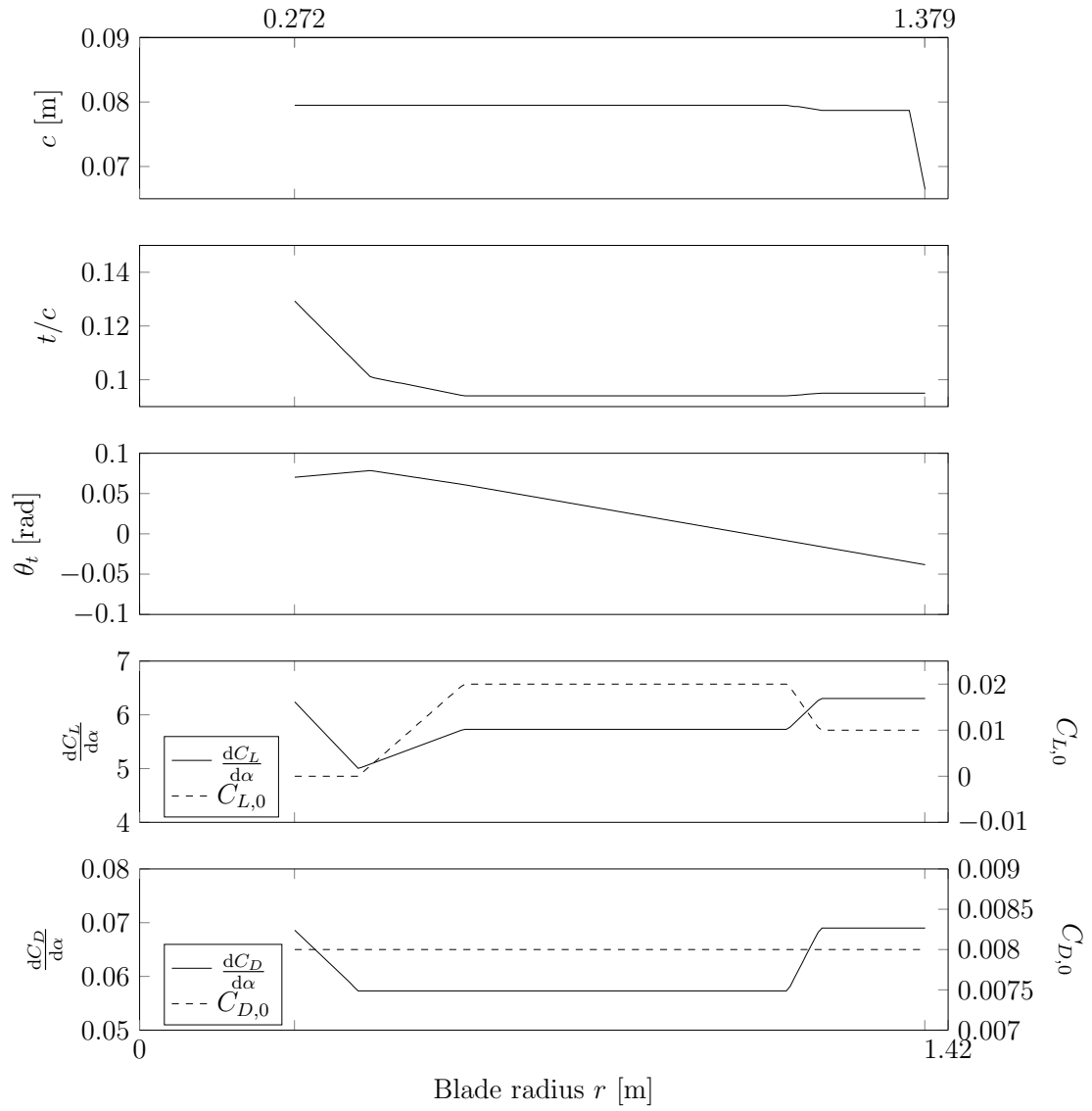


Figure C.3: Case 6.5 SRAMSS S-76 model rotor blade profile.

Table C.1: SRAMS S-76 model BEM parameters

Parameter	Variable	Value
Number of Rotor Blades	n_b	4
Number of Blade elements	N_e	160
Number of Rotor Disc Sectors	N_ψ	20
Rotor Blade Radius	R_b	1.42 m
Inner Effective Rotor Disc Radius	R_i	0.189 (0.272 m)
Outer Effective Rotor Disc Radius	R_o	0.972 (1.377 m)
Solidity ratio	σ	0.0704
Blade Chord Length	c	Fig.C.3
Blade Thickness Ratio	t/c	
Blade Twist	θ_t	
Uncorrected Lift Coefficient Slope	$\frac{dC_L}{d\alpha}$	
Uncorrected Lift Coefficient Offset	$C_{L,0}$	
Uncorrected Drag Coefficient Slope	$\frac{dC_D}{d\alpha}$	
Uncorrected Drag Coefficient Offset	$C_{D,0}$	

Appendix D

Case 8 Prescribed Parameters

D.1 Case 8: Prescribed Aerodynamics

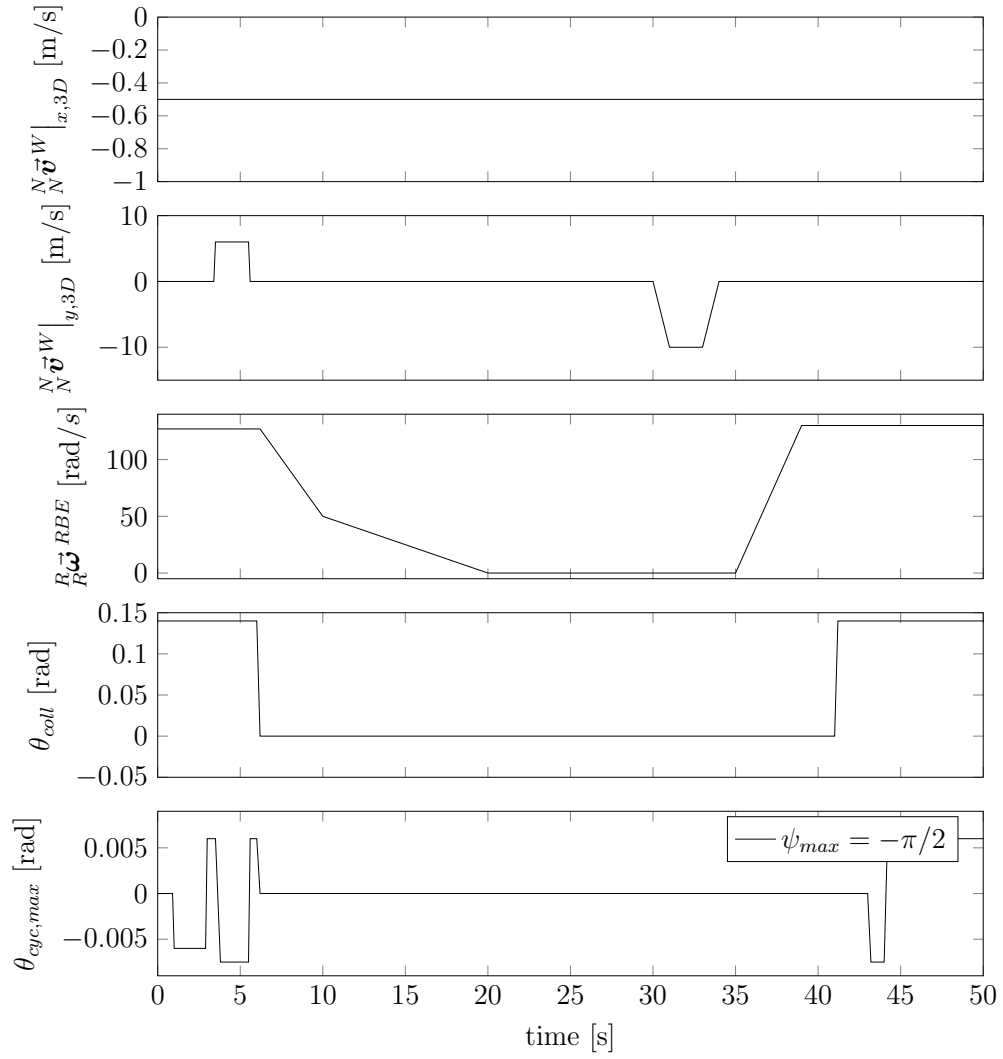


Figure D.1: Case 8 Prescribed aerodynamic values.

D.2 Case 8: Prescribed Motions

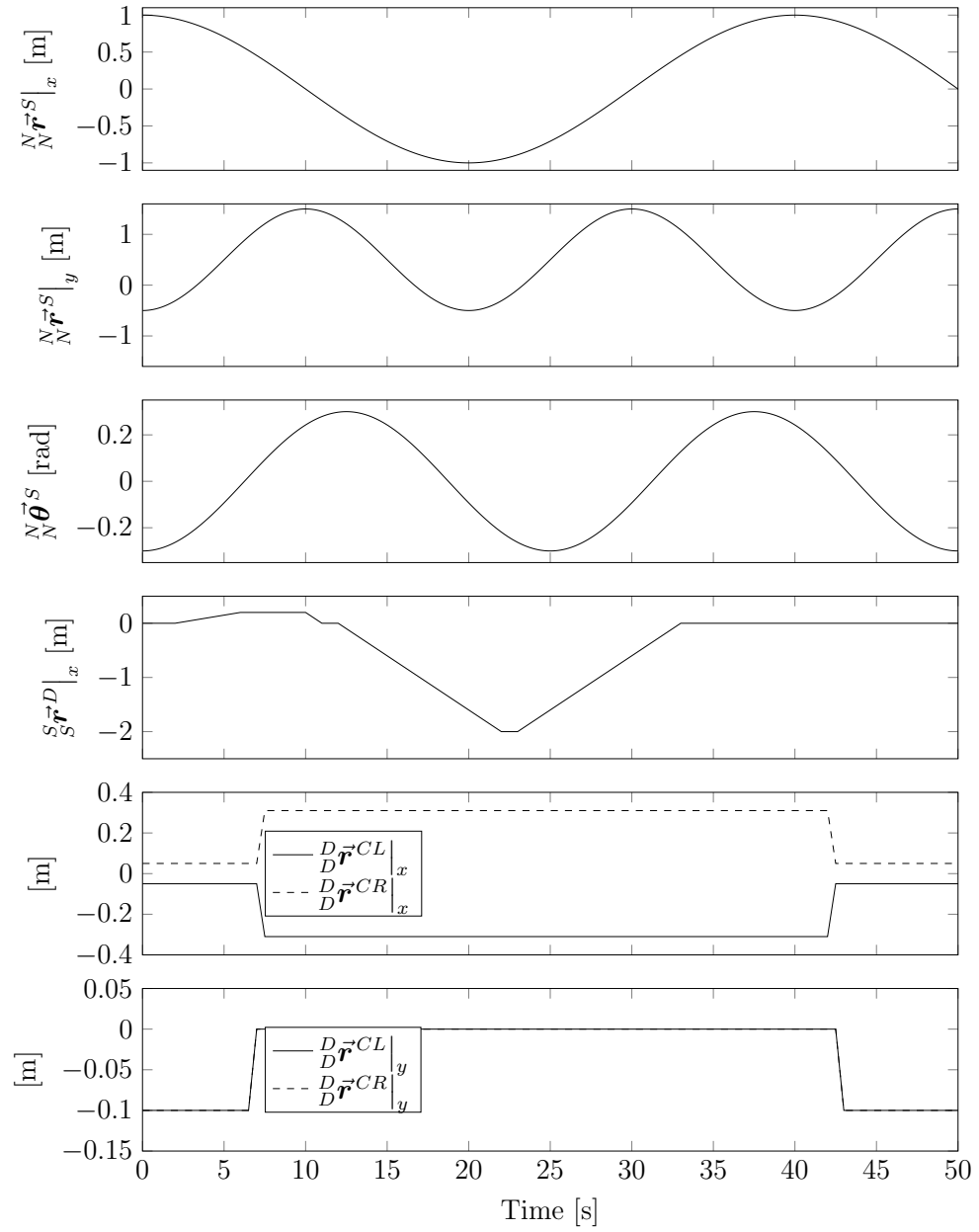


Figure D.2: Case 8 Prescribed polygon motions.

Appendix E

Simulation Statistics

E.1 Case 8: 18/20/160

step #	t	delt t/CPU	2441	6.1025	Inf	2483	6.2075	Inf	2525	6.3125	0.0533
2400	6	Inf	2442	6.105	Inf	2484	6.21	0.0533	2526	6.315	Inf
2401	6.0025	Inf	2443	6.1075	Inf	2485	6.2125	0.16	2527	6.3175	Inf
2402	6.005	0.0533	2444	6.11	0.0533	2486	6.215	Inf	2528	6.32	Inf
2403	6.0075	Inf	2445	6.1125	Inf	2487	6.2175	Inf	2529	6.3225	Inf
2404	6.01	0.04	2446	6.115	Inf	2488	6.22	Inf	2530	6.325	Inf
2405	6.0125	Inf	2447	6.1175	Inf	2489	6.2225	Inf	2531	6.3275	Inf
2406	6.015	Inf	2448	6.12	Inf	2490	6.225	Inf	2532	6.33	0.16
2407	6.0175	Inf	2449	6.1225	Inf	2491	6.2275	Inf	2533	6.3325	Inf
2408	6.02	0.16	2450	6.125	Inf	2492	6.23	Inf	2534	6.335	Inf
2409	6.0225	Inf	2451	6.1275	Inf	2493	6.2325	Inf	2535	6.3375	Inf
2410	6.025	Inf	2452	6.13	Inf	2494	6.235	Inf	2536	6.34	Inf
2411	6.0275	Inf	2453	6.1325	Inf	2495	6.2375	Inf	2537	6.3425	Inf
2412	6.03	Inf	2454	6.135	Inf	2496	6.24	Inf	2538	6.345	Inf
2413	6.0325	Inf	2455	6.1375	Inf	2497	6.2425	Inf	2539	6.3475	Inf
2414	6.035	Inf	2456	6.14	Inf	2498	6.245	Inf	2540	6.35	Inf
2415	6.0375	Inf	2457	6.1425	Inf	2499	6.2475	Inf	2541	6.3525	Inf
2416	6.04	Inf	2458	6.145	Inf	2500	6.25	Inf	2542	6.355	Inf
2417	6.0425	Inf	2459	6.1475	Inf	2501	6.2525	0.0533	2543	6.3575	Inf
2418	6.045	0.16	2460	6.15	0.16	2502	6.255	Inf	2544	6.36	Inf
2419	6.0475	Inf	2461	6.1525	Inf	2503	6.2575	Inf	2545	6.3625	0.04
2420	6.05	Inf	2462	6.155	Inf	2504	6.26	Inf	2546	6.365	Inf
2421	6.0525	Inf	2463	6.1575	Inf	2505	6.2625	0.032	2547	6.3675	Inf
2422	6.055	Inf	2464	6.16	0.0533	2506	6.265	Inf	2548	6.37	Inf
2423	6.0575	Inf	2465	6.1625	Inf	2507	6.2675	Inf	2549	6.3725	Inf
2424	6.06	0.0533	2466	6.165	Inf	2508	6.27	Inf	2550	6.375	Inf
2425	6.0625	Inf	2467	6.1675	Inf	2509	6.2725	Inf	2551	6.3775	Inf
2426	6.065	Inf	2468	6.17	Inf	2510	6.275	Inf	2552	6.38	Inf
2427	6.0675	Inf	2469	6.1725	Inf	2511	6.2775	Inf	2553	6.3825	0.16
2428	6.07	Inf	2470	6.175	Inf	2512	6.28	Inf	2554	6.385	Inf
2429	6.0725	0.16	2471	6.1775	Inf	2513	6.2825	Inf	2555	6.3875	Inf
2430	6.075	Inf	2472	6.18	Inf	2514	6.285	Inf	2556	6.39	Inf
2431	6.0775	Inf	2473	6.1825	Inf	2515	6.2875	Inf	2557	6.3925	Inf
2432	6.08	Inf	2474	6.185	Inf	2516	6.29	Inf	2558	6.395	Inf
2433	6.0825	Inf	2475	6.1875	Inf	2517	6.2925	Inf	2559	6.3975	Inf
2434	6.085	Inf	2476	6.19	0.16	2518	6.295	Inf	2560	6.4	Inf
2435	6.0875	Inf	2477	6.1925	Inf	2519	6.2975	Inf	2561	6.4025	Inf
2436	6.09	Inf	2478	6.195	Inf	2520	6.3	0.16	2562	6.405	Inf
2437	6.0925	Inf	2479	6.1975	Inf	2521	6.3025	Inf	2563	6.4075	Inf
2438	6.095	Inf	2480	6.2	Inf	2522	6.305	Inf	2564	6.41	Inf
2439	6.0975	Inf	2481	6.2025	Inf	2523	6.3075	Inf	2565	6.4125	0.032
2440	6.1	Inf	2482	6.205	Inf	2524	6.31	Inf	2566	6.415	Inf

2567	6.4175	Inf	2638	6.595	Inf	2709	6.7706	Inf	2780	6.9446	Inf
2568	6.42	Inf	2639	6.5975	Inf	2710	6.7731	0.0004	2781	6.9471	Inf
2569	6.4225	Inf	2640	6.6	Inf	2711	6.7733	0	2782	6.9496	Inf
2570	6.425	Inf	2641	6.6025	Inf	2712	6.7758	0.0001	2783	6.9521	Inf
2571	6.4275	Inf	2642	6.605	Inf	2713	6.7783	0.0001	2784	6.9546	Inf
2572	6.43	Inf	2643	6.6075	Inf	2714	6.7808	0.0001	2785	6.955	0.0003
2573	6.4325	Inf	2644	6.61	Inf	2715	6.7833	0.0001	2786	6.9575	0.0002
2574	6.435	Inf	2645	6.6125	0.04	2716	6.7858	0.0001	2787	6.96	Inf
2575	6.4375	Inf	2646	6.615	Inf	2717	6.7883	0.0001	2788	6.9625	Inf
2576	6.44	Inf	2647	6.6175	Inf	2718	6.7908	0.0001	2789	6.965	0.0533
2577	6.4425	Inf	2648	6.62	Inf	2719	6.7933	0.0001	2790	6.9675	Inf
2578	6.445	Inf	2649	6.6225	Inf	2720	6.7958	0.0013	2791	6.97	0.16
2579	6.4475	Inf	2650	6.625	Inf	2721	6.7983	0.0533	2792	6.9725	Inf
2580	6.45	Inf	2651	6.6275	Inf	2722	6.8008	Inf	2793	6.975	Inf
2581	6.4525	Inf	2652	6.63	Inf	2723	6.8033	Inf	2794	6.9775	Inf
2582	6.455	Inf	2653	6.6325	Inf	2724	6.8058	Inf	2795	6.98	Inf
2583	6.4575	Inf	2654	6.635	Inf	2725	6.8083	Inf	2796	6.9825	Inf
2584	6.46	Inf	2655	6.6375	Inf	2726	6.8108	Inf	2797	6.985	Inf
2585	6.4625	0.04	2656	6.64	Inf	2727	6.8133	0.04	2798	6.9875	0.0094
2586	6.465	0.16	2657	6.6425	Inf	2728	6.8146	0.0002	2799	6.9876	0.0001
2587	6.4675	Inf	2658	6.645	0.16	2729	6.8171	0.0001	2800	6.9901	0.0002
2588	6.47	Inf	2659	6.6475	Inf	2730	6.8196	0.0001	2801	6.9926	0.04
2589	6.4725	Inf	2660	6.65	Inf	2731	6.8221	0.0001	2802	6.9951	Inf
2590	6.475	Inf	2661	6.6525	Inf	2732	6.8246	0.0001	2803	6.9976	Inf
2591	6.4775	Inf	2662	6.655	0.001	2733	6.8271	0.0001	2804	7.0001	0.0013
2592	6.48	Inf	2663	6.6575	0.0001	2734	6.8296	0.0001	2805	7.0026	0.0073
2593	6.4825	Inf	2664	6.66	0.02	2735	6.8321	0.0001	2806	7.0051	Inf
2594	6.485	Inf	2665	6.6625	0.0533	2736	6.8346	0.0001	2807	7.0076	Inf
2595	6.4875	Inf	2666	6.665	Inf	2737	6.8371	0.0001	2808	7.0101	Inf
2596	6.49	Inf	2667	6.6675	Inf	2738	6.8396	0.0001	2809	7.0126	Inf
2597	6.4925	0.16	2668	6.67	Inf	2739	6.8421	0.0001	2810	7.0151	Inf
2598	6.495	Inf	2669	6.6725	Inf	2740	6.8446	0.0001	2811	7.0176	Inf
2599	6.4975	Inf	2670	6.675	0.0533	2741	6.8471	0.0057	2812	7.0201	Inf
2600	6.5	Inf	2671	6.6775	Inf	2742	6.8496	0.0533	2813	7.0226	Inf
2601	6.5025	Inf	2672	6.68	0.0229	2743	6.8521	Inf	2814	7.0251	Inf
2602	6.505	Inf	2673	6.6806	0.0003	2744	6.8546	Inf	2815	7.0276	Inf
2603	6.5075	Inf	2674	6.6831	0.0002	2745	6.8571	Inf	2816	7.0301	Inf
2604	6.51	Inf	2675	6.6856	0.04	2746	6.8596	Inf	2817	7.0326	0.16
2605	6.5125	0.0533	2676	6.6881	Inf	2747	6.8621	0.16	2818	7.0351	Inf
2606	6.515	Inf	2677	6.6906	0.04	2748	6.8646	Inf	2819	7.0376	Inf
2607	6.5175	Inf	2678	6.6931	Inf	2749	6.8671	Inf	2820	7.0401	Inf
2608	6.52	Inf	2679	6.6956	Inf	2750	6.8696	Inf	2821	7.0426	Inf
2609	6.5225	Inf	2680	6.6981	0.16	2751	6.8721	Inf	2822	7.0451	Inf
2610	6.525	Inf	2681	6.7006	0.0009	2752	6.8746	Inf	2823	7.0476	Inf
2611	6.5275	Inf	2682	6.7031	0.0229	2753	6.8771	Inf	2824	7.0501	Inf
2612	6.53	Inf	2683	6.7056	0.0533	2754	6.8796	Inf	2825	7.0526	0.0123
2613	6.5325	Inf	2684	6.7081	Inf	2755	6.8821	Inf	2826	7.0552	0.0001
2614	6.535	Inf	2685	6.7106	Inf	2756	6.8846	Inf	2827	7.0539	0.0001
2615	6.5375	Inf	2686	6.7131	Inf	2757	6.8871	Inf	2828	7.0564	0.0003
2616	6.54	Inf	2687	6.7156	Inf	2758	6.8896	Inf	2829	7.0589	0.0048
2617	6.5425	Inf	2688	6.7181	Inf	2759	6.8921	Inf	2830	7.0614	0.0533
2618	6.545	Inf	2689	6.7206	Inf	2760	6.8946	Inf	2831	7.0639	Inf
2619	6.5475	Inf	2690	6.7231	Inf	2761	6.8971	Inf	2832	7.0664	Inf
2620	6.55	Inf	2691	6.7256	0.0015	2762	6.8996	0.04	2833	7.0689	0.16
2621	6.5525	Inf	2692	6.7281	Inf	2763	6.9021	Inf	2834	7.0714	Inf
2622	6.555	Inf	2693	6.7306	Inf	2764	6.9046	Inf	2835	7.0739	Inf
2623	6.5575	Inf	2694	6.7331	Inf	2765	6.9071	Inf	2836	7.0764	Inf
2624	6.56	Inf	2695	6.7356	Inf	2766	6.9096	Inf	2837	7.0789	Inf
2625	6.5625	0.0533	2696	6.7381	Inf	2767	6.9121	0.0533	2838	7.0814	Inf
2626	6.565	Inf	2697	6.7406	0.0229	2768	6.9146	Inf	2839	7.0839	Inf
2627	6.5675	Inf	2698	6.7431	0.04	2769	6.9171	Inf	2840	7.0864	0.04
2628	6.57	Inf	2699	6.7456	Inf	2770	6.9196	Inf	2841	7.0889	Inf
2629	6.5725	Inf	2700	6.7481	Inf	2771	6.9221	Inf	2842	7.0914	Inf
2630	6.575	Inf	2701	6.7506	0.0533	2772	6.9246	Inf	2843	7.0939	Inf
2631	6.5775	Inf	2702	6.7531	Inf	2773	6.9271	0.16	2844	7.0964	Inf
2632	6.58	Inf	2703	6.7556	Inf	2774	6.9296	Inf	2845	7.0989	0.0229
2633	6.5825	Inf	2704	6.7581	Inf	2775	6.9321	Inf	2846	7.1014	0.0008
2634	6.585	Inf	2705	6.7606	Inf	2776	6.9346	Inf	2847	7.1039	Inf
2635	6.5875	0.16	2706	6.7631	Inf	2777	6.9371	Inf	2848	7.1064	Inf
2636	6.59	Inf	2707	6.7656	Inf	2778	6.9396	Inf	2849	7.1089	0.04
2637	6.5925	Inf	2708	6.7681	0.16	2779	6.9421	Inf	2850	7.1114	Inf

2851	7.1139	Inf	2922	7.2892	Inf	2993	7.4667	Inf	3064	7.6277	Inf
2852	7.1164	Inf	2923	7.2917	Inf	2994	7.4692	Inf	3065	7.6301	0.0013
2853	7.1189	Inf	2924	7.2942	Inf	2995	7.4717	Inf	3066	7.6326	0.0003
2854	7.12	0.0008	2925	7.2967	Inf	2996	7.4742	Inf	3067	7.6351	0.0533
2855	7.1225	0.0001	2926	7.2992	Inf	2997	7.4767	Inf	3068	7.6376	0.04
2856	7.1244	0.0015	2927	7.3017	0.0002	2998	7.4792	Inf	3069	7.6401	0.0267
2857	7.1269	0.0003	2928	7.3042	0.0267	2999	7.4817	0.16	3070	7.6421	0.0015
2858	7.1294	0.04	2929	7.3067	Inf	3000	7.4836	0.0009	3071	7.6446	0.0008
2859	7.1317	0.0018	2930	7.3092	0.04	3001	7.4844	0.0001	3072	7.6471	0.0533
2860	7.1342	0.0007	2931	7.3117	Inf	3002	7.4869	0.0002	3073	7.6496	Inf
2861	7.1367	0.0533	2932	7.3142	Inf	3003	7.4894	0.0267	3074	7.6521	0.0533
2862	7.1392	0.16	2933	7.3167	Inf	3004	7.4919	0.16	3075	7.6546	Inf
2863	7.1417	0.005	2934	7.3192	Inf	3005	7.4944	0.08	3076	7.6571	Inf
2864	7.1442	0.0022	2935	7.3217	Inf	3006	7.4969	Inf	3077	7.6596	Inf
2865	7.1467	0.0019	2936	7.3242	Inf	3007	7.4994	0.0229	3078	7.6621	Inf
2866	7.1492	0.0024	2937	7.3267	Inf	3008	7.5019	0.0002	3079	7.6646	Inf
2867	7.1517	0.04	2938	7.3292	Inf	3009	7.5019	0	3080	7.6671	0.16
2868	7.1542	Inf	2939	7.3317	Inf	3010	7.5044	0.0002	3081	7.6696	Inf
2869	7.1567	Inf	2940	7.3342	Inf	3011	7.5069	0.0267	3082	7.6721	Inf
2870	7.1592	Inf	2941	7.3367	Inf	3012	7.5094	Inf	3083	7.6746	Inf
2871	7.1617	Inf	2942	7.3392	Inf	3013	7.5119	Inf	3084	7.6771	Inf
2872	7.1642	0.04	2943	7.3417	0.16	3014	7.5144	Inf	3085	7.6796	Inf
2873	7.1667	0.0094	2944	7.3442	Inf	3015	7.5169	0.0533	3086	7.6821	Inf
2874	7.1692	0.016	2945	7.3467	Inf	3016	7.5194	0.0229	3087	7.6846	Inf
2875	7.1717	Inf	2946	7.3492	Inf	3017	7.5219	0.0533	3088	7.6871	Inf
2876	7.1742	Inf	2947	7.3517	Inf	3018	7.5244	0.016	3089	7.6896	Inf
2877	7.1767	Inf	2948	7.3542	Inf	3019	7.5266	0.001	3090	7.6921	Inf
2878	7.1792	Inf	2949	7.3567	Inf	3020	7.5272	0	3091	7.6946	Inf
2879	7.1817	Inf	2950	7.3592	0.0533	3021	7.5297	0.0002	3092	7.6971	Inf
2880	7.1842	Inf	2951	7.3617	Inf	3022	7.5322	0.0038	3093	7.6996	0.016
2881	7.1867	Inf	2952	7.3642	Inf	3023	7.5347	0.04	3094	7.7021	0.0008
2882	7.1892	Inf	2953	7.3667	Inf	3024	7.5372	Inf	3095	7.7046	0.0533
2883	7.1917	Inf	2954	7.3692	Inf	3025	7.5397	Inf	3096	7.7071	Inf
2884	7.1942	Inf	2955	7.3717	Inf	3026	7.5422	Inf	3097	7.7096	Inf
2885	7.1967	0.08	2956	7.3742	Inf	3027	7.5447	0.04	3098	7.7121	Inf
2886	7.1992	Inf	2957	7.3767	Inf	3028	7.5472	Inf	3099	7.7146	Inf
2887	7.2017	0.0004	2958	7.3792	Inf	3029	7.5497	Inf	3100	7.7171	0.16
2888	7.2042	Inf	2959	7.3817	Inf	3030	7.5522	Inf	3101	7.7196	Inf
2889	7.2067	0.04	2960	7.3842	Inf	3031	7.5547	Inf	3102	7.7221	Inf
2890	7.2092	Inf	2961	7.3867	Inf	3032	7.5572	0.0012	3103	7.7246	Inf
2891	7.2117	0.0533	2962	7.3892	Inf	3033	7.5597	0.0002	3104	7.7271	Inf
2892	7.2142	Inf	2963	7.3917	Inf	3034	7.5616	0.0005	3105	7.7296	Inf
2893	7.2167	Inf	2964	7.3942	Inf	3035	7.5641	0.0003	3106	7.7321	Inf
2894	7.2192	Inf	2965	7.3967	Inf	3036	7.5666	0.0031	3107	7.7346	Inf
2895	7.2217	Inf	2966	7.3992	0.016	3037	7.5691	Inf	3108	7.7371	Inf
2896	7.2242	Inf	2967	7.4017	0.0006	3038	7.5716	0.04	3109	7.7396	Inf
2897	7.2267	Inf	2968	7.4042	0.032	3039	7.5741	Inf	3110	7.7421	Inf
2898	7.2292	0.16	2969	7.4067	0.16	3040	7.5766	Inf	3111	7.7446	Inf
2899	7.2317	Inf	2970	7.4092	0.0533	3041	7.5791	Inf	3112	7.7471	Inf
2900	7.2342	Inf	2971	7.4117	Inf	3042	7.5816	Inf	3113	7.7496	Inf
2901	7.2367	Inf	2972	7.4142	Inf	3043	7.5841	0.032	3114	7.7521	0.0533
2902	7.2392	Inf	2973	7.4167	Inf	3044	7.5849	0.0006	3115	7.7546	Inf
2903	7.2417	Inf	2974	7.4192	Inf	3045	7.5874	0.0004	3116	7.7571	0.16
2904	7.2442	Inf	2975	7.4217	Inf	3046	7.5899	0.016	3117	7.7596	Inf
2905	7.2467	Inf	2976	7.4242	Inf	3047	7.5907	0.0004	3118	7.7621	Inf
2906	7.2492	Inf	2977	7.4267	Inf	3048	7.5932	0.0003	3119	7.7646	Inf
2907	7.2517	Inf	2978	7.4292	Inf	3049	7.5957	Inf	3120	7.7671	Inf
2908	7.2542	0.04	2979	7.4317	Inf	3050	7.5982	0.0533	3121	7.7696	Inf
2909	7.2567	Inf	2980	7.4342	Inf	3051	7.6007	0.0007	3122	7.7721	Inf
2910	7.2592	Inf	2981	7.4367	Inf	3052	7.6031	0.0013	3123	7.7746	Inf
2911	7.2617	0.0533	2982	7.4392	Inf	3053	7.6056	0.0002	3124	7.7771	Inf
2912	7.2642	Inf	2983	7.4417	Inf	3054	7.6081	0.0009	3125	7.7796	Inf
2913	7.2667	Inf	2984	7.4442	Inf	3055	7.6106	0.016	3126	7.7821	Inf
2914	7.2692	Inf	2985	7.4467	Inf	3056	7.6109	0.0003	3127	7.7846	Inf
2915	7.2717	Inf	2986	7.4492	Inf	3057	7.6134	0.0008	3128	7.7871	Inf
2916	7.2742	Inf	2987	7.4517	Inf	3058	7.6149	0.0009	3129	7.7896	Inf
2917	7.2767	0.16	2988	7.4542	Inf	3059	7.6152	0.0001	3130	7.7921	Inf
2918	7.2792	Inf	2989	7.4567	Inf	3060	7.6177	0.0006	3131	7.7946	Inf
2919	7.2817	Inf	2990	7.4592	0.0533	3061	7.6202	0.0533	3132	7.7971	Inf
2920	7.2842	Inf	2991	7.4617	Inf	3062	7.6227	Inf	3133	7.7996	0.0229
2921	7.2867	Inf	2992	7.4642	Inf	3063	7.6252	Inf	3134	7.8021	0.0009

3135	7.8046	0.0533	3206	7.9821	0.16	3277	8.1596	Inf	3348	8.3371	Inf
3136	7.8071	Inf	3207	7.9846	Inf	3278	8.1621	0.0533	3349	8.3396	Inf
3137	7.8096	Inf	3208	7.9871	Inf	3279	8.1646	Inf	3350	8.3421	Inf
3138	7.8121	Inf	3209	7.9896	Inf	3280	8.1671	Inf	3351	8.3446	Inf
3139	7.8146	0.0533	3210	7.9921	Inf	3281	8.1696	Inf	3352	8.3471	Inf
3140	7.8171	Inf	3211	7.9946	Inf	3282	8.1721	Inf	3353	8.3496	Inf
3141	7.8196	Inf	3212	7.9971	Inf	3283	8.1746	Inf	3354	8.3521	Inf
3142	7.8221	Inf	3213	7.9996	0.0178	3284	8.1771	Inf	3355	8.3546	Inf
3143	7.8246	Inf	3214	8.0021	0.0005	3285	8.1796	Inf	3356	8.3571	Inf
3144	7.8271	Inf	3215	8.0046	0.0003	3286	8.1821	0.0533	3357	8.3596	Inf
3145	7.8296	Inf	3216	8.0071	0.0003	3287	8.1846	Inf	3358	8.3621	Inf
3146	7.8321	0.16	3217	8.0096	0.0001	3288	8.1871	Inf	3359	8.3646	Inf
3147	7.8346	Inf	3218	8.0121	0.0001	3289	8.1896	Inf	3360	8.3671	Inf
3148	7.8371	Inf	3219	8.0146	0.0001	3290	8.1921	Inf	3361	8.3696	Inf
3149	7.8396	Inf	3220	8.0171	0.0001	3291	8.1946	Inf	3362	8.3721	Inf
3150	7.8421	Inf	3221	8.0196	0.0001	3292	8.1971	0.0533	3363	8.3746	Inf
3151	7.8446	Inf	3222	8.0221	0.0001	3293	8.1996	Inf	3364	8.3771	0.0533
3152	7.8471	Inf	3223	8.0246	0.0001	3294	8.2021	0.0009	3365	8.3796	Inf
3153	7.8496	Inf	3224	8.0271	0.0002	3295	8.2046	0.0533	3366	8.3821	Inf
3154	7.8521	Inf	3225	8.0296	Inf	3296	8.2071	Inf	3367	8.3846	0.16
3155	7.8546	Inf	3226	8.0321	0.04	3297	8.2096	Inf	3368	8.3871	Inf
3156	7.8571	Inf	3227	8.0346	Inf	3298	8.2121	Inf	3369	8.3896	Inf
3157	7.8596	Inf	3228	8.0371	0.0533	3299	8.2146	0.04	3370	8.3921	Inf
3158	7.8621	Inf	3229	8.0396	Inf	3300	8.2171	Inf	3371	8.3946	Inf
3159	7.8646	0.0533	3230	8.0421	Inf	3301	8.2196	Inf	3372	8.3971	Inf
3160	7.8671	Inf	3231	8.0446	Inf	3302	8.2221	Inf	3373	8.3996	0.0133
3161	7.8696	Inf	3232	8.0471	Inf	3303	8.2246	Inf	3374	8.4021	0.001
3162	7.8721	0.16	3233	8.0496	Inf	3304	8.2271	Inf	3375	8.4046	0.0533
3163	7.8746	Inf	3234	8.0521	0.16	3305	8.2296	Inf	3376	8.4071	Inf
3164	7.8771	Inf	3235	8.0546	Inf	3306	8.2321	Inf	3377	8.4096	Inf
3165	7.8796	0.0533	3236	8.0571	Inf	3307	8.2346	Inf	3378	8.4121	Inf
3166	7.8821	Inf	3237	8.0596	Inf	3308	8.2371	Inf	3379	8.4146	Inf
3167	7.8846	Inf	3238	8.0621	Inf	3309	8.2396	Inf	3380	8.4171	Inf
3168	7.8871	Inf	3239	8.0646	Inf	3310	8.2421	Inf	3381	8.4196	Inf
3169	7.8896	Inf	3240	8.0671	Inf	3311	8.2446	Inf	3382	8.4221	Inf
3170	7.8921	Inf	3241	8.0696	Inf	3312	8.2471	Inf	3383	8.4246	Inf
3171	7.8946	0.0533	3242	8.0721	Inf	3313	8.2496	Inf	3384	8.4271	0.04
3172	7.8971	Inf	3243	8.0746	Inf	3314	8.2521	Inf	3385	8.4296	Inf
3173	7.8996	0.0229	3244	8.0771	Inf	3315	8.2546	Inf	3386	8.4321	Inf
3174	7.9021	0.0012	3245	8.0796	Inf	3316	8.2571	Inf	3387	8.4346	Inf
3175	7.9046	Inf	3246	8.0821	Inf	3317	8.2596	0.16	3388	8.4371	Inf
3176	7.9071	0.04	3247	8.0846	Inf	3318	8.2621	Inf	3389	8.4396	Inf
3177	7.9096	Inf	3248	8.0871	0.0533	3319	8.2646	0.0533	3390	8.4421	Inf
3178	7.9121	0.0533	3249	8.0896	0.16	3320	8.2671	Inf	3391	8.4446	Inf
3179	7.9146	Inf	3250	8.0921	Inf	3321	8.2696	Inf	3392	8.4471	Inf
3180	7.9171	Inf	3251	8.0946	Inf	3322	8.2721	Inf	3393	8.4496	Inf
3181	7.9196	Inf	3252	8.0971	Inf	3323	8.2746	Inf	3394	8.4521	Inf
3182	7.9221	Inf	3253	8.0996	Inf	3324	8.2771	Inf	3395	8.4546	Inf
3183	7.9246	Inf	3254	8.1021	0.0004	3325	8.2796	0.0533	3396	8.4571	0.16
3184	7.9271	Inf	3255	8.1046	0.0005	3326	8.2821	Inf	3397	8.4596	Inf
3185	7.9296	Inf	3256	8.1071	0.08	3327	8.2846	Inf	3398	8.4621	Inf
3186	7.9321	Inf	3257	8.1096	Inf	3328	8.2871	Inf	3399	8.4646	Inf
3187	7.9346	Inf	3258	8.1121	0.04	3329	8.2896	Inf	3400	8.4671	Inf
3188	7.9371	Inf	3259	8.1146	Inf	3330	8.2921	Inf	3401	8.4696	Inf
3189	7.9396	Inf	3260	8.1171	Inf	3331	8.2946	0.04	3402	8.4721	Inf
3190	7.9421	Inf	3261	8.1196	Inf	3332	8.2971	Inf	3403	8.4746	Inf
3191	7.9446	Inf	3262	8.1221	Inf	3333	8.2996	0.0267	3404	8.4771	0.0533
3192	7.9471	Inf	3263	8.1246	Inf	3334	8.3021	0.001	3405	8.4796	Inf
3193	7.9496	0.16	3264	8.1271	Inf	3335	8.3046	0.0533	3406	8.4821	Inf
3194	7.9521	Inf	3265	8.1296	Inf	3336	8.3071	Inf	3407	8.4846	Inf
3195	7.9546	Inf	3266	8.1321	Inf	3337	8.3096	Inf	3408	8.4871	Inf
3196	7.9571	Inf	3267	8.1346	Inf	3338	8.3121	Inf	3409	8.4896	Inf
3197	7.9596	Inf	3268	8.1371	Inf	3339	8.3146	Inf	3410	8.4921	Inf
3198	7.9621	0.0533	3269	8.1396	Inf	3340	8.3171	Inf	3411	8.4946	Inf
3199	7.9646	Inf	3270	8.1421	Inf	3341	8.3196	Inf	3412	8.4971	0.16
3200	7.9671	Inf	3271	8.1446	Inf	3342	8.3221	Inf	3413	8.4996	0.0133
3201	7.9696	Inf	3272	8.1471	Inf	3343	8.3246	Inf	3414	8.5021	0.0004
3202	7.9721	Inf	3273	8.1496	Inf	3344	8.3271	0.0533	3415	8.5046	0.0533
3203	7.9746	0.0533	3274	8.1521	Inf	3345	8.3296	Inf	3416	8.5071	Inf
3204	7.9771	Inf	3275	8.1546	Inf	3346	8.3321	Inf	3417	8.5096	Inf
3205	7.9796	0.0533	3276	8.1571	0.16	3347	8.3346	Inf	3418	8.5121	Inf

3419	8.5146	Inf	3490	8.6921	Inf	3561	8.8696	Inf	3632	9.0471	Inf
3420	8.5171	0.16	3491	8.6946	0.04	3562	8.8721	Inf	3633	9.0496	Inf
3421	8.5196	Inf	3492	8.6971	Inf	3563	8.8746	0.0533	3634	9.0521	Inf
3422	8.5221	Inf	3493	8.6996	0.0267	3564	8.8771	Inf	3635	9.0546	Inf
3423	8.5246	Inf	3494	8.7021	0.0003	3565	8.8796	0.0533	3636	9.0571	Inf
3424	8.5271	Inf	3495	8.7046	0.0004	3566	8.8821	Inf	3637	9.0596	Inf
3425	8.5296	Inf	3496	8.7071	0.0004	3567	8.8846	Inf	3638	9.0621	Inf
3426	8.5321	Inf	3497	8.7096	0.0007	3568	8.8871	Inf	3639	9.0646	Inf
3427	8.5346	Inf	3498	8.7121	0.04	3569	8.8896	Inf	3640	9.0671	Inf
3428	8.5371	0.08	3499	8.7146	Inf	3570	8.8921	Inf	3641	9.0696	Inf
3429	8.5396	Inf	3500	8.7171	Inf	3571	8.8946	0.0533	3642	9.0721	0.16
3430	8.5421	Inf	3501	8.7196	Inf	3572	8.8971	Inf	3643	9.0746	Inf
3431	8.5446	Inf	3502	8.7221	Inf	3573	8.8996	0.016	3644	9.0771	Inf
3432	8.5471	Inf	3503	8.7246	Inf	3574	8.9021	0.0007	3645	9.0796	Inf
3433	8.5496	Inf	3504	8.7271	Inf	3575	8.9046	0.04	3646	9.0821	Inf
3434	8.5521	Inf	3505	8.7296	Inf	3576	8.9071	0.0533	3647	9.0846	Inf
3435	8.5546	Inf	3506	8.7321	Inf	3577	8.9096	Inf	3648	9.0871	0.0533
3436	8.5571	Inf	3507	8.7346	Inf	3578	8.9121	0.0533	3649	9.0896	Inf
3437	8.5596	0.04	3508	8.7371	Inf	3579	8.9146	Inf	3650	9.0921	Inf
3438	8.5621	Inf	3509	8.7396	Inf	3580	8.9171	Inf	3651	9.0946	Inf
3439	8.5646	Inf	3510	8.7421	Inf	3581	8.9196	Inf	3652	9.0971	Inf
3440	8.5671	Inf	3511	8.7446	Inf	3582	8.9221	Inf	3653	9.0996	0.0229
3441	8.5696	Inf	3512	8.7471	Inf	3583	8.9246	Inf	3654	9.1021	0.0002
3442	8.5721	Inf	3513	8.7496	0.16	3584	8.9271	Inf	3655	9.1046	0.0001
3443	8.5746	0.08	3514	8.7521	Inf	3585	8.9296	Inf	3656	9.1071	0.0002
3444	8.5771	Inf	3515	8.7546	Inf	3586	8.9321	Inf	3657	9.1096	Inf
3445	8.5796	0.0533	3516	8.7571	Inf	3587	8.9346	Inf	3658	9.1121	Inf
3446	8.5821	Inf	3517	8.7596	Inf	3588	8.9371	Inf	3659	9.1146	Inf
3447	8.5846	Inf	3518	8.7621	0.08	3589	8.9396	0.16	3660	9.1171	Inf
3448	8.5871	Inf	3519	8.7646	Inf	3590	8.9421	Inf	3661	9.1196	Inf
3449	8.5896	Inf	3520	8.7671	Inf	3591	8.9446	Inf	3662	9.1221	Inf
3450	8.5921	0.16	3521	8.7696	Inf	3592	8.9471	Inf	3663	9.1246	Inf
3451	8.5946	0.0533	3522	8.7721	Inf	3593	8.9496	Inf	3664	9.1271	Inf
3452	8.5971	Inf	3523	8.7746	0.0533	3594	8.9521	Inf	3665	9.1296	Inf
3453	8.5996	0.0267	3524	8.7771	Inf	3595	8.9546	Inf	3666	9.1321	Inf
3454	8.6021	0.001	3525	8.7796	0.04	3596	8.9571	Inf	3667	9.1346	Inf
3455	8.6046	0.0533	3526	8.7821	Inf	3597	8.9596	Inf	3668	9.1371	0.0533
3456	8.6071	Inf	3527	8.7846	Inf	3598	8.9621	0.0533	3669	9.1396	0.16
3457	8.6096	0.16	3528	8.7871	Inf	3599	8.9646	Inf	3670	9.1421	Inf
3458	8.6121	Inf	3529	8.7896	Inf	3600	8.9671	Inf	3671	9.1446	Inf
3459	8.6146	0.0533	3530	8.7921	Inf	3601	8.9696	Inf	3672	9.1471	Inf
3460	8.6171	Inf	3531	8.7946	0.0533	3602	8.9721	Inf	3673	9.1496	Inf
3461	8.6196	Inf	3532	8.7971	Inf	3603	8.9746	0.04	3674	9.1521	Inf
3462	8.6221	Inf	3533	8.7996	Inf	3604	8.9771	Inf	3675	9.1546	Inf
3463	8.6246	Inf	3534	8.8021	0.0009	3605	8.9796	0.0533	3676	9.1571	Inf
3464	8.6271	Inf	3535	8.8046	0.04	3606	8.9821	Inf	3677	9.1596	0.08
3465	8.6296	Inf	3536	8.8071	0.0533	3607	8.9846	Inf	3678	9.1621	Inf
3466	8.6321	Inf	3537	8.8096	Inf	3608	8.9871	Inf	3679	9.1646	Inf
3467	8.6346	Inf	3538	8.8121	0.0533	3609	8.9896	Inf	3680	9.1671	Inf
3468	8.6371	Inf	3539	8.8146	Inf	3610	8.9921	Inf	3681	9.1696	Inf
3469	8.6396	Inf	3540	8.8171	Inf	3611	8.9946	0.0533	3682	9.1721	Inf
3470	8.6421	Inf	3541	8.8196	Inf	3612	8.9971	Inf	3683	9.1746	0.04
3471	8.6446	Inf	3542	8.8221	Inf	3613	8.9996	0.0533	3684	9.1771	Inf
3472	8.6471	Inf	3543	8.8246	Inf	3614	9.0021	0.0007	3685	9.1796	0.0533
3473	8.6496	Inf	3544	8.8271	Inf	3615	9.0046	0.0533	3686	9.1821	Inf
3474	8.6521	Inf	3545	8.8296	Inf	3616	9.0071	Inf	3687	9.1846	Inf
3475	8.6546	Inf	3546	8.8321	Inf	3617	9.0096	0.0533	3688	9.1871	Inf
3476	8.6571	Inf	3547	8.8346	Inf	3618	9.0121	Inf	3689	9.1896	Inf
3477	8.6596	Inf	3548	8.8371	0.16	3619	9.0146	Inf	3690	9.1921	Inf
3478	8.6621	0.16	3549	8.8396	Inf	3620	9.0171	Inf	3691	9.1946	0.0533
3479	8.6646	0.0533	3550	8.8421	Inf	3621	9.0196	Inf	3692	9.1971	Inf
3480	8.6671	Inf	3551	8.8446	Inf	3622	9.0221	Inf	3693	9.1996	Inf
3481	8.6696	Inf	3552	8.8471	Inf	3623	9.0246	Inf	3694	9.2021	0.0007
3482	8.6721	Inf	3553	8.8496	Inf	3624	9.0271	Inf	3695	9.2046	0.0533
3483	8.6746	Inf	3554	8.8521	Inf	3625	9.0296	Inf	3696	9.2071	Inf
3484	8.6771	Inf	3555	8.8546	Inf	3626	9.0321	0.04	3697	9.2096	Inf
3485	8.6796	0.0533	3556	8.8571	Inf	3627	9.0346	Inf	3698	9.2121	Inf
3486	8.6821	Inf	3557	8.8596	Inf	3628	9.0371	0.0533	3699	9.2146	0.04
3487	8.6846	Inf	3558	8.8621	0.0533	3629	9.0396	Inf	3700	9.2171	Inf
3488	8.6871	Inf	3559	8.8646	Inf	3630	9.0421	Inf	3701	9.2196	Inf
3489	8.6896	Inf	3560	8.8671	Inf	3631	9.0446	Inf	3702	9.2221	Inf

3703	9.2246	Inf	3774	9.4021	0.0007	3845	9.5796	0.04	3916	9.7571	Inf
3704	9.2271	Inf	3775	9.4046	0.0533	3846	9.5821	Inf	3917	9.7596	Inf
3705	9.2296	Inf	3776	9.4071	Inf	3847	9.5846	Inf	3918	9.7621	0.0533
3706	9.2321	Inf	3777	9.4096	Inf	3848	9.5871	Inf	3919	9.7646	Inf
3707	9.2346	Inf	3778	9.4121	Inf	3849	9.5896	Inf	3920	9.7671	Inf
3708	9.2371	Inf	3779	9.4146	0.04	3850	9.5921	Inf	3921	9.7696	Inf
3709	9.2396	Inf	3780	9.4171	Inf	3851	9.5946	0.0533	3922	9.7721	Inf
3710	9.2421	Inf	3781	9.4196	Inf	3852	9.5971	Inf	3923	9.7746	0.04
3711	9.2446	Inf	3782	9.4221	Inf	3853	9.5996	0.0533	3924	9.7771	Inf
3712	9.2471	Inf	3783	9.4246	Inf	3854	9.6021	0.0008	3925	9.7796	0.0533
3713	9.2496	Inf	3784	9.4271	Inf	3855	9.6046	0.0533	3926	9.7821	Inf
3714	9.2521	Inf	3785	9.4296	Inf	3856	9.6071	0.0533	3927	9.7846	Inf
3715	9.2546	Inf	3786	9.4321	Inf	3857	9.6096	Inf	3928	9.7871	Inf
3716	9.2571	Inf	3787	9.4346	Inf	3858	9.6121	0.0533	3929	9.7896	Inf
3717	9.2596	0.16	3788	9.4371	Inf	3859	9.6146	Inf	3930	9.7921	Inf
3718	9.2621	Inf	3789	9.4396	Inf	3860	9.6171	Inf	3931	9.7946	0.0533
3719	9.2646	0.0533	3790	9.4421	Inf	3861	9.6196	Inf	3932	9.7971	Inf
3720	9.2671	Inf	3791	9.4446	Inf	3862	9.6221	Inf	3933	9.7996	0.0178
3721	9.2696	Inf	3792	9.4471	Inf	3863	9.6246	Inf	3934	9.8021	0.0008
3722	9.2721	Inf	3793	9.4496	Inf	3864	9.6271	0.16	3935	9.8046	0.0034
3723	9.2746	Inf	3794	9.4521	Inf	3865	9.6296	Inf	3936	9.8071	0.0035
3724	9.2771	0.0533	3795	9.4546	Inf	3866	9.6321	Inf	3937	9.8096	0.0033
3725	9.2796	Inf	3796	9.4571	Inf	3867	9.6346	Inf	3938	9.8121	0.0044
3726	9.2821	0.0533	3797	9.4596	0.16	3868	9.6371	Inf	3939	9.8146	Inf
3727	9.2846	Inf	3798	9.4621	Inf	3869	9.6396	Inf	3940	9.8171	Inf
3728	9.2871	Inf	3799	9.4646	0.0533	3870	9.6421	Inf	3941	9.8196	Inf
3729	9.2896	Inf	3800	9.4671	Inf	3871	9.6446	Inf	3942	9.8221	Inf
3730	9.2921	0.16	3801	9.4696	Inf	3872	9.6471	Inf	3943	9.8246	Inf
3731	9.2946	Inf	3802	9.4721	Inf	3873	9.6496	Inf	3944	9.8271	Inf
3732	9.2971	0.0533	3803	9.4746	Inf	3874	9.6521	Inf	3945	9.8296	0.0533
3733	9.2996	0.0533	3804	9.4771	Inf	3875	9.6546	Inf	3946	9.8321	0.16
3734	9.3021	0.0002	3805	9.4796	0.08	3876	9.6571	Inf	3947	9.8346	0.0533
3735	9.3046	0.0007	3806	9.4821	Inf	3877	9.6596	Inf	3948	9.8371	Inf
3736	9.3071	Inf	3807	9.4846	Inf	3878	9.6621	0.0533	3949	9.8396	Inf
3737	9.3096	Inf	3808	9.4871	Inf	3879	9.6646	0.16	3950	9.8421	Inf
3738	9.3121	Inf	3809	9.4896	Inf	3880	9.6671	Inf	3951	9.8446	Inf
3739	9.3146	0.04	3810	9.4921	Inf	3881	9.6696	Inf	3952	9.8471	Inf
3740	9.3171	Inf	3811	9.4946	0.04	3882	9.6721	Inf	3953	9.8496	Inf
3741	9.3196	Inf	3812	9.4971	Inf	3883	9.6746	0.0533	3954	9.8521	Inf
3742	9.3221	Inf	3813	9.4996	0.0267	3884	9.6771	Inf	3955	9.8546	Inf
3743	9.3246	Inf	3814	9.5021	0.0004	3885	9.6796	0.0533	3956	9.8571	Inf
3744	9.3271	Inf	3815	9.5046	0.04	3886	9.6821	Inf	3957	9.8596	Inf
3745	9.3296	Inf	3816	9.5071	Inf	3887	9.6846	Inf	3958	9.8621	Inf
3746	9.3321	Inf	3817	9.5096	Inf	3888	9.6871	Inf	3959	9.8646	Inf
3747	9.3346	Inf	3818	9.5121	Inf	3889	9.6896	Inf	3960	9.8671	Inf
3748	9.3371	Inf	3819	9.5146	Inf	3890	9.6921	Inf	3961	9.8696	Inf
3749	9.3396	Inf	3820	9.5171	Inf	3891	9.6946	0.0533	3962	9.8721	Inf
3750	9.3421	Inf	3821	9.5196	Inf	3892	9.6971	Inf	3963	9.8746	Inf
3751	9.3446	Inf	3822	9.5221	Inf	3893	9.6996	0.0267	3964	9.8771	0.16
3752	9.3471	Inf	3823	9.5246	Inf	3894	9.7021	0.001	3965	9.8796	Inf
3753	9.3496	Inf	3824	9.5271	0.0533	3895	9.7046	0.0533	3966	9.8821	Inf
3754	9.3521	Inf	3825	9.5296	Inf	3896	9.7071	0.0533	3967	9.8846	0.0533
3755	9.3546	Inf	3826	9.5321	Inf	3897	9.7096	Inf	3968	9.8871	Inf
3756	9.3571	Inf	3827	9.5346	Inf	3898	9.7121	0.0533	3969	9.8896	Inf
3757	9.3596	0.16	3828	9.5371	Inf	3899	9.7146	Inf	3970	9.8921	Inf
3758	9.3621	Inf	3829	9.5396	Inf	3900	9.7171	Inf	3971	9.8946	0.0533
3759	9.3646	0.0533	3830	9.5421	Inf	3901	9.7196	Inf	3972	9.8971	0.16
3760	9.3671	Inf	3831	9.5446	0.16	3902	9.7221	Inf	3973	9.8996	0.0229
3761	9.3696	Inf	3832	9.5471	Inf	3903	9.7246	Inf	3974	9.9021	0.0008
3762	9.3721	Inf	3833	9.5496	Inf	3904	9.7271	Inf	3975	9.9046	0.016
3763	9.3746	Inf	3834	9.5521	Inf	3905	9.7296	Inf	3976	9.9071	Inf
3764	9.3771	Inf	3835	9.5546	Inf	3906	9.7321	Inf	3977	9.9096	Inf
3765	9.3796	0.0533	3836	9.5571	Inf	3907	9.7346	Inf	3978	9.9121	Inf
3766	9.3821	Inf	3837	9.5596	Inf	3908	9.7371	Inf	3979	9.9146	Inf
3767	9.3846	0.16	3838	9.5621	Inf	3909	9.7396	0.16	3980	9.9171	Inf
3768	9.3871	Inf	3839	9.5646	Inf	3910	9.7421	Inf	3981	9.9196	Inf
3769	9.3896	Inf	3840	9.5671	Inf	3911	9.7446	Inf	3982	9.9221	Inf
3770	9.3921	Inf	3841	9.5696	Inf	3912	9.7471	Inf	3983	9.9246	Inf
3771	9.3946	0.0533	3842	9.5721	Inf	3913	9.7496	Inf	3984	9.9271	0.04
3772	9.3971	Inf	3843	9.5746	0.0533	3914	9.7521	Inf	3985	9.9296	Inf
3773	9.3996	0.0267	3844	9.5771	Inf	3915	9.7546	Inf	3986	9.9321	Inf

3987	9.9346	Inf	3994	9.9521	Inf	4001	9.9696	Inf	4008	9.9871	Inf
3988	9.9371	Inf	3995	9.9546	Inf	4002	9.9721	0.16	4009	9.9896	Inf
3989	9.9396	Inf	3996	9.9571	Inf	4003	9.9746	Inf	4010	9.9921	Inf
3990	9.9421	Inf	3997	9.9596	Inf	4004	9.9771	0.0533	4011	9.9946	Inf
3991	9.9446	Inf	3998	9.9621	Inf	4005	9.9796	Inf	4012	9.9971	Inf
3992	9.9471	Inf	3999	9.9646	Inf	4006	9.9821	Inf	4013	9.9996	0.0114
3993	9.9496	Inf	4000	9.9671	Inf	4007	9.9846	Inf	4014	10.002	0.0001